diamond

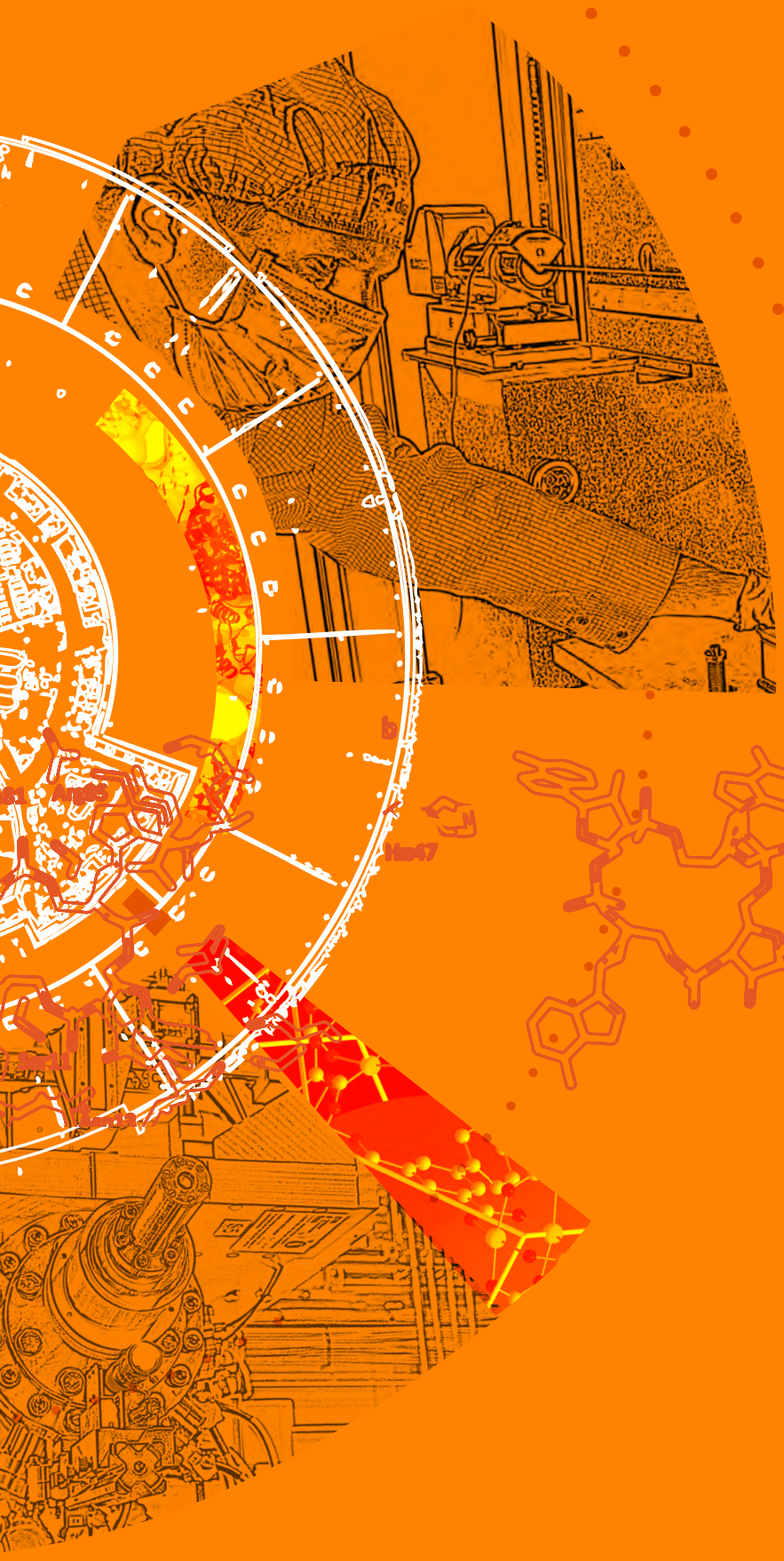

Diamond Light Source Ltd

2020/21

Contents

“As we look towards the second half of 2021 and beyond, we can hope for a more positive landscape thanks to the many efforts, including Diamond’s, towards creating vaccines to help protect us against COVID-19.”

Foreword

It has been a challenging year for all over the past 12 months. The COVID-19 pandemic has led to big changes all over the world, some temporary and some permanent. It is tragic that the pandemic has led to over three million deaths worldwide. Such an event highlights the importance of not only scientific research, but also collaboration; working together and supporting each other to get through a global crisis.

Diamond’s response to the pandemic has been all encompassing, from playing a key part in global research efforts to setting up robust and comprehensive safety measures on-site to supporting the local community by producing 3D printed visors for health workers. Adjustments have been made by all teams to enable remote working and remote use of nearly all microscopes and beamlines. As this review goes to press, the Government’s roadmap to bring the UK out of lockdown is on track and users are expected to return to the facility in limited numbers in the summer.

Research into SARS-CoV-2, the virus that causes COVID-19, became Diamond’s focus at the start of the pandemic. Combining state-of-the-art microscopes and beamlines, and staff and user expertise, Diamond can delve deep inside the inner workings of the virus. Understanding how it operates at the cellular level will open the doors to real possibilities of solutions and therapies. As we look towards the second half of 2021 and beyond, we can hope for a more positive landscape thanks to the many efforts, including Diamond’s, towards creating vaccines to help protect us against COVID-19.

Plans for the Diamond-II Programme, an integrated upgrade of the synchrotron, beamlines and computational facilities, are progressing well and are at the Outline Business Case stage. As social restrictions continue to lift, Diamond hopes to return to a more normal mode of operation and continue to be a world-leading centre for synchrotron science.

Professor Sir Adrian Smith
Chairman of the Board of Directors

CEO Welcome

A year on from the outbreak of the pandemic, a war is raging against the world: a new kind for our generation but a war that science can help win! At Diamond Light Source, we have kept operational throughout 2020 at varying levels, from COVID-19 related research only for the first quarter of the financial year to remote only experiments on all beamlines. It has obviously been challenging to welcome back users, although summer 2020 and early autumn attempts were successful. I was deeply impressed with the commitments of members of our staff mapping the virus at unprecedented scales, looking at targets to find possible roads to the development of therapeutics. I also commend all the people involved in other disciplines who remained focused on getting experiments delivered with users on the other side of a videoconference, together with all staff who worked so hard to keep operations going under very challenging circumstances.

The many COVID-19 related research projects that Diamond is working on are also a great demonstration of the powerful synergy between Diamond and its neighbouring research institutes, the Research Complex at Harwell and the Rosalind Franklin Institute. Diamond is working with its valued users and many partners to look at the fundamental interactions of the virus, from which it is hoped new therapies can be developed. Over 60 projects are enabling the study of how existing drugs, that have already been tested and approved for other diseases, can be repurposed and used to treat patients. The array of specialised tools and instruments at Diamond, along with the scientific and technical expertise of its staff, allow for many different techniques to be used, from looking at the structure of the virus and fitting drugs into it, like a tiny jigsaw puzzle, to taking direct images of the virus without its infectious component, making it possible to see how it interacts with potential drug chemicals.

Diamond also stole the headlines with the first paper on the study of the 3.67 million years old skull of the 'Little Foot' hominid, reaping over 168 pieces of media coverage and amounting to an estimated 10.2 million views of the story and, as you can imagine, driving great traffic to our website and blowing all records on social media!

We closed the year with another big project that is about to be published with our Socio-Economic Impact Study report where Technopolis, who carried out the assessment, estimated that Diamond has so far (2007-2020) had a cumulative, monetised impact of at least £1.8 billion, based on the evidence captured at this relatively early phase of the facility's operations. Bearing in mind that not all activities, outputs and outcomes could be monetised at this stage, this already compares very positively with the £1.2 billion investment in the facility (which includes all capital expenditure and operational costs so far). Of this total, 86% comes from UK taxpayers, with around £1 billion in investment from the Government via UKRI's Science and Technology Facilities Council (STFC), and 14% from the Wellcome Trust.

Diamond has wider societal benefits that it has not been possible to monetise. These include:

- 80,000 visitors reached so far through a programme of engagement at the heart of the facility supporting the UK Skills' agenda in science, technology, engineering and mathematics (STEM).
- Some of the leading scientific questions of the day being investigated by its 14,000-strong user community, with a part to play in 21st century challenges, from new technologies and environmental remediation to health and well-being.
- Widespread awareness of the value and relevance of STEM subjects to our everyday lives through many news articles and outreach activities.

In early 2021, Diamond celebrated its 10,000th publication with lead author Dr Jessica Wade from Imperial College London. The *Nature Communications* paper presented disruptive insights into chiral polymer films, which emit and absorb circularly polarised light, and offers the promise of achieving important technological advances, including high-performance displays, 3D imaging and quantum computing. This could fundamentally change the technology landscape by enabling a new generation of devices and is a great example of the amazing physical sciences being delivered with our instruments.

The Diamond-II Programme, an integrated upgrade of the synchrotron, beamlines and computational facilities, critical to maintaining our world-leading status, has progressed. Led by the Diamond-II Programme Director, Dr Laurent Chapon, and many staff, we have been working hard on the plans for the upgrade, and this is now leading to a formal Outline Business Case (OBC) for submission to the UK Government. We were pleased to have already received, after an independent reviewing process, an early indication of support from the Wellcome Trust subject to UKRI STFC's approval of the Programme. We are under no illusion that the fight for funding from all quarters will be fierce, and that the impact of the pandemic on our economy will be felt for decades to come; but I remain optimistic that the great science we have delivered over the past 14 years of operations sets us and our user community apart as a priority.

In the last financial year, we received 1,675 proposals for experiments on our instruments via peer reviewed access routes, requesting a total of 18,465 shifts. After peer review, 801 proposals were awarded beamtime. This resulted in 7,759 experimental shifts being awarded across 33 beamlines and 10 electron microscopes. We welcomed 488 on-site user visits from academia across all instruments, with an additional 4,473 remote user visits. The machine continues to perform to a high standard with 96.2% uptime and 132 hours mean time between failures (MTBF). Diamond also provides services critical to industry in the UK, with over 180 companies making use of the facility since operations began, normally paying £2.5 to £3 million per annum for proprietary access. We managed to switch all our engagement with the public to online, creating a dedicated site for our coronavirus research, along with many animations explaining how the science takes place and what is being uncovered about this devastating virus. In addition, during the past year Diamond has had approximately 6,161 significant interactions (30+ minutes) with 'virtual' visits from school students and members of the public, and we saw a 57% increase in attendance across our 33 virtual scientific and technical events this year. Likewise, our Student Engagement programme has continued to thrive despite pandemic restrictions, as we welcomed our 2020 Year in Industry and PhD cohorts in September and October respectively, and currently support a total of 116 studentships, at both undergraduate and PhD level, with our 2021 cohorts due to start later this year.

The past year also opened our eyes to more flexible working in certain areas, with always at the forefront of our minds, the importance of good internal support that ultimately sets us apart to deliver the best for our user community. I am grateful to all our staff and contractors who worked so hard to keep us going through these unprecedented times. As the financial year closes, we look forward to 2021-22 as we will be laying the foundations for a double anniversary again. In 2022 we will celebrate 20 years since the creation of the company and 15 years of innovation through the research we do and much more!

Professor Andrew Harrison OBE
CEO Diamond Light Source

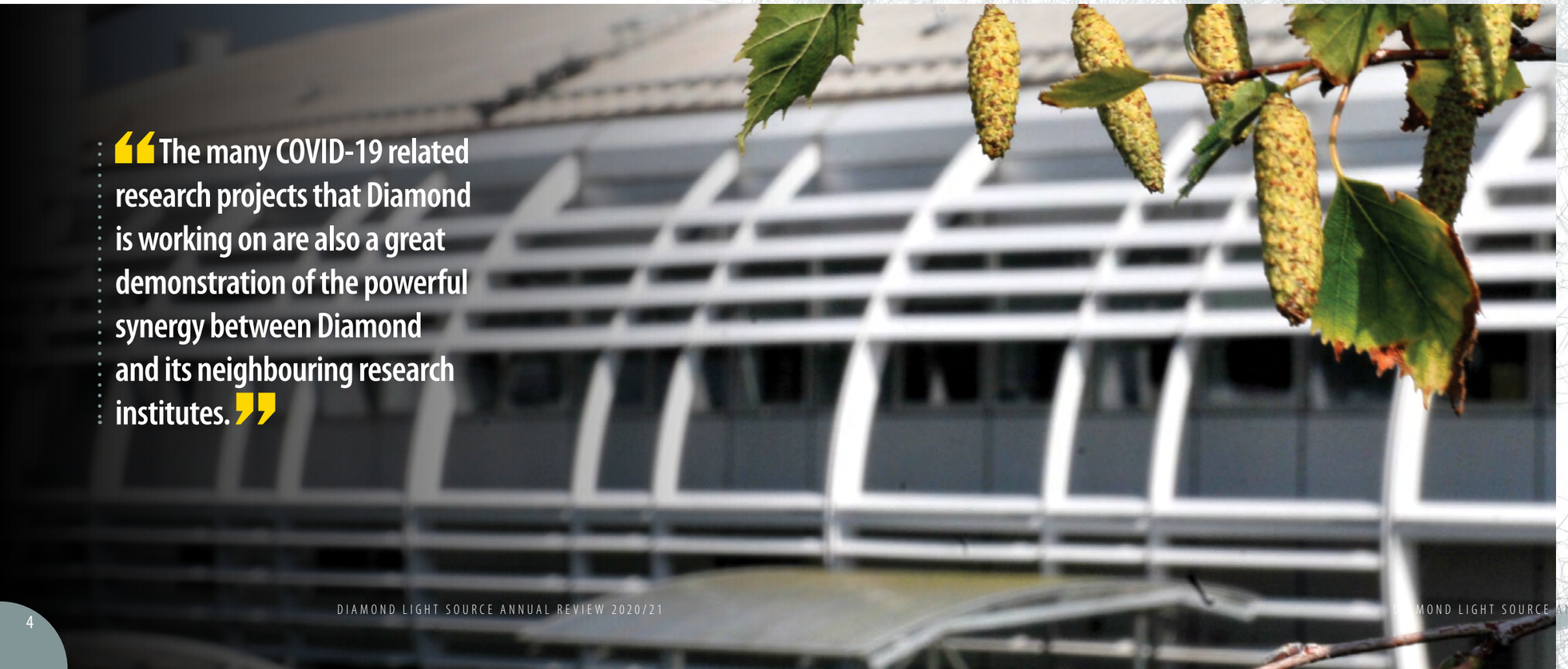

> "The many COVID-19 related research projects that Diamond is working on are also a great demonstration of the powerful synergy between Diamond and its neighbouring research institutes."

Rising to the Challenge of COVID-19

When the World Health Organisation (WHO) declared COVID-19 a pandemic on 11 March 2020, it was largely an unknown quantity. The priorities for researchers were to learn more about the virus, how it infects and how it spreads. A structural understanding of the virus was critical for developing therapies, and the Diamond synchrotron's X-rays, laboratories and integrated facilities, in particular the Electron Bio-Imaging Centre (eBIC) with its suite of high-end cryo-electron microscopes, would be crucial tools for researchers.

Diamond's first priority was to make its unique capabilities available to COVID-19 researchers. Over the past few years, Diamond has been developing technology and software for highly-automated, high-throughput beamlines, particularly for Macromolecular Crystallography (MX). This investment means that more and more experiments can be run remotely, with users sending samples to Diamond rather than visiting themselves. When the UK lockdown started, this became Diamond's standard way of working, with beamtime reserved for research related to COVID-19. Diamond allocated beamtime via a new COVID-19 specific rapid access route and more than 60 projects have benefitted from expedited access in the last year.

The many COVID-19 related research projects that Diamond has worked on, and continues to work on, are a great demonstration of the powerful synergy between Diamond and its neighbouring research institutes, the Research Complex at Harwell (RCaH) and the Rosalind Franklin Institute. The array of specialised tools and instruments at Diamond, along with the scientific and technical expertise of its staff, allow for many different techniques to be used, from looking at the structure of the virus and fitting drugs into it, like a tiny jigsaw puzzle, to taking direct images of the virus without its infectious component, making it possible to see how it interacts with drugs.

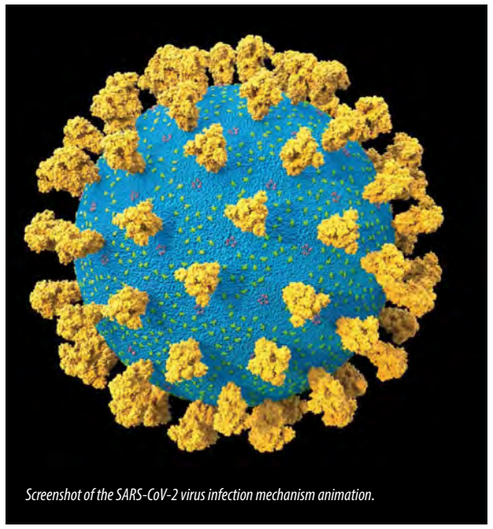

Screenshot of the SARS-CoV-2 virus infection mechanism animation.

The COVID-19 research taking place at Diamond can be loosely grouped into **five strands:** understanding the **virus structure and function, vaccine design,** the **development of new drugs,** the **development of new therapies,** and **screening existing drugs** as potential COVID treatments.

Understanding the virus, SARS-CoV-2

By August 2020, Diamond and an international team of researchers had

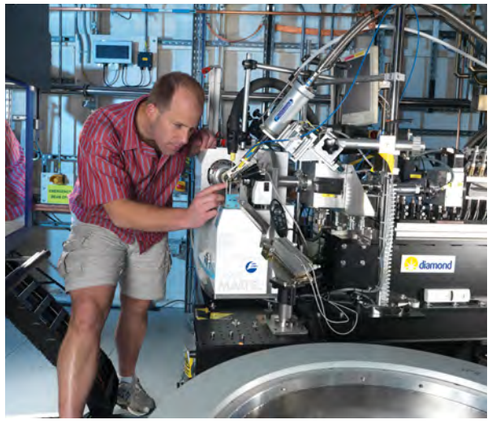

Principal Beamline Scientist on I04-1/XChem, Frank von Delft.

discovered a new and highly conserved site on SARS-CoV-2, the virus that causes COVID-19, that can be neutralised by a specific antibody. Previous studies showed that antibodies that block the virus interaction with the human receptor (ACE2) have a significant neutralising effect and can be used to save the lives of critically ill patients. This study (published in *Nature Structural and Molecular Biology*) described a different target that can be bound in synergy with ACE2 blocking antibodies for a stronger neutralising effect[1]. Using eBIC, and working with a group at a hospital in Taiwan, the team identified antibodies from a convalescent patient that could create a real potential for a drug target.

In November 2020, a research group led by Peijun Zhang, Director of eBIC and Professor of Structural Biology at the University of Oxford, published the results of their investigation of SARS-CoV-2 replication under near-native conditions[2]. They used a unique correlative imaging approach to depict the entire SARS-CoV-2 infected cell. Their results revealed - at the whole cell level - the profound cell changes caused by SARS-CoV-2 infection and enabled modelling of SARS-CoV-2 genome replication, virus assembly and egress pathways. Understanding the multistage infection process is critically important to help combat COVID-19.

Diamond then created a highly detailed scientific animation showing how the SARS-CoV-2 virus infection mechanism works at the cellular level, see *www.diamond.ac.uk/SARS-CoV-2_animation*. The aim was to inform researchers and the public and share the knowledge that scientists working with Diamond had uncovered on how the virus replicates itself. This was the first time the virus had been depicted in this way, showing in detail how the virus infection mechanism operates. The animation was entirely based on the work achieved at Diamond using cryogenic electron microscopy (cryo-EM), X-ray tomography and X-ray crystallography.

A research article published in the journal *Cell* in March 2021 is one of the

Titan Krios Electron Microscope at eBIC.

most comprehensive studies of its kind so far, examining antibodies from a large cohort of COVID-19 patients[3]. Every person infected with COVID-19 has the potential to produce many antibodies that target the virus in a slightly different way. By using Diamond, applying X-ray crystallography and cryo-EM, an international research team led by scientists from Diamond and Oxford were able to visualise and understand how antibodies interact with and neutralise the virus. Their results show that there are many different opportunities to attack the virus using different antibodies over a much larger area than initially thought. This has also provided a basis for understanding the effect on antibody neutralisation of mutations in several of the variant viruses which are now a cause for concern around the world.

Vaccine design

In April 2021, eBIC published the first images of cells exposed to the Oxford-AstraZeneca vaccine producing native-like coronavirus spikes[4]. The images showed that the spikes are highly similar to those of the virus and support the modified adenovirus used in the vaccine as a leading platform to combat COVID-19.

The challenge now is to stay ahead of the mutations, and the race is on to understand the consequences of these changes and to develop new vaccine constructs tailored to the variants. Three major new science papers, published in the journal *Cell* in April 2021, included data collected at Diamond and provided valuable new information about how previously infected or vaccinated individuals respond to these new variants and antibodies[5-7]. Their conclusions indicate that even if antibody responses to the new variants are compromised, they are likely to provide some protection. In addition, T cell responses to the virus spike may not be disrupted by the mutational changes and should be able to limit spread to the lower respiratory tract and prevent severe disease.

New drug development

To truly defeat COVID-19, we will need a combination of vaccines and treatments for people who become infected. An attractive drug target is the so-called main protease of SARS-CoV-2. This protein is essential for viral replication. Work initiated in the Walsh Group at Diamond in January 2020, in collaboration with the von Delft Group, inspired a novel crowd sourcing initiative led by PostEra Inc – the COVID Moonshot. The name derives from its unprecedented aim to develop a clinically effective antiviral more rapidly than ever before, by crowdsourcing designs of new inhibitors from chemists around the world who are mining the rich 'fragment' data measured at Diamond. All data was released in real-time and in the open to enable worldwide collaboration and rapid progress.

The COVID Moonshot asked chemists to come up with new molecules and to have a practical input towards the global efforts to combat COVID-19. Researchers submitted their designs to PostEra, who ran machine learning algorithms to triage suggestions and generate synthesis plans to enable a rapid turnaround. Promising compounds can be synthesised and tested for antiviral activity and toxicity. This is ongoing drug discovery work.

Most drugs work due to a chemical interaction between the medicine compound and a protein in the body. A powerful approach to early drug ('lead') discovery tests whether tiny fragments of compounds are connecting to a target protein. Fragment screening is quicker and easier than testing larger compounds, and Diamond's XChem fragment screening facility (developed in

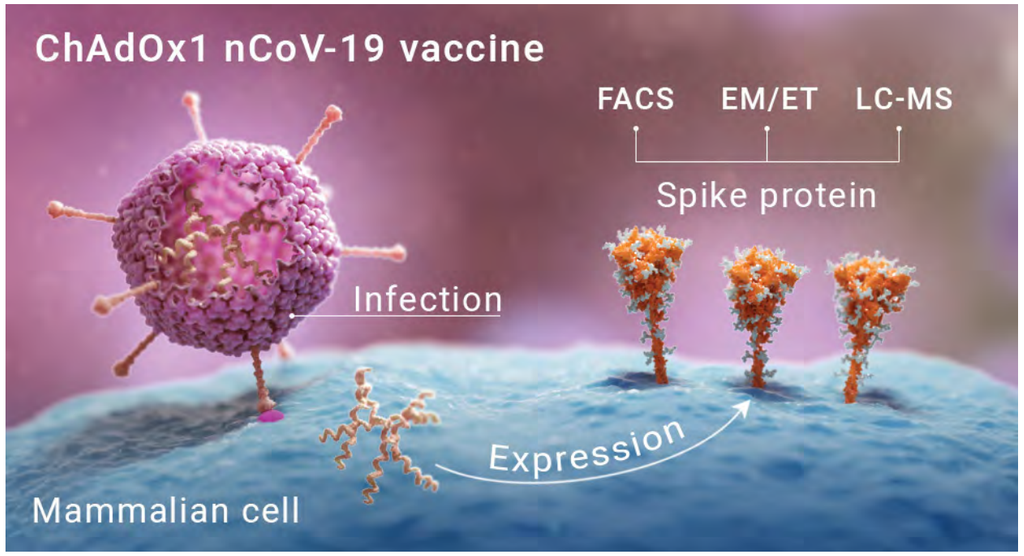

Graphic depiction of the process of creating protein spikes on cells.

partnership with the University of Oxford) can screen up to 1,000 compounds in less than a week. By the end of March 2020, a massive fragment screening effort to develop an antiviral targeting the SARS-CoV-2 main protease had identified potential ways forward to rapidly design improved and more potent compounds in the fight against COVID-19[8]. The project was led by Martin Walsh, Deputy Life Sciences Director at Diamond, Frank von Delft, Professor of Structural Chemical Biology at the University of Oxford and Principal Beamline Scientist of I04-1/XChem and Nir London, Assistant Professor at the Weizmann Institute Israel. The team combined mass spectrometry with the XChem facility to rapidly identify lead compounds for drug development to treat COVID-19.

Six SARS-CoV-2 proteins have now been subjected to fragment screening at Diamond in collaboration with internal and external groups. One of these protein drug targets forms part of another SARS-CoV-2 protein essential for viral replication. In this case researchers at XChem, in collaboration with the University of Oxford and the QCRG Structural Biology Consortium at the University of California San Francisco, targeted one of the domains of the largest SARS-CoV-2 proteins named non-structural protein 3 (Nsp3)[9]. Their research, published in *Science Advances*, focused on a specific protein domain of Nsp3 known as the macrodomain, which is an attractive target for drug discovery as previous research has shown that without a functioning macrodomain, coronaviruses are unable to replicate in human cells. This work is thus foundational for preparing for future pandemics.

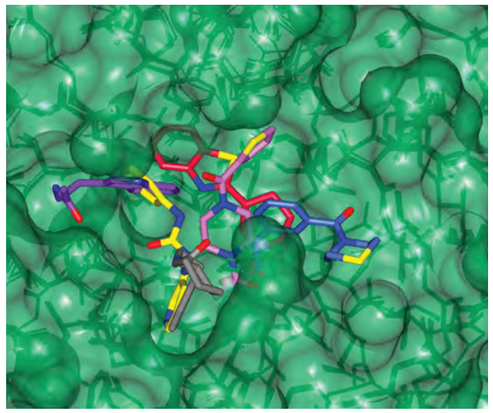

Surface representation of SARS CoV-2 Mpro protein with fragment hits from XChem platform bound in active site (green).

Developing new therapies

When patients critically ill with COVID-19 are given a transfusion of serum from convalesced individuals, which contains human antibodies against the virus, this has been shown to greatly improve their chances of survival. This process, known as passive immunisation, has been used for over 100 years. However, it is not straightforward to identify individuals with the right antibodies and to give such a blood product safely. A lab-based product that can be made on demand would have considerable advantages and could be used earlier in the disease where it is likely to be more effective.

In July 2020, a collaboration with researchers from Diamond, the Rosalind Franklin Institute, the University of Oxford and Public Health England (PHE) showed that antibodies derived from llamas could neutralise the SARS-CoV-2 virus in lab tests[10]. Using advanced imaging with X-rays and electrons at Diamond and Oxford, the team also showed that the antibodies bind to the spike protein in a new and different way to other antibodies already discovered. These antibodies – known as nanobodies due to their small size – could eventually be developed as a treatment for patients with severe COVID-19.

Screening existing drugs as potential COVID-19 treatments

Developing new drugs is a long and costly process. However, more than 15,000 compounds have been approved and extensively tested for human safety in clinical trials or regulatory pre-clinical safe studies. In March 2020, Diamond launched a new initiative with Exscientia and Scripps Research to accelerate the path to clinical trials for potential COVID-19 antiviral treatments. Using Diamond's research on COVID-19 and research facilities, Exscientia would screen nearly every known, approved and investigational drug against COVID-19 drug targets to search for rapid treatments. Using a collection of clinical drug molecules funded by the Bill & Melinda Gates Foundation and shipped from Scripps Research in California, Exscientia applied biosensor platforms to screen them against several viral drug targets of SARS-CoV-2.

Beyond the science

Diamond is a world-class research centre, but it is also a community of staff and users. In March 2020, when the worldwide demand for PPE outstripped supply, Diamond's staff joined forces with Covid Print Oxford, an initiative to create stocks of 3D printed visors for local health workers. They created a fully operational 3D printing farm in one of Diamond's labs, and a team of engineers, technicians and scientists used 20 3D printers to make over 1,000 visors a week. The collective brought all the visor parts to Diamond for sterilisation and packing before distributing them to health and care workers and schools. By June 2020, the effort had produced more than 10,000 visors, filling the gap until commercial production could meet demand.

In June, Diamond also provided more capacity for life sciences research beyond COVID-19, as sadly other diseases do not take a break during a global crisis.

After consultations about best practise with other leading institutions, including the Francis Crick Institute in London, Diamond started offering PCR tests for staff working on-site. With results available the same day, this meant it was possible to quickly identify any infected individuals and trace their contacts, preventing COVID-19 from spreading inside Diamond. Combined with other measures (including provision of PPE and hand sanitiser stations), this gave staff the confidence that working at Diamond was as safe as possible. Diamond also provides lateral flow tests for visiting contractors and users.

With a responsive and comprehensive operational response, Diamond has been able to run around the clock for four to five days each week during the first year of the pandemic, although not all of the beamlines could be operational. And by moving its programme of public events online, Diamond was able to engage with 6,000 people and continue educating the public, in a year in which the contribution of science to humanity's future has never been more prominent.

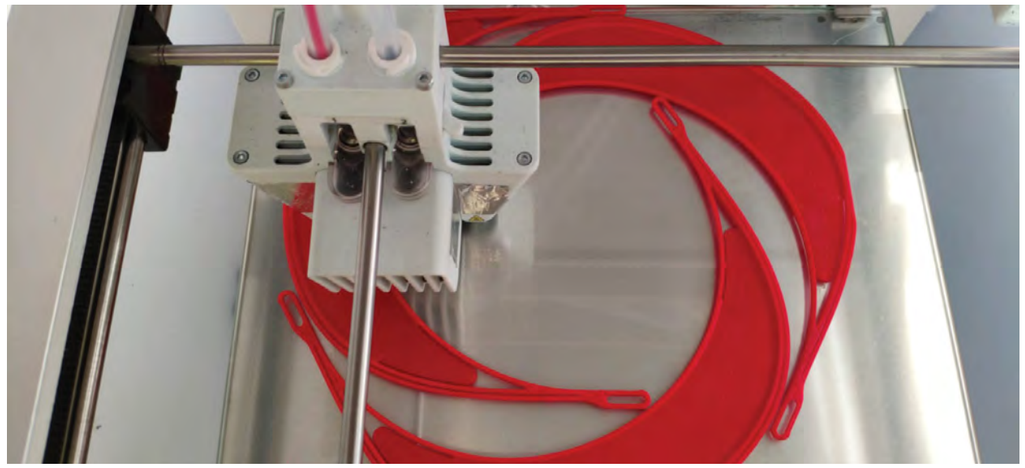

Diamond supported the local community by producing 3D printed visors for health workers.

References:

1. Zhou D. *et al.* Structural basis for the neutralization of SARS-CoV-2 by an antibody from a convalescent patient. *Nat. Struct. Mol. Biol.* **27**, 950–958 (2020). DOI: 10.1038/s41594-020-0480-y
2. Mendonça L. *et al.* SARS-CoV-2 Assembly and Egress Pathway Revealed by Correlative Multi-modal Multi-scale Cryo-imaging. *bioRxiv* 2020.11.05.370239 (2020). DOI: 10.1101/2020.11.05.370239
3. Dejnirattisai W. *et al*. The Antigenic Anatomy of SARS-CoV-2 Receptor Binding Domain. *Cell* **184**, (2021). DOI: 10.1016/j.cell.2021.02.032
4. Watanabe Y. *et al.* Native-like SARS-CoV-2 Spike Glycoprotein Expressed by ChAdOx1 nCoV-19/AZD1222 Vaccine. *ACS Cent. Sci.* **7**, 594–602 (2021). DOI: 10.1021/acscentsci.1c00080
5. Supasa P. *et al.* Reduced neutralization of SARS-CoV-2 B.1.1.7 variant by convalescent and vaccine sera. *Cell* **184**, 2201-2211.e7 (2021). DOI: 10.1016/j.cell.2021.02.033
6. Zhou D. *et al.* Evidence of escape of SARS-CoV-2 variant B.1.351 from natural and vaccine-induced sera. *Cell* **184**, 2348-2361.e6 (2021). DOI: 10.1016/j.cell.2021.02.037
7. Dejnirattisai W. *et al.* Antibody evasion by the P.1 strain of SARS-CoV-2. *Cell* (2021). DOI: 10.1016/j.cell.2021.03.055
8. Douangamath A. *et al.* Crystallographic and electrophilic fragment screening of the SARS-CoV-2 main protease. *Nat. Commun.* **11**, 5047 (2020). DOI: 10.1038/s41467-020-18709-w
9. Schuller M. *et al.* Fragment binding to the Nsp3 macrodomain of SARS-CoV-2 identified through crystallographic screening and computational docking. *Sci. Adv.* **7**, eabf8711 (2021). DOI: 10.1126/sciadv.abf8711
10. Huo J. *et al.* Neutralizing nanobodies bind SARS-CoV-2 spike RBD and block interaction with ACE2. *Nat. Struct. Mol. Biol.* **27**, 846–854 (2020). DOI: 10.1038/s41594-020-0469-6

Key Facts and Figures

Facility usage

Our fourteenth year of operations (1st April 2020 to 31st March 2021) was affected by the COVID-19 pandemic. With weekly operating hours reduced to four days, there was less experimental time available and the user programme was adjusted as a result. There was a limited call for proposals (for three months and for the physical sciences only) in that period, which had an impact on the number of submitted and awarded proposals, as well as the number of awarded shifts. We received 1,675 proposals for experiments on our instruments via peer reviewed access routes, requesting a total of 18,465 shifts. After peer review, 801 proposals were awarded beamtime. This resulted in 7,759 experimental shifts being awarded across 33 beamlines and 10 electron microscopes. We welcomed 488 on-site user visits from academia across all instruments, with an additional 4,473 remote user visits. Since March 2020, Diamond has been offering priority rapid access for groups who require instrument time for projects directly related to SARS-CoV-2 viral proteins. The machine continues to perform to a high standard with 96.2% uptime and 132 hours mean time between failures (MTBF).

User shifts requested, awarded and delivered by group, beamline and electron microscope 2020/21

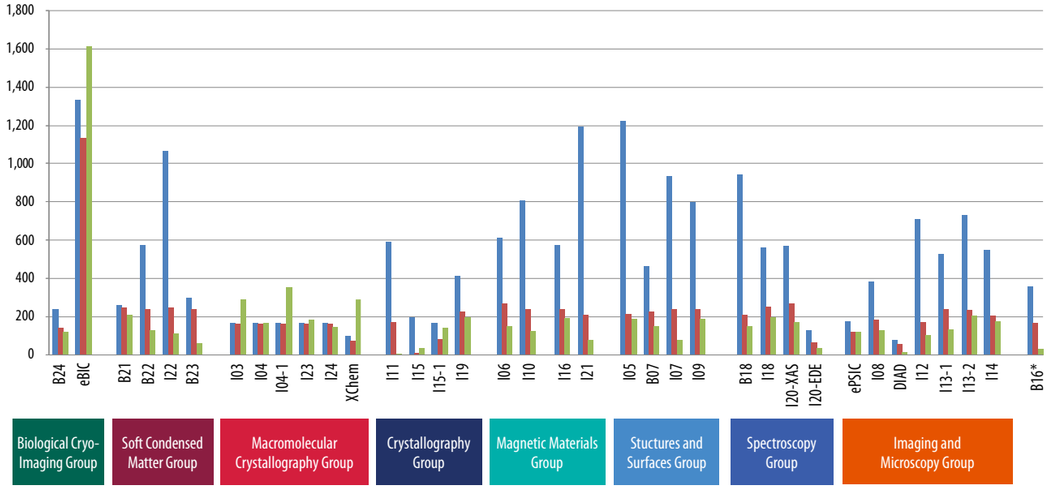

* B16 is the Test beamline, with 50% of beamtime for users. The rest is used for in-house developments for all beamlines.

Total user shifts requested, awarded and delivered

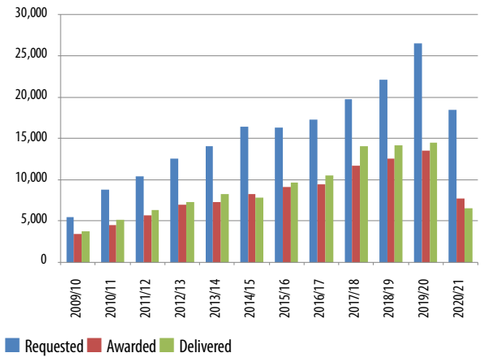

Total numbers of proposals and users per year

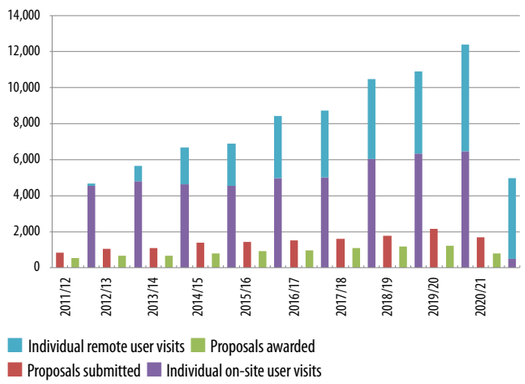

Members of staff visiting as part of peer reviewed access routes are included in the count for user visits. In-house research is excluded from this report.

Proposals by discipline and research theme

Experimental shifts scheduled by Diamond by main subject area for 2020/21

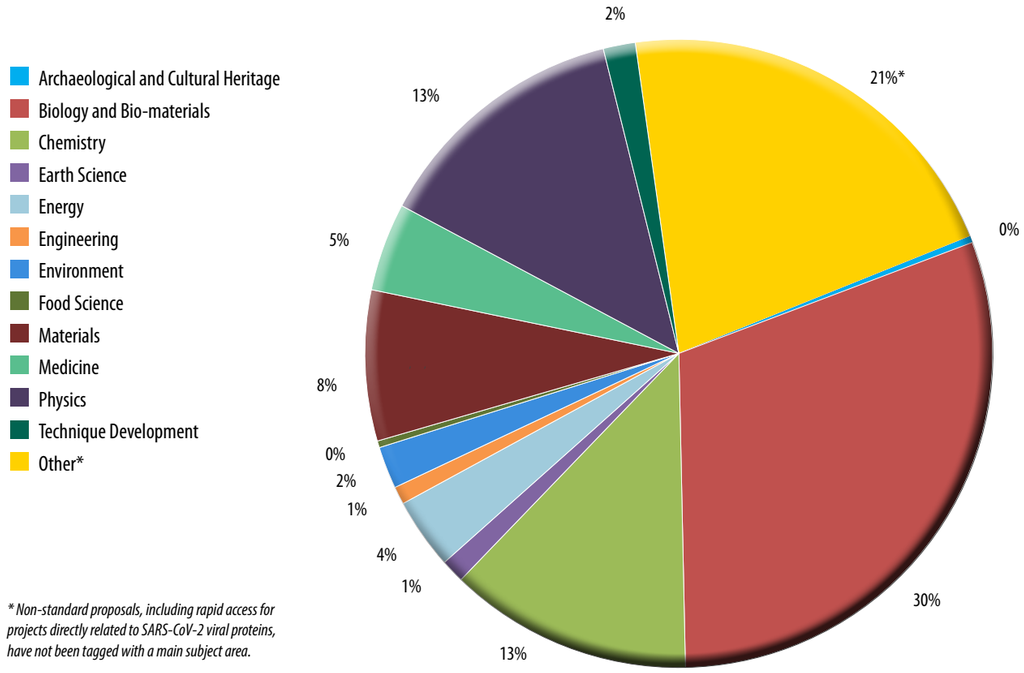

** Non-standard proposals, including rapid access for projects directly related to SARS-CoV-2 viral proteins, have not been tagged with a main subject area.*

Cumulative number of items in Diamond Publications Database by our scientists and users and cumulative number of protein structures solved

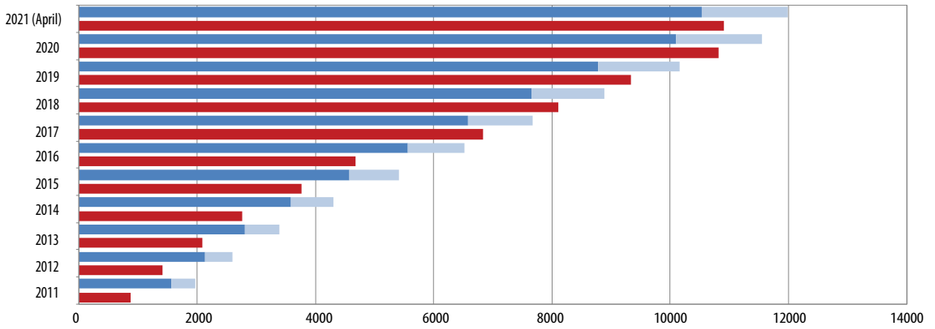

Machine performance

	2009/10	2010/11	2011/12	2012/13	2013/14	2014/15	2015/16	2016/17	2017/18	2018/19	2019/20	2020/21
Total no. operational beamlines by end FY	17	19	20	22	24	25	26	28	31	32	32	33
Scheduled hours of machine operation	5712	5808	6000	5832	5976	5808	5928	5688	6072	5904	5913	6120*
Scheduled hours of user operation	4728	4728	5064	4872	5088	4944	5040	4584	5160	4992	4992	5088*
Machine uptime %	97.0	97.5	97.7	98.3	98.2	97.6	97.6	98.7	98.2	98.4	98.1	96.2
Mean time between failures (hours)	26.2	28.5	55.4	52.4	60.3	38.6	119.4	103.1	79.9	90.3	104.7	132

** The number of machine and user operation hours delivered was reduced to 4345 and 3445 respectively, as a result of the pandemic.*

Beamline Development and Technical Summary

In its fourteenth year of experiments, Diamond is now operating with 33 beamlines and 14 electron microscopes. This year saw the DIAD beamline welcome first users, with experiments carried out remotely in February 2021 due to COVID-19 restrictions at Diamond. Of the electron microscopes, 11 are cryo-electron microscopes specialising in life sciences and make up eBIC (Electron Bio-Imaging Centre), with two provided for industry use in partnership with Thermo Fisher Scientific. The three remaining microscopes dedicated to advanced materials research are supplied by Johnson Matthey and the University of Oxford. These microscopes form ePSIC (Electron Physical Science Imaging Centre) and are operated under strategic collaboration agreements to provide for substantial dedicated peer reviewed user access. Both eBIC and ePSIC are next to the Hard X-ray Nanoprobe beamline (I14). Along with eBIC and ePSIC, the UK X-ray Free Electron Laser (XFEL) Hub, the Membrane Protein Laboratory (MPL) and the XChem fragment screening facility make up the complementary integrated facilities available at Diamond. For academic research, Diamond instruments (beamlines and microscopes) are free at the point of access through peer review. For proprietary research, access can be secured through Diamond's Industrial Liaison Office.

The instruments and beamlines are organised into eight science groups as described below.

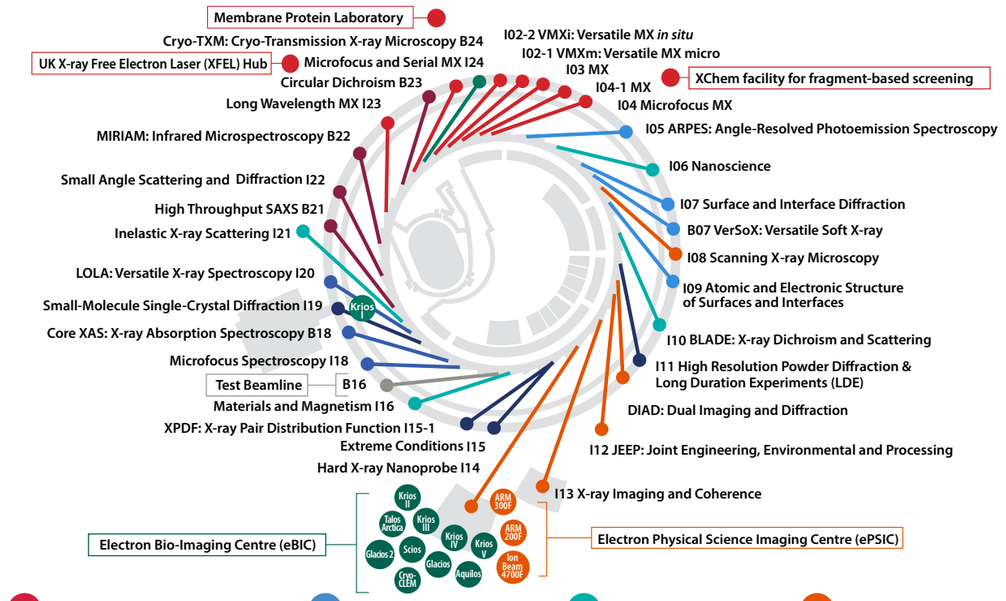

Electron Microscopes

Microscope	Main Capabilities	Accelerating Voltages	Operational Status
Titan Krios I	Cryo-EM, Cryo-ET	80, 120, 200, 300 kV	Operational since 2015
Titan Krios II	Cryo-EM, Cryo-ET	80, 120, 200, 300 kV	Operational since 2016
Titan Krios III	Cryo-EM, Cryo-ET	80, 120, 200, 300 kV	Operational since 2017
Titan Krios IV	Cryo-EM, Cryo-ET	80, 120, 200, 300 kV	Operational since 2017
Titan Krios V	Cryo-EM, Cryo-ET	80, 120, 200, 300 kV	Operational since 2018
Talos Arctica	Cryo-EM, Cryo-ET	200 kV	Operational since 2016
Glacios	Cryo-EM, Cryo-ET	200 kV	Operational since 2019
Glacios 2	Cryo-EM, Cryo-ET, MicroED	200 kV	Operational since 2021
Scios	Cryo-SEM, Cryo-FIB	3 to 30 kV	Operational since 2017
Aquilos 2	Cryo-SEM, Cryo-FIB	3 to 30 kV	Operational since 2019, updated to Aquilos 2 in 2020
Leica cryo-CLEM	Cryo-CLEM	n/a	Operational since 2021
JEOL ARM200F	Atomic scale STEM imaging, EELS, EDX, electron diffraction	80, 200 kV	Operational since 2017
JEOL ARM300F	Atomic scale TEM and STEM imaging, electron diffraction, 4D-STEM, EDX	30, 60, 80, 160, 200, 300 kV	Operational since 2017
JEOL Ion Beam 4700F	SEM, FIB	1 to 30 kV	Operational since 2020

Diamond's beamlines: current operational status April 2021

Beamline Name and Number	Main Techniques	Energy / Wavelength Range	Status
I02-1 - Versatile MX micro (VMXm)	Micro- and nano-focus in vacuum cryo-macromolecular crystallography (VMXm)	7 - 28 keV	Commissioning
I02-2 - Versatile MX *in situ* (VMXi)	*In situ* microfocus macromolecular crystallography, Serial Synchrotron Crystallography	10 - 25 keV	Commissioning
I03 - MX	Macromolecular crystallography (MX), Multiwavelength Anomalous Diffraction (MAD) , Containment Level 3 (CL3) capable	5 - 25 keV	Operational
I04 - Microfocus MX	MX, MAD, variable and microfocus MX	6 - 18 keV	Operational
I04-1 - Monochromatic MX	MX, XChem fragment screening	13.53 keV (fixed wavelength)	Operational
I05 - ARPES	Angle-Resolved PhotoEmission Spectroscopy (ARPES) and nano-ARPES	18 - 240 eV; 500 eV	Operational
I06 - Nanoscience	X-ray Absorption Spectroscopy (XAS), X-ray photoemission microscopy and X-ray magnetic circular and linear dichroism	80eV - 2200eV	Operational
I07 - Surface and Interface Diffraction	Surface X-ray diffraction, Grazing Incidence X-ray Diffraction (GIXD), Grazing Incidence Small Angle X-ray Scattering (GISAXS), X-ray Reflectivity (XRR)	6 - 30 keV	Operational
B07 - VerSoX: Versatile Soft X-ray	Branch C: Ambient Pressure XPS and NEXAFS	250 - 2800 eV	Operational
	Branch B: NEXAFS and High-Throughput XPS	50 - 2200 eV	Commissioning
I08 - Scanning X-ray Microscopy	Scanning X-ray microscopy, NEXAFS/ XANES, X-ray fluorescence	I08 branch: 250 eV - 4.4 keV	Operational
		J08 - Soft and Tender X-ray Ptychography branch: 250 - 2000 eV	Optimisation
I09 - Atomic and Electronic Structure of Surfaces and Interfaces	XPS (including HAXPES), X-ray Standing Waves (XSW), Near Edge X-ray Absorption Fine Structure (NEXAFS), energy-scanned photoelectron diffraction	Hard X-rays: 2.1 - 18+ keV Soft X-rays: 0.1 - 2.1 keV (currently 0.1 - 1.9 keV)	Operational
I10 - BLADE: Beamline for Advanced Dichroism Experiments	Soft X-ray resonant scattering, XAS and X-ray magnetic circular and linear dichroism	Circular: 400-1600eV; Linear Horizontal: 250-1600eV; Linear Vertical: 480-1600eV	Operational
I11 - High Resolution Powder Diffraction	X-ray powder diffraction	6 - 25keV (0.5 - 2.1 Å)	Operational
DIAD: Dual Imaging and Diffraction	Simultaneous imaging and diffraction	8 - 38 keV	Optimisation
I12 - JEEP: Joint Engineering, Environmental and Processing	Time-resolved imaging and tomography, 2D detector for time-resolved powder diffraction, single crystal diffraction and diffuse scattering, energy dispersive X-ray diffraction (EDXD), high-energy small angle X-ray scattering (under development)	53 keV - 150 keV monochromatic or continuous white beam	Operational
I13 - X-ray Imaging and Coherence	Phase contrast imaging, tomography, full-field microscopy, grating interferometry, (Diamond-Manchester Imaging branchline); ptychography combined with fluorescence and tomography, Bragg-coherent diffraction and imaging, innovative microscopy and imaging (Coherence branchline)	Imaging branch: 8 - 30keV Coherence branch: 7 - 20keV	Operational
I14 - Hard X-ray Nanoprobe	Nanofocus X-ray fluorescence (XRF), X-ray absorption spectroscopy (XAS), differential phase contrast (DPC), transmission diffraction (XRD), and ptychography for 2D and 3D imaging	5 - 23 keV	Operational
I15 - Extreme Conditions	Powder diffraction, single crystal diffraction	Monochromatic and focused 20 - 80 keV White beam	Operational
I15-1 - XPDF	X-ray Pair Distribution Function (XPDF)	40, 65, and 76 keV	Operational
I16 - Materials and Magnetism	Resonant and magnetic single crystal diffraction, fundamental X-ray physics	2.5 - 15 keV	Operational
B16 - Test beamline	Diffraction, imaging and tomography, topography, reflectometry	4 - 20 keV monochromatic focused 4 - 45 keV monochromatic unfocused White beam	Operational
I18 - Microfocus Spectroscopy	Microfocus X-ray Absorption Spectroscopy (XAS), X-ray fluorescence (XRF) and X-ray diffraction (XRD) mapping and tomography	2.05 - 20.5 keV	Operational
B18 - Core XAS	X-ray Absorption Spectroscopy (XAS)	2.05 - 35 keV	Operational
I19 - Small-Molecule Single-Crystal Diffraction	Small-molecule single-crystal diffraction	5 to 25 keV / 0.5 to 2.5 Å	Operational
I20 - LOLA: Versatile X-ray Spectroscopy	X-ray Absorption Spectroscopy (XAS), X-ray Emission Spectroscopy (XES) and Energy Dispersive EXAFS (EDE)	Dispersive branch: 6 - 26 keV	Operational
		Scanning branch: 4 - 20 keV	Operational
I21 - Inelastic X-ray Scattering	Resonant Inelastic X-ray Scattering (RIXS), X-ray Absorption Spectroscopy (XAS)	Currently 250 - 1500 eV (to be upgraded to 250 - 3000 eV)	Operational
B21 - High Throughput SAXS	BioSAXS, solution state small angle X-ray scattering	8 - 15 keV (set to 13.1 keV by default)	Operational
I22 - Small Angle Scattering and Diffraction	Small angle X-ray scattering and diffraction: SAXS, WAXS, USAXS, GISAXS. Micro-focus.	7 - 20 keV	Operational
B22 - MIRIAM: Multimode InfraRed Imaging And Mircrospectroscopy	Fourier Transform IR (FTIR) microscopy & Focal Plane Array (FPA) imaging FTIR and THz spectroscopy NEW: Nanospectroscopy FTIR via Atomic Force Microscopy (AFM) IR and scattering Scanning Nearfield Optical Microscopy (s-SNOM) (commissioning)	microFTIR: 5,000-500cm^{-1}(2-20µm) FTIR/THz: 10,000-10cm^{-1}(1-1000µm) nanoFTIR: 10,000-650cm^{-1}(1-15µm)	Operational
I23 - Long Wavelength MX	Long wavelength macromolecular crystallography	2.1 - 11 keV (1.1 - 5.9 Å)	Operational
B23 - Circular Dichroism	Mueller Matrix Polarimetry (MMP) Circular Dichroism (CD) High-Throughput CD (HTCD))	Module A: 125-500nm for CD Imaging at 50 µm spatial resolution, and 96-cell HTCD. Module B: 180-650nm for MMP Imaging at 50 µm spatial resolution.	Operational
I24 - Microfocus and Serial MX	MX, MAD, Serial Crystallography, high energy MX	6.5 - 30.0 keV	Operational
B24 - Correlative Cryo-Imaging; Soft X-ray Tomography and Fluorescence Imaging	Full field X-ray and laser light fluorescence imaging	Visible spectrum, 200-2600eV	Operational

Macromolecular Crystallography Group

Dave Hall, Science Group Leader

Biological interactions underpin and can undermine the processes of life, as exemplified this year by the SARS-CoV-2 pandemic. The technique of Macromolecular Crystallography (MX) uses X-rays to reveal the details of biological molecules at atomic and temporal scales and is an enabler in our understanding of the processes and interactions of life. Seven beamlines (I03, I04, I04-1, I23, I24, VMXi and VMXm), alongside the XChem fragment screening facility, the UK X-ray Free Electron Laser (XFEL) Hub and the Membrane Protein Laboratory (MPL) at Diamond Light Source are dedicated to exploiting the technique of MX for the benefit of the worldwide structural biology community.

The onset of the COVID-19 pandemic in early 2020 drove significant changes for MX user operations and beamline improvements. One of the biggest changes this year has been how users access MX beamtime. Historically a six-month schedule was published and users prepared samples for their scheduled slots. With lockdowns affecting user lab access and Diamond machine operations, we transitioned quickly to a responsive mode of user beamtime. Experiments are fully remote, via automated unattended data collection or undertaken by Diamond staff (I23, XChem fragment screening, VMXi crystallisation, Serial Synchrotron Crystallography (SSX)). These are scheduled once user samples are delivered to site, typically within a week. User feedback for this mode of access has been very supportive and we will incorporate this into our future offering.

> *"The onset of the COVID-19 pandemic in early 2020 drove significant changes for MX user operations and beamline improvements. One of the biggest changes this year has been how users access MX beamtime."*

In 2020 COVID-19 research was prioritised, with a special rapid access user call opened early on. Time has been awarded for scientists from across the world studying a range of SARS-CoV-2 targets. They have taken advantage of access to the high-throughput beamlines I03 and I04 for rapid turnaround of high-resolution structures, room temperature studies on I24 and VMXi, drug repurposing studies across the MX beamlines and the XChem I04-1 facility for large scale fragment screening, which in itself has kickstarted the COVID Moonshot project – a crowdsourcing molecular design initiative looking for an antiviral against the main protease. The XFEL Hub has coordinated user remote access experiments on targets from SARS-CoV-2 at XFELs around the world. Much of this work has been possible due to continued access to the MPL, crystallisation facilities and Diamond research support staff. The outcome of this research is already evidenced by the high number of structures released to the Protein Data Bank (PDB) and speed with which papers have been published.

Fully automated Unattended Data Collection (UDC) was introduced as a new mode of operation in 2020, firstly on I03 and then rolled out to I04 and I04-1. This provides fast and efficient data collection with no user interaction with the beamlines, enabling users to focus on their science and not be tied to collecting data, often at anti-social hours or when access to offices is limited during the pandemic. Users prepare samples for shipment with associated diffraction plans and then ship their samples. Once samples arrive at Diamond they are queued to an appropriate beamline and data collected at the earliest possible opportunity. This fits in well with the responsive mode of access to Diamond MX beamlines, with turnaround times typically within a week of arrival. Many academic and industrial user groups are now using this access method routinely, with tens of thousands of high quality data sets collected in 2020 alone.

Despite restrictions in working practices throughout the pandemic, we have continued to prioritise essential upgrades to ensure beamlines remain state of the art. The Microfocus beamline I24 installed a cryogenic permanent magnet undulator providing higher fluxes, in particular at higher energies. This is linked to the installation of a detector optimised for use at these high energies – the first CdTe Eiger2 9M. Together these upgrades provide the opportunity to explore further the possibilities of using higher energies for data collection, in particular from the small crystals typically used for SSX.

VMXi and VMXm were in the process of moving towards user operations prior to the pandemic and this progress has been slowed, however the sub-micron focus beamline VMXm recently installed an identical detector to that installed on I24 earlier in 2020. As further commissioning and user operations begin on VMXm this new detector, alongside its unique electron microscope equipped end station, will enable users to investigate the smallest of crystals to elucidate structures not previously tractable.

The room temperature *in situ* beamline VMXi saw a new goniometer successfully installed, which now enables the beamline to accurately and rapidly collect 1s datasets. The crystallisation facility associated with VMXi has been working with commissioning users to grow crystals from protein provided by them for use at VMXi. Data collections are configured remotely by the users and run automatically by the beamline. Over 2021, we expect to steadily increase access to VMXi in line with capabilities within the crystallisation facility and as users can access their labs and site as lockdowns retreat.

This year the Long Wavelength beamline, I23, implemented a significant upgrade for delivering their thermally conductive sample mounts into the in vacuum experimental end station. The new cryo-transfer system provides a user-friendly way of transferring the sample mounts, whilst maintaining samples at cryogenic temperatures within the vacuum environment. It has been successfully commissioned by the I23 team with user samples throughout the restrictions during the pandemic and several difficult structures could be solved.

During the pandemic, I04-1 and the XChem facility prioritised the seven user-submitted COVID-19 projects. By the last quarter of the year, the full focus had returned to previously scheduled academic and industry experiments. Remarkably, XChem staff managed to accommodate all projects despite having to perform all on-site experimental work. This year, two projects have been signed off that will transform the beamline's capabilities. Firstly, a new Eiger2 XE 9M detector has been ordered and delivered that has a frame rate up to 20 times higher than the existing detector. This will be installed in the very near future. Secondly, to fully exploit the detector capabilities, a new hybrid permanent magnet undulator insertion device has been approved that will bring a significant increase in flux. Together these will increase the throughput of I04-1, allowing it to run experiments on weaker diffracting crystals and providing increased opportunities for the fragment-based drug design community.

Work has continued on MX needs for Diamond-II (proposed upgrade programme) throughout 2020. Over the last year, proposals for flagship beamlines and projects for Diamond-II have been put forward in conjunction with user community support for review by Diamond's science and industrial advisory boards (SAC and DISCo). Beamline I04-1 cannot easily remain in its current position in the new Diamond-II lattice and it is proposed to build a new beamline with significantly enhanced features at a new position in the ring. The Microfocus beamline, I24, proposed upgrading and updating its microfocus capabilities, alongside further improving its SSX offering. Both of these proposals were highly regarded by SAC-DISCo and will proceed as part of the Diamond-II project. User community support for both proposals was key to their success and is very much appreciated.

In parallel to supporting user experiments and significant upgrades, we have also continued with our remit to train future generations of structural biologists. This year our annual Diamond-CCP4 training course in crystallography, which includes data collection at the MX beamlines for the students, was run completely remotely over two weeks for the first time. Following its success, we provided beamtime and support to a CCP4-South Africa crystallographic school, again remotely over two weeks.

Finally, it must not go unrecognised that an exceptional year was underpinned by the remarkable staff of the MX group, support groups and wider Diamond team who all stepped up in many ways to support our MX user community.

How we HUSH jumping genes and viruses

Related publication: Douse C. H., Tchasovnikarova I. A., Timms R. T., Protasio A. V, Seczynska M., Prigozhin D. M., Albecka A., Wagstaff J., Williamson J. C., Freund S. M. V, Lehner P. J. & Modis Y. TASOR is a pseudo-PARP that directs HUSH complex assembly and epigenetic transposon control. *Nat. Commun.* **11**, 4940 (2020). DOI: 10.1038/s41467-020-18761-6

Publication keywords: Chromatin; Transposons; Epigenetics; Genome stability; Viral restriction

The human silencing hub (HUSH) is a complex of three proteins discovered in 2015. It plays a role in repressing the replication of retroviruses such as HIV and 'jumping genes' (transposons) that can move within the genome. HUSH works by regulating chromatin, the material that packages our genomes, in particular ways. However, until recently little was known about the molecular and structural mechanisms underpinning HUSH function.

TASOR is the key scaffold protein of the HUSH complex. An international team of researchers investigated how TASOR features in HUSH assembly and regulates chromatin structure over transposons. They found that one end of the TASOR molecule contains a domain that is not needed for assembly but is critical for HUSH function. They used Diamond Light Source's Macromolecular Crystallography (MX) beamlines I02 and I03 to screen datasets of native and SeMet crystals of this domain. Their resulting structure revealed that this part of TASOR resembles a domain from enzymes called PARPs that maintain genome stability. Close examination of the structure revealed that TASOR's PARP domain is catalytically inactive – in other words, TASOR is a 'pseudo-PARP'.

Although we now have anti-retroviral treatments for HIV that are very efficient at inhibiting actively replicating viruses, we are left with the challenge of clearing latent (dormant) viruses. Inhibiting or degrading HUSH might reactivate latent viruses, allowing existing treatments to clear the infection – a 'shock and kill' strategy. Knowing the structure of functionally critical domains of HUSH, like the TASOR pseudo-PARP domain, will help develop HUSH inhibitors.

Mammalian genomes are under constant threat of colonisation by infectious retroviruses and 'jumping genes' called transposons. The danger that retroviruses can pose to humans is well known – HIV being perhaps the most famous example – but transposons also play important roles in health and disease. Unchecked mobilisation of such genetic elements could cause genome instability, which is a hallmark of cancer. On the flip side, transposons harbour great potential to spread regulatory genetic networks, so are powerful drivers of evolution. Since transposon sequences are now thought to account for more than half of all human DNA, there is tremendous biological interest in understanding how such elements are controlled.

One of the principal ways in which viruses and transposons alike are kept in check in human cells is through a process called epigenetic silencing. Through specific modifications to chromatin – the substance into which our genomes are packaged – expression of the underlying DNA can be tuned up or down. The '*epi*' prefix refers to the notion that epigenetic modifications are a layer of information *in addition to* the primary genetic code of DNA. Epigenetic modifications include chemical modification (e.g. methylation) of the DNA itself, or of molecules called histones that package DNA into chromatin.

The Human Silencing Hub (HUSH) complex has recently emerged as a central player in the epigenetic repression of exogenous viruses, including HIV, and endogenous transposons called long interspersed nuclear elements (LINEs). HUSH regulates methylation of histones in a particular pattern that is correlated with low conversion of the underlying DNA to its corresponding messenger RNA (Fig. 1). The latter is a process called transcription, which is the first step by which retroviruses replicate and most transposons jump to new positions. It has been known since HUSH was discovered in 2015 that

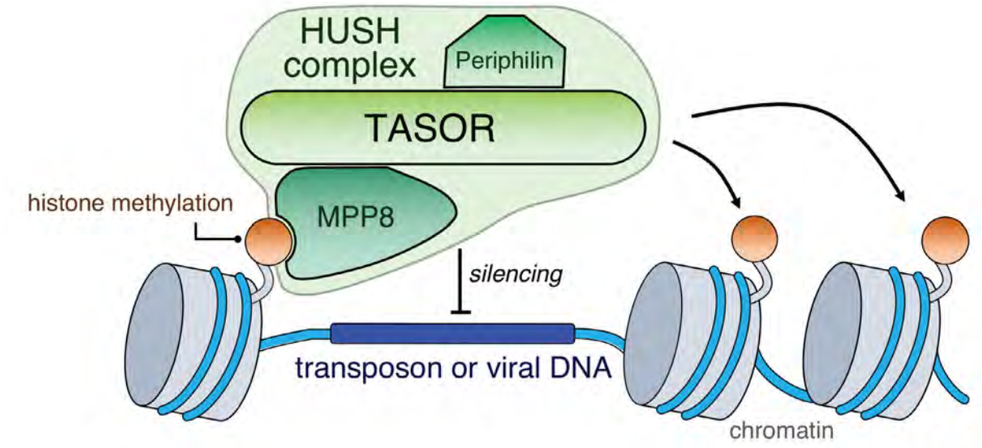

Figure 1: Schematic model for HUSH-dependent repression of integrated retroviral and transposon DNA (blue). Targeted histone methylation (red) depends on HUSH complex assembly at the chromatinised sequence.

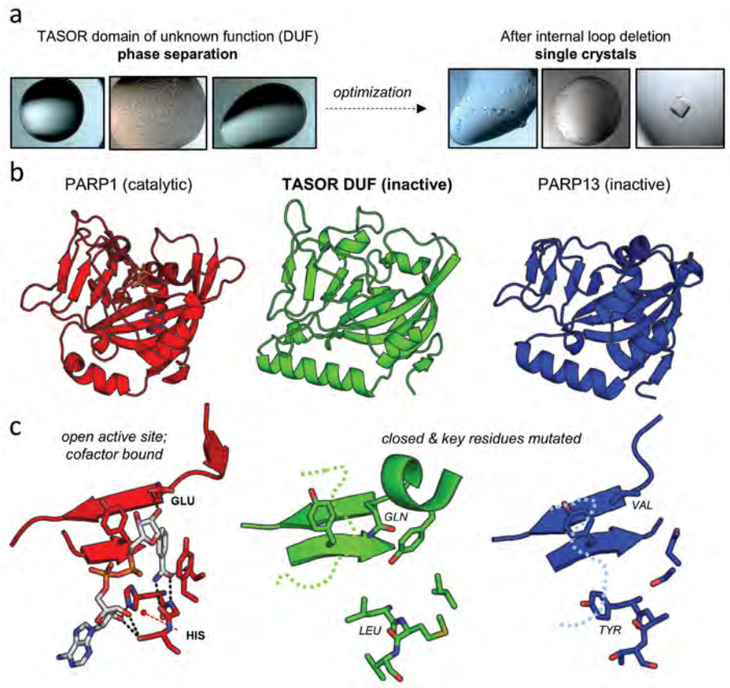

Figure 2: (a) Optimisation of crystal growth of TASOR domain of unknown function (DUF); (b) Overall structures of TASOR DUF (green) compared to active (PARP1, red) and inactive (PARP13, blue) members of the PARP superfamily; (c) Zoomed-in views of enzymatic sites show that inactive PARPs have closed, empty and mutated sites compared to PARP1, which can be seen bound to its cofactor.

the complex is composed of three proteins, called TASOR, Periphilin and MPP8, which team up to repress transcription through changes to chromatin structure[1]. However, almost nothing is known of the structure of these proteins, how they assemble together to form a functional complex, or what their key molecular activities are.

This highlighted research set out to answer some of these questions and focused on HUSH subunit TASOR, which was completely uncharacterised at the start of the project. TASOR (Transgene Activation SuppressOR) is the central scaffold of HUSH: the other two subunits cannot interact with one another in TASOR's absence. Careful biochemical delineation of the interaction sites of HUSH subunits allowed purification of binary complexes containing TASOR and either Periphilin or MPP8. Indeed, using Diamond's beamline I04-1, the structure of the TASOR-Periphilin subcomplex was successfully solved[2]. In the course of research figuring out HUSH interactions, one end of the TASOR molecule was found to be critical for function but not assembly of the complex. Notably, at the start of the project this was actually the only portion of TASOR to have any annotation at all: a cryptic sounding 'domain of unknown function' (DUF).

TASOR's DUF could be purified in large quantities but initially failed to crystallise in more than two thousand tested conditions. However, spectroscopic measurements on the protein solution suggested the presence of a short highly flexible part protruding from its core structure. Such disorder is often incompatible with forming well-ordered protein crystals. Sure enough, upon targeted removal of this internal loop, beautiful single prismatic crystals could be grown (Fig. 2a). Using data collected at Diamond's I02 and I03 beamlines, the high-resolution structure of the TASOR DUF could be solved.

The X-ray structure revealed that TASOR DUF closely resembled a poly-ADP-ribose polymerase (PARP) domain (Fig. 2b). PARPs are enzymes that maintain genome stability by stimulating a signalling cascade in response to DNA damage. This was interesting given the putative role of HUSH in protecting the genome against potential damage caused by unrestricted transposon jumping or viral activity. However, upon aligning the structures and zooming into their active sites (Fig. 2c), it was clear that the physical shape and chemistry that form a functional PARP active site were not present in TASOR. This is most clear from the observations that key amino acids involved in PARP activity are mutated. Indeed, TASOR more closely resembled PARP family members such as PARP13 which is thought to be catalytically inactive. Biochemical experiments confirmed that TASOR lacked canonical cofactor binding and enzymatic activity – in other words, TASOR was identified as a 'pseudo-PARP'[3].

Despite the lack of catalytic activity, all known HUSH activities – targeted histone methylation, restricting the expression of target LINE transposons and of integrating viruses – were found to be dependent on the TASOR pseudo-PARP domain. Remarkably, it was found that substitution of just a single conserved amino acid residue on the surface of this domain was sufficient to wipe out all these complex functions. Interestingly, mice bearing mutation at another site, that we now know is a structurally important residue of TASOR, die early in embryonic development. More work is required to fully understand the order of events in HUSH assembly and activity – but taken together, these observations imply that genome protection by TASOR and HUSH is critical for healthy human development. The work highlighted here is just the start: figuring out more about how HUSH works will continue to be an intense area of study for researchers for many years to come.

References:

1. Tchasovnikarova I. A. *et al.* Epigenetic silencing by the HUSH complex mediates position-effect variegation in human cells. *Science.* **348**, 1481–1485 (2015). DOI: 10.1126/science.aaa7227
2. Prigozhin D. M. *et al.* Periphilin self-association underpins epigenetic silencing by the HUSH complex. *Nucleic Acids Res.* **48**, 10313–10328 (2020). DOI: 10.1093/nar/gkaa785
3. Douse C. H. *et al.* TASOR is a pseudo-PARP that directs HUSH complex assembly and epigenetic transposon control. *Nat. Commun.* **11**, 4940 (2020). DOI: 10.1038/s41467-020-18761-6

Funding acknowledgement:
This work was supported by Wellcome Trust Senior Research Fellowships 101908/Z/13/Z and 217191/Z/19/Z to Y.M., a Wellcome Trust Principal Research Fellowship 101835/Z/13/Z to P.J.L., Swedish Society for Medical Research grant S19-0100 to C.H.D., and a BBSRC Future Leader Fellowship BB/N011791/1 to C.H.D.

Corresponding author:
Dr Christopher H. Douse, Lund University, Sweden,
christopher.douse@med.lu.se

Engineering enzyme cocktails to break down single-use plastics

Related publication: Knott B. C., Erickson E., Allen M. D., Gado J. E., Graham R., Kearns F. L., Pardo I., Topuzlu E., Anderson J. J., Austin H. P., Dominick G., Johnson C. W., Rorrer N. A., Szostkiewicz C. J., Copié V., Payne C. M., Woodcock H. L., Donohoe B. S., Beckham G. T. & McGeehan J. E. Characterization and engineering of a two-enzyme system for plastics depolymerization. *Proc. Natl. Acad. Sci.* **117**, 25476–25485 (2020). DOI: 10.1073/pnas.2006753117

Publication keywords: Polyethylene terephthalate; Recycling; Upcycling; Biodegradation; Serine hydrolase

An estimated 11 million tons of plastic waste enter our oceans annually, impacting wildlife, our food chain and our health. The UK government has set ambitious 2025 targets for plastics recycling, but effective means of achieving these are currently lacking. Therefore, an international team of researchers is focusing on the discovery and engineering of enzymes that can help break down plastics for recycling.

In previous work, they characterised the structure and function of PETase, a bacterial enzyme with the remarkable ability to deconstruct one of the most commonly polluting thermoplastics, polyethylene terephthalate, PET. This study looked in-depth at a partner enzyme called MHETase, secreted from the same bacterium, that can significantly speed up the breakdown process.

The structures they collected on Diamond Light Source's I03 Macromolecular Crystallography (MX) beamline are the highest resolution available and provide a detailed insight into the MHETase enzyme. Combined with detailed bioinformatics, biochemistry and molecular simulations, they show a highly synergistic relationship between the PETase and MHETase enzymes. The team investigated if tethering the proteins together could improve the breakdown and demonstrated that this was significantly faster than PETase alone or a PETase-MHETase cocktail.

Enzymes offer a low-energy solution and the potential to allow infinite recycling, reducing our growing requirements for fossil resources. There is a lot of excitement around the potential for naturally-evolved enzymes to tackle our plastic waste. This publication reached the Altmetric Top 100 (#39) from the 3.4 million papers published in 2020.

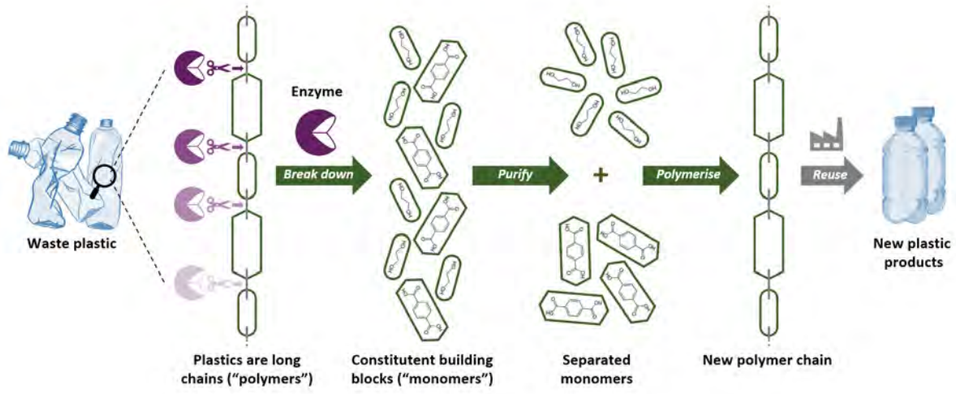

Figure 1: Enzymes can break down waste plastic polymers into building blocks that can be purified and re-polymerised, allowing infinite recycling of the materials as part of a circular plastics economy (Credit Prof. Andrew Pickford, CEI).

Plastic pollution represents a global environmental crisis, with growing levels of production from fossil resources contributing to greenhouse gas emissions and poor disposal resulting in the contamination of our land, rivers and oceans. Innovative solutions for dealing with our increasing appetite for plastics are urgently required. One of our most polluting single-use plastics is the polymer polyethylene terephthalate, commonly known as PET and recognisable with the triangle recycling label with the number one. This thermoplastic is most visible in the environment as discarded drinks bottles but is vastly more abundant in the form of polyester textiles. Both forms of this polymer have residence times in the natural environment of hundreds of years and while processes such as waves and sunlight break down these materials into smaller microplastics, their chemical structure remains largely intact. While technology exists to turn plastic bottles back into plastic bottles, even in countries with excellent infrastructure, typically this only represents around 7% of the total. Most are mechanically recovered and downcycled to lower value materials such as fibres for clothing and carpet. This material stream inevitably ends up being incinerated or dumped in landfill as there is little economic incentive to reclaim it with current processes and in less well-developed systems, large quantities escape to the environment.

In 2018 we reported the characterisation of the enzyme PETase, secreted by the bacterium, *Ideonella sakaiensis*, originally discovered in a Japanese recycling centre[1,2]. This naturally occurring enzyme is capable of breaking the ester bonds that hold the two monomers, ethylene glycol and terephthalic acid, together to form the long chains that provide PET with its high resistance and lightweight properties. This biological activity opens the door to use enzymes to regenerate these monomers for the infinite recycling of this type of plastic (Fig. 1), a central goal for our team at the Centre for Enzyme Innovation at the University of Portsmouth.

I. sakaiensis is known to secrete two key enzymes, PETase, which liberates soluble products, including mono(2-hydroxyethyl) terephthalate (MHET) and a partner enzyme called MHETase, which cleaves this MHET to form terephthalic acid and ethylene glycol. In order to investigate how these enzymes work in tandem, we cloned and expressed MHETase to study its structural and functional adaptations. We collected multiple datasets from several crystal forms of MHETase on beamline I03, utilising a selenomethionine derivative to solve the phases by SAD. The highest resolution data, with diffraction extending to 1.6 Å, provided detailed insights into the active site that included key residues captured in multiple conformations. MHETase has a core domain with a fold resembling PETase but has an additional extensive lid domain that covers the active site (Fig. 2). The overall fold is similar to some ferulic acid esterases from the tannase family. Bioinformatic searches revealed other potential MHETases and two of these identified homologues were shown to be active. While they had lower efficiency, they provided useful insights into the key residues required for MHET turnover. We were able to rationalise the structural basis of substrate specificity through mutational analysis and furthermore, these structural models provided an excellent platform for QM/MM molecular simulations which allowed us to determine that the deacylation is the rate limiting in the MHETase two-step reaction.

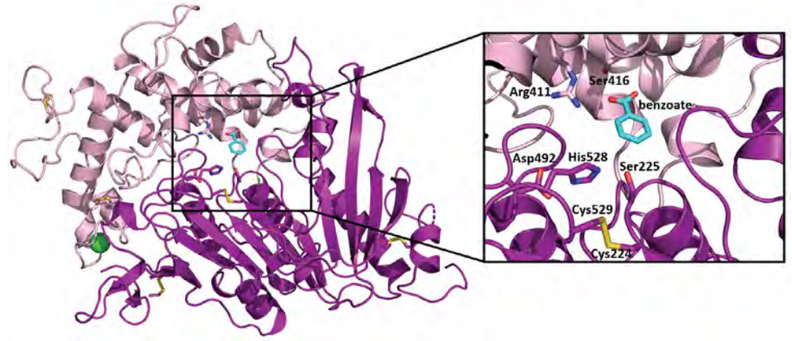

Figure 2: Structural model of MHETase highlighting the PETase-like core domain in purple with the lid domain in pink. (Inset) Key residues lining the active site with bound benzoate providing insights into ligand interactions.

We were particularly interested in how the MHETase enzyme interacts with PETase to enhance the deconstruction of PET, so we took a matrix approach, analysing 144 reactions at varying concentrations and ratios. This revealed significant synergy when employing these enzyme cocktails, with terephthalate acid production increased. This inspired the design of several chimeric constructs for a multi-enzyme approach, where the two enzymes were directly connected via a short flexible linker (Fig. 3). Hydrolysis rates were increased further, up to six-fold higher than PETase alone, suggesting that further improvements may be possible through this type of protein engineering.

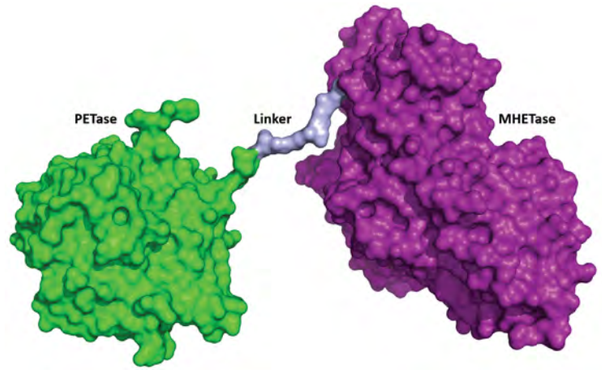

Figure 3: Cartoon representation of a PETase-MHETase chimera, with PETase in green, MHETase in purple and the 8 amino acid linker in blue.

Multi-enzyme systems have been previously described in the deconstruction of natural polymers including lignocellulose and chitin, with a range of enzyme mixtures produced by one species of bacteria, or sometimes large consortia working in parallel. A deeper understanding of these naturally evolved processes will provide further insights into how we may better engineer systems that can tackle polymers such as PET. In collaboration with our US colleagues at the National Renewable Energy Laboratory, our team is focused on the discovery and engineering of faster and more efficient enzyme systems. We aim to develop enhanced cocktails for polyesters, but also expand into enzymatic deconstruction of some of our other most polluting plastics.

The generation of monomers from waste plastic allows the regeneration of food-grade quality plastics and with the addition of other bio-based monomers, creates the potential for upcycling into higher-value materials. Structure-function relationships will remain a central part of this work and we look forward to utilising a wider range of beamlines at Diamond as new advanced facilities continue to come onstream. Given the range and scale of plastic pollution, we are certain that an interdisciplinary approach will be essential, combining advances in mechanical techniques, chemical catalysts and biochemical approaches. This will require working in large consortia such as BOTTLE.org to which we share membership, allowing us to productively share resources and expertise. While we recognise that we must reduce our reliance on plastic, particularly single-use materials, we believe that the low energy footprint and carbon capturing advantages of closed-loop circular enzyme systems can have a significant positive impact on our environment.

References:

1. Austin H. P. *et al.* Characterization and engineering of a plastic-degrading aromatic polyesterase. *Proc. Natl. Acad. Sci.* **115**, 201718804 (2018). DOI: 10.1073/pnas.1718804115
2. Yoshida S. *et al.* A bacterium that degrades and assimilates poly(ethylene terephthalate). *Science (80-.).* **351**, 1196–1199 (2016). DOI: 10.1126/science.aad6359

Funding acknowledgement:

We thank Research England (E3) and the BBSRC (grant BB/P011918/1) for funding and the National Renewable Energy Laboratory (NREL) and BOTTLE.org Consortium funded through the US Department of Energy contract DEAC3608GO28308.

Corresponding authors:

Prof. John McGeehan, Centre for Enzyme Innovation, University of Portsmouth, john.mcgeehan@port.ac.uk; Miss Rosie Graham, Centre for Enzyme Innovation, University of Portsmouth, rosie.graham@port.ac.uk

Biological wires for plugging cells into the environment

Related publication: Edwards M. J., White G. F., Butt J. N., Richardson D. J. & Clarke T. A. The Crystal Structure of a Biological Insulated Transmembrane Molecular Wire. *Cell* **181**, 665-673.e10 (2020). DOI: 10.1016/j.cell.2020.03.032

Publication keywords: Extracellular electron transfer; Shewanella; Porin-cytochrome complex; Iron oxidation; Metal reduction; Respiration; Outer membrane protein; Electrogenic bacteria; Geobacter; Decaheme

Some bacteria can survive in the absence of oxygen by using a metal, such as iron, instead. To do this, they require a system for getting electrons from the inside of the cell to the outside, which is usually prevented by the insulating membrane surrounding the cell. There was no known system that could do this.

Previous research identified three genes in the aquatic bacterium *Shewanella oneidensis* that could move electrons out of the cell. However, it was unclear how these three genes could cause such an effect. Researchers from the University of East Anglia investigated how the products of these genes could assemble into something allowing electron transport across the outer membrane of the cell.

They collected X-ray data on Macromolecular Crystallography (MX) beamlines I03 and I04, using intense, tuneable X-rays to collect data from the small and fragile protein crystals. Using this data, the team were able to identify the positions of the 20 iron atoms inside the protein structure, which allowed the building of the complete structure. For the first time, they were able to see how nature assembles wires out of biological material, and how to build complexes to allow electrons to flow into and out of a living cell. Complexes such as this have a range of potential applications, including biomining using microbes to extract copper and gold from low-grade ores.

Many microorganisms use extracellular electron transfer (EET) as a mechanism of generating energy from the environment. This process is common in the soils and sediments of the earth's subsurface, where substrates in the form of metal oxides and metal ions are used in place of oxygen. Microorganisms use EET to generate energy for growth and survival by moving electrons released from the breakdown of organic molecules into substrates outside the cell. This presents a challenge, as these substrates are often insoluble or toxic and cannot be taken into the cell, so electrons have to be transported through the impermeable barriers that cover the cell[1].

EET bacteria such as *Shewanella* have developed mechanisms to overcome this problem. *Shewanella* is a gram-negative bacterium that has an outer membrane that surrounds the cell. Cell membranes are insulative and impermeable, meaning that electrons and water-soluble molecules cannot pass through. To move these electrons across the outer membrane *Shewanella* assembles protein complexes, known as Mtr complexes, in the outer membrane. These function as biological wires to allow electrons to pass to the cell surface where they can react with a range of materials. For *Shewanella* these have been shown to include iron and manganese oxides, synthetic electrodes, soluble toxic metals such as uranium and chromium as well as organic soil matter such as humus[2].

The Mtr complex was known to consist of three components: a transmembrane barrel-like structure known as a porin, MtrB, and two proteins that contain ten haem groups, which are organic molecules that tightly bind individual iron atoms[3]. These proteins are known as cytochromes, as the ten haem groups give the protein a distinctive blood-like colour. The two cytochromes of the Mtr complex are known as MtrA and MtrC. MtrA is responsible for collecting electrons inside the cell, while MtrC is exposed on the cell surface and is important for the reduction of the majority of extracellular substrates.

The arrangement of the three component proteins of the Mtr complex was not clear until a 'porin-cytochrome' model was proposed[4]. This model suggested that the two cytochromes on opposite sides of the membrane made contact through the porin, allowing for electrons to move across the membrane using the twenty iron atoms in the two cytochromes. However, the absence of a complete structure of the complex made it hard to understand how it could assemble into a conductive wire and catalyse the reduction of a broad range of substrates. In 2020 we published the first structure of a complete Mtr complex, revealing the molecular details of bacterial extracellular electron transfer[5].

To solve the structure by X-ray protein crystallography, crystals were obtained for both the complete Mtr complex and the MtrC subunit. X-ray diffraction data were collected on beamlines I03 and I04 at Diamond Light Source where the structures were solved by single-wavelength anomalous diffraction phasing. 20 iron atoms were located for the Mtr complex corresponding to the 20 haems of the complex with a single copy in the asymmetric unit. A higher resolution native dataset was subsequently collected for the Mtr complex giving final resolutions of 0.27 nm (2.7 Å) and 0.23 nm (2.3 Å) for the Mtr complex and MtrC respectively.

The structure showed for the first time how the complex was constructed and revealed that MtrA formed an elongated protein which spanned the entire width of the outer membrane (Fig. 1), with MtrB wrapping around MtrA to form a membrane spanning porin cytochrome complex. MtrC is bound to the top of this complex, functioning as a highly exposed 'hub' for electron transfer to extracellular substrates (Fig. 1a).

This structure revealed that the MtrA-MtrB complex was the central component required for electron transfer across the outer membrane. The ten haem groups of MtrA formed a linear, closely packed chain of iron atoms, allowing rapid electron transport across 8 nm. The outer membrane is approximately ~ 4 nm wide, allowing MtrA to protrude from both sides (Fig. 1b). Because MtrA is water soluble, it cannot pass through the membrane and so is held in place in the outer membrane by MtrB. The interior of the MtrB barrel is water soluble while the exterior is membrane soluble, this allows MtrB to function as a collar for MtrA and holds it in place in the outer membrane. Long protein chains from the ends of the MtrB barrel wrap around the exterior facing end of MtrA, preventing the accidental leakage of water or other small molecules from the periplasm, while the cell interior facing end is loose, allowing it to swing freely and interact with electron donors inside the cell.

This MtrAB porin-cytochrome conduit is commonly found in bacteria that are capable of EET. This includes both 'metal breathing' bacteria and 'metal eating' bacteria, which take in electrons from the environment and use them to fix carbon dioxide. It is suggested that these bacteria may have been some of the earliest forms of metabolism on the planet. The homology between the MtrA-MtrB porin cytochrome complexes of metal breathing and metal eating bacteria provides insight into how these two-component complexes can function to accept electrons from soluble metals and transfer them into periplasmic electron acceptors.

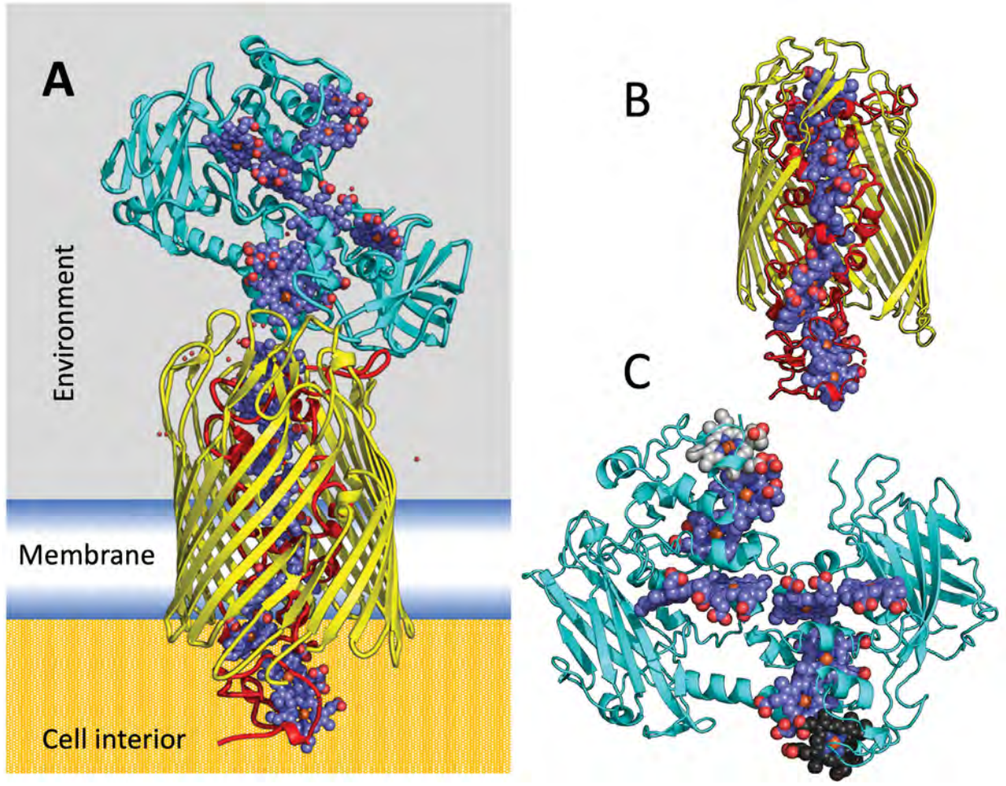

*Figure 1: Structure of a bacterial wire. (**a**) Structure and position of the Mtr complex in the outer membrane of a bacterial cell. The MtrA, MtrB and MtrC domains are coloured red, yellow and cyan respectively, while the haem chain that passes from the cell interior and extends into the environment is coloured blue; (**b**) Cut-through of the MtrAB porin-cytochrome component) revealing how MtrA (red) passes through the interior of the MtrB porin (yellow); (**c**) Crystal structure of MtrC revealing the cross-like configuration of the haem groups. The haems are shown in blue spheres, except for the haems likely involved in electron input (black) and export (light grey).*

The third component of the Mtr complex from the metal breathing system is MtrC, which binds to the top of the MtrAB complex without embedding within the porin. This means that the majority of the surface area remains exposed and capable of electron transfer to different substrates outside the cell. Unlike MtrA, the ten haems of MtrC are arranged in a planar cross-like configuration, allowing for electrons to enter or leave from four possible sites (Fig. 1c). The complex now reveals that electrons enter MtrC via one haem site. At the opposite end of the structure there is an exposed haem that is raised approximately 10 nm (100 Å) above the surface of the cell. The surface of MtrC is also tilted, allowing partial exposure of the other haems. This orientation would allow for direct reduction of insoluble minerals and metal through the top exposed haem, as well as soluble metals and electron acceptors.

This structure of an Mtr complex has finally resolved the mystery of how bacteria can move electrons across the outer membrane of the cell, by assembling a porin-cytochrome complex containing a chain of haems that stretches from one side of the membrane to another. Knowing the position and orientation of the MtrC on the cell surface allows for electron transfer to minerals, electrodes and other electrogenic reactions to be better understood and manipulated. Determining this structure has provided a molecular blueprint which will allow us to think about how to directly interface biological cells to electrical systems, as well as drive and control both metabolic and biosynthetic reactions, including synthesis of platform chemicals or efficient processing of wastewater.

References:

1. White G. F. *et al.* Mechanisms of Bacterial Extracellular Electron Exchange. *Advances in Microbial Physiology* (ed. Poole R. K. B. T.-A. in M. P.) **68**, 87–138 (Academic Press, 2016). DOI: 10.1016/bs.ampbs.2016.02.002
2. Beblawy S. *et al.* Extracellular reduction of solid electron acceptors by Shewanella oneidensis. *Mol. Microbiol.* **109**, 571–583 (2018). DOI: 10.1111/mmi.14067
3. Ross D. E. *et al.* Characterization of protein-protein interactions involved in iron reduction by Shewanella oneidensis MR-1. *Appl. Environ. Microbiol.* **73**, 5797–5808 (2007). DOI: 10.1128/AEM.00146-07
4. Hartshorne R. S. *et al.* Characterization of an electron conduit between bacteria and the extracellular environment. *Proc. Natl. Acad. Sci. U. S. A.* **106**, 22169–22174 (2009). DOI: 10.1073/pnas.0900086106
5. Edwards M. J. *et al.* The Crystal Structure of a Biological Insulated Transmembrane Molecular Wire. *Cell* **181**, 665-673.e10 (2020). DOI: 10.1016/j.cell.2020.03.032

Funding acknowledgement:
This research was supported by the Biotechnology and Biological Sciences Research Council grants BB/K009885/1, BB/L023733/1 and BB/H007288/1.

Corresponding authors:
Thomas A Clarke, University of East Anglia, tom.clarke@uea.ac.uk; Marcus J Edwards, University of Essex, m.edwards@Essex.ac.uk

Understanding the flow of potassium ions across cell membranes

Related publication: Lolicato M., Natale A. M., Abderemane-Ali F., Crottès D., Capponi S., Duman R., Wagner A., Rosenberg J. M., Grabe M. & Minor D. L. K_{2P} channel C-type gating involves asymmetric selectivity filter order-disorder transitions. *Sci. Adv.* **6**, eabc9174 (2020). DOI: 10.1126/sciadv.abc9174

Publication keywords: K_{2P} potassium channel; K_{2P}2.1 (TREK-1); C-type gate; Selectivity filter

The flow of potassium ions across the cell membrane is regulated by K_{2P} potassium channels, controlling electrical activity in the brain, heart and nervous system. These channels have important roles in pain, migraine, depression, anaesthetic responses, arrhythmias, hypertension and lung injury responses. K_{2P} channels regulate ion flow using a selectivity filter (C-type) gate. However, previous structural studies have not captured the gating mechanisms, and they remain poorly understood. Currently, there are no drugs available that selectively target K_{2P} potassium channels. To develop new ways to control their function, we need to understand more about the gating mechanisms and their roles in human biology.

In work published in *Science Advances*, researchers from Diamond Light Source, University of California, San Francisco and the University Pittsburgh, USA, combined X-ray crystallography in different potassium concentrations, potassium anomalous scattering, molecular dynamics and electrophysiology to uncover the changes that occur in K_{2P} C-type gating. At Diamond, the team used the Long-Wavelength Macromolecular Crystallography (MX) beamline (I23) to observe changes in potassium ions within the channel directly. I23 is the only beamline in the world optimised to measure signals from potassium ions directly, and its unique capabilities were central to these studies. The results show that K_{2P} gating involves pinching and dilation of two key elements of the channel selectivity filter gate. These structural changes are accompanied by the loss of potassium ions. Including a small molecule activator (ML335) suppressed these changes and demonstrated how stabilisation of the selectivity filter gate facilitates ion flow through the channel.

These studies show that small molecule activators bind to and stabilise the K_{2P} selectivity filter gate, preventing the pinching and dilation conformational changes and loss of potassium ions that lead to channel inactivation. These findings open a path to develop new K_{2P} channel-directed drugs to treat pain, ischemia (restricted blood flow), depression and lung injury.

K_{2P} potassium channels respond to diverse physical and chemical inputs that include pressure, temperature, pH, signalling lipids, phosphorylation and volatile anaesthetics[1]. Their actions control electrical activity in the nervous, cardiovascular and immune systems by regulating the flow of potassium ions across the cell membrane through the action of their selectivity filter (C-type) gate[2,3]. K_{2P}s are dimers of subunits that each contain two conserved elements, SF1 and SF2, that form the selectivity filter (Fig. 1). These channels have important roles in pain, migraine, depression, anaesthetic responses, arrhythmias, hypertension and responses to lung injury. Yet, despite much effort, K_{2P}s have remained the most poorly understood potassium channel class and suffer from a poor pharmacological profile that limits our ability to investigate their biological functions. Selectivity filter C-type gating occurs in many potassium channel classes and has a hallmark sensitivity to potassium due to interactions between the permeant potassium ions and selectivity filter. Structural studies of homotetrameric potassium channels have uncovered various selectivity filter rearrangements attributed to C-type gating, but whether C-type gating involves selectivity filter pinching, dilation or more subtle structural changes has remained unclear. Further, prior K_{2P} structural studies have failed to identify selectivity filter conformational changes that could explain how K_{2P} C-type gating occurs despite showing conformational changes in the channel transmembrane helices that impact activity. This lack of a structural framework has left open questions regarding the extent to which K_{2P} C-type gating mechanisms resemble homotetrameric channels and whether the innate heterodimeric K_{2P} selectivity filter architecture confers unique properties to their C-type gates.

Crystal structures of the thermo- and mechano-sensitive K_{2P}, K_{2P} 2.1 (TREK-1), alone and complexed with a small molecule activator of the C-type gate, ML335[4], under a series of seven different potassium concentrations revealed unprecedented conformational changes in the K_{2P} selectivity filter. These structures show that under low potassium concentrations (<50 mM [K^+]) both elements of the K_{2P} 2.1(TREK-1) selectivity filter, SF1 and SF2 , undergo potassium-dependent structural rearrangements that are accompanied by the loss of the two potassium ions in the outer portions of the selectivity filter (Fig. 1). These conformational changes pinch SF1 at the extracellular mouth of the pore and dilate the exterior portion of SF2 and unfold the linker that connects SF2 to transmembrane helix 4 (SF-M4 loop). Hence, K_{2P}s use both types of mechanisms that have been proposed to control the function of potassium channel selectivity filter C-type gates, pinching and dilation. Binding of the small molecule activator ML335 to a site behind the selectivity filter, the K_{2P} modulator pocket[4], completely suppresses these conformational changes and the loss of potassium ions (Fig. 1).

Measurement of anomalous scattering from potassium ions using long wavelength crystallographic methods[5] enabled by the unique capabilities of beamline I23 provided essential structural information about the changes in the occupancy of potassium ions in the selectivity filter. These studies showed that under high potassium conditions (200 mM [K^+]) all four potassium-binding sites were occupied regardless of the presence of the activator ML335. By contrast, all four selectivity filter potassium ion binding sites remained occupied under low potassium conditions (1 mM [K^+]) only when ML335 was bound (Fig. 1). These observations were corroborated by extensive molecular dynamics studies and single channel electrophysiology measurements that established that ML335 stabilisation of the filter enhances ion flow and channel open probability. These studies also identified a key functional role for the uniquely long SF2-M4 loop. This channel element unfolds when SF2 dilates, is stabilised by the binding of ML335, and connects the C-type gate with gating cues sensed by other parts of the channel[2].

These findings show that asymmetric order-disorder transitions enabled by the K_{2P} heterodimeric architecture are at the heart of K_{2P} gating mechanisms. They support a model in which the K_{2P} C-type gate transits between an inactive state in which there is a high degree of selectivity filter disorder having low potassium ion occupancy to a rigidified conductive state in which all potassium binding sites are occupied[4]. Selectivity filter mobility is influenced by diverse classes of physical and chemical signals as well as agents that stabilise the SF2-M4 loop such as ML335. Such findings pave the way for the development of new chemical or biologic K_{2P} modulators that target critical parts of the channel and highlight the potential of the SF2-M4 loop as a key control point for pharmacological intervention. K_{2P}- directed agents based on these findings may provide new avenues for treating physiological problems in which K_{2P} channels are important such as pain, migraine, ischemia and lung injury.

References:

1. Feliciangeli S. *et al.* The family of K_{2P} channels: Salient structural and functional properties. *J. Physiol.* **593**, 2587–2603 (2015). DOI: 10.1113/jphysiol.2014.287268
2. Bagriantsev S. N. *et al.* Multiple modalities converge on a common gate to control K_{2P} channel function. *EMBO J.* **30**, 3594–3606 (2011). DOI: 10.1038/emboj.2011.230
3. Piechotta P. L. *et al.* The pore structure and gating mechanism of K_{2P} channels. *EMBO J.* **30**, 3607–3619 (2011). DOI: 10.1038/emboj.2011.268
4. Lolicato M. *et al.* K_{2P}2.1 (TREK-1)-activator complexes reveal a cryptic selectivity filter binding site. *Nature* **547**, 364–368 (2017). DOI: 10.1038/nature22988
5. Wagner A. *et al.* In-vacuum long-wavelength macromolecular crystallography. *Acta Crystallogr. Sect. D Struct. Biol.* **72**, 430–439 (2016). DOI: 10.1107/S2059798316001078

Funding acknowledgement:
National Institutes of Health NIMH R01-MH093603 (D.L.M).

Corresponding author:
Dr Daniel Minor, Cardiovascular Research Institute, University of California, San Francisco, USA, USA, Lawrence Berkeley National Laboratory, USA, daniel.minor@ucsf.edu

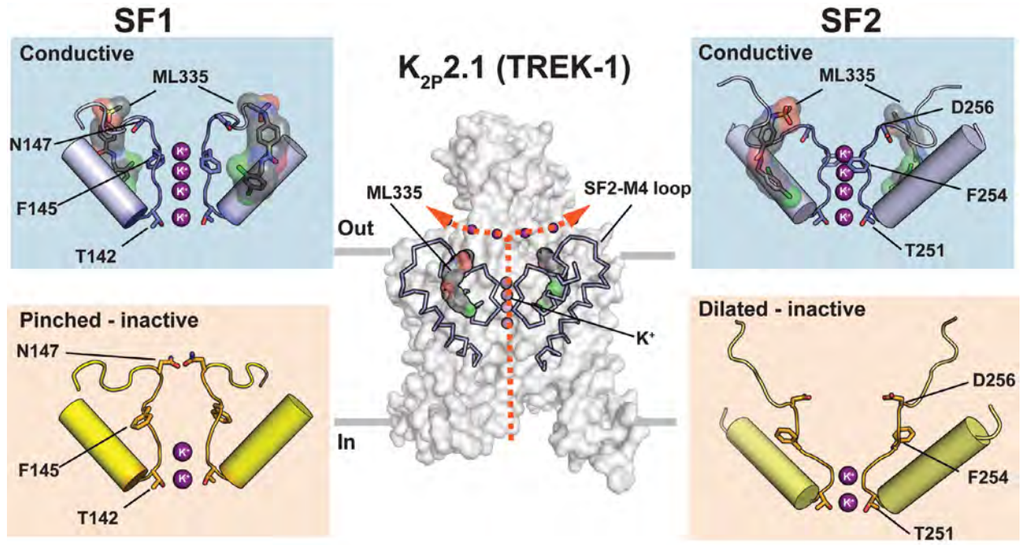

Figure 1: Structural changes in the K_{2P}2.1 (TREK-1) C-type selectivity filter gate. (Centre) overall structure of K_{2P}2.1 (TREK-1) (solid) highlighting SF2 and surrounding structures (wire frame), ML335 (black, space filling), and potassium ions (purple spheres). Orange arrows show K^+ ion flow through the channel. Grey bars indicate the membrane. (Left) SF1 structures in low [K^+] showing the conductive conformation with ML335 (top) and pinched, inactive conformation (bottom). (Right) SF2 structures in low [K^+] showing the conductive conformation with ML335 (top) and dilated, inactive conformation (bottom). K^+ ions are shown as purple spheres. ML335 is shown in space filling representation. Select selectivity filter residues are indicated.

Crystal structure of an anti-TB drug target

Related publication: 1. Zhang L., Zhao Y., Gao Y., Wu L., Gao R., Zhang Q., Wang Y., Wu C., Wu F., Gurcha S. S., Veerapen N., Batt S. M., Zhao W., Qin L., Yang X., Wang M., Zhu Y., Zhang B., Bi L., Zhang X., Yang H., Guddat L. W., Xu W., Wang Q., Li J., Besra G. S. & Rao Z. Structures of cell wall arabinosyltransferases with the anti-tuberculosis drug ethambutol. Science (80-.). 368, 1211–1219 (2020). DOI: 10.1126/science.aba9102

Publication keywords: *Mycobacterium tuberculosis*; Cell Wall; Structure; Arabinosyltransferase; Ethambutol; Drug target

Tuberculosis (TB), caused by *Mycobacterium tuberculosis* (*Mtb*), is a life-threatening disease that has plagued humanity for thousands of years. Mycobacteria, including *Mtb*, synthesise a complex cell wall to support and protect the bacterial cells. The front-line anti-TB drug ethambutol inhibits the synthesis of the mycobacterial cell wall by targeting the Emb proteins (EmbA, EmbB and EmbC). However, although the drug has been in use for fifty years, its mode of action remains unclear.

In *Mtb*, EmbC is required for the synthesis of lipoarabinomannan (LAM), an important virulence factor that adds to the pathogen's effectiveness and helps it infect host cells. LAM also plays a crucial role in host-pathogen interactions and modulating the host immune response during infection. However, the three-dimensional structure of the Emb proteins had yet to be determined. To address the lack of structural information and functional analysis, an international team of researchers determined the crystal structure of EmbC from *Mycobacterium smegmatis* in complex with a sugar substrate, using Macromolecular Crystallography (MX) on Diamond Light Source's I04-1 beamline.

Unexpectedly, they found that the mycobacterial acyl-carrier-protein (AcpM) is bound to EmbC to form a stable $EmbC_2$-$AcpM_2$ complex. A combination of the MX data with a cryo-EM structure of the ethambutol-bound $EmbC_2$-$AcpM_2$ complex suggests that ethambutol works by binding to the same sites as both donor and acceptor substrates of EmbC. These results provide a structural basis for understanding the biochemical function and inhibition of EmbC and the development of new anti-tuberculosis agents.

Tuberculosis (TB) caused by *Mycobacterium tuberculosis* (*Mtb*) is a life-threatening disease that accounts for more than 1.4 million deaths per annum[1]. Ethambutol is one of the five first line anti-TB drugs that are currently in clinical use to treat TB. The membrane-embedded Emb proteins EmbA, EmbB and EmbC, which are involved in cell wall biosynthesis, are regarded as the targets of ethambutol. In *Mtb*, EmbA and EmbB are responsible for the synthesis of arabinogalactan (AG), while EmbC is required for the synthesis of lipoarabinomannan (LAM)[2]. In particular, LAM is an important glycolipid which plays a key role in host–pathogen interactions, as well as in modulating the host immune response during infection[3].

EmbC, like other Emb proteins, is a GT-C family arabinofuranosyl-transferase. Its specific role is to transfer an arabinofuranose residue from decaprenyl-phosphate-arabinose (DPA) to its acceptor, a LAM precursor, leading to the elongation of the arabinan chain in LAM biosynthesis (Fig. 1A). To address the lack of structural information and paucity of functional analysis of any Emb proteins, EmbC from *Mycobacterium smegmatis* (*Msm*) was selected for structural and functional study. Purified $EmbC_{Msm}$ protein was shown functional as an $\alpha(1\rightarrow5)$ arabinosyltransferase in our established cell-free activity assay, whose activity was inhibited by ethambutol, thus confirming that ethambutol targets EmbC protein. The crystal structure of $EmbC_{Msm}$ was then determined in complex with a di-arabinose substrate at 3.3 Å resolution. The phase problem was solved by single-wavelength anomalous

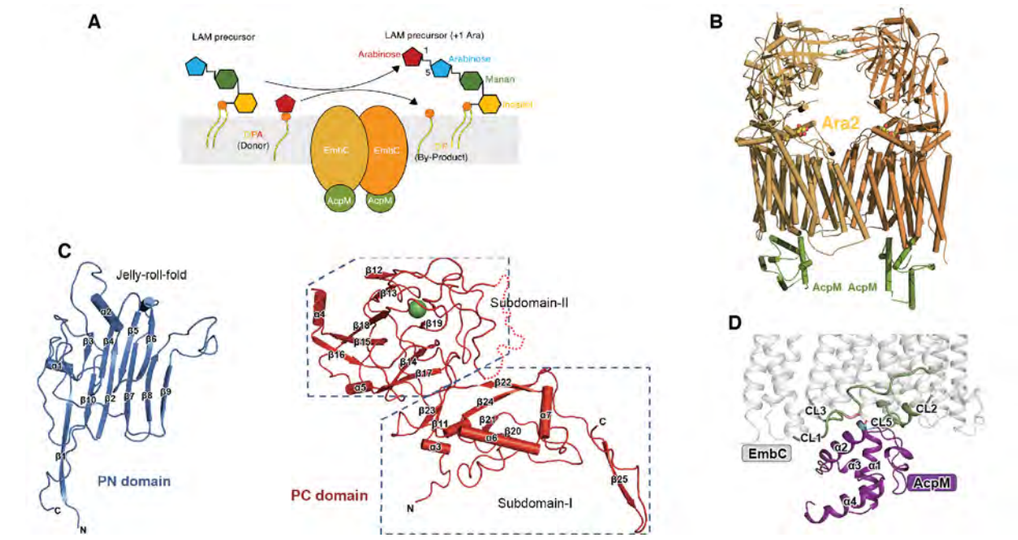

Figure 1: Function and structure of the $EmbC_2$-$AcpM_2$ complex. (A) Schematic representation of the catalytic reaction of $EmbC_2$-$AcpM_2$. (B) Overall structure of $EmbC_2$-$AcpM_2$. (C) Structural details of (left) PN and (right) PC domain. (D) Binding interface of EmbC and AcpM.

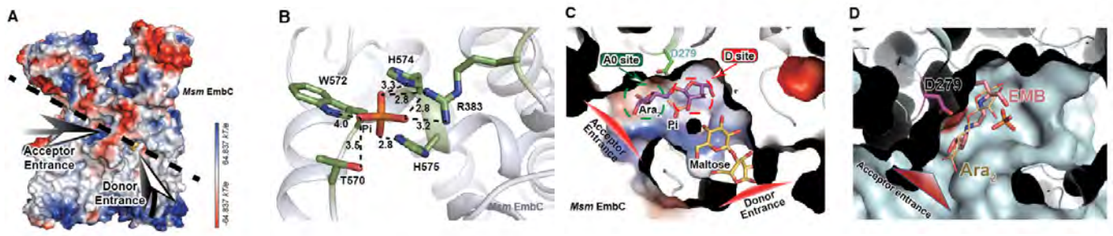

Figure 2: Substrates binding in the active site of the $EmbC_2$-$AcpM_2$ complex. (A) Overview of the substrate entrances to the active site. (B) Phosphate binding sites of EmbC. (C) Clipped view of the active site with acceptor entrance and donor entrance. Ara_2, maltose (part of detergent DDM), Pi (phosphate ion), and the catalytic residue (Asp279) are shown as sticks. (D) Structural superposition of di-arabinose bound EmbC in this paper and cryo-EM structure of ethambutol bound EmbC (PDB entry: 7BVE).

dispersion (SAD). The final model has R_{work}/R_{free} values of 0.232 and 0.265, respectively. Most of the polypeptide could be built into the electron density maps except for residues 1-9, 780-810 of EmbC. The structure has shown a homo-dimeric assembly of EmbC associated with an unexpected AcpM protein at the cytoplasmic surface of each EmbC monomer (Fig. 1B). Analysis of the active site and location of bound sugar substrate and ligands also provides valuable insights into the catalytic basis for arabinose transfer by EmbC.

Within the asymmetric unit there are two EmbCs which form a dimer at the transmembrane interface. The mode of dimerisation is characterised by forming hydrophobic clusters between transmembrane (TM) domains close to the cytoplasmic side and periplasmic side. The overall structure of $EmbC_{Msm}$ is composed of a 15-helix transmembrane (TM) domain and N-/C-terminal periplasmic domains (identified as PN and PC). The PN domain (also periplasmic domain linking TM1 and TM2) adopts a jelly-roll-fold (Fig. 1C), which is typical for polysaccharide binding units[4]. The PC domain can be divided into two subdomains, with subdomain-I displaying a mixed α/β structure and subdomain-II exhibiting a jelly-roll-fold (Fig. 1C). The active site is located in a pocket at the junction between the TM domain and the periplasmic domains, composed by PL2-6, helix $\alpha6$ in PC domain and residue Trp965 in PC domain.

The *Msm* AcpM has a four-helix topology arranged in a right-handed bundle, similar to that of *Mtb* AcpM (PDB code: 1KLP). AcpM binds to each EmbC protomer through extensive electrostatic interactions. Helix $\alpha2$ of AcpM and the connecting loops at its N-/C-terminus are intimately engaged with the CLs of the EmbC protein (Fig. 1D). This is consistent with the known role of $\alpha2$ in AcpM as a contact site with its target proteins (*e.g.* AcpS). Mutagenesis and functional studies showed AcpM plays a role in modulating LAM synthesis *in vivo* by forming complex with $EmbC_2$.

The Emb proteins have two substrates, an arabinose donor DPA and an acceptor arabinan. The structure shows that there are two substrate entrances leading to the active site, henceforth denoted as the donor entrance and the acceptor entrance (Fig. 2A). In the crystal structure of di-arabinose-bound $EmbC_2$, an endogenous phosphate ion appears to be trapped in the active site by the di-arabinose and maltose (part of detergent DDM used for purification) (Fig. 2B-C). It is bound to a positively charged region that includes Arg383, His574 and His575 and is near Thr570, Trp572 and the catalytic Asp279 (Fig. 2B-C). It is proposed that this phosphate represents the phosphate group of DPA as K_d values of DPA for any single mutant EmbC proteins were greatly reduced compared with the wildtype. Furthermore, enzymatic activity was also shown completely lost for these mutants of the phosphate binding site.

The di-arabinoside group, which is identified as part of the substrate analogue Ara_2OC8 soaked with EmbC during crystallisation, binds between the catalytic site Asp279 and the phosphate (Fig. 2C). Considering that the two arabinoside groups are located on different sites of Asp279, for clarity, the positions of the two-arabinofuranose rings were denoted as D site (arabinose from donor) and A_0 site (arabinose from the terminal residue of acceptor). The arabinofuranose in the D-site is most likely mimicking the one originated from donor DPA, while the other in the A_0-site resembles an arabinose from the terminal residue in the acceptor.

When superimposing the crystal structure of EmbC in complex with disaccharide to the cryo-EM structure of the ethambutol-bound EmbC, we found that ethambutol overlapped with the disaccharide in a high degree of similarity (Fig. 2D). Since the di-saccharide represents the arabinose groups from both donor and acceptor, we infer that ethambutol inhibits the arabinose transfer reaction by competing with the binding of both substrates in the active site, in accordance with the hypothesis that ethambutol interferes with transfer of arabinose as evidenced by the rapid accumulation of DPA in ethambutol treated *Msm* cells.

In summary, with the support from beamline I04-1 at Diamond, the crystal structure of a mycobacterial $EmbC_2$-$AcpM_2$ complex has been determined. The di-arabinose bound structure of the $EmbC_2$-$AcpM_2$ complex allows us to understand the structural features required for catalysis. By structural comparison it is suggested ethambutol functions by competing with the substrates for binding to EmbC. The structural information will greatly facilitate the development of new anti-tuberculosis agents.

References:

1. Global Tuberculosis Report 2020. https://www.who.int/publications/i/item/9789240013131
2. Jankute M. *et al.* Assembly of the Mycobacterial Cell Wall. *Annu. Rev. Microbiol.* **69**, 405–423 (2015). DOI: 10.1146/annurev-micro-091014-104121
3. Korkegian A. *et al.* Mutations in the Essential Arabinosyltransferase EmbC Lead to Alterations in Mycobacterium tuberculosis Lipoarabinomannan*. *J. Biol. Chem.* **289**, 35172–35181 (2014). DOI: 10.1074/jbc.M114.583112
4. Boraston A. B. *et al.* Carbohydrate-binding modules: fine-tuning polysaccharide recognition. *Biochem. J.* **382**, 769–781 (2004). DOI: 10.1042/BJ20040892

Funding acknowledgement:
This work was supported by grants from the National Key R&D Program of China (2017YFC0840300) and Project of International Cooperation and Exchanges NSFC (81520108019) to Z.R.

Corresponding authors:
Dr Lu Zhang, ShanghaiTech University, zhanglu1@shanghaitech.edu.cn;
Dr Zihe Rao, ShanghaiTech University; Tsinghua University; Institute of Biophysics, Chinese Academy of Sciences; Nankai University, raozh@tsinghua.edu.cn

Viruses that defeat microbe immunity could help fight drug-resistant bacteria

Related publication: Athukoralage J. S., McMahon S. A., Zhang C., Grüschow S., Graham S., Krupovic M., Whitaker R. J., Gloster T. M. & White M. F. An anti-CRISPR viral ring nuclease subverts type III CRISPR immunity. *Nature* **577**, 572–575 (2020). DOI: 10.1038/s41586-019-1909-5

Publication keywords: CRISPR; Viral infection; Cyclic nucleotide; Nuclease

Viruses can infect all cellular organisms, from bacteria to humans. Once they have tricked their way into the cell, they exploit the host's cellular machinery to make more copies of themselves, which can be released and go on to infect other cells. Organisms have developed strategies to recognise and defend against any virus infection, called adaptive immunity. However, viruses have evolved a way to combat the host defence mechanism, meaning they ultimately win the infection battle.

Microbes use an adaptive immunity mechanism called CRISPR against virus infection. An international team of researchers focussed on one type of CRISPR (type III) and investigated how viruses overcome the microbial CRISPR defence system. Data they collected on the Microfocus Macromolecular Crystallography (MX) beamline I24 at Diamond Light Source provided vital insights into the mechanism used by viruses to overcome the microbial defence.

Microbes with the type III CRISPR defence system produce a cyclic molecule in response to virus detection. It signals that there is an infection and kick-starts cellular processes to combat the attack. However, viruses have evolved an enzyme that binds to and destroys the cyclic molecule, neutralising the defence mechanism. This research used the structure of the viral enzyme, bound to the cyclic molecule, to reveal key details of how the viral enzyme recognises this molecule and how this translates into function. The results show the fundamental mechanism underlying how viruses out-manoeuvre microbe defences against infection. We may be able to use this understanding to engineer viruses to target drug-resistant bacteria that infect humans.

The CRISPR system is a prokaryotic adaptive immune system, providing defence against viruses and other mobile genetic elements in bacteria and archaea[1]. CRISPR systems are mechanistically and structurally diverse and have been classified into six main types based on their signature proteins, with type II (Cas9) undoubtedly the best known due to its application in genome engineering. Type III CRISPR systems use a large multi-subunit ribonucleoprotein complex to detect RNA from invading genetic elements. Binding of this target RNA activates a specialised polymerase domain in the Cas10 subunit, which polymerises ATP into a set of cyclic oligoadenylate (cOA) signalling molecules[2]. These act as second messengers of infection, analogous to the role of cGAMP in the cGAS-STING innate immunity pathway of eukaryotic cells. cOA potentiates type III CRISPR defence by binding to a receptor CARF (CRISPR associated Rossman Fold) domain found in a wide range of ancillary effector proteins. This causes an allosteric activation of degradative enzymatic domains such as HEPN family ribonucleases, which are licensed to degrade RNA or DNA. These defence enzymes in turn degrade nucleic acids non-specifically, which can destroy the invading virus, but also lead to cell death if not regulated[3]. While altruistic suicide is often an appropriate response for virally-infected microbes, there are mechanisms to switch off the defence system by degrading the cOA second messenger using enzymes known as ring nucleases[4].

Viruses can combat CRISPR defence by expressing anti-CRISPR (Acr) proteins that inactivate the cellular effectors, often by binding directly to them. In this study, the hypothesis that viruses might use ring nucleases to neutralise type III CRISPR defence in the host was explored. A gene of unknown function present in many viruses was identified and experiments conducted to establish whether the gene expressed an Acr protein[5]. This was tested against the archaeon *Sulfolobus islandicus*, which was engineered to have only a type III CRISPR system. *S. islandicus* was grown on plates, and when challenged with a lytic virus which lacked the Acr predicted to combat cellular defence there was no viral plaque formation. However, when the experiment was repeated in the presence of a plasmid expressing a candidate Acr, subsequently named AcrIII-1, plaque formation was evident (Fig. 1a). AcrIII-1 was recombinantly over-expressed and tested for activity on several (cOA) signalling molecules to establish if it was a ring nuclease. Experiments showed AcrIII-1 rapidly degraded cyclic tetra-adenylate (cA_4), at a rate 100-fold higher than the

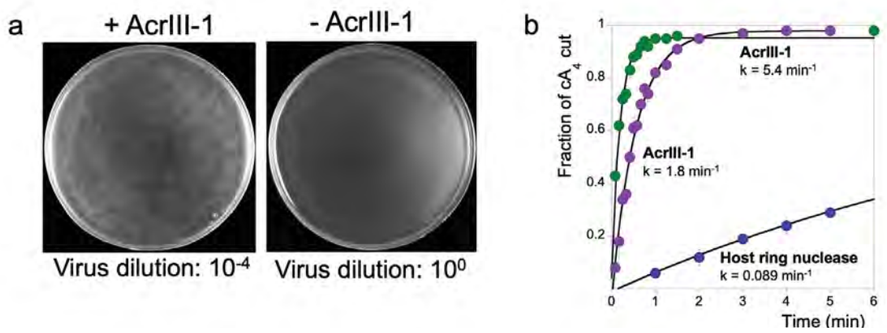

Figure 1: AcrIII-1 acts as an effective Acr, by utilising highly efficient ring nuclease activity with specificity for cA_4. (a) Viral challenge assay on S. islandicus in the presence (left) and absence (right) of a plasmid expressing AcrIII-1. Viral plaques were observed in the presence of AcrIII-1, but not in the control, demonstrating the enzyme can neutralise the host CRISPR defence system; (b) Comparison of in vitro activity for cA_4 degradation by two different viral AcrIII-1 enzymes (green, purple) and a host ring nuclease (Crn1; blue). There is ~100-fold higher activity for the viral enzymes compared to the host, meaning the cellular cA_4 levels are rapidly reduced.

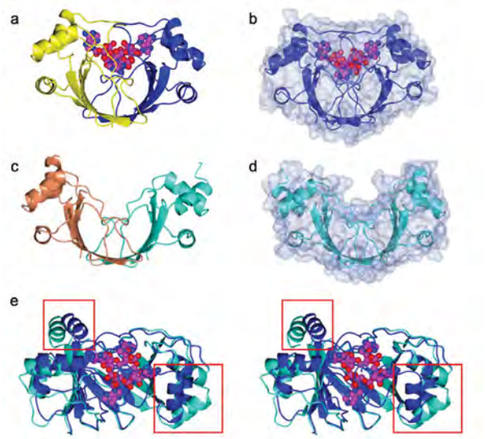

Figure 2: Structure of AcrIII-1 in complex with cA_4. (a) AcrIII-1 (dimer formed from monomers shown in blue and yellow) in complex with cA_4 (magenta); (b) AcrIII-1 in complex with cA_4 with surface representation; (c) Apo AcrIII-1 (dimer formed from monomers in orange and cyan); (d) Apo AcrIII-1, with surface representation; (e) Divergent stereo figure of superimposition of apo AcrIII-1 (cyan) and AcrIII-1 (blue) in complex with cA_4 (magenta); the red squares indicate the α-helices where most movement is observed. Apo AcrIII-1, PDB code 2X4I; AcrIII-1 + cA_4, PDB code 6SCF.

host cellular ring nuclease (Fig. 1b), demonstrating it is a highly specific and efficient enzyme, and thereby acts as an effective mechanism for blocking type III CRISPR defence mounted by the host.

To understand the mechanism for AcrIII-1 activity, a mutant enzyme, lacking a highly conserved histidine residue (H47A), was crystallised in the presence of cA_4 and X-ray diffraction data to 1.55 Å resolution collected using beamline I24. The structure was solved using molecular replacement with the apo structure of the same enzyme which had been reported as part of a structural genomics program a decade earlier (PDB 2X4I). The structure shows AcrIII-1 is a dimer with cA_4 bound at the interface (Fig. 2a). Strikingly cA_4 is completely buried in the structure (Fig. 2b), suggesting movement of residues in AcrIII-1 following binding. While the apo structure (Fig. 2c,d) essentially shows the cA_4 binding site is pre-formed, a large loop encompassing residues 82-94 is flexible and was difficult to model. Comparison of the apo structure with the structure with cA_4 bound (Fig. 2e) shows there is a significant movement of this loop and subsequent α-helix following cA_4 binding, causing the cA_4 to become completely buried. This is no mean feat, given AcrIII-1 is just 16 kDa in size, and cA_4 is >1 kDa.

The interactions made between AcrIII-1 and cA_4 are symmetrical, and hydrogen bonds are formed with ten residues in the active site (Fig. 3a). The residues that form interactions with cA_4 are fully or highly conserved in homologues, suggesting a consistent mode of binding. Arg85 is located on the large loop that folds over the cA_4 binding site, and interacts with the phosphate group on the opposite side of the cA_4 molecule (relative to the side of the cA_4 where the rest of the residues in the monomer interact) suggesting it acts as a 'lock' to keep the loop in position and binding site closed. Insights were also gleaned into the likely catalytic residues important for degradation of cA_4. His47, which is fully conserved in homologues, and is likely to act as the general acid to protonate the leaving group, following in-line nucleophilic attack of the 2' hydroxyl group in the ribose on the phosphodiester bond, on both sides of cA_4 (Fig. 3b). The H47A mutant showed a 2,500-fold decrease in activity, and enabled capture of the structure of AcrIII-1 in complex with cA_4. Glu88 was also shown to be important for activity and may be involved in the modulation of the pK_a of His47.

The elucidation of the ring nuclease activity of AcrIII-1 demonstrates a powerful way in which viruses can neutralise the host defence system. Given cA_4 is a key signalling molecule in initiation of the host CRISPR type III defence system for a range of bacteria and archaea, the evolution of this ingenious system by viruses means it is difficult for a host to respond, without a fundamental change to the signalling molecule required to activate their own defence upon infection. The study has provided highlights into the structure, function and mechanism of AcrIII-1. Such an understanding may provide opportunities to engineer viruses as a way to kill drug resistant bacteria that infect humans in the future.

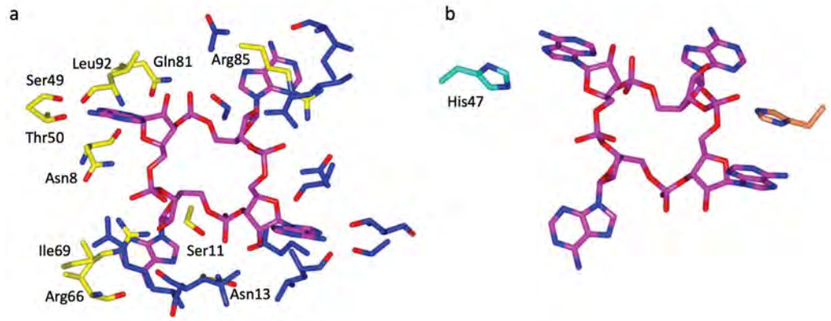

Figure 3: Binding site of AcrIII-1 with cA_4. (a) Residues from the AcrIII-1 dimer (different monomers shown in blue and yellow) that interact with cA_4 (magenta); (b) His47 of AcrIII-1 (position taken from the apo structure; different monomers shown in orange and cyan) is predicted to act as the general acid in catalysis for degradation of cA_4 (magenta). Apo AcrIII-1, PDB code 2X4I; AcrIII-1 + cA_4, PDB code 6SCF.

References:

1. Makarova K. S. *et al.* Evolutionary classification of CRISPR–Cas systems: a burst of class 2 and derived variants. *Nat. Rev. Microbiol.* **18**, 67–83 (2020). DOI: 10.1038/s41579-019-0299-x
2. Kazlauskiene M. *et al.* A cyclic oligonucleotide signaling pathway in type III CRISPR-Cas systems. *Science.* **357**, 605–609 (2017). DOI: 10.1126/science.aao0100
3. Rostøl J. T. *et al.* Non-specific degradation of transcripts promotes plasmid clearance during type III-A CRISPR–Cas immunity. *Nat. Microbiol.* **4**, 656–662 (2019). DOI: 10.1038/s41564-018-0353-x
4. Athukoralage J. S. *et al.* Ring nucleases deactivate type III CRISPR ribonucleases by degrading cyclic oligoadenylate. *Nature* **562**, 277–280 (2018). DOI: 10.1038/s41586-018-0557-5
5. Athukoralage J. S. *et al.* An anti-CRISPR viral ring nuclease subverts type III CRISPR immunity. *Nature* **577**, 572–575 (2020). DOI: 10.1038/s41586-019-1909-5

Funding acknowledgement:
This work was supported by grants from the Biotechnology and Biological Sciences Research Council (BB/S000313/1 to M.F.W. and BB/R008035/1 to T.M.G.).

Corresponding authors:
Dr Tracey Gloster, University of St Andrews, tmg@st-andrews.ac.uk;
Prof. Malcolm White, University of St Andrews, mfw2@st-andrews.ac.uk

Sweet enzymes from gut bacteria: from discovery to diagnostics

Related publication: Wu H., Rebello O., Crost E. H., Owen C. D., Walpole S., Bennati-Granier C., Ndeh D., Monaco S., Hicks T., Colvile A., Urbanowicz P. A., Walsh M. A., Angulo J., Spencer D. I. R. & Juge N. Fucosidases from the human gut symbiont *Ruminococcus gnavus*. *Cell. Mol. Life Sci.* **78**, 675–693 (2020). DOI: 10.1007/s00018-020-03514-x

Publication keywords: Antennary fucose; Glycoside hydrolase; Gut microbiota; Lewis epitopes; Mucin glycosylation; Mucus

The microorganisms that live in the human gut have a profound impact on our health. The microbes living in intestinal mucus, a complex network of proteins and attached sugars, act as 'gatekeepers' by maintaining gut barrier function. However, the mechanisms by which they interact with the host remain largely unknown. Researchers investigated *Ruminococcus gnavus*, a common resident of the human gut that has a major role in health and disease. They investigated its potential to process the sugar fucose using enzymes called fucosidases. They also explored the pool of fucosidases produced by different *R. gnavus* strains.

Using Diamond Light Source's Versatile Macromolecular Crystallography *in situ* (VMXi) beamline allowed the team to track their crystallisation experiments in real time. They were also able to test crystal diffraction quickly and easily, rapidly optimising crystallisation conditions to produce consistent, high-quality protein crystals for X-ray diffraction experiments on MX beamlines I03 and I04. The high-resolution diffraction datasets of the *R. gnavus* fucosidase they collected allowed them to solve its structure and locate the part that performs the sugar cleaving chemical reaction.

Fucosylation (adding a fucose sugar to a molecule) is a common modification involved in many human physiological processes including ABO blood grouping, antibody effector functions, cancer progression, and lymphocyte development and adhesion. As such, fucosidases are relevant to many aspects of human health and disease. This work may have potential applications in diagnosing several diseases, including diabetes and certain cancers.

The microbial community inhabiting the human gut (gut microbiota) exerts a profound effect on human health[1]. In the adult colon, gut bacteria have not only access to non-digestible polysaccharides from the diet, but also to complex oligosaccharides from host mucins[2,3]. Mucins are large glycoproteins with a high carbohydrate content of up to 80%. Mucin O-glycan chains are based on core structures which are further elongated with galactose (Gal), N-acetylglucosamine (GlcNAc) and N-acetylgalactosamine (GalNAc) modified by fucosylation, sialylation and sulfation[3]. The main source of glycan diversity is provided by the peripheral terminal epitopes, sialic acid and fucose. These sugars show considerable variation along the GI tract and provide a food source to gut bacteria species inhabiting different regions of the gut[3].

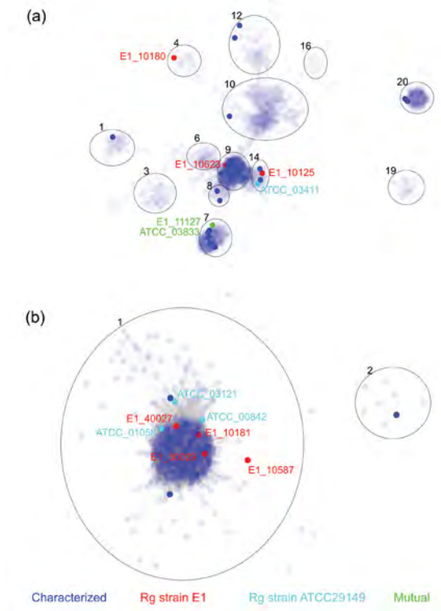

Figure 1: The distribution of R. gnavus GH29 and GH95 fucosidases based on SSN analysis. (a) Partial representation of SSN analysis of GH29 family containing fucosidases from R. gnavus E1 and ATCC 29149 strains. (b) Representation of the SSN central cluster of GH95 family containing all GH95 from R. gnavus E1 and ATCC 29149 strains. Blue nodes sequences extracted from the CAZy database encoding functionally characterised enzymes. Red nodes sequences from R. gnavus E1 strain. Cyan nodes sequences from R. gnavus ATCC 29149 strain. Green nodes sequences common to both R. gnavus E1 and ATCC 29149 strains.

To access this source of nutrients, gut bacteria encode glycoside hydrolases (GHs) with α-L-fucosidases (fucosidases) catalysing the hydrolysis of terminal α-L-fucosidic linkages. Based on sequence identity, α-fucosidases are classified into GH29 and GH95 families of the CAZy database (www.cazy.org). To date, functionally characterised GH95 enzymes show strict substrate specificity to the terminal Fuc α1-2Gal linkage and hydrolyse the linkage via an inverting mechanism whereas GH29 enzymes show relatively relaxed substrate specificities for α-1–3, α-1–4 and α-1–6 linked fucose with hydrolysis proceeding via a retaining mechanism (www.cazy.org).

Ruminococcus gnavus is a prevalent member of the gut microbial community belonging to the Firmicutes division[4]. *R. gnavus* is an early coloniser of the human gut but persists in healthy adults where it is strongly associated with human health and diseases such as inflammatory bowel disease. *R. gnavus*' ability to grow on mucins is strain-dependent, reflecting the distribution of GH families between *R. gnavus* strains[5].

The objectives of this work were to determine the substrate and linkage specificities of fucosidases across *R. gnavus* strains. Sequence similarity network identified strain-specific fucosidases in *R. gnavus* ATCC 29149 and E1 strains that were further validated structurally and enzymatically and against a range of defined oligosaccharides and glycoconjugates. X-ray crystallography combined with saturation transfer difference (STD) nuclear magnetic resonance (NMR) and molecular dynamics simulation unravelled the structural basis for *R. gnavus* unique fucosidase specificity. A sequence similarity network (SSN) analysis was first conducted to identify putative functional relationships between GH29 or GH95 fucosidases from *R. gnavus* and related protein sequences. The SSN analysis covered 6,736 amino acid sequences from the GH29 family extracted from Interpro database 66.0 and

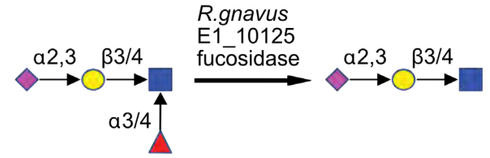

Figure 2: R. gnavus E1_10125 fucosidase can act on sialyl Lewis X/A epitopes. Schematic representation of the enzymatic reaction. Monosaccharide symbols follow the Symbol Nomenclature for Glycans system. Key: fucose (red triangle), GlcNAc (blue square), sialic acid (purple diamond), galactose (yellow circle).

CAZy (www.cazy.org/GH29_characterised.html) and 825 GH95 sequences from Interpro IPR027414. Representative fucosidases were chosen for further characterisation, E1_10125, E1_10180, and ATCC_03833 from the GH29 family and ATCC_00842 and E1_10587 from the GH95 family (Fig. 1a,b).

The genes encoding the selected GH29 and GH95 fucosidases from *R. gnavus* strains ATCC 29149 and E1 were heterologously expressed in *Escherichia coli*. Enzyme activity was first screened against the synthetic substrate pNP-α-L-fucopyranoside (pNP-Fuc). Fucosidase ATCC_03833 showed the highest catalytic efficiency with a k_{cat} of 83.6 s^{-1} and a K_M of 28.77 μM. Next, the substrate specificity of the recombinant fucosidases was tested on a range of fucosylated oligosaccharides including 2'FL (Fucα1,2Galβ1,4Glc), 3FL (Galβ1-4[Fucα1-3]Glc), Lewis A (LeA, Galβl-3[Fucα1-4]GlcNAc) and Lewis X (LeX, Galβ1-4[Fucα1-3]GlcNAc). These oligosaccharides represent different glycan structures present in the human host. Fucosidases E1_10125 and E1_10180 showed substrate specificity towards α1,3/4 fucosylated linkages while fucosidases ATCC_00842 and ATCC_03833 showed preference for α1,2 linkages. Activity against more complex oligosaccharides and glycoproteins was also assayed, including sialyl Lewis X (sLeX), sialyl Lewis A (sLeA), sialylated as well as non-sialylated human plasma *N*-glycans, horseradish peroxidase *N*-glycans containing core a-1,3-fucose (HRP), blood group A type II, blood group B type II and fucosylated IgG glycoform (FA2G2) and the product of the reactions analysed by LC-MS. These screens revealed that E1_10125 was active against fucosylated substrates presenting a terminal sialic acid modification. This unique specificity prompted further enzymatic and structural analyses.

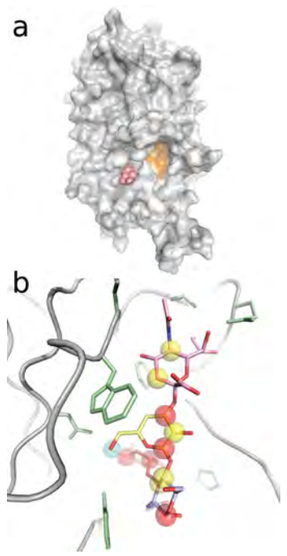

Figure 3: Crystal structure of the R. gnavus E1_10125. (a) The location of the active site is highlighted by the presence of the fucose molecule, with its atoms shown as red spheres. The region proposed to accommodate the sialic acid moiety is shown in orange. (b) The substrate binding site with sLeX (fucose (red), GlcNAc (blue), galactose (yellow) and sialic acid (pink)) shown as positioned by MD simulations. Nearby binding site residues are shown in green. The spheres represent STD NMR transfer intensities. Red indicates greatest intensity (52%-100%), yellow medium (25%-50%) and blue low (0-24%). Stronger normalised STD intensities correlate with closer ligand contacts with the surface of the protein in the bound state.

Using a combination of glycan microarrays, mass spectrometry, and isothermal titration calorimetry (ITC), we showed that *R. gnavus* E1_10125 fucosidase has the capacity to recognise sialic acid-terminated fucosylated glycans (sialyl Lewis X/A epitopes) and hydrolyse α1-3/4 fucosyl linkages in these substrates without the need to remove sialic acid (Fig. 2). The catalytically inactive mutant E1_10125 D221A bound to LeX with a Kd of 51.43 ± 1.93 μM and to sLeX (3'-Sialyl Lewis X) with a Kd of 6.12 ± 1.08 as determined by ITC.

To gain structural insights into the unique ligand specificity of E1_10125, the enzyme was crystallised in the presence of 2'FL. The trisaccharide was cleaved by the fucosidase during the crystallisation experiment presenting a single fucose sugar bound in the crystal structure (Fig. 3a). This allowed us to locate the active site and confirmed the reaction mechanism. The fucose binding site was conserved with other homologous GH29 fucosidases, including from *Streptococcus pneumoniae* and *Bifidobacterium longum* however the structure highlighted a region nearby the catalytic residues, which is absent in fucosidases with different reaction specificities. As it was confirmed by STD NMR that the sialic acid moiety of sLeX makes contacts with the enzyme, it was proposed that the sialic acid would be accommodated by this region, conferring the demonstrated specificity. Further, the high-resolution crystal structure, with data to 1.45Å, provided a starting point for molecular dynamics (MD) simulations and *in silico* docking experiments that demonstrated that sLeX could be accommodated by the E1_10125 fucosidase binding site (Fig. 3b).

This specificity of *R. gnavus* fucosidases characterised in this work may contribute to the adaptation of *R. gnavus* strains to the infant and adult gut and has potential applications in diagnostic glycomic assays for diabetes and certain cancers. In particular, the antennary fucosidase specificity reported here for sialic acid-terminated fucosylated glycans could be used as a discriminatory tool to identify N-glycan biomarkers of diseases and as a valuable tool for the purpose of glycoprofiling bio-pharmaceutical glycoproteins.

References:

1. Thursby E. *et al.* Introduction to the human gut microbiota. *Biochem. J.* **474**, 1823–1836 (2017). DOI: 10.1042/BCJ20160510
2. Ndeh D. *et al.* Biochemistry of complex glycan depolymerisation by the human gut microbiota. *FEMS Microbiol. Rev.* **42**, 146–164 (2018). DOI: 10.1093/femsre/fuy002
3. Tailford L. E. *et al.* Mucin glycan foraging in the human gut microbiome. *Front. Genet.* **5**, 81 (2015). DOI: 10.3389/fgene.2015.00081
4. Qin J. *et al.* A human gut microbial gene catalogue established by metagenomic sequencing. *Nature* **464**, 59–65 (2010). DOI: 10.1038/nature08821
5. Crost E. H. Utilisation of Mucin Glycans by the Human Gut Symbiont Ruminococcus gnavus Is Strain-Dependent. *PLOS ONE* (2013). DOI: 10.1371/journal.pone.0076341

Funding acknowledgement:
The authors gratefully acknowledge the support of the Biotechnology and Biological Sciences Research Council (BBSRC); this research was mostly funded by the Innovate UK Biocatalyst grant Glycoenzymes for Bioindustries (BB/M029042/) with contribution from the Royal Society and the BBSRC Institute Strategic Programmes BB/J004529/1 'The Gut Health and Food Safety' and BB/R012490/1 'Gut Microbes and Health'.

Corresponding authors:
Prof. Nathalie Juge, Quadram Institute Biosciences, nathalie.juge@quadram.ac.uk; Dr Haiyang Wu, Quadram Instititute Biosciences, haiyang.wu@quadram.ac.uk;
Dr David Owen, Diamond Light Source, david.owen@diamond.ac.uk

Biological Cryo-Imaging Group

Martin Walsh, Deputy Director of Life Sciences and Science Group Leader

The Biological Cryo-Imaging Group brings together dedicated facilities for X-ray, light and electron microscopy at Diamond Light Source. The Electron Bio-Imaging Centre (eBIC) is the national centre for cryo-electron microscopy (cryo-EM) in the UK and provides a range of capabilities and supporting facilities for cryo-EM and Correlative Light and Electron Microscopy (CLEM). Beamline B24 hosts a full field cryo-transmission X-ray microscope dedicated to biological X-ray imaging and has also established a cryo super resolution fluorescence microscopy facility, which is a joint venture between Diamond and the University of Oxford. The group provides a unique platform for correlative light and X-ray microscopy, as well as cryo-EM.

The Biological Cryo-Imaging (BCI) group has continued to grow and expand its capabilities during 2020 in spite of the COVID-19 pandemic. At eBIC, the team has expanded with a new Principal Electron microscopist, additional cryo-EM scientists and Post-Doctoral Researchers. At B24 we welcomed a new Beamline Scientist and a Post-Doctoral Researcher who is jointly funded by iNEXT-Discovery. In addition, the B24 team is hosting a Masters student from the University of Birmingham, funded through Diamond's Year in Industry placement scheme.

Remote access for both eBIC and B24 has been successfully established during 2020 and has quickly been taken up by our users. It has allowed us to sustain a user programme for supporting COVID-19 research during the first UK lockdown. Following on from these experiences, remote access has been extended to cover access to all instruments presently. At the time of writing, access to eBIC and B24 is still primarily through remote access, although as we come out of the current UK lockdown, users will be gradually welcomed back on-site.

On 2nd March 2020, Diamond published a rapid access call specifically for COVID-19 research proposals to ensure that we were doing everything possible to support researchers in their efforts to discover more about the virus and bring us closer to an effective vaccine or treatment. Although the UK went into its first lockdown in late March, the Diamond machine and eBIC microscopes were kept operating, albeit under reduced hours with core staff, to allow COVID-19 research to continue. This allowed us and our colleagues in Macromolecular Crystallography (MX) in particular to provide access and support to both internal and external groups working on COVID-19.

At eBIC, a major focus of activity has been the spike (S) protein working in collaboration with groups at the Rosalind Franklin Institute and the University of Oxford. The first paper from this activity showed that lab-based production of novel potent single chain camelid antibodies (known as nanobodies) can successfully neutralise the SARS-CoV-2 virions[1]. The rapid characterisation of new variants, and the analysis of antibody binding to the Wuhan virus and its variants, has also been achieved at break-neck speed in a series of papers published in the journal *Cell*[2-5], in which eBIC and the MX beamlines at Diamond have been instrumental in delivering the structural data. Combining cryo-electron tomography (cryo-ET) and X-ray tomography, in collaboration with the Central Laser Facility (CLF), Peijun Zhang's group were able to track the SARS-CoV-2 assembly and egress pathway using correlative microscopy workflows that are being developed within the BCI group[6]. Zhang's group are also collaborating with Sarah Gilbert, the lead researcher of the Oxford vaccine team, and have applied cryo-ET to characterise the structure of the spike (S) proteins generated by the Oxford/Astra Zeneca vaccine. They have confirmed the use of the technology for SARS-CoV-2 vaccines by showing that the structures of the expressed S proteins on the surface of cells mimicked that of cells infected with SARS-CoV-2[7]. At B24, in addition to collaborating with eBIC on visualising the life cycle of the SARS-CoV-2 virus in a cellular context, the beamline has also been used through Diamond's industry access to help fast track new diagnostic tests for COVID-19.

On the instrument front at eBIC, a new partnership with Diamond and the Research Complex at Harwell (RCaH) has resulted in eBIC hosting a new 200 keV Thermofisher Scientific Glacios cryo transmission electron microscope. This has been made possible through funding by UKRI-Medical Research Council (MRC) to the RCaH. eBIC has integrated the microscope into the facility and is working with RCaH to provide a user and training programme to Harwell campus-based groups. On the correlative side at eBIC, we have finalised commissioning of our recently purchased Leica cryo Correlative Light and Electron Microscope (cryo-CLEM) and published a user commissioning call in spring of 2021. Finally, eBIC have worked extensively with the manufacturer Thermofisher to commission and benchmark their prototype energy filter - Selectris. Performance and stability tests showed the Krios hall to be an exceptionally stable environment.

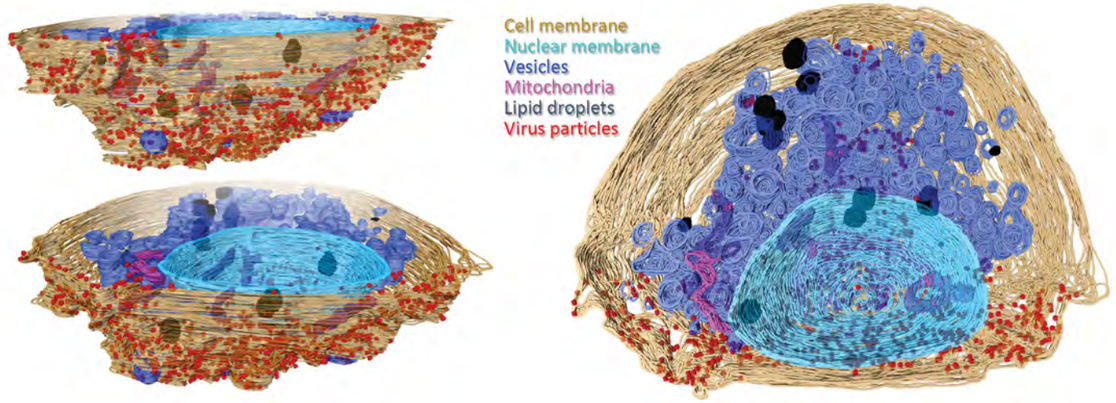

Serial cryoFIB/SEM volume imaging of entire SARS-CoV-2 infected cell. Shown are various views of a surface rendering of the segmented volume of SARS-CoV-2 infected cell. Segmented organelles and virus particles are labelled with colours indicated. Figure adapted from Mendonça et al. (2020).

Newly recruited cryo-EM scientist, David Owen, working on the RCaH Glacios transmission cryo-electron microscope, which has been recently installed at eBIC and will be run in partnership with RCaH.

The Selectris filter has been used preferentially by many user groups for COVID-19 related projects in cryo-EM and cryo-ET, where the unparalleled stability and performance have enabled many novel observations. Full access is now available to all eBIC Rapid Access and BAG users. At B24, we have streamlined the cryo Correlative Light and X-ray Tomography (cryo-CLXT) workflow with new protocols for sample and data correlation. In addition, in the last year at B24 a huge effort has gone into detailing all our protocols, with major updates to our webpages and publication of the protocols in a series of articles[8-10].

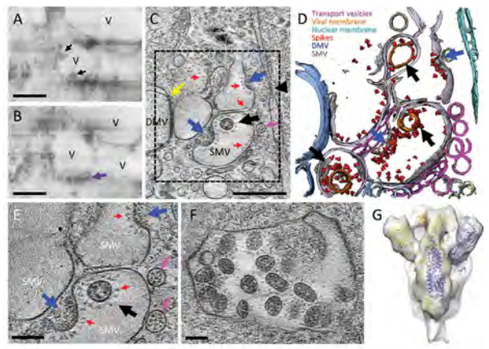

SARS-CoV-2 cytoplasmic viral assembly (Figure reproduced from Mendonça et al. (2020). (A-B) CryoFIB/SEM images of two sequential slices separated by 80 nm. Black arrows point to virus particles in single membrane vesicle (SMV). Pink arrow points to small dense vesicles lining the outside of virus-containing SMV. (C) Tomographic slice of cryoFIB lamella depicting SARS-CoV-2 assembly, with DMV portals (yellow arrow), assembling viruses (blue arrow), assembled virus (black arrow), viral spikes on SMV membranes (red arrows), dense vesicles around the assembly site (pink arrow, as in B) and a nucleopore (black arrowhead). (D) Density segmentation of C, displaying three virus particles (black arrows) and two assembly sites (blue arrows). (E) An enlarged view (at a different angle) of boxed area in C, showing assembled virus (black arrow), assembling viruses (blue arrows), spikes (red arrows) and spike-containing vesicles (pink arrows). (F) Large intracellular virus-containing vesicle (LVCV) full of readily assembled viruses. (G) Subtomogram average of viral spikes of intracellular viruses from cell lamellae at 11 Å resolution, fitted with an atomic model of spike trimer (PDB 6ZB5) (Toelzer et al., 2020). Scale bar is 300 nm in A and B; and 100 nm in C, E and F.

Training continues to be a major focus for the group and in spite of the lockdown, we have been able to successfully carry out and plan remote training across a wide audience. Workshops at eBIC include an Instruct-ERIC sponsored workshop on fully remote data collection, which took place in May 2021, while at B24 the team were involved in, and contributed to, an iNEXT-Discovery two-day Zoom workshop focused on the basics, pros/cons and opportunities in using the techniques of cryo-ET and cryo soft X-ray tomography to answer biological questions. The B24 user base were also provided with intensive training to take full advantage of remote access that is now implemented at the beamline.

It has been a very different year and as always, what we have achieved would not have been possible without the dedication of our scientific staff, technicians, software and engineering teams who support biological cryo-imaging, and the administrative and infrastructure support groups across Diamond, our colleagues at RCaH, The Franklin and our users!

References:

1. Huo J. *et al.* Neutralizing nanobodies bind SARS-CoV-2 spike RBD and block interaction with ACE2. *Nat. Struct. Mol. Biol.* **27**, 846–854 (2020). DOI: 10.1038/s41594-020-0469-6
2. Dejnirattisai W. *et al.* The Antigenic Anatomy of SARS-CoV-2 Receptor Binding Domain. *SSRN Electron. J.* (2021). DOI: 10.2139/ssrn.3754542
3. Dejnirattisai W. *et al.* Antibody evasion by the P.1 strain of SARS-CoV-2. *Cell* (2021). DOI: 10.1016/j.cell.2021.03.055
4. Supasa P. *et al.* Reduced neutralization of SARS-CoV-2 B.1.1.7 variant by convalescent and vaccine sera. *Cell* **184**, 2201-2211.e7 (2021). DOI: 10.1016/j.cell.2021.02.033
5. Zhou D. *et al.* Evidence of escape of SARS-CoV-2 variant B.1.351 from natural and vaccine-induced sera. *Cell* **184**, 2348-2361.e6 (2021). DOI: 10.1016/j.cell.2021.02.037
6. Mendonça L. *et al.* SARS-CoV-2 Assembly and Egress Pathway Revealed by Correlative Multi-modal Multi-scale Cryo-imaging. *bioRxiv* 2020.11.05.370239 (2020). DOI: 10.1101/2020.11.05.370239
7. Watanabe Y. *et al.* Native-like SARS-CoV-2 Spike Glycoprotein Expressed by ChAdOx1 nCoV-19/AZD1222 Vaccine. *ACS Cent. Sci.* **7**, 594–602 (2021). DOI: 10.1021/acscentsci.1c00080
8. Iudin A. *et al.* Data-deposition protocols for correlative soft X-ray tomography and super-resolution structured illumination microscopy applications. *STAR Protoc.* **2**, 100253 (2021). DOI: 10.1016/j.xpro.2020.100253
9. Kounatidis I. *et al.* 3D Correlative Cryo-Structured Illumination Fluorescence and Soft X-ray Microscopy Elucidates Reovirus Intracellular Release Pathway. *Cell* **182**, 515-530.e17 (2020). DOI: 10.1016/j.cell.2020.05.051
10. Phillips M. A. *et al.* CryoSIM: super-resolution 3D structured illumination cryogenic fluorescence microscopy for correlated ultrastructural imaging. *Optica* **7**, 802 (2020). DOI: 10.1364/optica.393203

A novel correlative 3D microscopy platform for studying cells in their native state

Related publication: Kounatidis I., Stanifer M. L., Phillips M. A., Paul-Gilloteaux P., Heiligenstein X., Wang H., Okolo C. A., Fish T. M., Spink M. C., Stuart D. I., Davis I., Boulant S., Grimes J. M., Dobbie I. M. & Harkiolaki M. 3D Correlative Cryo-Structured Illumination Fluorescence and Soft X-ray Microscopy Elucidates Reovirus Intracellular Release Pathway. *Cell* **182**, 515-530.e17 (2020). DOI: https://doi.org/10.1016/j.cell.2020.05.051

Publication keywords: Correlative imaging; Structured illumination microscopy; X-ray tomography; Reovirus biology; Correlative light/X-ray tomography (CLXT)

Researchers have developed a new technique for studying cells in their native state. The goal was to obtain high-quality imaging data from cells without the need for sectioning or chemical fixation. The new method avoids any treatment that would disturb cell structure, so that no artefacts (errors) are introduced into the images.

To demonstrate this novel correlative microscopy platform's effectiveness, the team studied the early stages of cell infection by reoviruses. Although the specific viruses have been studied extensively, there is a debate regarding the method of infection. This research focused on the way that the virus escapes from vesicles, a required step for replication. At beamline B24, using a correlative imaging approach by combining soft X-ray tomography with super resolution microscopy in cryogenic conditions, the team tracked the infection mechanism. The results revealed that the virus had already escaped from the host vesicles two hours after infection, with the vesicles preserving their circular shape, suggesting a gentle, pore-based exit mechanism for the virus.

Reoviruses are valuable tools that could be engineered to express proteins and have the potential to be used in vaccines. Knowing the infection mechanism will facilitate their handling and manipulation for biomedical purposes. The new imaging platform has also been used to validate anticancer compounds, study cell structure during development and investigate clearance of human pathogenic microorganism by immune host cells. The work is the outcome of a collective effort between Diamond Light Source and research groups and facilities across Europe, including the University of Oxford, Heidelberg University Hospital, the Université de Nantes and CryoCapCell.

Imaging is currently going through an evolutionary process with many new imaging techniques providing more details with greater sensitivity, thereby elucidating critical biomedical topics. Currently, electron microscopy (EM) techniques provide details of cellular ultrastructure at a resolution level of typically 2-5 nm by using scanning or transmission EM. This valuable information is coming though with a cost, the limited technical penetration depth, which introduces the necessity of sample sectioning accompanied by chemical fixation steps (with the possibility of disturbing the cellular ultrastructure and the introduction of fixation artefacts) or laborious cryogenic workflows.

At B24, a new alternative imaging platform has been developed in order to obtain high-quality 3D imaging data from cells preserved in their native state, avoiding the introduction of artefacts but also allowing the cross-correlation of data coming from complimentary imaging techniques. The core of the new correlative platform is the combination of a cryo-soft X-ray tomography (cryo-SXT) microscope with a bespoke cryo-structured illumination microscope (cryo-SIM) (Fig. 1).

The cryo-SXT microscope allows imaging of 3D cellular structures of up to 10 µm in thickness at a spatial resolution down to 25 nm using radiation deriving from a bending magnet at the synchrotron[1]. The purpose built 3D-cryoSIM complements the tomographic data by providing 3D super resolution fluorescence data on chemical localisation based on the fluorescence of cellular trackers used. The reconstructed data provide high contrast, low-background imaging details even below 200 nm surpassing the limitations of conventional light microscopy[2]. The combination of the two imaging techniques, followed by a cross-correlation of the provided data, delivers a comprehensive view of both cellular ultrastructure and molecular organisation over extended cellular volumes.

The new imaging platform has been used to elucidate the infection route of reovirus; an advanced experimental model for viral pathogenesis with potential applications in vaccines development[3] and anticancer treatments[4]. Despite reoviruses being extensively studied, certain steps of the virus entry mode and delivery of reovirus particles inside the cell remain poorly understood. At B24 the previously unsolved questions related to the early stages of reovirus infection were clarified including details of: i) how soon after infection viral particles get released in the cell, ii) where inside the cells those particles are released and iii) are the organelle-carriers of the viruses morphologically affected by the trafficking and the subsequent release of the viral particles?

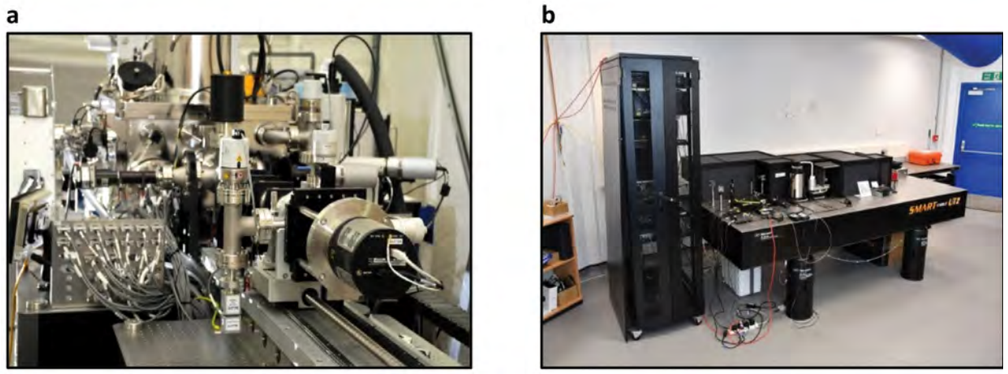

Figure 1: (a) Image of the cryo-SXT microscope and (b) the cryo-SIM modalities on site at Diamond B24. Figure panels reproduced from Kounatidis et al. (2020).

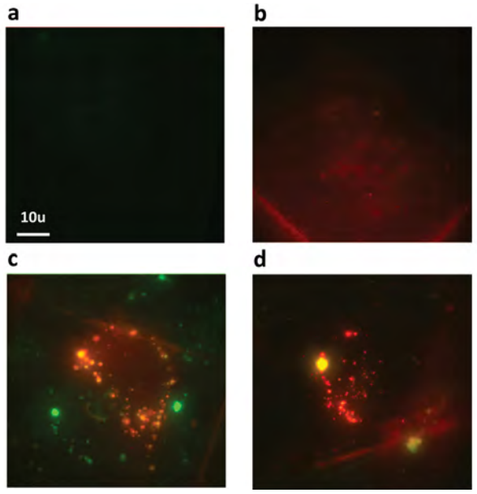

Figure 2: Cryo-SIM images of green-labelled virus in human cells expressing membrane disturbance marker in distinct vesicles in red (a) at non-infected cell, (b) at 1 hour (c) at 2 hours (d) at 4 hours after infection. Figure panels reproduced from Kounatidis et al. (2020).

In the present study human cells were grown on gold grids and subsequently infected with reovirus following cryo-preservation of the samples by plunge freezing at specific time points (1, 2 and 4 hours upon infection). The samples were then scanned using both cryo-SIM and cryo-SXT microscopes at B24 to provide a comprehensive structural and functional, view of the intracellular organisation. This approach facilitated the determination of the location of both the virus and equally important of its carrier vesicles at each of the above time points. Virus detection was enabled with the use of fluor-labelled reoviruses strains while the use of a specific chemical reporter allowed tracking and evaluation of membrane-compromised and/or partially quenched carrier organelles.

At 1 hour post-infection (PI) the 3D imaging data from the cryo-SIM revealed the presence of intracellular vesicles positive for reovirus, and those structures are recorded to increase further both in number and size by 2 hours PI, gradually forming large vesicles located perinuclearly at 4 hours (Fig. 2). The accumulation of the red fluor membrane disturbance reporter denotes that by 1 hour PI reovirus started to disrupt the membranes of the carrier organelles. Whether the above infection process affects the general morphology of the carrier vesicles and/or the overall landscape of the cell was still a question. Structural 3D data at higher resolution could elucidate any possible intracellular structural effects and these were available by the use of the cryo-SXT microscope. Therefore, the same samples were imaged with X-rays allowing us to define the structure of cellular organelles across extended perinuclear areas of the cytoplasm, not accessible with other nanometer-resolution techniques.

The following step is the correlation of the of cryo-SIM and the cryo-SXT data leading to a complete view of both carriers and virus alongside the surrounding cellular micro-environment using specific registration imaging software namely eC-CLEM[5]. The combination of the two data sets revealed the presence of simple vesicles carrying viral load at all the time points were checked, allowing viral particles to spread from the vesicle to the cytoplasm with a subpopulation of them gradually enlarging and forming multi-vesicular bodies (MVBs) trackable from 2 hours after infection (Fig. 3). Another subpopulation of carrier vesicles showed distinctive, carbon-rich domed structures available only in infected samples from 2 hours after infection. Interestingly, the outer membrane of carriers vesicle remain relatively consistent suggesting that virus escapes without disrupting the membrane (Fig. 3). A possible route for the escape of virus is through a pore-based machinery that selectively allows the exit of the virus without compromising the vesicles membrane.

Beyond the reovirus experimental evidence, the imaging technology at B24 so far has been used to study a wide range of biomedical topics ranging from host-pathogen interaction topics (viruses, fungi or bacteria affecting immune cells) and autoimmune diseases, to stem cell development and differentiation as well as the effect of vaccines on cell morphology. The common request for all of the above studies was the requirement for imaging at the appropriate resolution combined with the preservation of the cellular ultrastructure, which the newly developed imaging technology at B24 can now cater for.

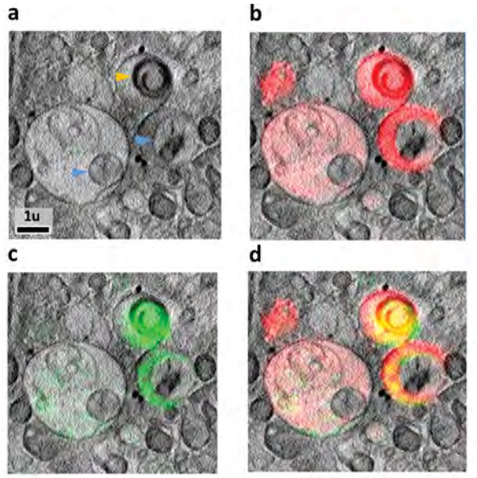

Figure 3: (a) X-ray data from a cellular region 2hr after infection. Yellow arrow indicates virus-induced carbon-rich substructures and blue arrows denote vesicle areas within MVBs that remain impermeable. The same region with correlated SIM data (b) red for the membrane marker (c) green for the viral presence (d) with both fluorescent signals overlaid. Figure panels reproduced from Kounatidis et al. (2020).

The imaging platform will continue to be improved aiming for a higher degree of automation in the near future and in this respect, the experimental demands and the feedback of the user community have proved valuable. Importantly, the method can be used as a scaffold that can combine other advanced imaging techniques like electron microscopy, providing further opportunities for the development of multi-modal imaging technologies and serving the demands of the wider biomedical field.

References:

1. Harkiolaki M. *et al.* Cryo-soft X-ray tomography: using soft X-rays to explore the ultrastructure of whole cells. *Emerg. Top. Life Sci.* **2**, 81–92 (2018). DOI: 10.1042/ETLS20170086
2. Schermelleh L. *et al.* Subdiffraction Multicolor Imaging of the Nuclear Periphery with 3D Structured Illumination Microscopy. *Science (80-.).* **320**, 1332–1336 (2008). DOI: 10.1126/science.1156947
3. Demidenko A. A. *et al.* Engineering recombinant reoviruses with tandem repeats and a tetravirus 2A-like element for exogenous polypeptide expression. *Proc. Natl. Acad. Sci.* **110**, E1867--E1876 (2013). DOI: 10.1073/pnas.1220107110
4. Thirukkumaran C. *et al.* Oncolytic Viral Therapy Using Reovirus BT - Gene Therapy of Solid Cancers: Methods and Protocols. in (eds. Walther W. et al.) 187–223 (Springer New York, 2015). DOI: 10.1007/978-1-4939-2727-2_12
5. Paul-Gilloteaux P. *et al.* eC-CLEM: flexible multidimensional registration software for correlative microscopies. *Nat. Methods* **14**, 102–103 (2017). DOI: 10.1038/nmeth.4170

Funding acknowledgement:
This work was carried out with the support of Diamond Light Source, instrument B24 (proposals MX21046 and MX18314).

Corresponding author:
Dr Ilias Kounatidis, Diamond Light Source, ilias.kounatidis@diamond.ac.uk

A 'protein bomb' used by the immune system to kill infected and cancerous cells

Related publication: Bálint, Müller S., Fischer R., Kessler B. M., Harkiolaki M., Valitutti S. & Dustin M. L. Supramolecular attack particles are autonomous killing entities released from cytotoxic T cells. *Science.* **368**, 897–901 (2020). DOI: 10.1126/science.aay9207

Publication keywords: Immunology; Immunotherapy; Apoptosis; Secretion; Synapse; 3D imaging; Cryo Soft X-ray Tomography (CSXT); Correlative Light and X-ray Tomography (CLXT)

Cytotoxic T cells (CTLs) kill infected and cancerous cells by secreting cytotoxic proteins. An international team of researchers investigated how these cytotoxic proteins avoid dilution in the vast extracellular space and enter target cells that need to be killed. The question they were seeking to answer was whether these proteins organise into particles.

Diamond Light Source's 3D X-ray tomography and super resolution fluoresence microscopy for the life sciences beamline (B24) uses soft (low-energy) X-rays to generate 3D maps of organic material in cells and small particles released from cells. For this research, B24 provided correlative information about 'protein bombs' released by cytotoxic T cells and within the cells. Soft X-rays were better than electrons in this case as they allow imaging of entire T cells, although the resolution is lower. The results allowed the team to confirm that the 'protein bombs' had a 'core-shell' structure and identify potential storage sites for the 'protein bombs' in the T cells.

Whereas most biological drugs are single protein molecules, 'protein bombs' are 'supramolecular', a loose assembly of hundreds or thousands of proteins that deliver the active components to targets in the body. These 'protein bombs' have the potential to be used in immunotherapy applications, which help the body's immune system to fight cancer and other diseases. One of the next steps for the research team is to try to make synthetic 'protein bombs'. B24 will be helpful in characterising these 'supramolecular' drugs.

Cytotoxic T lymphocytes (CTL) and Natural Killer (NK) cells are components of the immune system that help cure viral infections and prevent the progression of cancers. CTL and NK cells migrate through the body to the location of target cells, directly embrace these targets and secrete cytotoxic proteins onto their surface. Cytotoxic proteins were identified 30 years ago and it was determined that one of them, perforin (Prf1), forms holes in the surface of the target cells and the others, granzymes (for example, Gzmb), enter the cytoplasm and trigger a chain reaction leading to target cell death. The prevailing hypothesis over the past 15 years is that when CTL and NK cells embrace targets, they create an immunological synapse with an isolated extracellular compartment into which cytotoxic proteins can be released while maintaining a high, active concentration[1]. However, single proteins disperse rapidly and the functional impact of Prf1 and Gzmb may be better achieved if they can be transferred to targets in functional quanta without dilution as they traverse the gap between cells. A challenge of studying such entities is they may be consumed rapidly by target cells or destroyed on interaction with incompatible surfaces, which makes their recovery impossible. A breakthrough in this regard was achieved by using supported lipid bilayers (SLB) as surrogate targets to capture putative supramolecular attack particles (SMAPs)[2].

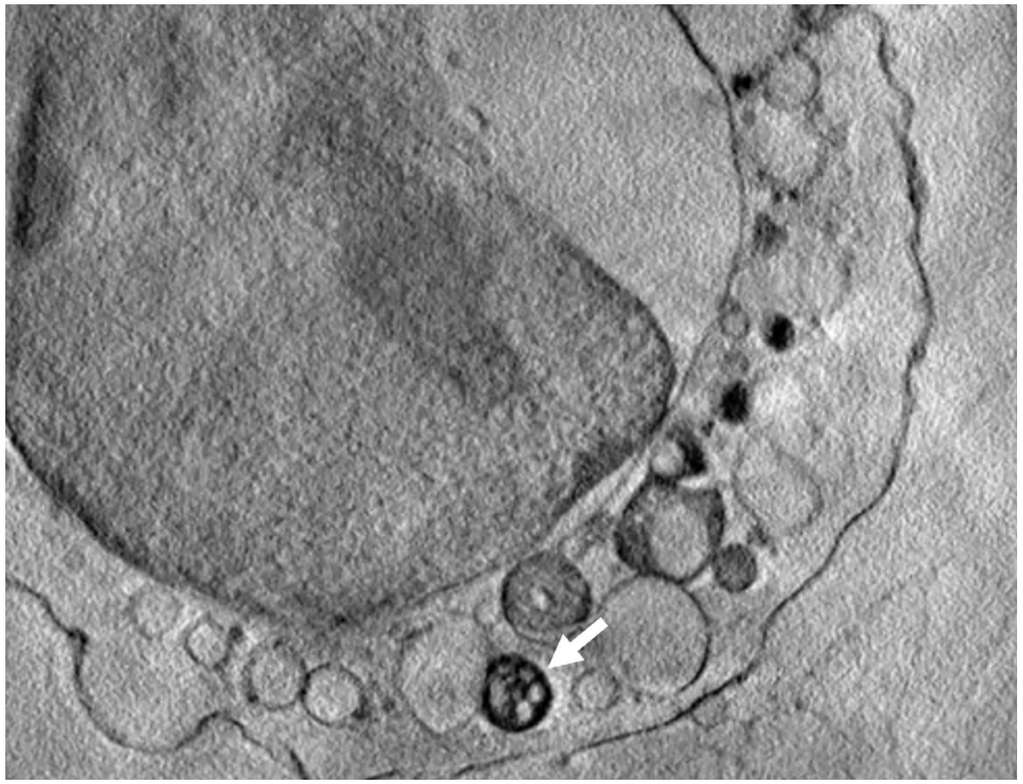

Figure 1: Image from a tomogram of a CTL interacting with an EM grid and highlighting a multicore granule (arrow). Captured during a rapid access visit to B24.

SLB are formed by liposome fusion onto a glass substrate and enable coupling of proteins to their surface through the lipid head groups. T cells can be activated by SLBs presenting the adhesion molecule I CAM1 and a ligand for the T cell antigen receptor (TCR), which can be a histocompatibility antigen-peptide complex or anti-TCR antibodies. These SLB induce live T cells to form immunological synapses characterised by a ring of adhesion molecules surrounding a central cluster of antigen receptors, which is also the location of the secretory domain. The CTL then attempt to kill these mock targets, releasing Prf1 and Gzmb into the centre of the immunological synapse on the SLB. We have previously shown that T cells can then be removed to expose any released particles that are adherent to the SLB surface. This approach has enabled analysis of proteins and lipids from the synaptic output of helper T cells[3] and similar experiments were performed with CTL[2]. Total Internal Reflection Fluorescence Microscopy on CTL attached to SLB showed that T cells release particles containing Gzmb and Prf1 and that these particles accumulated ICAM1 at the point of particle contact with the SLB. Proteomics analysis revealed the presence of thrombospondin-1 (TSP1) in the particles, which was verified by staining of the particles with anti-TSP1 antibodies and by expression of green fluorescent proteins (GFP) conjugated TSP1, which co-localised with Gzmb and Prf1. We also verified that TSP1 had a role in CTL mediated killing using Crispr/Cas9 targeting. Super-resolution localisation microscopy revealed that the particles had a shell of TSP1 surrounding a core of Gzmb and Prf1 with overall particle size of 120 nm. The properties of these particles were unexpected in that antibodies to Gzmb and Prf1 access the core of the particles without permeabilisation. These data collectively suggested that the shell had static pores or that the shell was sufficiently dynamic to allow entry of antibodies into the core without allowing the Prf1 and Gzmb to escape. The particles were physically characterised by Cryo-Soft X-ray Tomography (CSXT) at beamline B24.

We developed methods to activate CTL on electron microscopy grids of the type used for plunge freezing and CSXT. Analysis of released particles on these grids confirmed a core-shell structure with a dense shell having a diameter of 110 nm and a relatively translucent core. The discrepancy in size in comparison to previous localisation microscopy imaging could be explained by the increased diameter contributed by the ~10 nm antibodies used for staining in the localisation microscopy studies, which were not present in the unstained samples analysed by CSXT. Another feature identified by CSXT was that the CTL contain multicore cytoplasmic granules with many translucent voids consistent with densely packed core-shell particles (Fig. 1). Cryo-Structured Illumination Microscopy (CSIM), performed using the newly developed cryoSIM microscope at beamline B24, correlated with CSXT data revealed that the core-shell particles had signals for both Prf1 and Gzmb (Fig. 2), although this data is not yet published in a peer reviewed journal and is thus labelled as preliminary.

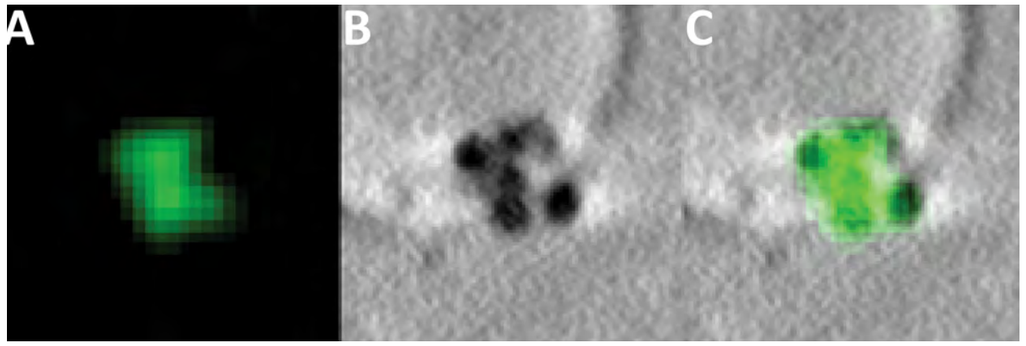

Figure 2: Preliminary demonstration of Correlative Light and X-ray Tomography (CLXT) for cytotoxic particles released onto an EM grid by a CTL. A focus of Prf1 staining in the cryo-SIM image (A) and a cluster of SMAPs in the CSXT image (B) are well correlated (C). Captured during a standard access session to beamline B24. S. Balint, University of Oxford.

Biochemical analysis of the cytotoxic particles detected a ~60 kDa fragment of TSP1 as the major form of TSP1 in SMAPs along with Prf1 and Gzmb. These data suggest that the cytotoxic particles are built around a network of non-covalent interactions of TSP1 C-terminus with glycoproteins that are readily detected by wheat germ agglutinin staining. Thus, we refer to the particles as supramolecular attack particles or SMAPs. The structures can be likened to 'protein bombs' as they are large structures with many copies of Prf1 and Gzmb that may be left by CTL to disrupt entire microenvironments when conditions do not favour classical one-to-one synaptic killing[4]. SMAPs are also released from NK cells[2,5].

CSXT at beamline B24 has great potential for the study of cellular structures relevant to T cell mediated killing. Future work will focus on correlative imaging inside T cells transfected with fluorescently tagged TSP1 and Gzmb. This will determine if the observed multicore granules are the cellular source of SMAPs and may open up experiments to understand SMAP biogenesis.

References:

1. Stinchcombe J. C. *et al.* The immunological synapse of CTL contains a secretory domain and membrane bridges. *Immunity* **15**, 751–761 (2001). DOI: 10.1016/S1074-7613(01)00234-5
2. Bálint *et al.* Supramolecular attack particles are autonomous killing entities released from cytotoxic T cells. *Science (80-.).* **368**, 897–901 (2020). DOI: 10.1126/science.aay9207
3. Saliba D. G. *et al.* Composition and structure of synaptic ectosomes exporting antigen receptor linked to functional CD40 ligand from helper T cells. *Elife* **8**, e47528 (2019). DOI: 10.7554/eLife.47528
4. Immune cells blast infections and cancer with protein 'bombs'. *Science Magazine* (2020). DOI:10.1126/science.abc6849
5. Ambrose A. R. *et al.* Synaptic secretion from human natural killer cells is diverse and includes supramolecular attack particles. *Proc. Natl. Acad. Sci. U. S. A.* **117**, 23717–23720 (2020). DOI: 10.1073/pnas.2010274117

Funding acknowledgement:
This work was funded by the European Commission Advanced Grant 'Immunological synapse derived ectosomes in T cell effector function (SYNECT)' ERC-2014-AdG_670930 and Wellcome Principal Research Fellowship 'Translation of the Immunological synapse' 100262Z/12/Z. This work was carried out with the support of the Diamond Light Source, beamline B24 (proposals BI26084, BI23581 and BI23000).

Corresponding author:
Prof. Michael Dustin, Kennedy Institute of Rheumatology, University of Oxford, michael.dustin@kennedy.ox.ac.uk

Cryo-EM visualises dynamic molecular machines

Related publication: López-Perrote A., Hug N., González-Corpas A., Rodríguez C. F., Serna M., García-Martín C., Boskovic J., Fernandez-Leiro R., Caceres J. F. & Llorca O. Regulation of RUVBL1-RUVBL2 AAA-ATPases by the nonsense-mediated mRNA decay factor DHX34, as evidenced by Cryo-EM. *eLife* **9**, 1–23 (2020). DOI: 10.7554/eLife.63042

Publication keywords: AAA-ATPases; DHX34; RUVBL1-RUVBL2; Human; Molecular biophysics; Nonsense mediated mRNA decay; Structural biology

Messenger RNA (mRNA) is a single-stranded molecule of RNA that corresponds to the genetic sequence of a gene. Inside a cell, mRNA is used as a template to build a protein. However, mRNA molecules are prone to errors, and cells use quality-control processes called mRNA surveillance mechanisms to ensure the mRNA molecules (and hence proteins) are correct. Nonsense-mediated mRNA decay (NMD) is one of these quality-control mechanisms. Its role is to degrade mRNAs with premature termination codons (PTCs), which might otherwise produce truncated proteins.

AAA-ATPases are proteins found in all organisms. They are essential for many cellular functions, including DNA replication, protein degradation and the regulation of gene expression. RUVBL1 and RUVBL2 are two closely related AAA-ATPases required for the initiation of the NMD pathway. However, how RUVBL1 and RUVBL2 regulate NMD and how interacting partners regulate the ATPase activity of RUVBL1 and RUVBL2 remain poorly understood.

Researchers from the Spanish National Cancer Research Centre (CNIO) and the University of Edinburgh investigated which of the core NMD factors could form a direct complex with RUVBL1-RUVBL2 to determine the structure of the complex and study if the interaction affected the ATPase activity of the chaperone. To image these dynamic molecular machines to this level of detail, they used cryo-electron microscopy (cryo-EM). Access to the high-end instrumentation at the Electron Bio-Imaging Centre (eBIC) at Diamond Light Source was essential to solve these structures. Their results revealed the regulation of RUVBL1-RUVBL2 by a factor participating in the NMD pathway, and the core elements of their model may apply to other processes where these ATPases participate.

RUVBL1 and RUVBL2 proteins are two closely related AAA-ATPases that are essential in a wide variety of cellular processes[1]. Their known functions can be broadly classified in at least three categories. On the one hand, they are constituent subunits of several chromatin remodelling complexes such as INO80, SWR1, SRCAP and TIP60 where they act as scaffolds to organise other subunits in the complexes[2]. On the other hand, RUVBL1 and RUVBL2 interact with RPAP3 and PIH1D1 proteins to constitute R2TP, a co-chaperone complex that works in concert with the HSP90 chaperone in the assembly and activation of a growing list of macromolecular complexes, including members of the Phosphatidylinositol 3-kinase-related kinase (PIKK) family members such as mTOR and ATR, and RNA polymerase II[3]. Finally, RUVBL1 and RUVBL2 have been found to work as chaperones in some processes without the involvement of HSP90[1].

RUVBL1 and RUVBL2 organise hetero-hexameric complexes of alternating subunits. Domains I and III of each protein assemble to form an hexameric ring with ATPase activity. Domain II (DII) from each subunit protrudes from the hexameric ring and they function as modules that can interact with different proteins and clients[2,3]. The ATPase activity of RUVBL1-RUVBL2 complexes is essential for most of their known cellular activities, but a clear understanding of how this is regulated and what its role in each of the processes where RUVBL1-RUVBL2 participates is missing.

Nonsense-mediated mRNA decay (NMD) promotes the degradation of mRNAs containing premature termination codons (PTCs) to prevent the production of truncated proteins with potential deleterious effects[4]. NMD is also involved in fine-tuning gene expression by the regulation of some physiological transcripts. Initiation of the NMD response occurs during the first round of translation when the ribosome is stalled at a PTC, allowing the recruitment of several NMD factors including SMG1, UPF1 and the DHX34 helicase. Remodelling of this complex by interaction with additional NMD factors promotes SMG1-mediated phosphorylation of UPF1, triggering the recruitment of the RNA degradation machinery.

RUVBL1 and RUVBL2 are essential to initiate the NMD response[5]. Their depletion reduced UPF1 phosphorylation and affected the degradation of a PTC-containing reporter transcript, but these defects were recovered by the

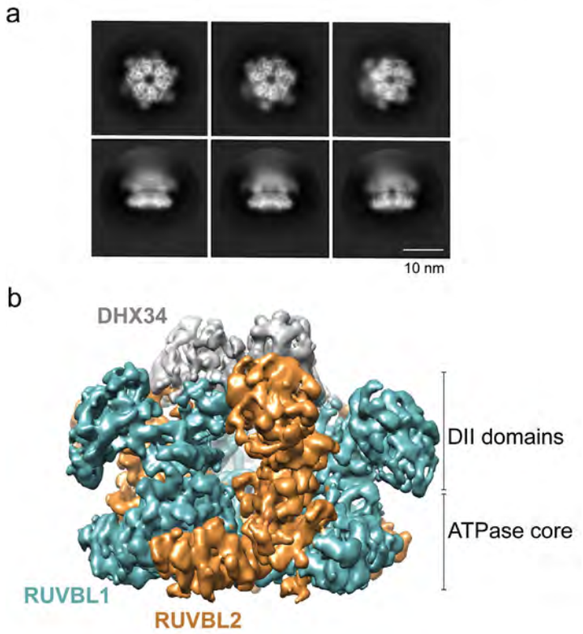

Figure 1: (a) Representative 2D class averages of the RUVBL1-RUVBL2-DHX34 complex. Top views (top panels) and side views (bottom panels); (b) Side view of the cryo-EM reconstruction of RUVBL1-RUVBL2-DHX34. RUVBL1 is coloured in green, RUVBL2 in orange, and DHX34 in grey.

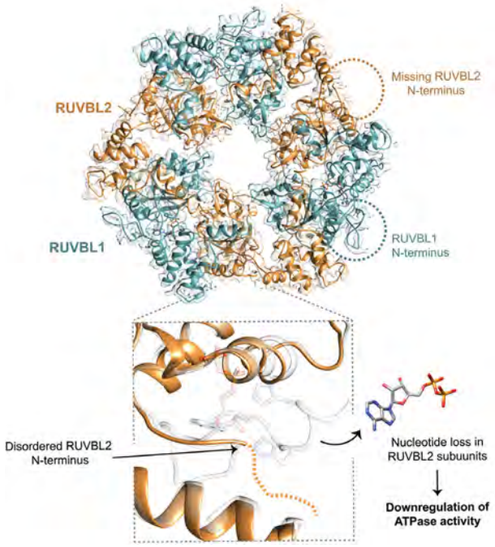

Figure 2: Conformational changes of RUVBL1-RUVBL2 hexameric ring upon DHX34 binding. Top panel shows the atomic structure of RUVBL1-RUVBL within the cryo-EM map as a transparent density. ADP is bound to RUVBL1 subunits. Bottom panel shows a close-up view of the nucleotide binding pocket of RUVBL2 after DHX34 binding (orange) superimposed to the structure of free RUVBL2 (PDB 2XSZ) in transparent grey colour. The disordered N-terminal segment of RUVBL2, missing in the cryo-EM map, is indicated with an orange dotted line. A displaced ADP molecule indicates the release of the nucleotide from its binding site after DHX34 binding.

wild-type proteins but not ATPase-deficient mutants. How RUVBL1-RUVBL2 regulates NMD remains to be elucidated.

The present study starts characterising the mechanisms involved in the functions of RUVBL1-RUVBL2 in NMD, but in addition the NMD pathway was used as a model to study the regulation of RUVBL1-RUVBL2 ATPase activity by the interaction with other proteins. A novel interaction of RUVBL1-RUVBL2 with the DHX34 helicase, a factor essential to initiate NMD, was described using cryo-EM in combination with biochemical and cellular experiments. The RUVBL1-RUVBL2-DHX34 complex was identified in cellular immunoprecipitation experiments and reconstituted *in vitro*. Imaging of the complex by cryo-EM revealed that DHX34 attaches to the face of the RUVBL1-RUVBL2 ring containing the DII domains (Fig. 1a). Whereas the density for the RUVBL1-RUVBL2 hexameric ring was well defined in the 2D averages of the complex, smeared signal for DHX34 and the DII domains denoted the flexible attachment of DHX34 to the chaperone. Accordingly, the 3D reconstruction of the complex revealed DHX34 interacting with all RUVBL subunits at the DII face of the hexameric ring but the resolution of DHX34 in the complex was insufficient for atomic modelling (Fig. 1b).

In contrast, the structure of the ATPase ring of RUVBL1-RUVBL2 in the complex was determined by omitting flexible regions using focus refinement (Fig. 2). Large conformational rearrangements were identified in RUVBL1-RUVBL2 upon binding of DHX34 by comparing to the structure of the unliganded RUVBL1-RUVBL2. The DII domains in both RUVBL1 and RUVBL2 subunits were slightly displaced, but major changes were found at the N-terminus of all three RUVBL2 subunits.

An N-terminal segment of both RUVBL1 and RUVBL2 contains two histidine residues that are involved in the binding to nucleotides. When bound to nucleotide this region acts as a "gatekeeper" that blocks accessibility to the nucleotide binding site, traps the nucleotide and hampers nucleotide exchange. In complex with DHX34, this N-terminal region of all three RUVBL2 subunits is disordered and missing from the cryo-EM map (Fig. 2). Interestingly, DHX34 interacts with all RUVBL1 and RUVBL2 subunits but only the N-terminus of RUVBL2 subunits were affected by these large conformational changes. As a consequence, all RUVBL2 subunits lost the nucleotide whereas RUVBL1 subunits showed ADP trapped by the N-terminal region in the cryo-EM structure. By measuring how DHX34 affects the ATPase hydrolysis by RUVBL1-RUVBL2 using a combination of wild type and mutant proteins, a clear inhibitory effect of DHX34 in the ATPase activity of RUVBL2 subunits but not RUVBL1 was observed, suggesting that DHX34 traps RUVBL2 in a conformation that is incapable of binding to ATP.

Thanks to this work together with previous research, a model starts to emerge of how the ATPase activity of the RUVBL1-RUVBL2 chaperone is regulated. Protruding DII domains serve as a hub capable of interacting with different partners, and these domains can communicate this "signal" as conformational changes at the N-terminus of RUVBL2 subunits and regulate the access to the ATP-binding site. In NMD, conformational changes induced by DHX34 trap the RUVBL2 subunits in a nucleotide-free conformation unable to interact back with nucleotides, thus inhibiting their ATPase activity. Hypothetically other proteins could work to stimulate ATP hydrolysis if an open access to the nucleotide pocket is compatible with binding to a new ATP molecule and the subsequent closure of the "gatekeeper" N-terminal segment, but examples of this have not been described yet. Further work is needed to understand how different clients may regulate RUVBL1-RUVBL2 differently, if RUVBL1 and RUVBL2 ATPase activity is coordinated and to define what is the actual role of this ATPase activity in the cellular functions of these chaperones.

References:

1. Jha S. *et al.* RVB1/RVB2: Running Rings around Molecular Biology. *Mol. Cell* **34**, 521–533 (2009). DOI: 10.1016/j.molcel.2009.05.016
2. Dauden M. I. *et al.* RUVBL1–RUVBL2 AAA-ATPase: a versatile scaffold for multiple complexes and functions. *Curr. Opin. Struct. Biol.* **67**, 78–85 (2021). DOI: 10.1016/j.sbi.2020.08.010
3. Martino F. *et al.* RPAP3 provides a flexible scaffold for coupling HSP90 to the human R2TP co-chaperone complex. *Nat. Commun.* **9**, 1501 (2018). DOI: 10.1038/s41467-018-03942-1
4. Hug N. *et al.* Mechanism and regulation of the nonsense-mediated decay pathway. *Nucleic Acids Res.* **44**, 1483–1495 (2015). DOI: 10.1093/nar/gkw010
5. Izumi N. *et al.* AAA+ proteins RUVBL1 and RUVBL2 coordinate PIKK activity and function in nonsense-mediated mRNA decay. *Sci. Signal.* **3**, ra27--ra27 (2010). DOI: 10.1126/scisignal.2000468

Funding acknowledgement:
This work was funded by grant SAF2017-82632-P to OL by the Spanish Ministry of Science, Innovation and Universities (MCIU/AEI), co-funded by the European Regional Development Fund (ERDF); the support of the National Institute of Health Carlos III to CNIO; grants Y2018/BIO4747 and P2018/NMT4443 from the Autonomous Region of Madrid and co-funded by the European Social Fund and the European Regional Development Fund to the activities of the group directed by OL. This work was also supported by the Human Frontiers Science Project (HFSP) grant RGP0031/2017 to OL.

Corresponding author:
Dr Oscar Llorca, Structural Biology Programme, Spanish National Cancer Research Centre (CNIO), ollorca@cnio.es

Visualising a membrane receptor complex to enhance drug development

Related publication: Lee Y., Warne T., Nehmé R., Pandey S., Dwivedi-Agnihotri H., Chaturvedi M., Edwards P. C., García-Nafría J., Leslie A. G. W., Shukla A. K. & Tate C. G. Molecular basis of β-arrestin coupling to formoterol-bound β1-adrenoceptor. *Nature* **583**, 862–866 (2020). DOI: 10.1038/s41586-020-2419-1

Publication keywords: Cryo-EM; GPCR; Membrane protein; Structure; Arrestin

A third of all FDA approved drugs target G protein-coupled receptors (GPCRs) but often have side effects. GPCRs have two signalling pathways - the G protein-coupled pathway and the arrestin-mediated pathway - and one may be the therapeutic pathway whilst the other may produce side effects. To understand this phenomenon at the molecular level, researchers needed to determine the structure of a GPCR coupled to arrestin and compare its structure to the G protein-coupled state, with the same agonist bound to both receptors. The GPCR-arrestin complex is highly mobile, which means it would not form crystals suitable for X-ray diffraction experiments. Therefore, the team used cryogenic-electron microscopy (cryo-EM) at the Electron Bio-Imaging Centre (eBIC) at Diamond Light Source to determine its structure at a 3.3Å resolution.

Producing a stable GPCR-arrestin complex suitable for structure determination was still a challenge. Arrestin coupling to a GPCR requires the presence of membrane lipids, so they prepared the receptor in lipid nanodiscs. The receptor also has to be phosphorylated, so they developed a method for ligating phosphorylated peptides to the end of the receptor. Their results allowed them to identify two regions of the GPCR that could be used in the development of 'biased' agonists that signal predominantly through either the G protein or arrestin pathways. The structures will be an invaluable input into structure-based drug design, a powerful tool for the development of new therapeutic drugs.

The human body relies on an extensive network of signalling molecules (agonists) such as hormones and neurotransmitters to co-ordinate bodily functions. GPCRs are the major family of receptors on the surface of cells that bind hormones. Upon a GPCR binding a hormone, there is a subsequent conformation change on the intracellular face of the receptor resulting in binding and activation of G proteins and arrestins, which then activate downstream signalling cascades to alter the cells' biochemistry.

The pivotal role GPCRs play in intercellular communication makes them ideal drug targets. Over 80 years of drug discovery has resulted in an incredible array of molecules that bind to GPCRs and either activate or inhibit them. Currently 34% of FDA approved drugs target GPCRs for the treatment of diverse conditions such as high blood pressure, pain, asthma, heart conditions and migraines[1]. However, many drugs have side effects that limit their use and there is a continual drive to understand the molecular pharmacology of GPCRs and how to develop new drugs. Structural biology of GPCRs offers the opportunity for targeted drug development through structure-based drug design, and there are now examples of such therapeutics in clinical trials[2].

There are many reasons why drugs have side effects, such as they bind to other receptors or they are metabolised to compounds that have a different pharmacology. However, some side effects of drugs at GPCRs arise through the ability of agonists to signal through both the G protein pathway and the arrestin pathway. In many cases, only one of these pathways produces the therapeutic effect, whilst the other pathway produces side effects. Thus, if a therapeutic could be developed that could signal down only the therapeutic pathway, a so-called biased agonist, then side effects could be significantly reduced[3]. To understand the molecular basis of biased signalling, it is necessary to determine the structure of a GPCR bound to an agonist and coupled to either β-arrestin or a G protein. This is what we have done in the current work.

In the present study, we determined the structure of the β_1-adenoceptor (β_1AR) coupled to β-arrestin 1 (βarr1) by cryo-EM. Preparation of the sample was not straightforward because βarr1 couples to only a phosphorylated receptor and requires lipids around the receptor for efficient coupling. We ligated a phosphorylated peptide containing six phosphoresidues (V_2R_{6P}) to the C-terminus of the receptor by sortase mediated ligation and then inserted the purified receptor into lipid nanodiscs. The complex was then formed by adding the agonist formoterol, βarr1 and a conformation-specific antibody F_{ab} fragment, F_{ab}30, that binds to βarr1 and locks it in an active receptor-coupled state. The additional mass provided by the F_{ab} was also essential for good alignment of particles during image processing. The sample was then imaged by cryo-EM, although the sample had to be tilted at 30˚ to reduce the effects during processing of insufficient different views of the complex. Computational

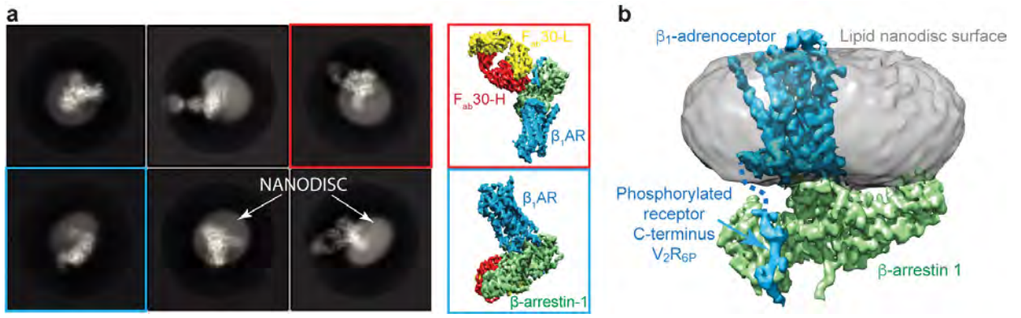

Figure 1: (a) Selected 2D class averages of the β_1AR-βarr1 complex with the orientation of the complex indicated for two examples (red and blue boxes); (b) Overall structure of the β_1AR-βarr1. The F_{ab} fragment has been removed for clarity. Figure panels are reproduced from Lee et al. (2020).

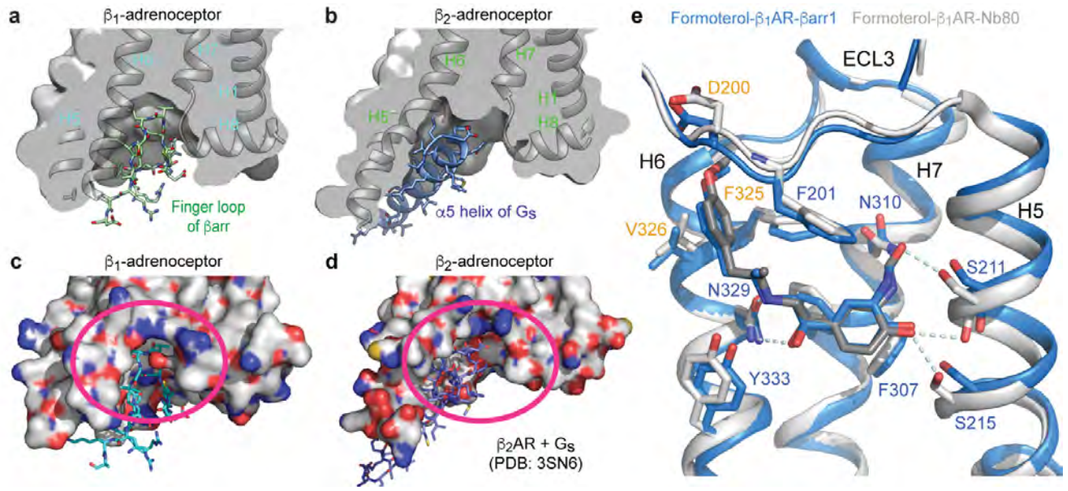

Figure 2: (a,b) Differences in engagement of the finger loop of arrestin and the C-terminal α5 helix of the G protein G_s; (c,d) Surface representations of the β_1AR-βarr1 complex and β_2AR-G_s complex highlighting the distinct junctions at the receptor-transducer interfaces suitable for the development of biased drugs (pink oval); (e) Superposition of the formoterol-β_1AR-βarr1 complex with the formoterol-β_1AR-Nb80 complex around the orthosteric binding site. Side chains (sticks) that interact with formoterol (sticks) are shown with hydrogen bonds (dashed lines, pale blue). Transmembrane helices and extracellular loop 3 (ECL3) are labelled. Figure panels are reproduced from Lee et al. (2020).

processing of the images generated a 3D structure with an overall resolution of 3.3 Å which allowed modelling of the whole receptor (Fig. 1).

The β_1AR- βarr1 structure showed that the arrestin made three distinct interactions. Firstly, there was a direct interaction with the lipids within the nanodisc, explaining the requirement of βarr1 for lipids during coupling to a GPCR. Secondly, there were extensive interactions between βarr1 and each of the six phosphate groups in the phosphorylated C-terminus. Thirdly, there were extensive interactions between β_1AR and βarr1, and in particular the finger loop of βarr1 inserted into a cleft in the cytoplasmic face of the receptor at a site that is known to couple G proteins (Fig. 2). We could compare the interfaces between βarr1 and β_1AR with the interface between β_2AR and the G protein G_s, as β_2AR is known to be virtually identical to β_1AR in multiple different conformations. This showed that there were distinct differences in both the positions of transmembrane helices and residues involved in binding to either a G protein or arrestin. The junction between a receptor and either arrestin or G protein is therefore distinct (Fig. 2) and could be targeted by small molecules that would result in preferential binding of either transducer, resulting in biased signalling.

Agonists bind to the orthosteric binding site in the extracellular half of the receptor and there is allosteric coupling to the intracellular surface of the receptor to promote transducer coupling. Coupling of a G protein to a receptor increases its affinity for agonists by decreasing the volume of the binding site by up to 40% and thus increasing the number and/or strength of receptor-ligand interactions[4]. However, arrestin coupling does not result in such a large increase in affinity, suggesting that there were structural differences in the orthosteric binding site depending whether arrestin or a G protein were coupled. To determine this, we also solved a structure by X-ray crystallography of β_1AR bound to the same agonist (formoterol) and coupled to a conformation-specific nanobody Nb80, which is a G protein mimetic. Comparing the two binding sites identified subtle changes in the position of transmembrane helices that resulted in fewer formoterol- β_1AR hydrogen bonds and van der Waals interactions when β_1AR was coupled to βarr1 compared to when it was coupled to Nb80. These, and other changes in the orthosteric binding site, such as the different position of extracellular loop 3, would be sufficient to develop novel ligands that had biased signalling towards arrestin rather than a G protein.

The new structure of β_1AR coupled to βarr1 and its comparison with G protein-coupled states allows an understanding of the molecular basis for biased signalling. This will aid the design of new and improved therapeutics targeting GPCRs that will have reduced side effects through activating preferentially only desirable intracellular pathways.

References:

1. Hauser A. S. *et al.* Trends in GPCR drug discovery: New agents, targets and indications. *Nat. Rev. Drug Discov.* **16**, 829–842 (2017). DOI: 10.1038/nrd.2017.178
2. Congreve M. *et al.* Impact of GPCR Structures on Drug Discovery. *Cell* **181**, 81–91 (2020). DOI: 10.1016/j.cell.2020.03.003
3. Kenakin T. Biased receptor signaling in drug discovery. *Pharmacol. Rev.* **71**, 267–315 (2019). DOI: 10.1124/pr.118.016790
4. Warne T. *et al.* Molecular basis for high-affinity agonist binding in GPCRs. *Science.* **364**, 775–778 (2019). DOI: 10.1126/science.aau5595

Funding acknowledgement:
Medical Research Council MC_U105197215, European Research Council (EMPSI 339995) and Sosei Heptares. We acknowledge Diamond Light Source for access and support of the cryo-EM facilities at the UK's national Electron Bio-imaging Centre (eBIC) [under proposal BI23268], funded by the Wellcome Trust, MRC and BBRSC.

Corresponding author:
Dr Christopher G. Tate, MRC Laboratory of Molecular Biology,
cgt@mrc-lmb.cam.ac.uk

Molecular view of a key protein could help make cancer cells more vulnerable to treatments

Related publication: Tannous E. A., Yates L. A., Zhang X. & Burgers P. M. Mechanism of auto-inhibition and activation of Mec1ATR checkpoint kinase. *Nat. Struct. Mol. Biol.* **28**, 50–61 (2021). DOI: 10.1038/s41594-020-00522-0

Publication keywords: Mec1/ATR; DNA damage response; Checkpoint control; Enzyme kinetics; Serine/threonine protein kinase; Cryo-EM structures; Activation mechanism

Damage to DNA needs to be repaired quickly, or it can result in defects that eventually cause cancer and ageing, particularly when a cell is replicating. Fortunately, our cells have evolved sophisticated pathways to counter the damage. One key process in the cell is the 'DNA damage response', where signalling factors are recruited that coordinate cell cycle progression with DNA repair. In humans, ATR is a key protein involved in the start of the repair process. A team of scientists at Imperial College London and Washington University School of Medicine in St. Louis used high-resolution cryo-electron microscopy (cryo-EM) structures to identify how ATR kick-starts the DNA repair process.

ATR is sometimes mutated in cancer cells and is a validated drug target for cancer treatment. It and similar proteins are normally turned off (autoinhibited). They are activated when damage is detected. One key question is how ATR is maintained in an auto-inhibited state and how it is activated. The Mec1 yeast protein is essentially the same as human ATR. Using data collected at the Electron Bio-Imaging Centre (eBIC) at Diamond Light Source, the team obtained high-resolution structures of Mec1, in complex with its integral binding partner, Ddc2. In combination with biochemistry and genetics, these structures explain how this protein maintains an inhibited (off) state and the key steps required for its activation. These results allowed the researchers to propose a molecular mechanism for activation. This information helps to rationalise cancer mutations and provides a molecular framework for novel rational drug design of anticancer treatments.

Protein kinases are enzymes that hydrolyse ATP to phosphorylate substrates. Unlike conventional ATPases where γ-phosphate is released and the chemical energy generated by ATP hydrolysis is often converted into mechanical forces, γ-phosphates generated by protein kinases are subsequently transferred onto an amino acid (such as Ser, Thr, Tyr or His), resulting in protein phosphorylation, which is a major post-translational modification utilised to modulate protein functions.

PIKKs (phosphatidylinositol 3-kinase-like kinases) are a family of giant protein kinases with conserved domain structures. They are characterised by a variable length of helical repeats (called HEAT repeats) at the amino-terminus followed by another region of helical repeats (called FAT domain) preceding the carboxy-terminal kinase domain. PIKKs are critical for a broad range of cellular processes, for example: DNA-PKc, ATM, ATR are apical kinases in DNA damage response; TRRAP is involved in chromatin remodelling and transcription control; SMG1 plays a key role in messenger RNA decay; and mTOR is the central coordinator in cellular metabolism and cell growth. Due to their large size and the requirement of specific chaperones, these protein giants have been difficult to produce recombinantly, therefore hindering structural and biochemical characterisations. With the cryo-EM resolution revolution, which combines the requirement of relatively small quantities of samples with the ability to separate conformational heterogeneity, we have seen a remarkable increase in structural information for these proteins, revealing their conserved structural domains and functional motifs[1,2] the tumour suppressors ATM and ATR (Tel1 and Mec1 in yeast). All PIKKs have relatively low basal kinase activity, via auto-inhibition, and must be activated by specific factors and/or post-translational modifications. A number of structures have identified key elements that help to maintain some of the PIKKs in auto-inhibited states and several recent studies have started to shed light on how they are activated[2,3]. We present the structure of Tel1 in a nucleotide-bound state. Our structure reveals molecular details of key residues surrounding the nucleotide binding site and provides a structural and molecular basis for its intrinsically low basal activity. We show that the catalytic residues are in a productive conformation for catalysis.

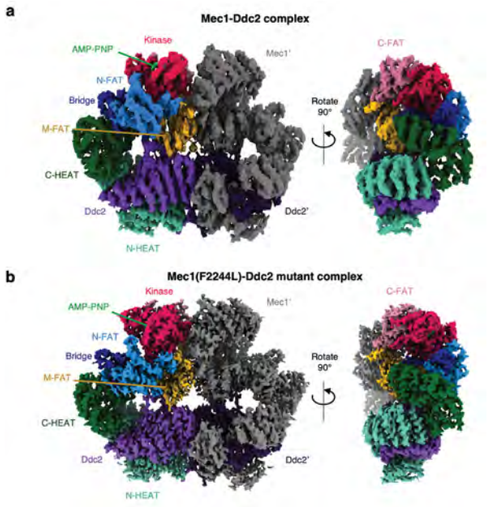

Figure 1: The structure of the Mec1-Ddc2 complex, which is formed of two Mec1 proteins bound to two Ddc2 proteins. Two orthogonal views of the Mec1–Ddc2 AMP-PNP-bound complex resolved to 3.8 Å (a); and two orthogonal views of the constitutively active Mec1(F2244L)–Ddc2–AMP-PNP mutant complex resolved to 2.8-Å resolution (b). Structurally distinct domains are coloured; red, kinase; pink, C-terminal-FAT; yellow, middle-FAT; blue, N-terminal-FAT; navy, bridge; green, C-terminal HEAT; teal, N-terminal HEAT. The Ddc2 subunit is coloured purple, and the nucleotide is coloured bright green. The second Mec1–Ddc2 heterodimer is shown in grey (Mec1') and dark purple (Ddc2').

ATR is an apical signalling kinase in DNA damage repair, especially in homology-dependent repair, and a key player in replication stress response as well as regulating normal replication[4]. ATR activation results in the phosphorylation of a myriad of downstream proteins, including repair proteins (e.g. CtIP and EXO1), and proteins involved in cell cycle regulation, such as CHK1 leading to cell cycle arrest. ATR signalling can therefore coordinate cell cycle progression with DNA repair[4]. Mutations in ATR have frequently been found in cancer cells and ATR is a validated drug target for cancer treatment.

ATR is conserved from yeast to man and Mec1 is the yeast orthologue of ATR. Taking advantage of simpler yeast genetics, a screen of *MEC1* mutations in key functional regions identified a single point mutation that renders Mec1 constitutively active. Using data collected at eBIC, cryo-EM structures of Mec1 with its integral partner Ddc2 and in a complex with the ATP analogue AMPPNP

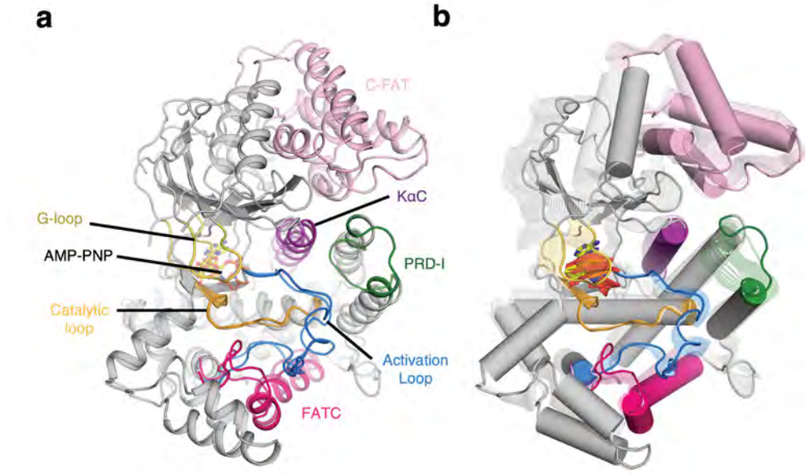

Figure 2: (a) Comparison of the kinase domains between the auto-inhibited and active mutant form; (b) Kinase domain motion between autoinhibited (transparent states) and active state (opaque). Nucleotide (coloured by heteroatom) and Catalytic features are shown. The catalytic features are coloured; orange, catalytic loop; blue, activation loop; green, PRD-I; yellow, G-loop; purple, KaC; hot pink, FATC; C-FAT, light pink.

were resolved, both in an auto-inhibited state (wild-type at 3.8 Å), and in the constitutively active state (Mec1(F2244L)-Ddc2 at 2.8 Å) (Fig. 1). These structures reveal molecular details of how Mec1 maintains its low basal activity, they correct previous structural models derived from lower resolution cryo-EM reconstructions, and they reconcile a previous crystal structure of Ddc2 with biochemical data. The structures reveal the conformation of the activated state and the conformational changes required for activation when compared to the auto-inhibited structure. Three key features are critical for maintaining the low basal activities of the protein: (1) elements of the ATP binding pocket, including the conserved glycine-rich loop, are not positioned for optimal nucleotide binding, resulting in a reduced affinity for ATP. Biochemical data confirmed that wildtype Mec1-Ddc2 has a lower affinity for ATP than the constitutively active mutant form; (2) In the autoinhibited state the ATP is too far away from the active site for catalysis; (3) The catalytic residues in the active site are in an unproductive conformation.

The most notable key residues in the active site are the conserved DFD motif. We show in this study that the two Asp residues in DFD are involved in the binding of two Mg^{2+} ions - a prerequisite for catalysis. In the auto-inhibited state, the DFD does not have a defined conformation. This is due to the constraints imposed by interactions with a region in the protein called the PRD-I (PIKK-regulatory domain insert), which was shown in other PIKKs to restrict substrate access, thereby inhibiting kinase activity. In the activated state of Mec1-Ddc2, the Phe residue in DFD motif, which we mutated to Leu, is inserted into a hydrophobic pocket, helping the two Asp residues to orientate in correct conformations. This local change in the active site coincides with a set of larger conformational changes including the retraction of the PRD-I region from the active site, the rotation of the FAT domain relative to the kinase domain, the closure of the N-lobe and glycine-rich loop of the kinase domain, and a shift in ATP position. The range of changes result in the correct orientation and positions of all the catalytic elements. These observations of the active F2244L mutant structure corroborate cellular studies, showing that the constitutively active form of Mec1 no longer requires an activator. These studies provide unprecedented molecular details on the exact conformation of an activated Mec1/ATR and the range of changes that are required to overcome the inhibited state and to convert to the activated state – a process that may be conserved in other PIKKs.

Importantly, structural, genetic and biochemical data, when taken together, suggest a mechanism that involves the release of inhibition imposed by the PRD-I coupled to re-configuration and closure of the ATP-binding pocket (Fig. 2). Both cellular and biochemical studies of additional mutant Mec1 proteins support the molecular details observed in the cryo-EM structures, highlighting the necessity to reconfigure the kinase domain in order to establish the activated state of the enzyme.

Genetical and biochemical data of mutant proteins support the idea that the enzyme exists in an equilibrium between the auto-inhibited state and the activated state, with the inhibited state dominating in basal conditions. Activator binding drives the equilibrium toward the activated state. Significantly, the genetic and biochemical data indicate that different levels of kinase activity are required for optimal health of the cell during different cellular processes such as normal cell growth, DNA replication and DNA repair.

Overall, this study illustrates the greater insight gained from combining functional and structural studies to understand a complex biological system. The next steps are to understand how these enzymes are recruited to the damage sites and how they engage with activator proteins to induce the changes required for their activation.

References:

1. Williams R. M. *et al.* Structures and regulations of ATM and ATR, master kinases in genome integrity. *Curr. Opin. Struct. Biol.* **61**, 98–105 (2020). DOI: 10.1016/j.sbi.2019.12.010
2. Yates L. A. *et al.* Cryo-EM Structure of Nucleotide-Bound Tel1ATM Unravels the Molecular Basis of Inhibition and Structural Rationale for Disease-Associated Mutations. *Structure* **28**, 96-104.e3 (2020). DOI: 10.1016/j.str.2019.10.012
3. Yang H. *et al.* Mechanisms of mTORC1 activation by RHEB and inhibition by PRAS40. *Nature* **552**, 368–373 (2017). DOI: 10.1038/nature25023
4. Williams R. M. *et al.* Roles of ATM and ATR in DNA double strand breaks and replication stress. *Prog. Biophys. Mol. Biol.* (2020). DOI: 10.1016/j.pbiomolbio.2020.11.005

Funding acknowledgement:
This work was funded in part by the Wellcome Trust 210658/Z/18/Z (to X. Z.) and GM118129 from the National Institutes of Health (to P. M. B.).

Corresponding authors:
Prof. Xiaodong Zhang, Department of Infectious Disease, Imperial College London, xiaodong.zhang@imperial.ac.uk; Dr Luke A. Yates, Department of Infectious Diseases, Imperial College London, luke.yates@imperial.ac.uk

Visualising a bacterial multi-substrate recruitment machine in action

Related publication: Meir A., Macé K., Lukoyanova N., Chetrit D., Hospenthal M. K., Redzej A., Roy C. & Waksman G. Mechanism of effector capture and delivery by the type IV secretion system from Legionella pneumophila. *Nat. Commun.* **11**, 2864 (2020). DOI: 10.1038/s41467-020-16681-z

Publication keywords: Type IV secretion system; T4SS; Host-pathogen interaction; *Legionella pneumophila*

Bacteria use a wide range of trans-membrane machineries, called secretion systems, to transfer proteins into target cells. These 'bacterial effector proteins' interfere with host cell functions. Gaining a better understanding of how secretion systems work will provide a basis for novel design strategies of antibiotics to combat bacterial infectious diseases.

The pathogen that causes Legionnaires' disease, *Legionella pneumophila* (*L. pneumophila*), uses a Type IV Secretion System (T4SS) to infect human cells. To understand its mechanism, an international team of researchers purified the part of the T4SS responsible for the recruitment and delivery of effector proteins from the *Legionella* membrane, the 'Type IV Coupling Complex (T4CC)'. They were then able to determine the structure of T4CC using single-particle cryo-electron microscopy (cryo-EM) with data collected at the Electron Bio-Imaging Centre (eBIC) at Diamond Light Source and the ISMB cryo-EM facility at Birkbeck, University of London. The atomic resolution structure revealed a five-protein core complex from which the T4CC recruitment module interacts with via a flexible linker. Six of these protein complexes combine to form a large nanomachine, containing a channel in the membrane, that effector molecules can pass through. Analysis of multiple cryo-EM maps, further modelling and mutagenesis provided working hypotheses for the mechanism of binding and delivery of two of the classes of *Legionella* effectors.

***L. pneumophila* bacteria secrete over 300 effectors during infection and blocking their recruitment is known to stop the disease. The high-resolution structure of the *Legionella* T4CC provides essential information for designing T4CC-blocking antibiotics. Mechanistic understanding of the T4CCs gained in this study could also provide the basis for engineering T4SSs capable of injecting therapeutic drugs into human cells.**

The gram-negative bacterium *L. pneumophila,* the causative agent of Legionnaires' disease, infects human alveolar macrophages, as well as diverse protozoan hosts[1]. *L. pneumophila* injects over 300 effector proteins (most pathogenic bacteria settle for less than a dozen) into host cells by utilising the Dot/Icm T4SS. The large number of effector proteins that *L. pneumophila* is required to secrete in order to invade host organisms makes its T4SS a particularly interesting model system to study effector recruitment and translocation in pathogenic bacteria.

L. pneumophila employs a protein complex embedded in the inner membrane called T4CC, that acts as a recruitment platform for effectors and translocates them through the secretion channel[2]. This complex was thought to be formed by three proteins, the AAA+ ATPase DotL, DotM and DotN. How this T4CC orchestrates the recruitment and transfer of so many different effectors was unclear prior to the work described in Meir *et al*. (2020), the subject of this review.

Meir *et al*. (2020) were fascinated by this functionally essential complex, and in order to elucidate its mechanism of action, they sought to solve its cryo-EM structure. Their initial approach, to purify the complex recombinantly in *Escherichia coli*, failed despite extensive attempts. A creative solution to overcome this obstacle was the introduction of an affinity tag at the C-terminus of DotL directly in the *L. pneumophila* genome. This enabled the purification of a stable complex from *L. pneumophila* cells.

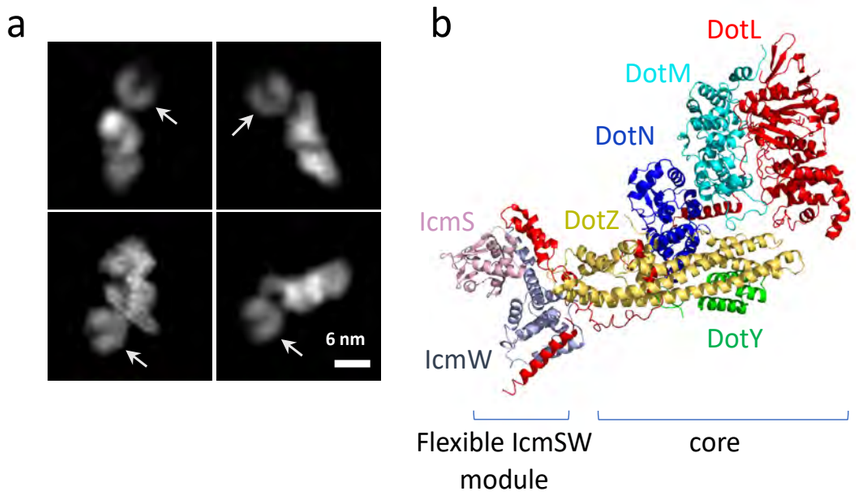

Figure 1: (a) Representative 2D class averages of the T4CC showing IcmSW in various orientations. The IcmSW module U-shaped density is indicated in white arrows; (b) Ribbon diagram of the T4CC core and IcmSW flexible module. All proteins are indicated in a different colour and labelled. The DotLMNZY core as well as the flexible IcmSW module are indicated. As shown in panel (a), the IcmSW module is flexible relative to the core and therefore panel (b) here reports on only one configuration of this module. Panel (a) is reproduced from Meir et al. (2020).

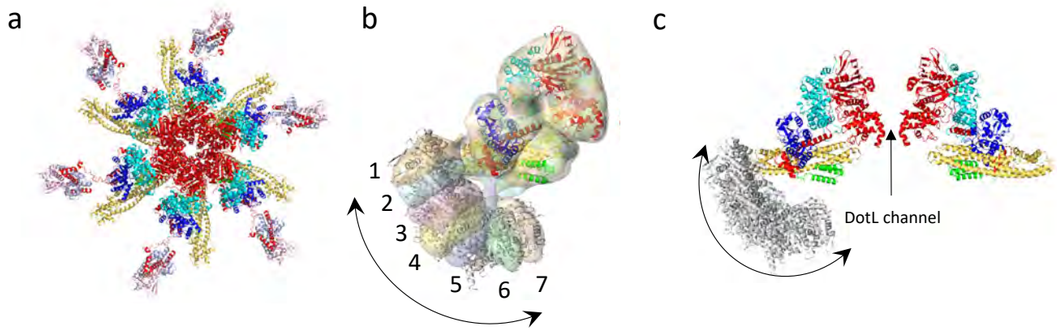

Figure 2: (a) Ribbon diagram of the hexameric form of the T4CC including the IcmSW modules in the relative orientation shown in Fig. 1b; (b) Positional flexibility and trajectory of the IcmSW module, as indicated by the superposition of 7 low resolution EM maps of the DotLMNZY-IcmSW complex; (c) Two diametrically opposite DotLMNZY-IcmSW complexes of the T4CC hexamer are shown, one of them includes the 7 flexible conformations of the IcmSW modules as shown in (b). The T4CC channel is indicated as 'DotL channel.' In (b) and (c), the double arrow indicates the flexible orientation of IcmSW relative to the core in the context of the monomeric (b) or hexameric (c) assembly. Colour-coding is as in Fig. 1. Panels (b) and (c) are similar, but not identical to those published in Meir et al. (2020).

The purified apparatus revealed surprising findings. First, as mentioned above, a complex of three proteins was expected. However, the purified complex consisted of eight components: the expected DotL, DotM and DotN proteins, as well as the chaperone module IcmS, IcmW (IcmSW), LvgA and two previously uncharacterised proteins, DotY and DotZ. The second surprising outcome was that the T4CC, although it contains a AAA+ ATPase that would usually form hexamers, purified as a stable complex of monomeric nature where one copy only of each protein was present.

The initial EM data (Fig. 1a) suggested a dynamic structure with a stable core and a more flexible U-shape density with various orientations relative to the core.

Thanks to multiple data collections (at eBIC and at the ISMB EM facility at Birkbeck), a 3D density map for the core was obtained at a nominal resolution of 3.7 Å. It revealed that the core is composed of five proteins: DotL, DotM, DotN and the two newly discovered proteins, DotY and DotZ (Fig. 1b). A specific analysis of the EM data focusing on the flexible U-shape density (at mid-range resolution of 9.7 Å) revealed that it consists of IcmSW bound to a part of the DotL C-terminal tail (this partial structure had been previously solved by Kwak et al[3]) (Fig.1b). IcmSW is known to bind a particular class of effectors called the IcmSW-dependent effectors, so-called because of their dependence on IcmSW for recruitment. Density for the LvgA protein was not found.

The main protein of the complex is the ATPase DotL, which has a very long C-terminal tail onto which all other components assemble like pearls on a string, including IcmSW which is found bound to the C-terminus of the DotL tail. Because AAA+ ATPases function as channel-forming hexamers, Meir *et al*. (2020) proposed a hexameric model of the entire T4CC based on a close homologue of DotL (Fig. 2a). Hexamerisation produces a large complex resembling a starfish 26 nm in diameter, with a central channel large enough for effectors to go through. A previous mutational analysis provided experimental data that showed that the hexameric interface is biologically relevant, likely suggesting that the T4CC functions as a hexamer of DotLMNZY-IcmSW heptameric units.

As mentioned previously, the U-shape IcmSW is positioned flexibly relative to the core. Meir *et al*. (2020) were able to show that the IcmSW module bound to the DotL tail moves along a defined trajectory (Fig. 2b) which maximises delivery of IcmSW-bound effectors to the central T4CC hexameric channel formed by DotL (Fig. 2c).

DotM is also known to form a platform for recruitment of a second class of effectors, the DotM-dependent effectors[4]. The T4CC structure revealed a binding region on DotM where these effectors bind, thereby providing a mechanism for their uptake by the T4CC channel.

In conclusion, the results elucidated the overall architecture of the *Legionella* T4CC recruitment platform, revealed the binding regions for two different classes of effectors, provided information regarding the dynamics of the system, and delineated a potential mechanism for the sequential and selective recruitment of effectors of various size and function. More generally, this study greatly enhanced our scientific understanding of effector recruitment platforms in bacterial secretion systems.

References:

1. Mondino S. *et al.* Legionnaires' Disease: State of the Art Knowledge of Pathogenesis Mechanisms of Legionella. *Annu. Rev. Pathol. Mech. Dis.* **15**, 439–466 (2020). DOI: 10.1146/annurev-pathmechdis-012419-032742
2. Vincent C. D. *et al.* Identification of the DotL coupling protein subcomplex of the Legionella Dot/Icm type IV secretion system. *Mol. Microbiol.* **85**, 378–391 (2012). DOI: 10.1111/j.1365-2958.2012.08118.x
3. Kwak M. J. *et al.* Architecture of the type IV coupling protein complex of Legionella pneumophila. *Nat. Microbiol.* **2**, 17114 (2017). DOI: 10.1038/nmicrobiol.2017.114
4. Meir A. *et al.* Legionella DotM structure reveals a role in effector recruiting to the Type 4B secretion system. *Nat. Commun.* **9**, 507 (2018). DOI: 10.1038/s41467-017-02578-x

Funding acknowledgement:
This work was funded by ERC grant 321630 and Wellcome grant 098302 to G.W. and NIAID grants R21AI130671 and R37AI041699 to CR. Most of the cryo-EM data for this investigation were collected at the ISMB EM facility at Birkbeck College, University of London with financial support from Wellcome (202679/Z/16/Z and 206166/Z/17/Z). We would also like to thank Diamond Light Source for access to the cryo-EM facilities at the UK National electron bio-imaging centre (eBIC, proposal EM14704) funded by the Wellcome Trust, the Medical Research Council UK and the Biotechnology and Biological Sciences Research Council.

Corresponding authors:
Dr Amit Meir, Yale University, amit.meirbenefraim@yale.edu; Dr Kevin Macé, Birkbeck, University of London, k.mace@mail.cryst.bbk.ac.uk; Prof. Gabriel Waksman, Birkbeck, University of London, g.waksman@mail.cryst.bbk.ac.uk

Mapping antibody recognition of SARS-CoV-2 spike protein

Related publication: Dejnirattisai W., Zhou D., Ginn H. M., Duyvesteyn H. M., Supasa P., Case J. B., Zhao Y., Walter T. S., Mentzer A. J., Liu C., Wang B., Paesen G. C., Slon-Campos J., Lopez-Camacho C., Kafai N. M., Bailey A. L., Chen R. E., Ying B., Thompson C. P., Fyfe A., Gupta S., Tan T., Gilbert-Jaramillo J., James W., Buttigieg K., Coombes N., Carroll M. W., Skelly D., Dold C., Peng Y., Levin R., Dong T., Pollard A., Knight J., Klenerman P., Temperton N., Hall D. R., Williams M. A., Paterson N. G., Bertram F. K. R., Seibert C. A., Clare D. K., Howe A., Raedecke J., Song Y., Townsend A., Huang K.-Y. A., Fry E. E., Mongkolspaya J., Diamond M. S., Ren J., Stuart D. I. & Screaton G. R. The Antigenic Anatomy of SARS-CoV-2 Receptor Binding Domain. *Cell* **184**, (2021). DOI: 10.1016/j.cell.2021.02.032

Publication keywords: SARS-CoV-2; Antibody; Germline; V-gene; Receptor-binding-domain; Spike; Neutralisation; Protection; Glycosylation

The COVID-19 vaccines currently in use in Europe and the USA aim to generate antibodies against the virus spike. We need to know where these antibodies bind and how they neutralise the virus. Viruses mutate to escape antibody binding, and changes to the spike structure can stop antibody attachment.

An international team of researchers identified 377 human monoclonal antibodies (mAbs) from recovered SARS-CoV-2 patients that recognised the virus spike. They used cryo-electron microscopy (cryo-EM) at the Electron Bio-Imaging Centre (eBIC) and Macromolecular Crystallography (MX) on beamline I03 at Diamond Light Source to investigate the complex structures of the SARS-CoV-2 spike or the receptor binding domain (RBD) with the antibody Fabs (a region on an antibody that binds to antigens).

The team determined the structures of 11 spike/Fab complexes by cryo-EM and 18 RBD/fab complexes by crystallography. Using a combination of structural methods, and a novel computational algorithm utilising competition bio-layer interferometry data, they localised binding epitopes of 80 on the surface of the RBD. Three of the potent neutralising mAbs are glycosylated, and the glycans contribute to neutralisation.

Their results identify the precise binding sites on the spike and their detailed interactions. This information can guide combinations for antibody cocktail therapy. More potent neutralising monoclonal antibodies (mABs) can be designed through structural analysis. Understanding how the binding of these antibodies is affected in variant viruses is helpful in understanding how we might design next-generation vaccines. The project involved many groups working closely together, and success in such a difficult time was only possible due to tremendous support and collaboration with eBIC, the Oxford Particle Imaging Centre (OPIC) and I03.

The current COVID-19 pandemic has had an unprecedented impact on both human health and economics globally. The causative agent, SARS-CoV-2, is related to SARS-CoV-1 and MERS-CoV, and all are beta coronaviruses causing severe respiratory syndromes. The spike, a glycoprotein, is the only molecule protruding outside the virus membrane, and is composed of two subunits, S1 which mediates receptor binding and S2 responsible for viral and host cell membrane fusion. The prefusion spike has an elongated trimeric structure that transitions to the post-fusion state by cleavage between S1 and S2 following receptor binding or trypsin treatment. This conformational change allows the virus to infect the host cell. The S1 fragment occupies the membrane distal tip of S and can be subdivided into an N-terminal domain (NTD) and the receptor binding domain (RBD).

SARS-CoV-2 infected or vaccinated individuals produce a large number of antibodies which are crucial for immune protection against the virus.

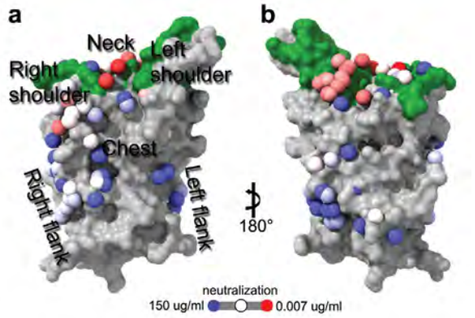

Figure 1: Epitope mapping of RBD binding antibodies. The RBD is shown as grey surface representation with region labelled in analogy to the torso. The footprint of the receptor ACE2 is coloured in green. Antibodies are shown as spheres positioned based on the BLI competition data and colour-coded according to their ability to neutralise SARS-CoV-2.

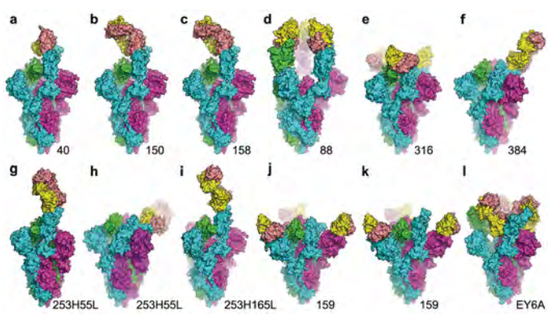

Figure 2: Cryo-EM structures of SARS-CoV-2 spike and Fab complexes. Each structure is drawn as surface representation with chains A, B and C of the spike, and heavy chain and light chain of Fab coloured in green, cyan, magenta, yellow and salmon, respectively. Note, in panels (a), (d), (e), (j) and (k) only the VhVl domains of the Fabs are modelled.

We obtained 377 monoclonal antibodies (mAbs) targeting the viral spike glycoprotein from B-cells in the blood of convalescent patients. 80 of these react with the RBD and include nearly all the potent neutralisers (which we define as giving 50% virus neutralisation at < 0.1 µg/ml). To acquire greater insight to the mAb binding sites on the RBD, we measured pairwise competition between antibodies using biolayer interferometry (BLI) in a 96-well plate format. 79 of the current set of mAbs (one has known structure), and three 'external' antibodies of known binding positions, were used. Combining the BLI data and the four known binding positions, we were able to map the positions of the mAbs on the surface of the RBD. The predicted locations, covering most of the RBD surface, clustered into five groups and were named by analogy to a human torso (Fig. 1). There is generally good correlation between overlap with ACE2 footprint and neutralisation.

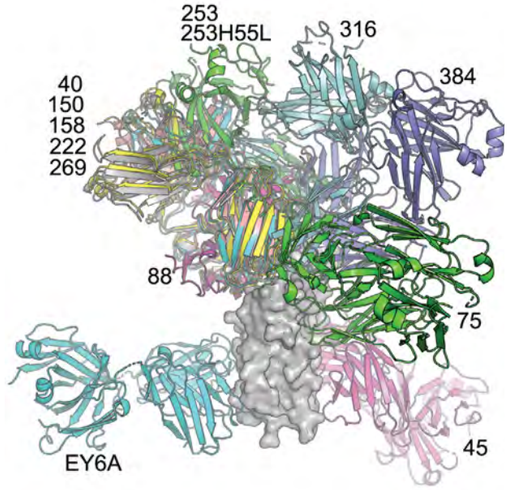

Figure 3: The binding positions and orientations of 12 Fabs whose structures with RBD or spike are determined by either cryo-EM or X-ray crystallography. The RBD is shown as grey surface, and Fabs are drawn as ribbons.

However, there were notable examples of non-neutralising antibodies that were good ACE2 blockers. Interestingly, antibodies co-locating with known neutralising/protecting antibodies EY6A and S309, in the left and right flank clusters respectively, did not show appreciable neutralisation in our assays[1,2].

To confirm the mapped positions of the mAbs and visualise detailed interactions with the antigen, we determined 11 spike/Fab cryo-EM and 18 RBD/Fab crystal structures with excellent support from eBIC, Oxford Particle Imaging Centre (OPIC) and the Macromolecular Crystallography (MX) beamline I03 (a Fab is a fragment of the antibody that binds the antigen). The complex structures include 10 natural and two hybrid mAbs, one mAb (159) that binds at the NTD, some had two Fabs bound at the same time, and some were with mutant RBD of the virus variants of concern[3,4]. The binding positions of the mAbs agreed with the predicted locations, with an average error of 7.6 *Å*.

In the isolated prefusion trimeric spike, the RBD is mainly found in two orientations, 'up' and 'down'. The cell receptor ACE2 can only bind the RBD in the up conformation. The most common configuration of the spike observed in the present study is one RBD-up and two RBD-down, with a Fab bound only to the RBD in the up conformation (Fabs 40, 150, 158, and the chimeras 253H55L and 253H165L). Fabs 316 and 384 bind the spike in all RBD-down configuration with Fab:spike stoichiometry of 3:1 and 1:1 respectively. The chimera 253H55L can also bind the spike in all RBD-down configuration with 1:1 stoichiometry. In contrast, 3 Fabs of mAb 88 bind the spike in all RBD-up configuration, which we observed previously for EY6A, despite the fact that these two mAbs recognise quite different epitopes on the RBD[2]. In the case of mAb 159, the most potent neutraliser (IC_{50} of 5ng/mL) that interacts with the NTD, three Fabs bind the spike in either all RBD-down or one RBD-up configuration (Fig. 2).

Antibodies that recognise glycan epitopes are well documented. In contrast, the role of sugars on the variable part of the antibody, although found in 15%-25% of immunoglobulin Gs (IgGs), is poorly studied at the molecular level. Fourteen of 80 RBD-binding antibodies in the present study contain glycosylation sequons arising from somatic mutations in their variable region. Three of the Fabs we determined structures for, 88, 253 and 316 have glycosylation sites, in CDRs H1, H3 and H2 respectively. The glycans are presented close to the top of the left shoulder of the RBD. In two out of three cases the sugars interact directly but rather weakly with the antigen. mAbs 88 and 316 could be de-glycosylated without denaturation, and BLI analysis showed that this had negligible effect on RBD/Fab binding affinities. However, mutations that eliminate glycosylation had a deleterious effect on neutralisation for these two and the 253H165L chimera.

The most potent RBD-binding mAbs bind in the regions of the neck and left shoulder, achieving neutralisation by blocking the ACE2 binding (Fig. 3). There is a close association between potent neutralisers and public V-genes (antibody genes shared by many people) suggesting that vaccination responses should be strong. Three public heavy chain V-region genes are represented at least twice in our set, i) IGHV3-53: mAbs 150, 158, 175, 222 and 269, ii) IGHV3-66: 282 and 40 (this is very similar to IGHV3-53) and iii) IGHV1-58: 55, 165, 253 and 318. mAb 40 together with IGHV3-53 mAbs are all bound in the neck region with an almost identical pose determined by their highly conserved CDRs H1 and H2. Notably IGHV3-30 is found in 11 RBD binders, none of which are potent neutralisers. Structures of two representatives, 45 and 75, show binding on the left flank and right shoulder respectively. By switching light chains within the same IGHV set, we found a 10-fold increase in neutralisation potency when the heavy chain of mAb 253 was combined with the light chains of mAbs 55 and 165. mAb 384, an IGHV3-11 antibody, the most potent neutraliser with IC_{50} of 2 ng/ml, adopts a unique pose with a footprint extending from the left shoulder epitope to the neck epitope, via its extended CDR H3.

We tested neutralisation of the 20 most potent neutralisers against three variants of concern: B.1.1.7, B.1.351 and P.1. All three variants carry a N501Y mutation, B.1.351 and P.1 have additional E484K, and K417N in the former and K417T in the latter in the RBD. Neutralisation of the majority of the mAbs are affected by one or more variants, but 222 and 253 are unaffected [3-5]. 253 has no direct contact with any of the mutations, while 222 contacts residues 501 and 417. Complex structures of 222 with the RBD which carry the N501Y mutation show P30 of 222 makes stacking contact with Y501, strengthening the interaction with the mutant RBD. The structural information has prompted us to change the light chain of other IGHV3-53 mAbs to that of 222, which restored the activity of mAbs 150 and 158 against all three variants. In fact, the modified mAb 150 is 50-fold and 13-fold more potent against B.1.351 and P.1, than the original 150, respectively.

References:

1. Huo J. *et al.* Neutralization of SARS-CoV-2 by Destruction of the Prefusion Spike. *Cell Host Microbe* **28**, 445-454.e6 (2020). DOI: 10.1016/j.chom.2020.06.010
2. Zhou D. *et al.* Structural basis for the neutralization of SARS-CoV-2 by an antibody from a convalescent patient. *Nat. Struct. Mol. Biol.* **27**, 950–958 (2020). DOI: 10.1038/s41594-020-0480-y
3. Dejnirattisai W. *et al.* Antibody evasion by the P.1 strain of SARS-CoV-2. *Cell* (2021). DOI: 10.1016/j.cell.2021.03.055
4. Supasa P. *et al.* Reduced neutralization of SARS-CoV-2 B.1.1.7 variant by convalescent and vaccine sera. *Cell* **184**, 2201-2211.e7 (2021). DOI: 10.1016/j.cell.2021.02.033
5. Zhou D. *et al.* Evidence of escape of SARS-CoV-2 variant B.1.351 from natural and vaccine-induced sera. *Cell* **184**, 2348-2361.e6 (2021). DOI: 10.1016/j.cell.2021.02.037

Funding acknowledgement:
Wellcome Trust (grant 095541/A/11/Z). UK Medical Research Council (MR/N00065X/1).

Corresponding authors:
Dr Jingshan Ren, Division of Structural Biology, University of Oxford, ren@strubi.ox.ac.uk; Prof. David I. Stuart, Division of Structural Biology, University of Oxford, and Diamond Light Source, dave@strubi.ox.ac.uk

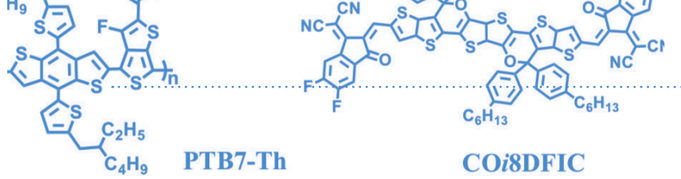

Structures and Surfaces Group

Chris Nicklin, Science Group Leader

The Structures and Surfaces Group at Diamond Light Source comprises four beamlines: I05 (Angle Resolved Photoelectron Spectroscopy – ARPES), I07 (Surface and Interface X-ray Diffraction), B07 (Versatile Soft X-ray Scattering – VerSoX) and I09 (Atomic and Electronic Structure of Surfaces and Interfaces). These offer a variety of techniques to examine the atomic scale structure, chemical nature and electronic state at buried interfaces or the surfaces of materials. The focus this year has been on improving the user interface and accessibility for control of experiments to ensure that as many experiments as possible could be carried out remotely by users with the support of the beamline teams on-site. The success of the majority of these studies has been enabled by the strong partnership of the Diamond scientists with the user groups, leading to stronger collaborations and exceptional results. It has continued to be a busy year for beamline developments (as detailed below) whilst also taking a strategic view for the future, in particular the important role that surfaces and interfaces play in broader research areas such as battery technology, photovoltaic structures, and catalytic/electrochemical systems under *operando* conditions. Expanding the techniques to these communities remains a key aim for the group.

On I05, the high resolution branch has continued with its upgrade programme to install new gratings and a new electron energy analyser. The team also took the opportunity to fully realign the beamline, leading to a reduced spot size and increased flux. Together, these developments will maintain the high resolution branch at the forefront of ARPES facilities and continue to enable its world leading research. The NanoARPES end station has delivered improved flux and reduced spot size through the incorporation of a capillary mirror, with further improvements possible with another capillary. The sample preparation and mounting facilities have also been enhanced through the recent installation of a glove box and micromanipulation system to enable precise alignment of crystals that are air sensitive. The group have ambitious plans for developing photoelectron spectroscopy at Diamond to complement the high resolution facilities available on I05, the arrival of a soft X-ray ARPES system (momentum microscope) this year on I09, the Hard X-ray (HAXPES) station also on I09 and the Near Ambient Pressure X-ray Photoelectron Spectroscopy (NAP-XPS) capability on B07.

The surface and interface diffraction facilities on I07 continue to be upgraded to enhance the capabilities. Continuous scanning of the diffractometer will improve the data collection efficiency and automated fast attenuators will enable fast measurement of crystal truncation rods that cover many orders of magnitude changes in intensity. The new Excalibur detector is now in use, with updated software control to integrate fully with the continuous scanning capability and offering a high dynamic range. The diffractometer upgrade has been delayed due to lockdown restrictions, but the beamline team has commissioned the new hexapod to increase the reliability and speed of experiments. The ultrahigh vacuum experiment capabilities have been improved through the integration of the XPS system into the end station and a sample preparation chamber that incorporates a small integrated glove box for improved sample handling. A new optical layout of the beamline has been investigated with the Optics Group that would give much greater control and reduction of the beam size, whilst increasing the flux at the sample. Discussions are continuing about the optimal approach that will enable these developments to be realised.

This year, the second branch of B07 (VerSoX) has opened to users, initially enabling NEXAFS studies using soft X-rays to study processes such as molecular adsorption or catalysis, using an end station built in partnership with Prof. Sven Schroeder at the University of Leeds. This will be complemented towards the end of the year by a high throughput XPS system that will allow chemical state analysis of many samples. It has been installed and is currently undergoing commissioning. The two branchlines work independently and this will therefore bring additional capability and supplement the techniques offered by the group. The NAP-XPS system available on Branch C of the beamline continues to work well and has been enhanced by the addition of a bespoke gas panel to enable automated exposure to pure and well controlled mixtures of gases. Full scripting of this facility through the data acquisition system will enable complex studies to be semi-automated. Additional capability for nanoscale cluster studies is also being provided through a collaboration between Diamond and Prof. Richard Palmer from the University of Swansea, to house a vacuum cluster source close to B07 with vacuum suitcase transfer capabilities. This system is available for user experiments and its potential use should be discussed with the beamline team.

Beamline I09 continues to maintain a very active user programme whilst also developing new capabilities. The Hard X-ray Photoelectron Spectroscopy (HAXPES) system is commissioned with X-rays and ready to host single sample experiments; new X-ray windows are being tested to allow emission-angle dependent studies and a multipurpose sample manipulator stick will be developed for high-throughput experiments. The delivery of the soft X-ray ARPES system (also known as a momentum microscope) was delayed by the COVID-19 pandemic. The end station has been designed and the construction is underway, with delivery of the bespoke analyser due in the summer of 2021. This challenging project, undertaken together with Prof. Gerd Schönhense from the University of Mainz and Prof. Ralph Claessen from the University of Wurzburg, will provide world-leading capabilities for such soft X-ray ARPES studies. Smaller scale upgrades are also underway including a modified manipulator design that enables sample biasing and more accurate sample temperature control whilst still allowing sample transfer. Future developments include replacing the simple (three fixed-energy) monochromator with a fully tuneable version to enhance the HAXPES studies and an upgraded plane grating monochromator for the soft X-ray branch.

The group is aiming to enhance the associated infrastructure available for surface science research including the design of a new offline ultrahigh vacuum system to characterise samples, a proposal that was well received by the Diamond Scientific Advisory Committee (SAC). This was delayed due to the lockdown restrictions but design work has started as this system continues to be a high priority that will position Diamond to be able to rapidly study new samples and enhance the link between laboratory and synchrotron based experiments. We aim for this capability to be at the core of many of the joint PhD studentships that we support.

The range of science undertaken at the Structures and Surfaces beamlines continues to be a combination of detailed surface science characterisation through to application of the methods to novel samples, as outlined in the contributions from a selection of our users. These highlight a broad range of investigations from studies of materials in device structures to purely fundamental research. The report by the group of Tao Wang in collaboration with David Lidzey, highlighting work on I07, indicates how the addition of a third component into a blend of polymers used in organic photovoltaics (OPVs) could change the crystalline structure and increase the device efficiency. Work relating to energy materials is also the subject of the highlight report from B07, by Dr Victor A. de la Peña O'Shea, which focused on understanding the charge dynamics in metal-organic frameworks (MOFs) and how this is related to their photocatalytic behaviour. The long term aim is to use these types of material for fuel production via artificial photosynthesis. Some of the more fundamental studies are highlighted by the work of Dr Veronika Sunko in collaboration with Prof. Phil King, who have identified a method to investigate the magnetic behaviour of a material using a combination of energy dependent soft X-ray ARPES on I09 and lower energy ARPES on I05. The report from Dr Niels Schröter also focuses on the key parameters of a material system, showing how ARPES on I05 can be applied to complex chiral crystals to understand the origin of the topological charge in PdGa.

The members of the Structures and Surfaces Group are committed to continue offering the best support to our users to ensure the highest quality scientific output from the beamlines. The combination of strong interactions and collaborations, together with continuous improvements to the instrumentation and technique development, is key to our success. Please contact us if you would like to discuss any of the possibilities that we offer and how such synchrotron based studies could help in your research.

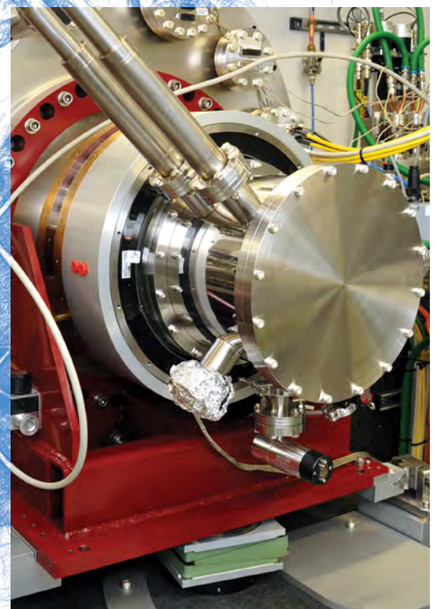

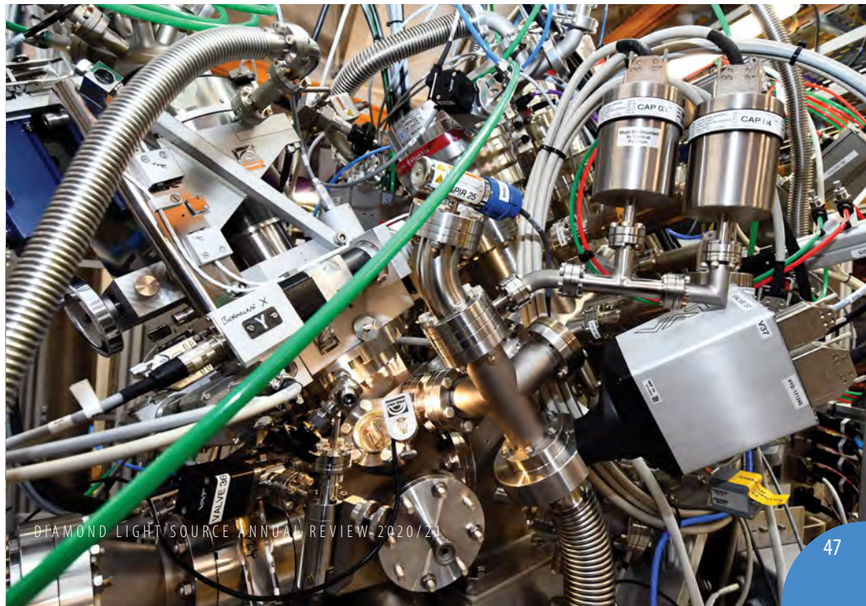

Visualising the handedness and topological charge of electrons in chiral crystals

Related publication: Schröter N. B. M., Stolz S., Manna K., De Juan F., Vergniory M. G., Krieger J. A., Pei D., Schmitt T., Dudin P., Kim T. K., Cacho C., Bradlyn B., Borrmann H., Schmidt M., Widmer R., Strocov V. N. & Felser C. Observation and control of maximal Chern numbers in a chiral topological semimetal. *Science (80-.).* **369**, 179–183 (2020). DOI: 10.1126/science.aaz3480

Publication keywords: Topology; Chern number; ARPES; Chirality; Fermi-arcs; Surface-state; Handedness; New fermions; Rarita-Schwinger; Weyl-fermion

Chirality refers to objects that - like our hands - do not coincide with their mirror image. Chirality can also manifest itself in crystals, for instance, where atoms wind around each other to form a helix. Recent research showed that chiral crystals can host 'exotic' topological phenomena in their electronic structure. However, we do not yet know how large they could become in real materials and whether the chirality of the crystal structure is related to the electrons surrounding the atoms.

An international team of researchers investigated two crystals of the chiral crystal palladium gallium (PdGa). They were mirror copies of each other, meaning that in one crystal the gallium atoms formed a right-handed helix and in the other a left-handed one. The team performed high-resolution spectroscopic measurements to resolve the fine details of the electronic structure in the crystals using Diamond Light Source's Angle-Resolved Photoemission Spectroscopy (ARPES) beamline, I05.

They observed that the chirality of the atomic structure imprints a handedness to the wavefunction of the electrons. Due to the very high-resolution and quality of the data, they resolved an energy splitting in the surface electronic structure. This splitting indicates that the topological charges in these materials can reach the maximum value allowed in any metallic crystal. That this is possible in a real material has never been shown before. These materials may lend themselves to useful applications, such as efficient photodetectors in the infrared- and terahertz-spectrum.

Topological semimetals have attracted much attention over the past five years because their electronic band structure can host quasiparticles that mimic the behaviour of elementary particles predicted in high-energy physics that have so far remained elusive as free particles, such as Weyl-fermions in topological Weyl-semimetals. These materials are called topological because the two-band crossing in their electronic band structure that forms the Weyl-fermion is protected by a topological invariant known as the "Chern-number" (C), which is closely related to the quantised Hall conductance that is observed in the quantum Hall effect, and which is also called the topological charge of the Weyl-fermion. Weyl-fermions have a Chern number with magnitude |C|=1 and can occur in non-centrosymmetric or magnetic crystals.

Recently it has been predicted that chiral crystals, which possess neither mirror- nor inversion-symmetries, could host new fermionic quasiparticles that can be considered as a generalisation of Weyl-fermions and have no equivalent as elementary particles[1]. It is expected that these quasiparticles could realise the largest possible topological charge in any metallic crystal with a maximal magnitude of 4. Finding materials with such a large Chern number is important because many of the exotic phenomena predicted for topological semimetals are directly proportional to |C|, such as the number of Fermi-arc surface states, the number of chiral Landau levels at large magnetic fields, or the strength of quantised photocurrents. Moreover, since the sign of the topological charge embodies the electronic wave function with a handedness, it would be interesting to see how the structural chirality of the atoms is linked to the chirality of the electronic structure.

Although there have been many recent photoemission studies that detected the presence of new fermionic excitations in chiral crystals[2,3,4], the magnitude of their topological charge, as well as the connection between the atomic and electronic chirality of these materials has not been investigated in detail until now. Previous efforts have been hindered by two factors: on the one hand, preparing clean and flat surfaces of the studied crystals has been difficult, which meant that spectroscopic signatures were washed out. On the other hand, at least some of the previously studied materials contained light atoms with weak spin-orbit coupling, which made it difficult to resolve small energy splitting of interest.

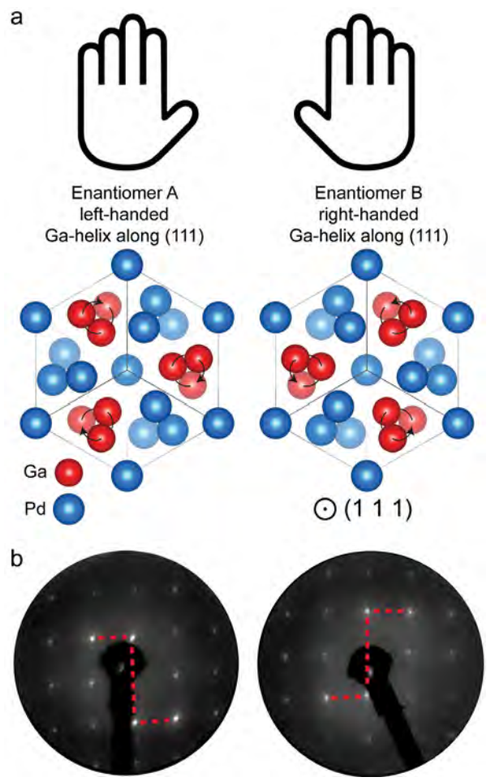

Figure 1: (a) Illustration of the crystal structure of the two enantiomers of PdGa. In enantiomer A, the Ga atoms (red spheres) form a left-handed helix along the (111) direction of the cubic unit cell, whilst the Pd atoms (blue sphere) form a right-handed helix. The direction of the helices is reversed in enantiomer B, for which the crystal structure forms a mirror copy of the structure in A; (b) Low-energy electron diffraction patterns for both enantiomers. The red dashed lines indicate the S-shaped intensity modulation, which is mirrored for the two enantiomers.

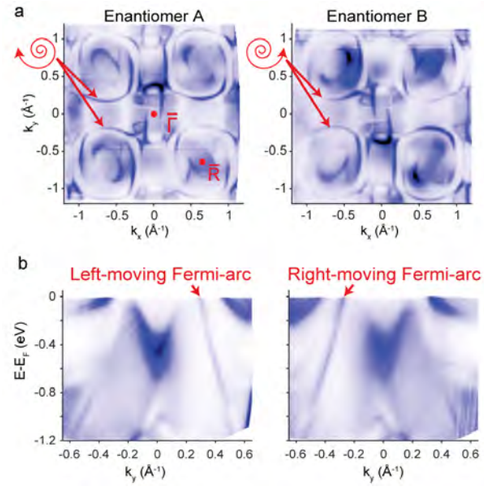

Figure 2: (a) Fermi surface of the two enantiomers of PdGa measured at beamline I05. The red arrows indicate the Fermi-arc surface states that are connecting the bulk pockets at the $\bar{\Gamma}$ and $\bar{R}$ points; (b) Band dispersions along a line cut at k_x=0.39 Å^{-1}. Red arrows indicate Fermi-arcs that have a reversed propagation direction for the two enantiomers.

In the present work, both of these limitations were overcome by working with crystals of palladium gallium (PdGa), an intermetallic catalyst with strong spin-orbit coupling for which established methods exist to produce clean and flat surfaces in ultra-high vacuum. Moreover, by using a chiral seed crystal during crystal growth, it is possible to grow two mirror copies (called enantiomers) of the same crystal structure; in one of them, the gallium atoms form a left-handed helix along the (111) direction, in the other one this helix is right-handed (Fig. 1a). Low-energy electron diffraction (LEED) patterns from clean surfaces of both crystals revealed the structural chirality of the surface atoms through the observation of a characteristic S-shaped intensity modulation of the diffraction pattern that is mirrored between the two enantiomers (Fig. 1b).

By performing high-resolution Angle-Resolved Photoelectron Spectroscopy (ARPES) at beamline I05, the surface electronic structure of the PdGa crystals was studied. These measurements revealed the presence of long Fermi-arc surface states that are connecting the and high symmetry points across the full diagonal of the surface Brillouin zone (Fig. 2a). Complimentary soft X-ray ARPES measurements at the Swiss Light Source of the Paul Scherrer Institute confirmed that new fermionic Rarita-Schwinger and Weyl-1 excitations are located at the corresponding Γ and R points of the bulk Brillouin zone, which are referred to as multifold fermions. Interestingly, the propagation direction of the Fermi-arcs is reversed between the two enantiomers (Fig. 2b), which implies that the handedness of the electronic structure (represented by the sign of the Chern numbers) is directly linked to the chirality of the host structure. Structural chirality can therefore be considered as a control parameter to manipulate the topological properties of these crystals, such as the direction of topological photocurrents.

Moreover, by making use of the high instrumental resolution of the ARPES endstation I05 at Diamond, a spin-orbit induced splitting of the Fermi-arcs was revealed (Fig. 3), which means that a total of four Fermi-arcs connecting the multifold fermions were observed. This finding implies that the topological charge of the multifold fermions realises the largest magnitude that can exist in any metallic material in nature. This is the first time that such a maximal Chern number has been observed experimentally, but it can be expected that similar topological properties are shared by many other chiral crystals. The hunt for more exotic topological phenomena in chiral compounds, such as the quantised circular photogalvanic effect[5], has therefore only just begun.

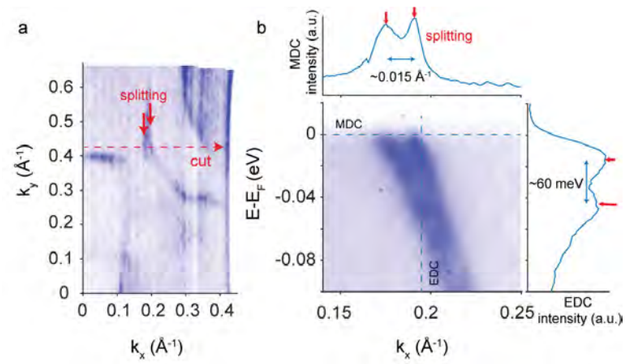

Figure 3: (a) Zoom-in of the Fermi-surface of enantiomer A. Red arrows indicate a splitting of the Fermi-arcs. Red dashed arrow indicates the direction of the line-cut shown in (b); (b) Band dispersion along the direction shown in (a). Blue dashed lines show the direction of the momentum distribution curve (MDC) and the energy distribution curve (EDC), shown in the inset on top and on the right, respectively. The red arrows indicate the position of the two bands, and the magnitude of the band splitting.

References:

1. Bradlyn B. *et al.* Beyond Dirac and Weyl fermions: Unconventional quasiparticles in conventional crystals. *Science (80-.).* **353**, aaf5037 (2016). DOI: 10.1126/science.aaf5037
2. Rao Z. *et al.* Observation of unconventional chiral fermions with long Fermi arcs in CoSi. *Nature* **567**, 496–499 (2019). DOI: 10.1038/s41586-019-1031-8
3. Takane D. *et al.* Observation of Chiral Fermions with a Large Topological Charge and Associated Fermi-Arc Surface States in CoSi. *Phys. Rev. Lett.* **122**, 76402 (2019). DOI: 10.1103/PhysRevLett.122.076402
4. Schröter N. B. M. *et al.* Chiral topological semimetal with multifold band crossings and long Fermi arcs. *Nat. Phys.* **15**, 759–765 (2019). DOI: 10.1038/s41567-019-0511-y
5. De Juan F. *et al.* Quantized circular photogalvanic effect in Weyl semimetals. *Nat. Commun.* **8**, 15995 (2017). DOI: 10.1038/ncomms15995

Funding acknowledgement:
N.B.M.S. was supported by Microsoft. K.M. and C.F. acknowledge financial support from the European Research Council (ERC) Advanced Grant nos. 291472 "Idea Heusler" and 742068 "TOP-MAT", and Deutsche Forschungsgemeinschaft (project ID 258499086 and FE 633/30-1). M.G.V. acknowledges support from DFG INCIEN2019-000356 from Gipuzkoako Foru Aldundia. S.S. and R.W. acknowledge funding from the Swiss National Science Foundation under SNSF project number 159690. D.P. acknowledges support from the Chinese Scholarship Council. J.A.K. acknowledges support from the Swiss National Science Foundation (SNF-grant no. 200021_165910).

Corresponding author:
Dr Niels B. M. Schröter, Swiss Light Source, Paul Scherrer Institute and Max Planck Institute for Microstructure Physics, niels.schroeter@mpi-halle.mpg.de

Gaining magnetic insights from a non-magnetic probe

Related publication: Sunko V., Mazzola F., Kitamura S., Khim S., Kushwaha P., Clark O. J., Watson M. D., Marković I., Biswas D., Pourovskii L., Kim T. K., Lee T. L., Thakur P. K., Rosner H., Georges A., Moessner R., Oka T., Mackenzie A. P. & King P. D. C. Probing spin correlations using angle-resolved photoemission in a coupled metallic/Mott insulator system. *Sci. Adv.* **6**, eaaz0611 (2020). DOI: 10.1126/sciadv.aaz0611

Publication keywords: PdCrO2; Delafossite; Spin correlations; Angle-resolved photoemission

An international group of researchers wanted to study the electronic properties of an unusual coupled system. It has one layer that supports very mobile carriers, and one that supports Mott insulating and magnetically-ordered states. They performed initial studies using angle-resolved photoemission spectroscopy (ARPES) on beamline I05 at Diamond Light Source, observing some unusual spectral signatures. Theoretical calculations suggested that correlations and interlayer interactions had an unusual role in their generation.

To understand the origin of these unusual spectral signatures, the team used Diamond's Surface and Interface Structural Analysis beamline (I09) to perform ARPES measurements in the soft X-ray regime. The combined nature of the study, with closely integrated work on I09 and I05, applying photoemission measurements in different regimes, was crucial to the success of this work. By combining theory with the results from I09 and I05, the team were able to show that an intertwining of the spin and charge response in the system dominates the photoemission response.

ARPES is usually a non-magnetic probe, but this work demonstrated that in certain circumstances it becomes sensitive to spin-correlations in solids. Scientists could use the same approach to study materials that are incompatible with other, more conventional probes of spin-spin correlation functions. This potentially opens up new systems to experimental study, and an improved understanding of their magnetic properties would be important for real-world applications such as 2D spintronics.

$PdCrO_2$ is a layered triangular lattice material, which can be thought of as an alternating stack of Pd and CrO_2 layers[1]. The electronic properties of the two layers are strikingly different: the Pd layer is highly metallic, while the CrO_2 layer is strongly correlated and magnetically-ordered. Coupling between them can be expected to yield exotic physics, which is the main focus of this work. The properties of the metallic Pd layer are best understood by referring to the non-magnetic sister compound $PdCoO_2$, which has been extensively studied due to its remarkably high conductivity. Its electronic structure features a single broad conduction band derived from Pd states, forming a two-dimensional hexagonal Fermi surface (Fig. 1a,b). The CoO_2 layers in $PdCoO_2$ are rather benign. In contrast, the Cr ions in $PdCrO_2$ carry a localised spin of $S = 3/2$ and order into a 120° antiferromagnetic structure at 37.5 K[2]. The low-energy electronic structure is still dominated by the Pd-derived states: consistent with previous findings[3,4], our high resolution ARPES measurements taken at I05 reveal a "main band" very similar to the conduction band in $PdCoO_2$. But additional weak spectral weight appears in $PdCrO_2$ as copies of the main band, offset by the antiferromagnetic ordering vector (Fig. 1c,d).

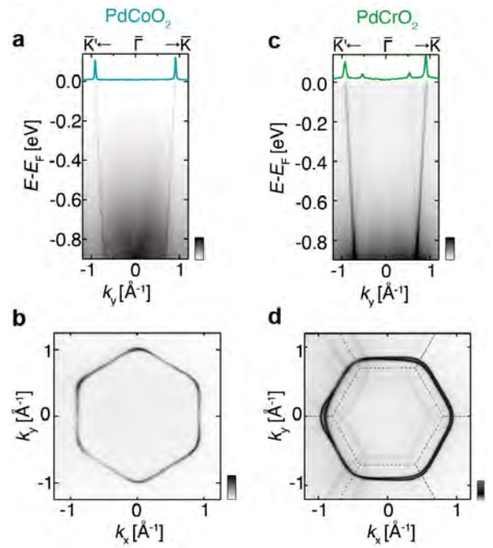

Figure 1: Low-energy electronic structure of Pd-based delafossites measured using ARPES at I05. (a) Dispersion and (b) Fermi surface of $PdCoO_2$; (c) dispersion and (d) Fermi surface of $PdCrO_2$. Note the additional weak spectral weight in (c,d) which appears as a copy of the main underlying band, similar to in $PdCoO_2$, but shifted by the antiferromagnetic wavevector of the CrO_2 layer.

The observation of localised 3/2 spins on the Cr sites suggests that the CrO_2 layer is Mott insulating. This hypothesis has been supported by dynamical mean-field theory calculations, which predicted that the Cr-derived states form a lower Hubbard band 1 to 2 eV below the Fermi level (E_F). To experimentally verify this picture, we have used soft X-ray ARPES at I09 to investigate the atomically resolved electronic structure, tuning the probing photon energy into resonance with the Cr $L_{2,3}$ absorption edge. Comparing on- to off-resonant spectra reveals a marked enhancement of spectral weight of a very weakly dispersing and broad feature centred at approximately 2 eV below E_F (Fig. 2a-c). The integrated weight of this feature follows the absorption spectrum (Fig. 2d), thus establishing its Cr-derived origin and providing strong evidence that this is the spectroscopic signal of a lower Hubbard band of a Mott insulating state. $PdCrO_2$ can therefore be considered as an unusual combination of an atomic layer-by-layer superlattice of a nearly free electron metal and a Mott insulator.

Given the antiferromagnetic order of the latter, the observation of replicas of the metallic main band shown in Fig. 1c-d might seem unremarkable: when electrons feel an additional periodic potential the band structure is reconstructed. This standard picture, however, cannot explain the experimental observations of $PdCrO_2$. The spectral weight of the replicas observable by ARPES should fall off rapidly away from the new zone boundaries. Experimentally, however, the replicas are clearly observed all the way from the magnetic zone boundary to the E_F (Fig. 1c); over the same energy range, the simple "band folding" model predicts a 100-fold decrease in spectral weight (Fig. 3a, dashed line). In contrast, the measured intensity of the reconstructed weight (IRW) changes by less than a factor of 2 (Fig. 3a, symbols).

We have discovered that the answer to the above puzzle lies in Mott insulator–free electron coupling. Rather than treating the CrO_2 layer as a passive source of a periodic potential, it is necessary to take into account its dynamical degrees of freedom. Once this is done formally, it becomes apparent that $PdCrO_2$ can be described by the well-known Kondo Hamiltonian[5], but with the Kondo coupling being an interlayer effect. The key insights it provides come from using it to calculate the photoemission spectral functions. While photoemission from the Pd layer is not significantly altered by this coupling, an entirely new route for photoemission from the Cr layer becomes available. For finite interlayer coupling,

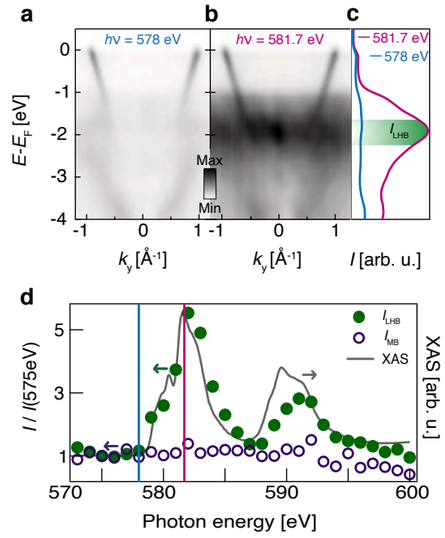

Figure 2: Resonant photoemission of $PdCrO_2$ using soft X-ray ARPES at I09. Valence band spectra measured using photon energies (a) Just below and (b) On-resonance with the Cr L_3 absorption edge; (c) Comparison of the integrated spectra; (d) The spectral weight of the non-dispersive states at ~2 eV binding energy tracks the X-ray absorption across the Cr $L_{2,3}$ edge, indicating their Cr-derived character. In contrast, the steep band shows no spectral weight enhancement across this absorption edge, pointing to its dominant Pd-derived character.

a hole created in the Mott layer can rapidly move to the itinerant layer where it can propagate. This results in the spectral function for the removal of electrons from the Mott layer becoming a convolution of the itinerant electron spectrum with the spin correlation function of the Mott layer. In this way, the spin response of the Mott layer and the charge response of the itinerant layer become intertwined. In the case of antiferromagnetically ordered $PdCrO_2$, the resulting prediction is that Cr spectral weight follows the dispersion of the nearly free electron Pd band, but translated by the wave vector of the AF order, with no significant binding energy dependence of its intensity (Fig. 3a, full line). The intertwined spin-charge model therefore agrees with the experiment, but it is also making a remarkable and falsifiable prediction: the backfolded spectral weight, despite appearing as a sharp band-like feature, is actually a property of the Cr removal spectral function rather than the Pd one.

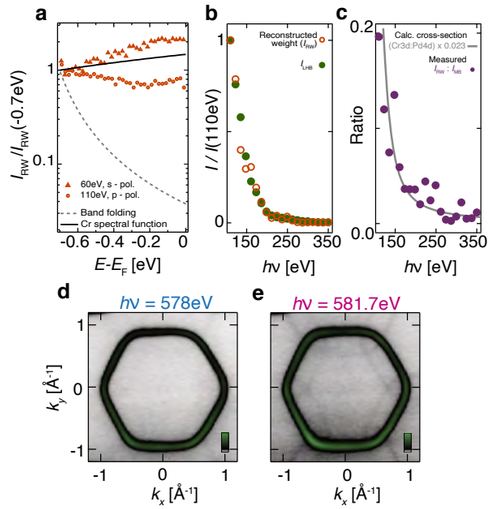

Figure 3: Cr-character of the reconstructed weight. (a) Analysis of the apparent main-band replica shows its spectral weight is nearly constant vs. binding energy, inconsistent with typical pictures for band folding, but consistent with our theoretical model for an intertwined spin-charge response arising due to coupling between the layered sub-systems. Consistent with this picture, our measurements indicate this feature has dominant Cr character; (b) Its spectral weight follows that of the Hubbard band; (c) The cross-section variation with photon energy matches that of a Cr-derived state; (d) It is clearly visible only on-resonance, and barely resolved in Fermi surfaces measured off-resonance.

The key diagnostic for the validity of the intertwined spin-charge model is, therefore, to establish the underlying atomic origin of the reconstructed spectral weight. To do this, we again employed soft X-ray ARPES at I09. Quantitative analysis of measurements over a broad photon energy range shows (i) that the photon energy dependence of the IRW closely traces that of the Cr-derived lower Hubbard band (Fig. 3b) and (ii) that its ratio to the Pd-derived main band intensity tracks the Cr 3d:Pd 4d ionic cross-section ratio (Fig. 3c). These observations all point to a dominant Cr character of the backfolded spectral weight. To provide an independent confirmation, we again made use of resonant measurements, finding that the reconstructed weight is markedly enhanced when the photon energy is tuned to the Cr L_3-edge resonance (Fig. 3d-e), thus proving its Cr-derived nature.

Although the initial motivation for this work was understanding the physics of the spectroscopic signatures in $PdCrO_2$, its implications are much broader. First of all, it establishes $PdCrO_2$ as a benchmark system to study the properties of the Kondo Hamiltonian with experimentally-constrained parameters. Furthermore, it opens a new route to investigate static and dynamical spin susceptibilities using ARPES, including systems that are not accessible to more traditional magnetic probes. The ability to identify the orbital content of the various features of the electronic structure, made possible by the soft X-ray ARPES experiments at I09, was critical to this discovery.

References:

1. Shannon R. D. *et al.* Chemistry of Noble Metal Oxides. I. Syntheses and Properties of ABO2 Delafossite Compounds. *Inorg. Chem.* **10**, 713–718 (1971). DOI: 10.1021/ic50098a011
2. Takatsu H. *et al.* Magnetic structure of the conductive triangular-lattice antiferromagnet PdCrO 2. *Phys. Rev. B - Condens. Matter Mater. Phys.* **89**, 104408 (2014). DOI: 10.1103/PhysRevB.89.104408
3. Sobota J. A. *et al.* Electronic structure of the metallic antiferromagnet PdCrO2 measured by angle-resolved photoemission spectroscopy. *Phys. Rev. B - Condens. Matter Mater. Phys.* **88**, 125109 (2013). DOI: 10.1103/PhysRevB.88.125109
4. Noh H. J. *et al.* Direct Observation of Localized Spin Antiferromagnetic Transition in PdCrO2 by Angle-Resolved Photoemission Spectroscopy. *Sci. Rep.* **4**, 3680 (2014). DOI: 10.1038/srep03680
5. Löhneysen H. V. *et al.* Fermi-liquid instabilities at magnetic quantum phase transitions. *Rev. Mod. Phys.* **79**, 1015–1075 (2007). DOI: 10.1103/RevModPhys.79.1015

Funding acknowledgement:
We acknowledge support from the European Research Council (grant nos. ERC-714193-QUESTDO and ERC-319286-QMAC), the Royal Society, the Leverhulme Trust (grant nos. RL-2016-006 and PLP-2015-144R), the Max-Planck Society, the Simons Foundation, and the International Max-Planck Partnership for Measurement and Observation at the Quantum Limit. V.S. and O.J.C. acknowledge EPSRC for PhD studentship support through grant numbers EP/L015110/1 and EP/K503162/1. I.M. acknowledges PhD studentship support from the IMPRS for the Chemistry and Physics of Quantum Materials. We thank Diamond Light Source for access to beamlines I09 (proposal no. SI19479) and I05 (proposal no. SI17699). The work at the Max Planck Institute for the Physics of Complex Systems was supported in part by the Deutsche Forschungsgemeinschaft under grants SFB 1143 (project-id 247310070) and the cluster of excellence ct.qmat (EXC 2147, project-id39085490).

Corresponding authors:
Dr Veronika Sunko, Max Planck Institute for Chemical Physics of Solids, sunko@cpfs.mpg.de; Prof. Phil King, School of Physics and Astronomy, University of St Andrews, philip.king@st-andrews.ac.uk

Exploring the use of metal-organic frameworks as catalysts for solar fuel production

Related publication: García-Sánchez A., Gomez-Mendoza M., Barawi M., Villar-Garcia I. J., Liras M., Gándara F. & De La Peña O'Shea V. A. Fundamental Insights into Photoelectrocatalytic Hydrogen Production with a Hole-Transport Bismuth Metal-Organic Framework. *J. Am. Chem. Soc.* **142**, 318–326 (2020). DOI: 10.1021/jacs.9b10261

Publication keywords: Solar Fuels; Artificial photosynthesis; Metal organic frameworks; Charge dynamics; *In situ* characterisation

Solar fuels are made from common substances, such as water and carbon dioxide, using solar energy. Producing fuels using artificial photosynthesis is one of the most crucial challenges in sustainable energy. Photocatalytic materials can be used in photo-electrochemical cells to perform water splitting or carbon dioxide reduction for fuels and chemicals. For example, hydrogen production is a key process in the transition towards sustainable energy generation technologies. However, the current generation of photo(electro) catalysts suffer from several limitations related to charge carrier recombination phenomena and inefficient light harvesting. To overcome these problems we need to develop more sustainable and efficient materials. We also need to understand the charge transfer dynamics and identify which species are involved in the process at different timescales.

Researchers from the Instituto de Ciencia de Materiales and the IMDEA Energy Institute in Madrid investigated the potential for metal-organic frameworks (MOFs) to act as photo(electro)catalysts. They used Diamond Light Source's Versatile Soft X-ray (VerSoX) beamline (B07), which can perform core-hole clock experiments at the sulphur K edge that provide information on the charge dynamics processes between linkers and metals. These experiments were critical to determining the delocalisation rates of charges in the initial steps of the process. The results demonstrated the organic linker's key role during the photo(electro)catalytic process with the MOF catalyst. They helped identify intermediate species generated during the reaction and improve our understanding of the charge dynamic process.

In the current situation of climate change it is necessary to find sustainable energy by developing processes that exploit renewable resources. In this field solar fuels production is one of the most promising areas aiming to mimic the natural photosynthesis[1]. The evolution of these technologies strongly relies on finding novel materials able to act as photoelectrodes in solar devices.

In general, a photoelectrode is a material that, upon light absorption, leads to a charge generation process that results in the formation of an electron-hole (e^--h^+) pair. Although metal oxides are the most common materials used, they present several limitations such as high recombination rates and limited absorption. In order to overcome these limitations different strategies are being studied.

Metal-organic frameworks (MOFs) are porous, crystalline structures formed by metal ions and clusters, which are joined through organic linkers. These materials are emerging in the field of photocatalytic hydrogen production because of their tailorable capacity of light absorption by the judicious selection of their components. However, few examples have been reported employing bare MOFs as photo-electrodes, likely owing to their limited stability under the reaction conditions. In most of the reported examples, H_2 production is not directly measured, only density current is given. Most importantly, the role of photogenerated charges when using MOFs in the photocatalytic reaction mechanism remains unknown mainly due to the different time scales in which the electronic processes occur[2].

In this pioneering work, we have performed the synthesis and characterisation of a new bismuth MOF, denoted IEF-5 (Imdea Energy Framework-5, Fig. 1a). IEF-5 was synthesised by the solvothermal reaction between dithieno[3,2-b:2′,3′-d] thiophene-2,6-dicarboxylic acid[3] (H_2DTTDC) and $Bi(NO_3)_3{\cdot}5H_2O$. H_2DTTDC was selected as organic linkers due to its structure based on three fused thiophene rings, which is expected to be beneficial for the charge separation process. Thus, once the new IEF-5 was prepared and structurally characterised (Fig. 1 b,c), we determined their electronic properties in the fundamental and excited state by DFT calculations (Fig.1 d, e) and we investigated its use as photoelectrode for H_2 evolution reaction from water using 0.5M Na_2SO_3 as sacrificial agent. The result, applying 0.35V vs Ag/AgCl using a solar simulator light source, was a hydrogen production of 2.35 µmol·cm^{-2} or in 1 hour of illumination (Fig. 1f).

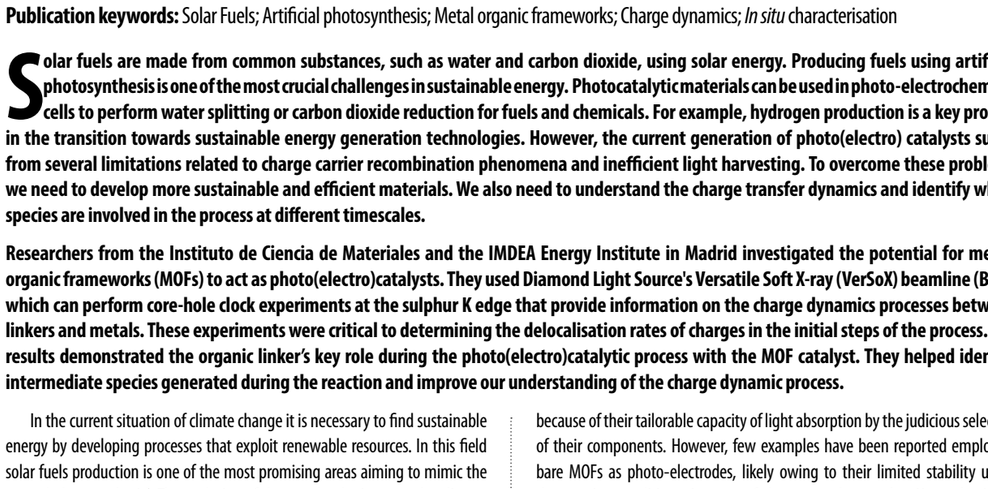

*Figure 1: (a) Structure of IEF-5 with simulated DMA cations within the framework; (b) Experimental band diagram obtained with the water splitting redox couples at pH=0; (c) Scheme of MOF electrodes deposited onto ITO and AFM topography image; (d) ELF isosurfaces and sections of IEF-5, Bi (magenta), C (brown), H (white) S (yellow), O (red); (e) **A**tom-projected partial density of states (PDOS) for Bi2s (magenta), Bi2p (blue), C2p (grey), S (yellow), O (red); (f) Photoelectrochemical H_2 production accumulated in 60 min under AM1.5 irradiation at 0.35 V.*

To unravel the effects of photoinduced charge dynamics in the photo(electro)catalytic H_2 production, we have performed a complete study combining the DFT simulations (Fig. 1 d,e) with time resolved spectroscopic measurements at different time scales, from fs to ms.

To this end, the measurements on B07 were critical to finally understand the charge dynamics of the overall process, which provides a unique insight for the development of materials for light-induced processes. The core-hole clock (CHC) synchrotron experiments were critical to determine charge delocalisation rates in the attosecond scale for the first steps of charge separation in the IEF-5. These kinds of measurements can only be undertaken on delocalised systems containing sulphur atoms[4] by recording the S KLL Auger spectra at different excitation energies around the sulphur K-edge. In Fig. 2a it can be seen that the resonant signal increases in kinetic energy with the excitation energy while the non-resonant signal does not change, as expected. Electron delocalisation times are obtained from the S KLL Auger spectra using the lifetime of the S 1s hole (1.27 fs)[5] and the ratio of the area between non-resonant and resonant signals. The delocalisation times depend on the conduction band orbital to which the electrons are promoted, varying from 0.2 to 18 fs (Fig. 2b). These data are in the range of the times reported for a series of thiophene containing polymers[5]. It can be seen how electron delocalisation times decrease as the excitation energy increases, meaning that electrons promoted to more energetic conduction band orbitals (such as σ*) exhibit faster delocalisation than when they are promoted to lower-lying energy states such as π*.

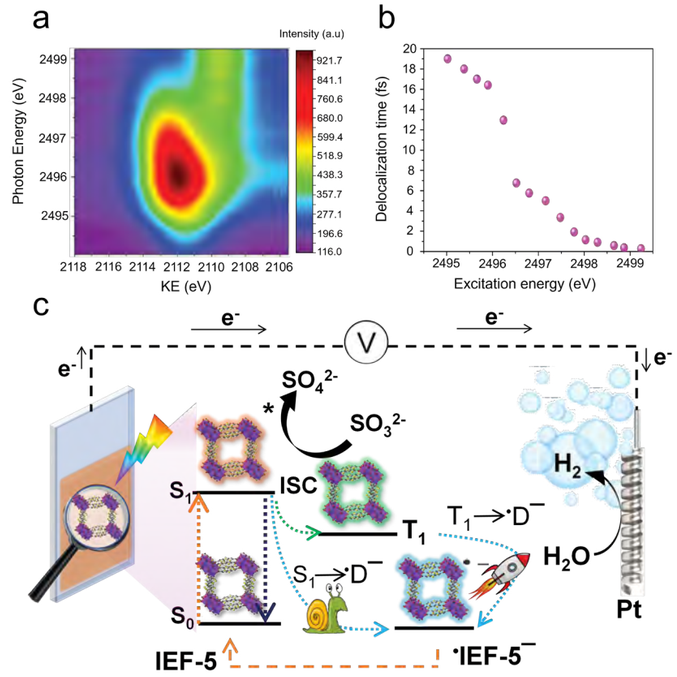

Figure 2: (a) 2D core hole clock measurements of IEF-5; (b) Electron delocalisation times at the different excitation energies where the resonant peak is observed; (c) Scheme of photo(electro)catalytic H_2 production mechanism, where IEF-5 is excited after light exposition. The excited state form of the MOF interacts with sulphite anions, the triplet state being faster than the singlet one, to form an anion radical specie, which transfer electrons to the Pt cathode where hydrogen evolves.

All these data combined with the information obtained (DFT calculations, solid state photoluminescent and transient absorption spectroscopy) and in addition to the general characterisation, allowed us to finally determine the mechanism involved in the charge dynamic process during the photo-electrocatalytic hydrogen production reaction with IEF-5 (Fig. 2c).

Under illumination, IEF-5 undergoes charge separation leading to a singlet excited state (^{1}IEF-5*) which by intersystem crossing (IC) transforms into a triplet excited state (^{3}IEF-5*). At this time, the hole scavenger used in the reaction SO_3^{2-} interacts with the holes generated, pumping charge into IEF-5, with the subsequent formation of a radical anion intermediate (IEF-5^·-). This oxidation reaction can take place in ^{1}IEF-5* as well as ^{3}IEF-5*, being faster in the second one. Finally, the photogenerated electron is transferred from IEF-5 to the cathode, Pt, where the H_2 evolution takes place closing the redox cycle.

References:

1. De La Peña O'Shea V. A. *et al.* Current challenges of CO2 photocatalytic reduction over semiconductors using sunlight. in *From Molecules to Materials: Pathways to Artificial Photosynthesis* (eds. Rozhkova E. A. et al.) 171–191 (Springer International Publishing, 2015). DOI: 10.1007/978-3-319-13800-8_7

2. Fresno F. *et al.* Mechanistic View of the Main Current Issues in Photocatalytic CO 2 Reduction. *J. Phys. Chem. Lett.* **9**, 7192–7204 (2018). DOI: 10.1021/acs.jpclett.8b02336

3. Strakova K. *et al.* Dithienothiophenes at Work: Access to Mechanosensitive Fluorescent Probes, Chalcogen-Bonding Catalysis, and beyond. *Chem. Rev.* **119**, 10977–11005 (2019). DOI: 10.1021/acs.chemrev.9b00279

4. Arantes C. *et al.* Femtosecond electron delocalization in poly(thiophene) probed by resonant Auger spectroscopy. *J. Phys. Chem. C* **117**, 8208–8213 (2013). DOI: 10.1021/jp312660d

5. Garcia-Basabe Y. *et al.* The interplay of electronic structure, molecular orientation and charge transport in organic semiconductors: Poly(thiophene) and poly(bithiophene). *Org. Electron.* **14**, 2980–2986 (2013). DOI: 10.1016/j.orgel.2013.08.022

Funding acknowledgement:
This work was supported by the EU (ERC CoG HyMAP 648319) and Spanish MINECO (ENE2016-79608-C2-1-R, CTQ2017-87262-R) and also wish to thank to Comunidad de Madrid and European Structural Funds for their financial support to FotoArt-CM project (S2018/NMT-4367). F.G., M.L and M.B thank the MINECO and European Social Fund for a Ramón y Cajal contract (RyC-2015-18384, RyC-2015-18677) and Juan de la Cierva Formación contract (FJCI-2016-30567), respectively. We thank Diamond for the access to beamline B07 and CESCA for computational resources.

Corresponding authors:
Dr Felipe Gándara, Instituto de Ciencia de Materiales de Madrid, CSIC, gandara@icmm.csic.es; Dr Victor A. de la Peña O'Shea, Photoactivated Processes Unit, IMDEA Energy Institute, Móstoles, Madrid, victor.delapenya@imdea.org

X-rays unravel molecular packing and help create high-efficiency solar cells

Related publication: Li W., Xiao Z., Smith J. A., Cai J., Li D., Kilbride R. C., Spooner E. L. K., Game O. S., Meng X., Liu D., Jones R. A. L., Lidzey D. G., Ding L. & Wang T. Enhancing the efficiency of PTB7-Th:CO i 8DFIC-based ternary solar cells with versatile third components. *Appl. Phys. Rev.* **6**, 41405 (2019). DOI: 10.1063/1.5125438

Publication keywords: Organic solar cells; Ternary active layer; Non-fullerene acceptor; Morphology

Organic solar cells can generate low-cost renewable energy. These cells usually use a blend of carbon-based materials that can absorb light and create an electrical current. However, not all combinations work efficiently. The way that the molecules order themselves is fundamentally important in determining device efficiency. Researchers at Wuhan University of Technology, the National Center for Nanoscience and Technology in Beijing and the University of Sheffield explored what occurs in blends at the scale of a single molecule to determine device efficiency. They were interested in understanding the structure of a new type of solar cell, based on a blend of three different organic semiconductors. Although adding a third component can improve a solar cell's ability to absorb light, it does not always enhance device efficiency.

The I07 beamline at Diamond Light Source offers high-resolution X-ray investigations of the structure of surfaces and interfaces. The research team carried out X-ray scattering experiments on I07, combined with other techniques, to determine why adding a third component can positively or negatively affect organic solar cell efficiency.

Their measurements provided critical information on how adding a third component changes the molecular ordering of the blend. They were then able to correlate the thin film morphology with the electronic properties of the solar cell. Their results also allow predictions of whether a third component is likely to enhance device efficiency. Their work will help develop high-efficiency solar cells and is another step towards commercialisation of this technology.

Organic solar cells (OSCs) usually generate electricity using a photoactive layer consisting of a mixture of two different types of organic semiconductor – so-called electron-donors and electron-acceptors. Here, both donor and acceptor components can absorb photons which, following charge transfer from the donor to the acceptor, produce the holes and electrons that constitute an electrical current. The synthesis of new organic semiconductors, e.g. non-fullerene electron acceptors, has recently resulted in a significant improvement of OSC efficiency. However, recent work has shown that additional efficiency enhancements can be realised by mixing three organic semiconductors together creating a 'ternary blend'. Here, by selecting a third component that has a complementary absorption to the binary system, it is possible to enhance the absorption of optical absorption by an OSC device and potentially enhance overall device efficiency. However, the selection of third component materials can be challenging, as such materials can easily change the molecular packing of the binary host system which in turn reduces the efficiency by which photo-generated charges can be generated or extracted from the device[1,2]. This issue has prompted us to make a detailed investigation into the molecular-scale interactions between the third component and the binary-host materials, with our aim being to explore molecular packing and ordering in ternary OSCs and its effects on device efficiency.

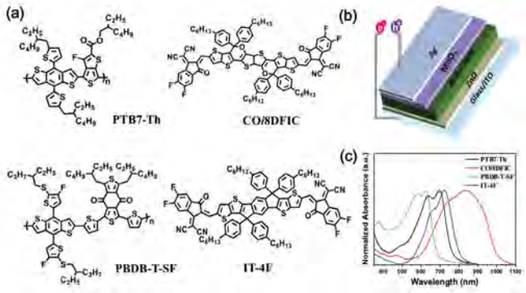

Figure 1: (a) Chemical structure of PBT7-Th, COi8DFIC, PBDB-T-SF and IT-4F; (b) A schematic structure of the organic solar cells explored; (c) Absorbance of PBT7-Th, COi8DFIC, PBDB-T-SF and IT-4F.

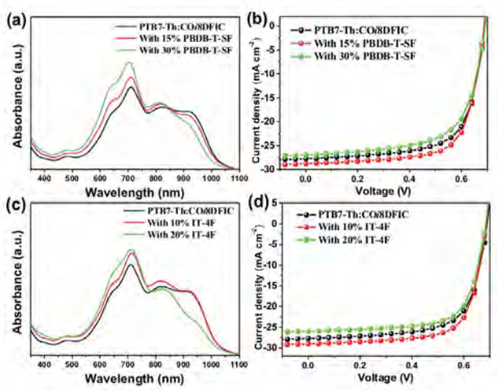

Figure 2: Absorption spectra and J-V curves of PTB7-Th:COi8DFIC based ternary solar cells containing different concentrations of PBDB-T-SF and IT-4F.

Our work builds on our recent study published in Applied Physics Reviews in which we presented a practical guide to select materials to fabricate high efficiency non-fullerene based ternary organic solar cells. Here, we started from the binary PTB7-Th:COi8DFIC polymer:non-fullerene blend which can be used as the photoactive layer in an OSC, with devices having a maximum power conversion efficiency of around 13%. This efficiency is however highly dependent on the molecular packing of the electron acceptor material COi8DFIC. Here we found that when this molecule is cast onto a surface from solution, it can either undergo lamellar-crystallisation or form H- or J-type aggregates. Here, J-type aggregation was shown to result in light-harvesting at near-infrared wavelengths and is beneficial in enhancing device efficiency[3]. In this work, an electron-donating polymer called PBDB-T-SF and a small molecular acceptor IT-4F were separately mixed with the host PTB7-Th:COi8DFIC system, with such 3rd component materials having a different absorption spectrum compared to the host system (Fig. 1). Our objective was to explore the extent to which the 3rd component material allowed OSC efficiency to be enhanced.

In our experiments we found that by incorporating either 15% of PBDB-T-SF or 10% of IT-4F in the host system, it was possible to enhance the overall optical absorption of the blend over the wavelength range 350 to 1,000 nm due to the complementary light absorbance of the 3rd component. Such films were fabricated into the active layer of an OSC and it was found that devices had an improved short-circuit current (indicative of enhanced optical absorption) and enhanced power conversion efficiency. However, when the concentration of PBDB-T-SF and IT-4F was increased to 30% and 20% respectively, a significant decrease in absorption was observed over the wavelength range of 900 to 1,100 nm. Such absorption is associated with the J-type π-π stacking characteristic of COi8DFIC; a result that indicates that molecular aggregation of the host acceptor component COi8DFIC is modified by excessive quantities of either PBDB-T-SF or IT-4F. It was found that such reduced absorption lead to a reduced OSC performance in the ternary OSCs composed of 30% PBDB-T-SF and 20% IT-4F (Fig. 2).

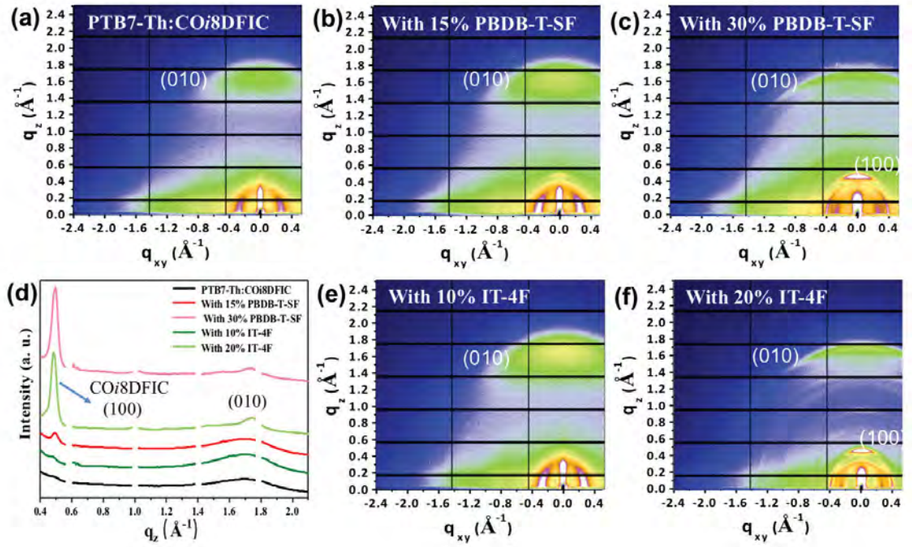

Figure 3: 2D GIWAXS patterns and 1D profiles along q_z axis for PTB7-Th:COi8DFIC films containing different amounts of PBDB-T-SF or IT-4F.

To gain a deeper insight into the role of PBDB-T-SF and IT-4F third components in directing the molecular ordering of the PTB7-Th:COi8DFIC host blend, we performed grazing-incidence wide-angle X-ray scattering (GIWAXS) measurements at the Wide-Angle Scattering & Diffraction beamline (I07) at Diamond (Fig. 3). Here, PTB7-Th:COi8DFIC binary films were found to exhibit a distinct diffraction signal at $q_{xy} = 0.28$ Å^{-1} in the in-plane direction and a dispersion ring located at $q_z = 1.7$ Å^{-1} in the out-of-plane direction, with the former attributed to the alkyl chain stacking of PTB7-Th whilst the latter ascribed to the overlap of π-π stacked PTB7-Th and COi8DFIC[4]. When 15% of PBDB-T-SF or 10% of IT-4F were introduced into the host blend, the molecular packing of both PTB7-Th and COi8DFIC were found to be unchanged with both enhanced alkyl chain stacking and π-π stacking observed; a characteristic that may well facilitate charge transport in the device[5]. In contrast, when the concentration of PBDB-T-SF and IT-4F were increased to 30% and 20% respectively, the PTB7-Th alkyl chain stacking was found to reduce significantly whilst a new intense diffraction peak at $q_z = 0.5$ Å^{-1} appeared, with this feature being associated with the edge-on lamellar crystal of COi8DFIC. This significantly increased lamellar order of COi8DFIC results from enlarged phase separation caused by the presence of an excessive amount of third component. The suppression of J-aggregation at higher loadings of PBDB-T-SF and IT-4F is thought to be responsible for the reduced light absorption at longer wavelengths (Fig. 2a,c).

Our results suggest therefore that the relative extent of J-aggregation and lamellar crystallisation of COi8DFIC can be strongly modified by the incorporation of a third component; a process that strongly affects the efficiency of solar cell devices incorporating such materials. By controlling such processes, we were able to increase device efficiency by around 10% compared to devices based on a simple binary blend, with further improvements expected using new generations of materials.

References:

1. Li W. *et al.* Contrasting Effects of Energy Transfer in Determining Efficiency Improvements in Ternary Polymer Solar Cells. *Adv. Funct. Mater.* **28**, 1704212 (2018). DOI: 10.1002/adfm.201704212
2. Li W. *et al.* Achieving over 11% power conversion efficiency in PffBT4T-2OD-based ternary polymer solar cells with enhanced open-circuit-voltage and suppressed charge recombination. *Nano Energy* **44**, 155–163 (2018). DOI: 10.1016/j.nanoen.2017.12.005
3. Li W. *et al.* Molecular Order Control of Non-fullerene Acceptors for High-Efficiency Polymer Solar Cells. *Joule* **3**, 819–833 (2019). DOI: 10.1016/j.joule.2018.11.023
4. Li W. *et al.* Correlating the electron-donating core structure with morphology and performance of carbon–oxygen-bridged ladder-type non-fullerene acceptor based organic solar cells. *Nano Energy* **61**, 318–326 (2019). DOI: 10.1016/j.nanoen.2019.04.053
5. Li D. *et al.* Aggregation of non-fullerene acceptors in organic solar cells. *J. Mater. Chem. A* **8**, 15607–15619 (2020). DOI: 10.1039/d0ta03703f

Funding acknowledgement:
This work was supported by the National Natural Science Foundation of China (Grants No. 21774097) and the Natural Science Foundation of Hubei Province (Grant No. 2018CFA055). We also thank the UK STFC for part-funding this work via grant ST/R002754/1 "Synchrotron Techniques for African Research and Technology", and EPSRC for funding studentships via the New and Sustainable Photovoltaics CDT (EP/L01551X/1). GIWAXS measurements were performed on I07 at Diamond Light Source (UK) on beamtime project reference S120419.

Corresponding authors:
Prof. Tao Wang, Wuhan University of Technology, twang@whut.edu.cn;
Prof. David G. Lidzey, University of Sheffield, d.g.lidzey@sheffield.ac.uk

Magnetic Materials Group

Sarnjeet Dhesi, Science Group Leader

The Magnetic Materials Group (MMG) at Diamond Light Source uses and develops a range of polarised X-ray probes including Resonant Elastic X-ray scattering (REXS), PhotoEmission Electron Microscopy (PEEM), X-ray Absorption Spectroscopy (XAS) and Resonant Inelastic X-ray Scattering (RIXS). Over the last year, our research community has gained fundamental insights into the electronic and magnetic degrees of freedom underpinning the physical properties of a host of materials using these probes. In this contribution, we present research demonstrating how PEEM can unveil the complex antiferromagnetic domain structure in CuMnAs thin films following intense pulsed electrical switching. We also present results reporting how soft X-ray scattering combined with soft X-ray imaging can reveal the tubular structure of magnetic Skyrmions in FeGe thin films. The power of REXS combined with neutron scattering has been deployed to understand the driving force behind helical magnetic ordering in parity and time odd systems such as the Fe-based langasites. Finally, the versatility of high-resolution RIXS is showcased in a remarkable study of lithium-ion (Li-ion) battery cathodes, demonstrating how metal migration and molecular oxygen formation degrade the charge-discharge cycle. The results demonstrate how polarised X-rays can uncover a wealth of electronic and magnetic detail to aid the development of advanced materials in applications ranging from low-power consumption electronics to next-generation energy materials.

On the Nanoscience beamline (I06), PEEM combined with X-ray Magnetic Linear Dichroism (XMLD) has been developed into a versatile and powerful probe of antiferromagnetic ordering in thin films and single crystals. The electrical switching of an antiferromagnet, via a spin-orbit torque, can be detected using anisotropic magnetoresistance and was first directly observed in CuMnAs using XMLD-PEEM imaging on I06. A new development is the extremely large changes in resistance in CuMnAs after intense current pulsing or irradiation using focused picosecond laser light that has been reported recently. Using XMLD-PEEM on I06, the origin of the large change in resistance has been linked to a very high degree of domain fragmentation leading to a very high density of domain walls.

On I10, the Beamline for Advanced Dichroism Experiments (BLADE), REXS has been used to explore the phase diagram of the Skyrmion structures formed in FeGe thin films. The tubular structure of Skyrmions has been studied using X-ray Magnetic Circular Dichroism (XMCD) depth-profiling on I10 previously, but in a new twist, researchers have applied a field in the plane of the film and created horizontal Skyrmions in the plane of the film that could be imaged using X-ray Scanning Transmission Microscopy (STXM). This opens an exciting route to directly image the destruction and formation of Skyrmions using polarised soft X-ray imaging and holography.

On the Materials and Magnetism beamline (I16), REXS and non-resonant magnetic scattering have been used to explore the relationship between the chiral crystal structure in an iron-based langasite and the helical magnetic ordering of the frustrated triangular antiferromagnetic lattice. By conducting a detailed analysis of the REXS scattering as a function of photon energy, the crystal handedness could be determined. On the other hand, an analysis of the X-ray scattering intensity of the magnetic reflections with analyser angle, for left and right polarised light, revealed that the magnetic chirality follows the crystal chirality. The results were independently confirmed on separate samples using neutron scattering. The results pave the way to explore electric field control of chiral magnetic domains by combining the newly developed X-ray probe of magnetic chirality with high spatial resolution.

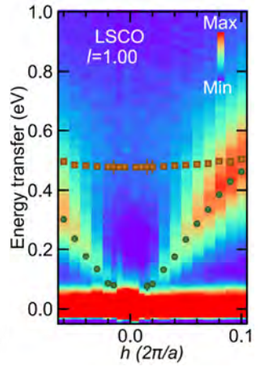

*Figure 1: RIXS dispersion map along h, for l=1.0. The orange squares show a non-dispersive bimagnon and the green circles show the dispersion of the acoustic plasmon. Taken from A. Nag et al. Phys. Rev. Lett. **125**, 257002 (2020).*

On the RIXS beamline (I21), the high-energy resolution of the spectrometer has been used to understand the charging and discharging cycle in Li-ion battery cathodes. The high-energy resolution was key to measuring the small energy spacing changes between sharp inelastic peaks, which indicate the formation of molecular oxygen during the redox reaction. The results were combined with nuclear magnetic resonance data to show that the molecular oxygen is physically trapped in the lattice rather than chemically bonded in any nanovoids. The cycling of molecular oxygen in the lattice then leads to irreversible structural changes in the cathode materials, which reduces the practical energy density for storage. Significant gains can be made for energy storage materials if the formation and trapping of molecular oxygen can be supressed. RIXS has also been used to study charge ordering in p- and n-type cuprates in considerable detail, but the study of collective excitations or plasmons is less well established. In this respect, acoustic plasmons have been observed in n-type cuprates, but their observation in p-type cuprates has remained elusive. The high-resolution of I21 has allowed the detection of acoustic phonons in p-type $La_{1.84}Sr_{0.16}CuO_4$ (LSCO) and $Bi_2Sr_{1.6}La_{0.4}CuO_{6+\delta}$ (Bi2201) for the first time. Figure 1 shows RIXS maps with momentum transfer along h, for l=1.0 for LSCO. The dispersion and loss of amplitude towards the zone-centre is indicative of the presence of acoustic plasmon. The same behaviour was found for Bi2201 implying that acoustic plasmons are a general feature of cuprates.

The MMG has continued to innovate and develop the capabilities of its X-ray research facilities. The new Aberration-Corrected PEEM on I06, capable of operating at a sample temperature of 20 K, is currently being installed and will be available in the summer of 2021. This latest upgrade to the suite of instruments of the MMG allows higher-resolution spatial imaging using polarised soft X-rays and will be equipped with sample preparation and sample storage facilities as well as a purpose-built electromagnet. The existing Spectroscopic PhotoEmission and Low Energy Electron Microscope (SPELEEM) that has been in operation on I06 since January 2007 will be moved to a new purpose-built laboratory and combined with a continuous wave laser funded by the Engineering and Physical Sciences Research Council (EPSRC). I21 has upgraded its monochromator optics so that the beamline now reaches ~2.8 keV, essential for work on the ruthenates and irridates. In the coming year, the MMG beamlines will implement a NeXus file structure, which will enable faster data acquisition as well as a more detailed metadata structure.

The MMG is dedicated to continually improving its facilities and would welcome further input from our user community. We organise regular workshops to explore new scientific and technical opportunities together with our user community. Our objective is to operate a suite of state-of-the-art polarised X-ray beamlines with leading edge data acquisition, data logging and data analysis software.

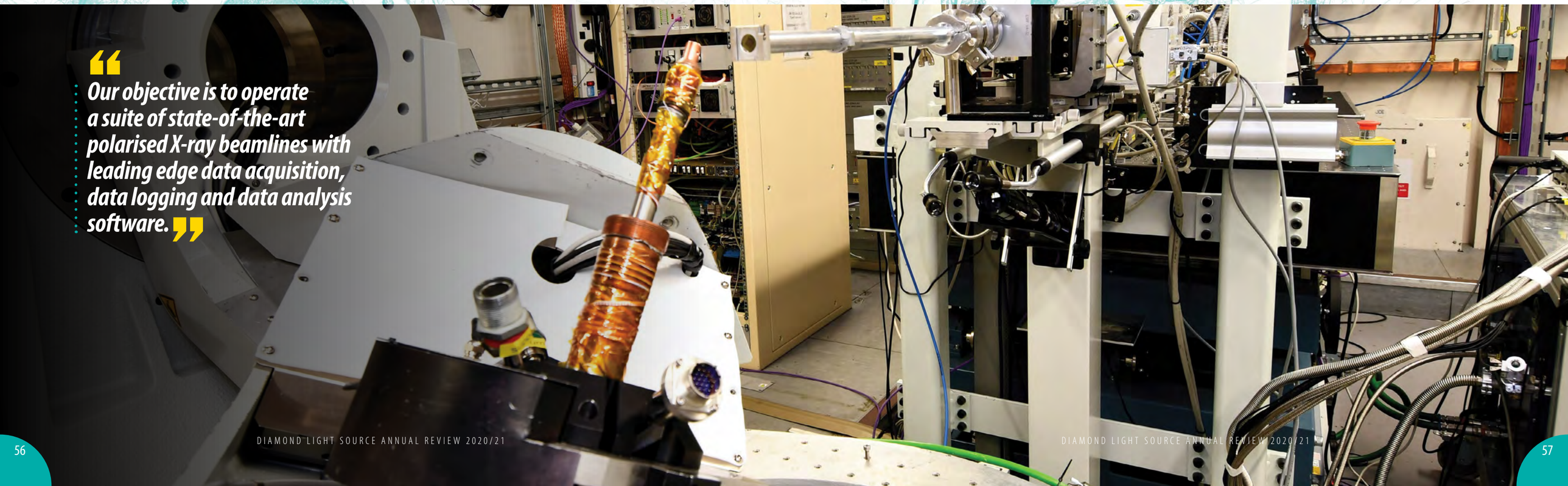

“Our objective is to operate a suite of state-of-the-art polarised X-ray beamlines with leading edge data acquisition, data logging and data analysis software.”

Nano-fragmentation of antiferromagnetic domains

Related publication: Kašpar Z., Surýnek M., Zubáč J., Krizek F., Novák V., Campion R. P., Wörnle M. S., Gambardella P., Marti X., Němec P., Edmonds K. W., Reimers S., Amin O. J., Maccherozzi F., Dhesi S. S., Wadley P., Wunderlich J., Olejník K. & Jungwirth T. Quenching of an antiferromagnet into high resistivity states using electrical or ultrashort optical pulses. *Nat. Electron.* **4**, 30–37 (2021). DOI: 10.1038/s41928-020-00506-4

Publication keywords: Electronic and spintronic devices; Magnetic properties and materials

Antiferromagnets are of potential use in spintronic devices due to their ultrafast dynamics, insensitivity to external magnetic fields and absence of magnetic stray fields. Researchers have observed large, transient changes in the electrical resistance in some antiferromagnetic thin film devices after applying electrical or optical pulses. Although the origin of these effects was unknown, it is now understood that they are related to the magnetic order.

Researchers from the Czech Academy of Sciences and Charles University in Prague, the University of Nottingham, ETH Zurich, the University of Regensburg in Germany and Diamond Light Source investigated the micro-scale antiferromagnetic order in CuMnAs films before and after applying current pulses. They aimed to relate changes in the electrical resistance to changes in the magnetic microstructure. Using the X-PEEM End station on Diamond's Nanoscience beamline (I06) enabled them to take images of the antiferromagnetic structures in microscale device structures. Electrical contacts on the sample allowed them to probe the magnetic state before and after applying current pulses.

The results show that a fragmentation of micrometre-scale antiferromagnetic domains accompanies the changes in the electrical resistance. The resulting textured structure has lengthscales comparable to, or even smaller than, the 30 nm spatial resolution of the X-PEEM End station. Their results establish a clear relationship of the electrical resistance changes with changes in the micromagnetic structure. The electrical switching and relaxation behaviour they observed can potentially mimic the characteristics of neural network components, offering the potential to develop efficient and high-speed neuromorphic computing applications that mimic neuro-biological architectures present in the human nervous system.

In an antiferromagnet, the electron spins of adjacent atoms are ordered such that the total magnetic moment is zero. Information can be stored in the orientation of this collective magnetic order, but compared to their ferromagnetic counterparts, antiferromagnetism is challenging to harness for applications[1]. Current-induced spin-orbit fields have been shown to reorient the magnetic order vector, allowing antiferromagnetic devices to show a rewritable memory functionality. However, the magnetoresistive read-out signals in such devices are typically very small[2].

Thermally-induced quenching of the magnetic order offers prospects for realising large, tuneable, reversible resistive read-out in antiferromagnetic spintronic devices. Figure 1 shows the results of quench switching by unipolar electrical current pulses in an antiferromagnetic CuMnAs thin film resistor. A step increase in the electrical resistance is observed after applying a 100 µs current pulse of amplitude $1.2x10^7$ A/cm^2. Applying a current pulse of 8% smaller amplitude, in the same direction, then results in the resistance dropping back to a lower value. This pattern of changes in the resistance is

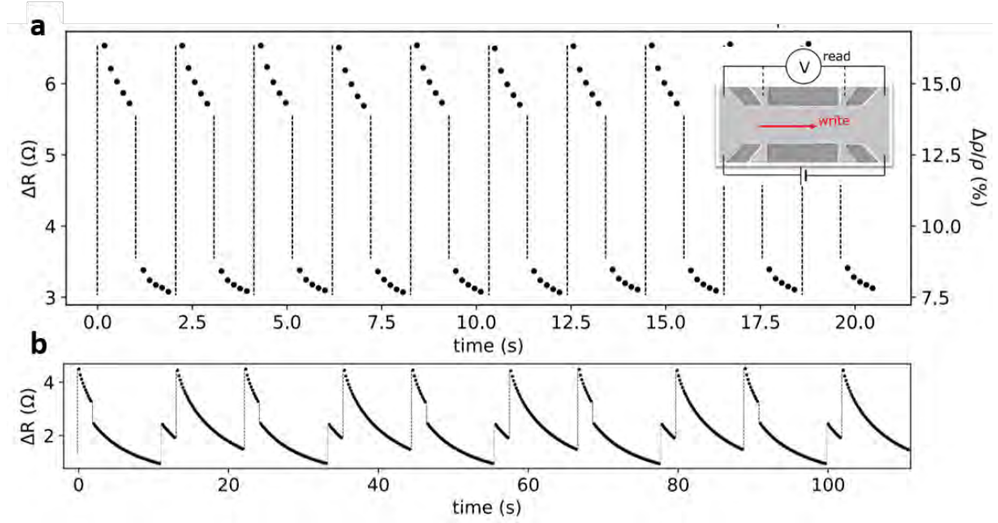

Figure 1: (a) Electrical switching and relaxation in a CuMnAs antiferromagnet device, with the high and low resistance metastable states obtained using 100µs writing currents of $1.2x10^7$ A/cm^2 and $1.0x10^7$ A/cm^2 respectively. The device structure and measurement schematic are shown in the inset; (b) A sequence of repeated switching to high/low/low/high resistance states for the same device.

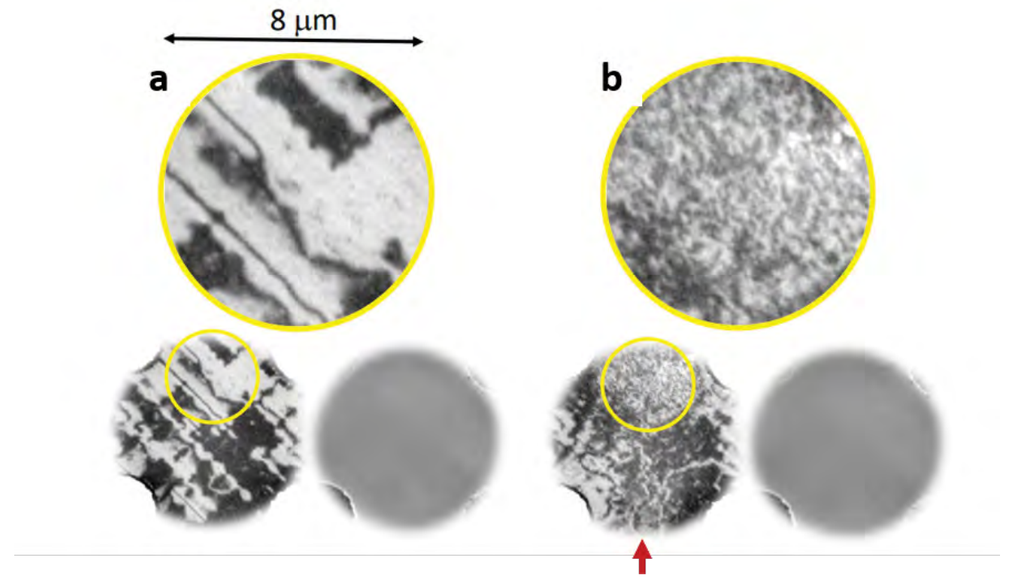

Figure 2: (a) X-PEEM images for an as-processed CuMnAs device, showing the antiferromagnetic domain structure (bottom left and top zoomed-in) and the X-ray absorption signal (bottom right); (b) X-PEEM images for the same device after applying a 100 ms current pulse of amplitude ≈10^7 A/cm^2 along the direction indicated by the red arrow.

highly reproducible, as demonstrated by the behaviour shown in Fig. 1a,b for two different pulsing sequences. The rate of relaxation following each current pulse shows a simple exponential dependence on temperature. Furthermore, the quench switching can be induced by trains of sub-picosecond laser pulses, and can be probed optically using the sample reflectivity, opening prospects for ultrafast all-optical unconventional computing applications.

Measurements were performed using X-ray PhotoEmission Electron Microscopy (XPEEM) on I06 in order to better understand the magnetic origin of the current-induced quench switching. Figure 2 shows antiferromagnetic domain images of a CuMnAs device before and after applying a current pulse at room temperature. The magnetic contrast is achieved using X-ray magnetic linear dichroism at the Mn L_3 absorption edge. The micron-sized magnetic domains in the as-grown sample are observed to fragment to lengthscales approaching the resolution of the XPEEM instrument (≈30 nm) after applying large-amplitude current pulses *in situ*. On the other hand, the X-ray absorption images displayed in the bottom-right of Fig. 2a,b show no significant difference after the current pulse, ruling out significant chemical or structural changes.

The ability to directly image antiferromagnetic domains with XPEEM, combined with the chemical sensitivity given by the X-ray absorption images, provides invaluable insight into the microscopic origins of the resistive readout mechanism in CuMnAs devices. The fragmentation of the antiferromagnetic domain structure can be ascribed to local joule heating bringing the system close to the Néel temperature, where entropy gain favours local spin disorder. Further studies will be required to determine the origin of the high metastability of the nanoscale fragmented domain state, as well its precise relationship to the resistive signal.

The quench switching observed in these antiferromagnetic materials has no counterpart in ferromagnetic systems. The observed tuneable multi-level output signals may allow antiferromagnetic spintronic devices to mimic components of spiking neural networks for neuromorphic computing applications[3]. Because electronic and magnetoelastic fluctuations may accompany the strong magnetic disorder, charge and spin-sensitive imaging with higher spatial and temporal resolution may shed new light on the underlying physics of this effect.

References:

1. Železný J. *et al.* Spin transport and spin torque in antiferromagnetic devices. *Nat. Phys.* **14**, 220–228 (2018). DOI: 10.1038/s41567-018-0062-7
2. Wadley P. *et al.* Spintronics: Electrical switching of an antiferromagnet. *Science.* **351**, 587–590 (2016). DOI: 10.1126/science.aab1031
3. Kurenkov A. *et al.* Artificial Neuron and Synapse Realized in an Antiferromagnet/Ferromagnet Heterostructure Using Dynamics of Spin–Orbit Torque Switching. *Adv. Mater.* **31**, 1900636 (2019). DOI: 10.1002/adma.201900636

Funding acknowledgement:
The EU FET Open RIA grant no. 766566; the UK EPSRC (EP/P019749/1); the Ministry of Education of the Czech Republic (LM2018110, LNSM-LNSpin and LM2018096); the Czech Science Foundation (19-28375X).

Corresponding author:
Dr Kevin Edmonds, University of Nottingham,
Kevin.Edmonds@nottingham.ac.uk

Imaging the vertical dimension of magnetic skyrmions

Related publication: Birch M. T., Cortés-Ortuño D., Turnbull L. A., Wilson M. N., Groß F., Träger N., Laurenson A., Bukin N., Moody S. H., Weigand M., Schütz G., Popescu H., Fan R., Steadman P., Verezhak J. A. T., Balakrishnan G., Loudon J. C., Twitchett-Harrison A. C., Hovorka O., Fangohr H., Ogrin F. Y., Gräfe J. & Hatton P. D. Real-space imaging of confined magnetic skyrmion tubes. *Nat. Commun.* **11**, 1726 (2020). DOI: 10.1038/s41467-020-15474-8

Publication keywords: Skyrmions; Imaging; Diffraction

Magnetic skyrmions are hedgehog-like particles that can be found in some magnetic materials. They are typically portrayed as two-dimensional whirl-like objects, but in reality, skyrmion lattices have a vertical, tube-like structure. The limitations of most magnetic imaging techniques meant that scientists had not observed this three-dimensional structure. Imaging the three-dimensional structure of the skyrmions is important for understanding the stability of skyrmions.

A team of researchers used I10: Beamline for Advanced Dichroism Experiments (BLADE) to perform magnetic diffraction measurements on a thin slice of skyrmion material, approximately ~100 nanometres thick. They needed low energy X-rays to probe the magnetic state of the sample, and the experiment had to be performed under vacuum. Using the beamline's soft X-ray diffractometer, Reflectivity and Advanced Scattering from Ordered Regimes (RASOR), allowed them to perform the experiment while controlling the temperature of the sample and applying external magnetic fields. With these results, the team could determine at what temperatures and applied magnetic fields the magnetic skyrmions exist within the sample. This information allowed them to acquire images of skyrmions' vertical structure at X-ray imaging beamlines at SOLEIL and BESSY II. And by imaging their vertical structure, they were able to study the nanoscale mechanisms that govern the formation and destruction of skyrmions.

Skyrmions have potential applications in future electronic devices. The computers and smartphones of the future may use skyrmions to store data. Understanding the stability of skyrmions is essential so that the data is not lost when the skyrmion device is turned off. This research is, therefore, a crucial step towards realising this goal.

Magnetic skyrmions, nanoscopic whirls composed of magnetic spins[1], are promising candidates for information elements in future low-power data storage and logic devices[2]. For such applications, enhancing the skyrmion stability is vital: any data encoded in the form of skyrmions must remain unchanged when the device is powered off[3]. This stability is determined by the dynamics which govern skyrmion destruction.

While they are commonly portrayed as two-dimensional objects arranged in a hexagonal lattice, in reality skyrmion lattices exist as extended tube-like objects in three-dimensions (Fig. 1). This vertical dimension holds the key to understanding skyrmion annihilation: a skyrmion tube is destroyed when it breaks in half, forming magnetic singularities known as Bloch points at the break locations[4,5]. The subsequent motion of these Bloch points unwinds the skyrmion tube along its length (Fig. 1).

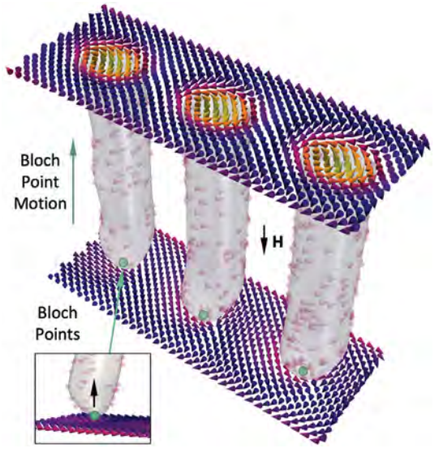

Figure 1: Three-dimensional visualisation of three magnetic skyrmion tubes, depicting the Bloch-point annihilation mechanism. The orientation of the applied magnetic field, H, is indicated.

Due to the limitations of commonly used magnetic imaging techniques, images of skyrmion tubes, and thus true understanding of skyrmion annihilation dynamics, have remained elusive. In a work recently published in *Nature Communications*, such limitations were overcome using a combination of X-ray diffraction and X-ray imaging to acquire the first direct observations of magnetic skyrmion tubes.

Before commencing imaging experiments, it was vital to determine the magnetic phase diagram of the FeGe lamella sample. Various magnetic states compete with the skyrmion state. At low applied magnetic fields, a helical state is realised, i.e. a spiral arrangement of magnetic spins (Fig. 2a) with uncompensated moments. When applying a magnetic field out of the plane of the sample, the skyrmion state is formed, with skyrmions arranging into a hexagonal lattice (Fig. 2b). In contrast, when an in-plane magnetic field is applied, the conical state is formed, which differs from the helical state because the spins are tilted towards the applied field direction (Fig. 2c). One would also expect skyrmion tubes to form with their cylindrical axes in the plane of the sample in this field configuration.

Small angle X-ray scattering (SAXS) experiments were carried out using the RASOR diffractometer at the beamline I10 at Diamond Light Source. The X-ray beam was directed through the FeGe lamella, with a CCD placed downstream to collect the resulting diffraction pattern. By tuning the energy of the X-rays to an absorption edge of the Fe atoms within the sample, the diffraction peaks arising from the ordered magnetic structures were resonantly enhanced.

Representative diffraction patterns for the helical, skyrmion lattice and conical states were measured (Fig. 2d-f), revealing twofold or sixfold symmetry around the central main beam. By performing such diffraction experiments as a function of temperature and applied magnetic field, magnetic phase diagrams for both out-of-plane and in-plane magnetic fields were determined (Fig. 2g and h, respectively).

Magnetically-sensitive imaging was performed using X-ray holography and scanning transmission X-ray microscopy (STXM) techniques, at the SEXTANTS

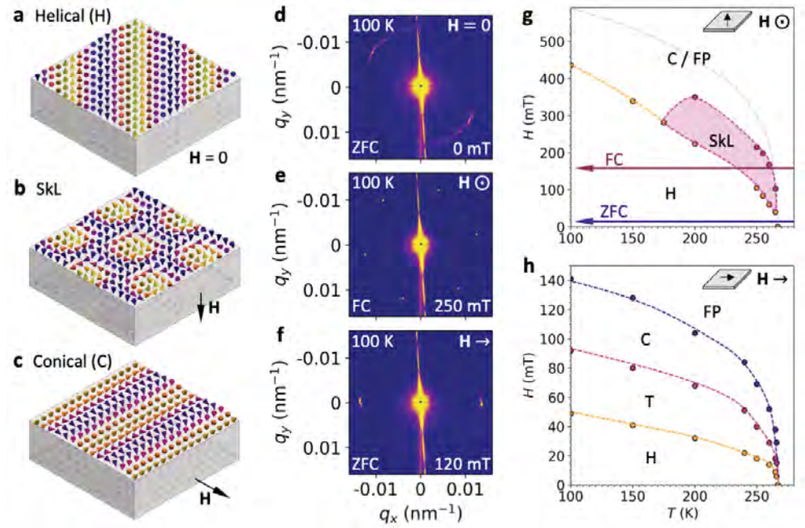

Figure 2: (a-c) Visualisations of the Helical (H), skyrmion lattice (SkL), and conical (C) states; (d-f), Corresponding SAXS diffraction patterns acquired after zero-field cooling (ZFC) or field cooling (FC) to 100 K at different applied magnetic fields H; (g-h) Magnetic phase diagrams determined for out-of-plane and in-plane fields respectively. The helical rotation transition region between H and C is labelled T. The zero field cooling and field cooling paths are illustrated.

beamline at SOLEIL and the MAXYMUS instrument at BESSY II respectively. An example microscopy image of the skyrmion lattice state for an out-of-plane field is shown (Fig. 3a). The result agrees well with the simulated image created from micromagnetic simulations of a skyrmion lattice state (Fig.3b). The images highlight that X-ray imaging provides magnetic contrast parallel or anti-parallel to the X-ray beam.

We then investigated the possibility of observing skyrmion tubes with the field applied in-plane. When observed from the side, an individual skyrmion tube is expected to exhibit both light and dark contrast, as the spins point in opposing directions either side of the skyrmion core. We observed such a contrast pattern in the corner of the FeGe lamella, showing three pairs of horizontal stripes (bottom left of Fig. 3c), which have the appearance of three skyrmion tubes (horizontal stripes) embedded within the surrounding conical state (vertical stripes).

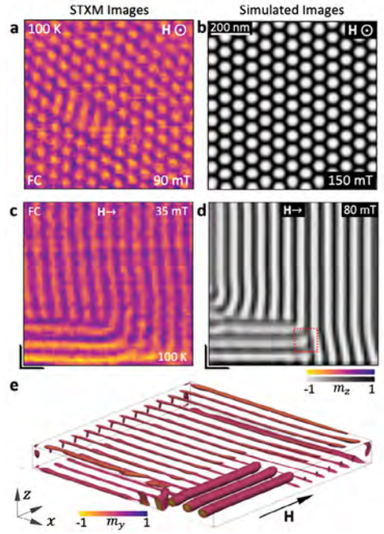

Figure 3: STXM (a,c) and simulated (b,d) images of the skyrmion lattice (a,b) and skyrmion tube (c,d) states; (e) Three-dimensional visualisation of skyrmion tubes within a conical structure from the micromagnetic simulation.

To validate the identity of these structures as skyrmion tubes, complimentary micromagnetic simulations of skyrmion tubes within a conical state background were performed. The resulting simulated image (Fig. 3d), shows remarkable agreement to the experimental data. A three-dimensional visualisation of the simulated magnetic state (Fig. 3e), reveals the skyrmion tube structures. Future experiments will allow us to observe these skyrmion tubes unwinding under different external stimuli, such as by the application of electric currents.

The combination of diffraction techniques performed at Diamond and the imaging techniques carried out at SOLEIL and BESSY II was vital to the success of this project. Furthermore, initial development of the SAXS technique at Diamond enabled us to expand our research into X-ray holography and microscopy techniques. In the future, we look forward to the possibility of performing such imaging experiments in the UK, utilising the flagship coherent soft X-ray imaging and diffraction beamline which was recently proposed for the Diamond-II upgrade.

References:

1. Mühlbauer S. *et al.* Skyrmion lattice in a chiral magnet. *Science.* **323**, 915–919 (2009). DOI: 10.1126/science.1166767
2. Nagaosa N. *et al.* Topological properties and dynamics of magnetic skyrmions. *Nat. Nanotechnol.* **8**, 899–911 (2013). DOI: 10.1038/nnano.2013.243
3. Yu X. Z. *et al.* Real-space observation of a two-dimensional skyrmion crystal. *Nature* **465**, 901–904 (2010). DOI: 10.1038/nature09124
4. Milde P. *et al.* Unwinding of a skyrmion lattice by magnetic monopoles. *Science (80-.).* **340**, 1076–1080 (2013). DOI: 10.1126/science.1234657
5. Kagawa F. *et al.* Current-induced viscoelastic topological unwinding of metastable skyrmion strings. *Nat. Commun.* **8**, 1332 (2017). DOI: 10.1038/s41467-017-01353-2

Funding acknowledgement:
EPSRC grants: EP/M028771/1 and EP/N032128/1. Beamline proposals: Diamond Light Source (SI20866-2), SOLEIL (20180679) and BESSY II (181-06589ST).

Corresponding authors:
Prof. Peter Hatton, Durham University, p.d.hatton@durham.ac.uk; Dr Max Birch, Max Planck Institute for Intelligent Systems, birch@is.mpg.de

Absolute determination of crystal and magnetic chiralities in an iron-based langasite

Related publication: Qureshi N., Bombardi A., Picozzi S., Barone P., Lelièvre-Berna E., Xu X., Stock C., McMorrow D. F., Hearmon A., Fabrizi F., Radaelli P. G., Cheong S. W. & Chapon L. C. Absolute crystal and magnetic chiralities in the langasite compound $Ba_3NbFe_3Si_2O_{14}$ determined by polarized neutron and x-ray scattering. *Phys. Rev. B* **102**, 54417 (2020). DOI: 10.1103/PhysRevB.102.054417

Publication keywords: Antiferromagnetism; Chirality; XRMS

Chirality is a concept first proposed by Lord Kelvin in the 19th century, referring to objects that do not coincide with their mirror image. Chirality can be thought of as 'handedness', with the most obvious example being a pair of human hands. Theoretical models suggest that chiral materials will give rise to exotic physical phenomena.

Langasite (lanthanum gallium silicate) is a piezoelectric crystal with optoelectronic applications. An international team of researchers used X-ray scattering and polarised neutrons to investigate the magnetic and structural chirality in a langasite crystal. The crystal has a chiral atomic arrangement. When it orders magnetically, it forms a triangular arrangement of magnetic helices. The triangular configuration adopted by the spins, the rotational direction of the helices and their relationship with the structural chirality were unclear.

Diamond Light Source's Materials and Magnetism beamline (I16) was perfect for this study. It allows full control of the energy and polarisation of the X-ray beam and analysis of the final polarisation of the diffracted beam. These features are all necessary to study the chiral properties of a crystal. The research team determined the system's absolute structural and magnetic chirality and the unusual mechanism controlling the direction of rotation of the magnetic helix. Chirality is an elusive property to measure. However, it is robust and can be associated to topological properties. In future, it may be possible to use topologically chiral objects to store information.

Chirality, from the ancient Greek χείρ-hand, is an embodied characteristic of humans that appear during the embryonic development and is shared across bilaterians from snails to vertebrate. Such morphological characteristic was recently loosely associated to the existence of functional lateralisation in our daily actions[1]. This feature makes us perfect detectors to discriminate between left and right handed objects through our interaction with them, so we can easily distinguish not only between a left and right shoe, but also between the smell of spearmint and cumin. Chirality is not only an essential ingredient of life. It appears amongst the subatomic particles properties and it can give origin to amazing novel magnetic and electronic properties in chiral crystals.

In magnetic crystals, the absence of inversion symmetry leads to helical magnetic exchange paths and allows antisymmetric magnetic exchange interactions. Examples of chiral systems in condensed matter systems include magnetic skyrmions, whose topological charge can be manipulated and potentially used to store information. Likewise, chiral magnetic domains can be manipulated by electric fields in systems belonging to the so-called ferroaxial groups supporting magnetically induced ferroelelectricity[2,3].

In this combined polarised neutron and X-ray scattering experiment, the relationship between the structural and magnetic chiralities in two enantiopure iron-based langasite single crystals was investigated. Langasites crystallise in the chiral P321 space group (Fig. 1). The magnetic moments associated to the Fe ions form a triangular network in the basal plane and order in a helical spiral out of plane below TN = 27 K[4]. The first task of this investigation was to establish the absolute structural and magnetic chiralities of two samples of opposite structural chirality. The second task was to understand what stabilises a given magnetic handedness. The experimental results together with simple energy considerations reveal that it is not the antisymmetric Dzyaloshinskii-Moriya (DM) interaction but the local Fe single-ion anisotropy (SIA) which plays a key role in stabilising one of the two magnetic helices.

Determining structural chirality in a transparent crystal can be done directly by optical rotation, measuring the angular deviation of linearly polarised light transmitted through the medium. But surprisingly, given our ability to immediately identify chiral objects, chirality is not directly observable, and we can only make use of small effects to discriminate amongst different handedness.

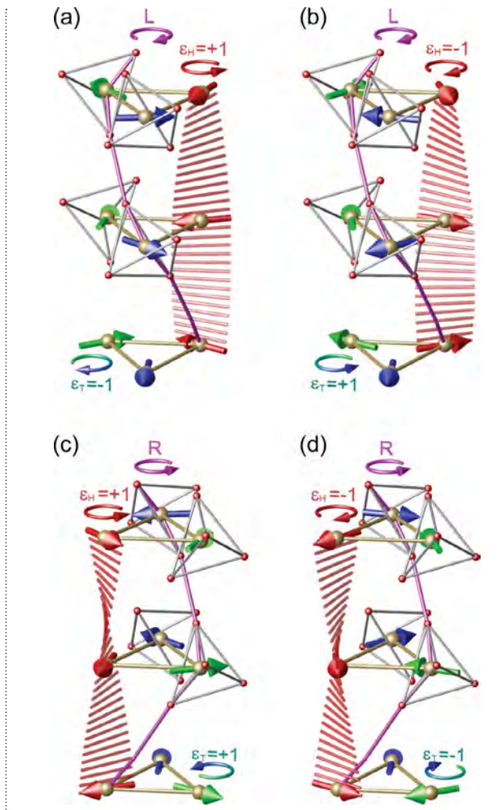

Figure 1: Four different chiral configurations which all yield the same nuclear and magnetic structure factors and therefore are indistinguishable by unpolarised X-rays diffraction. The structural crystal chirality (L/R), the helical (hc) and triangular (tc) magnetic chiralities are also shown.

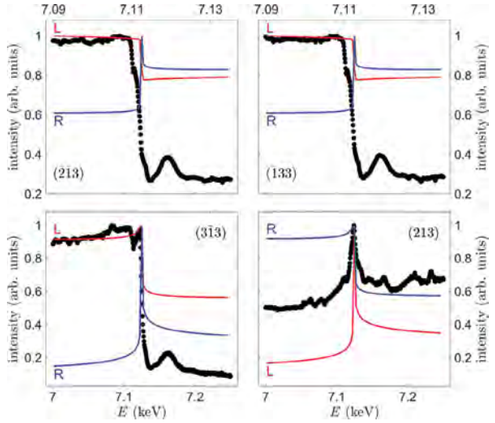

Figure 2: The behaviour of four noncoplanar reflections shows great contrast in the simulations for the left-handed (red lines) and right-handed (blue lines) enantiomers. As is immediately evident, only simulations with the left-handed structure match the trend of the experimental data. No attempt was made to simulate the subtle feature shown by the experimental data across the transition.

In the domain of the X-ray, determining the structural chirality is routinely achieved by collecting the integrated intensity from many reflections and including the anomalous form factor in the data analysis. In our I16 study we pushed this approach to the extreme by measuring the intensity variation of few reflections across the Fe K absorption edge. In this region, the energy dependent part of the form factor starts to dominate and the different interferences given by the mirror related arrangement of the crystal ions in the two enantiomers lead to large contrast on some reflections across the Fe K-edge (Fig. 2). Once all the conventions were carefully checked we established a uniform left structural chirality for our specimen across the whole surface.

The determination of the absolute magnetic chirality can not be obtained in a similar manner and requires not only the full brightness of synchrotron radiation, but also full control over the incident polarisation of the light to create a chiral probe.

The horizontally linearly polarised photon was tuned at 5.0 keV, to minimise the noise due to the edges of all the chemical elements present in $Ba_3NbFe_3Si_2O_{14}$. Circular polarisation of the beam was achieved by transmission through a 100 µm thick diamond plate. The diamond crystal was aligned close to the (111) reflection in the Laue scattering geometry. Under these precise geometrical conditions, the crystal behaves as a quarter-wave plate producing circular light. The handedness of the light is determined by precise orientation of the diamond, which was calculated by dynamical scattering theory and confirmed through experimental absolute calibration of the beamline by measuring the X-ray dichroism of a standard ferromagnet.

The magnetic chirality was investigated at T = 5K. A large area of the sample was mapped with respect to its magnetic chirality, revealing the same character, from which we can deduce that it is magnetically enantiopure. The results are reported in Fig. 3 and are based on a L-handed spiral clearly showing that the magnetic chirality follows the structural one. For an opposite magnetic chirality, the calculated curves would be reversed. Finally, an azimuthal investigation of few reflections confirms the elliptical modulation of the magnetic helix with Sh/Se = 0.94(2), where Sh and Se are the spin components along the hard and easy axis of the magnetic envelope.

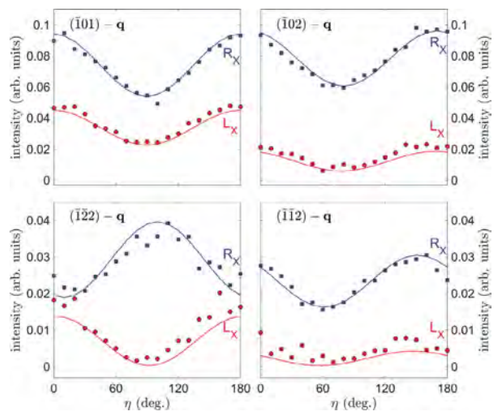

Figure 3: The X-ray dichroic intensity as a function of the deviation angle η of the linear polarisation analyser from the scattering plane for four different magnetic Bragg reflections at T = 5K. Red circles represent data taken with a photon beam of left-handed polarisation; blue squares, data measured with a photon beam of right-handed polarisation. The calculated intensities are based on a left-handed enantiomer and are shown as solid lines in the corresponding colours.

Theoretical calculations including SIA effect indicates that there is no energetic advantage to distort the circular modulation in the cases of negative triangular chirality (εT = -1) , whereas an energetic gain is obtained, independently of the spin-orbit coupling, for εT = +1. This selection mechanism of chirality where the SIA in the planar triangular arrangement, in itself not 'chiral', not only distorts the helix but it chooses the global magnetic chirality almost independently from the strength of the spin orbit coupling and hence of the DM chiral term appearing in the microscopic Hamiltonian.

In conclusion, the capability of tuning the energy and controlling of the X-ray polarisation available on the I16 beamline were essential in determining absolutely and simultaneously the sign of all the microscopic chiral elements appearing in the system.

References:

1. Brandler W. M. *et al.* The genetic relationship between handedness and neurodevelopmental disorders. *Trends Mol. Med.* **20**, 83–90 (2014). DOI: 10.1016/j.molmed.2013.10.008
2. Johnson R. D. *et al.* Giant improper ferroelectricity in the ferroaxial magnet CaMn 7O 12. *Phys. Rev. Lett.* **108**, 67201 (2012). DOI: 10.1103/PhysRevLett.108.067201
3. Hearmon A. J. *et al.* Electric field control of the magnetic chiralities in ferroaxial multiferroic $RbFe(MoO_4)_2$. *Phys. Rev. Lett.* **108**, 237201 (2012). DOI: 10.1103/PhysRevLett.108.237201
4. Marty K. *et al.* Single domain magnetic helicity and triangular chirality in structurally enantiopure $Ba_3NbFe_3Si_2O_{14}$. *Phys. Rev. Lett.* **101**, 247201 (2008). DOI: 10.1103/PhysRevLett.101.247201

Funding acknowledgement:
We acknowledge Diamond Light Source for time on Beamline I16 under Proposals mt4073-1, mt1803-1, and 17569. The work at Rutgers University was supported by the DOE under Grant No. DOE: DE-FG02-07ER46382. Work in London was supported by the Engineering and Physical Sciences Research Council, UK (Grant No. EP/N027671/1).

Corresponding author:
Dr Alessandro Bombardi, Diamond Light Source,
alessandro.bombardi@diamond.ac.uk

Trapped oxygen molecules provide an energy storage mechanism in lithium-ion battery cathodes

Related publication: House R. A., Rees G. J., Pérez-Osorio M. A., Marie J. J., Boivin E., Robertson A. W., Nag A., Garcia-Fernandez M., Zhou K. J. & Bruce P. G. First-cycle voltage hysteresis in Li-rich 3d cathodes associated with molecular O2 trapped in the bulk. *Nat. Energy* **5**, 777–785 (2020). DOI: 10.1038/s41560-020-00697-2

Publication keywords: Li-ion Batteries; Cathode Materials; Resonant Inelastic X-ray Scattering

Lithium-rich cathode materials exhibit a pronounced drop in voltage between the charging and discharging processes (known as 'voltage hysteresis') that limits the available energy density. This needs to be overcome for them to be used in next-generation battery applications. In lithium-rich materials, the charging and discharging processes are accompanied by chemical changes to the oxide ions that form part of the cathode's crystal structure. The reversibility of these chemical processes is critical in determining how well a cathode material functions. The voltage hysteresis seen in the lithium-rich materials implies the oxide ions undergo chemical changes that are not fully reversible, but the mechanism behind this was not well understood.

Researchers used the Resonant Inelastic X-ray Scattering (RIXS) beamline (I21) at Diamond Light Source to study the chemical changes to the oxide ions at different stages of the battery charge-discharge cycle using RIXS. The measurements acquired from this technique offer a direct probe of the electronic structure on oxygen. Using high-resolution RIXS, they detected underlying vibrational fine structure that revealed the identity of the oxidised oxide ions as molecular oxygen. These oxygen molecules are trapped within the charged cathode material, but they can be reduced back to oxide ions on discharge. However, this process takes place at a lower voltage, giving rise to the voltage hysteresis.

Researchers can now devise strategies to suppress the release of oxygen, or prevent its formation, in next-generation lithium-ion (Li-ion) batteries with higher energy density. Higher energy density batteries will extend the driving range of electric vehicles and increase the battery life of portable electronics between charges.

Lithium-rich layered transition metal oxide materials, such as $Li_{1.2}Ni_{0.13}Co_{0.13}Mn_{0.54}O_2$ (Fig. 1a) are closely being considered as high energy density cathodes for next generation Li-ion batteries; they can store and release more charge than conventional cathodes by utilising redox chemistry of the oxide anions in addition to that of the transition metal cations[1]. This so-called *oxygen redox* (or *O-redox*) process is, however, accompanied by complex changes to the cathode crystal structure, gas evolution from the surface and a severe loss of voltage between the first charge and discharge (known as *voltage hysteresis*), (Fig. 1b)[2]. This reduces the practical energy density that can be achieved and represents a key challenge preventing their full exploitation.

Understanding how the O-redox process works is crucial to unlocking the potential of these materials but, uncovering the mechanism has proved difficult. Since the discovery of lithium-rich materials in the early 2000s, it has been established that dimerisation of oxidised oxide ions in the lattice to form O-O species takes place along with the migration of transition metal ions within the structure[3,4], but there is still debate on the nature of the O-O dimer and how these processes translate into voltage hysteresis.

In the study of O-redox chemistry, Resonant Inelastic X-ray Scattering (RIXS) has proven to be an insightful tool[5]. To examine the O-redox process in depth in $Li_{1.2}Ni_{0.13}Co_{0.13}Mn_{0.54}O_2$, RIXS measurements were performed at the I21 beamline at Diamond on cathode samples extracted from batteries at different stages of the charge-discharge cycle. RIXS emission spectra were collected in increments of excitation energy across the oxygen K-edge, generating a RIXS map that revealed the valence states on oxygen, (Fig. 2a). The state-of-the-art capabilities at beamline I21 enabled this RIXS data following the O-redox process to be obtained with much higher resolution than previously possible[5].

The results showed the appearance of a series of sharp, intense peaks in emission energy in the charged cathodes at an excitation energy of 531 eV. Closer analysis of this peak progression revealed a regularly decreasing spacing between the peaks consistent with the spacing between vibrational energy

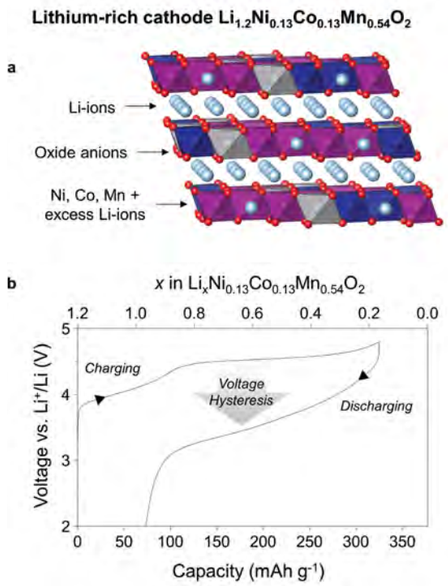

Figure 1: (a) Crystal structure for lithium-rich cathode $Li_{1.2}Ni_{0.13}Co_{0.13}Mn_{0.54}O_2$, pale blue, Li; purple, Mn; grey, Ni; dark blue, Co. (b) First-cycle charge-discharge voltage profile for $Li_{1.2}Ni_{0.13}Co_{0.13}Mn_{0.54}O_2$ in a Li-ion battery.

levels of a diatomic O_2 molecule, (Fig. 2b). Tracking the evolution of this feature over the charge-discharge cycle confirmed the molecular O_2 was formed as a direct result of the oxidation of lattice oxide ions and that, once formed, it could be reduced back into oxide during discharge. This demonstrates that molecular O_2 partakes reversibly in the energy storage mechanism of these high energy density O-redox cathodes, albeit accompanied by voltage hysteresis.

Since the cathodes were measured under ultra-high vacuum conditions within the RIXS spectrometer, the O_2 molecules that were detected must have been trapped within the crystal structure of the material, (Fig. 2c). The close match of the peak spacing to that of free, gaseous O_2, suggests there is minimal bonding interaction between the O_2 molecules and their surrounding crystal lattice. Furthermore, careful beam exposure studies were undertaken to critically examine the influence of the measurement conditions upon the spectroscopic features. Even under reduced temperature, lower photon flux and shorter exposure times, very little change was observed in the signal, indicating the O_2 was intrinsic to the cathode and not radiation-induced.

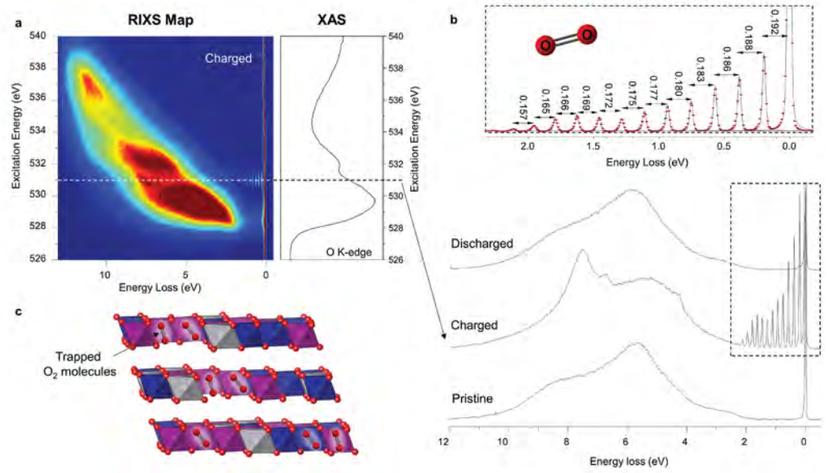

Figure 2: (a) RIXS map and XAS spectrum for $Li_{1.2}Ni_{0.13}Co_{0.13}Mn_{0.54}O_2$ in the charged state. (b) RIXS emission spectrum recorded at 531 eV in the pristine, charged and discharged states. Inset shows close-up of peak progression detected in the charged cathode with peak spacing closely corresponding to the spacing between vibrational energy levels of molecular O_2. (c) Structural schematic for the charged cathode with trapped O_2 molecules.

To independently verify the formation and reduction of trapped O_2 and investigate its local chemical environment, a ^{17}O Nuclear Magnetic Resonance (NMR) study was performed on ^{17}O-labelled material. The NMR experiments detected a new, strongly paramagnetic O environment in the charged cathode with a shift and sideband manifold width consistent with previous measurements on O_2 in the condensed state. The sharp sideband peaks indicated that the molecular O_2 was rigidly trapped within the lattice, which, together with the vibrational RIXS data, suggests physical confinement rather than chemical bonding within sub-nano-sized void defects. In line with the RIXS results, this new O environment corresponding to O_2 disappeared during subsequent discharge demonstrating the reversible nature of the O^{2-}/O_2 charge storage mechanism.

Despite its Coulombic reversibility[2], the formation and reduction of molecular O_2 is accompanied by pronounced voltage hysteresis, resulting in a loss of energy density and poor efficiency. To uncover the origin of this hysteresis, density functional theory calculations were employed using structural models for $Li_{1.2}Ni_{0.13}Co_{0.13}Mn_{0.54}O_2$ at different states of charge. In some of the fully charged models investigated, where the transition metal ions had been permitted to migrate, O_2 molecules were found to form spontaneously during structural relaxation leading to substantially more stable, lower energy structures. Once these structures were re-populated with lithium ions, the O_2 molecules were reformed into O^{2-} ions, however the new, disordered arrangement of transition metal ions resulted in a higher energy structure than the original, pristine ordered one. Thus, it was determined that the irreversible structural changes triggered by the formation of molecular O_2 were to blame for the electrochemical voltage hysteresis observed.

This new understanding, in which transition metal migration and molecular O_2 formation are both implicated in the voltage hysteresis mechanism of lithium-rich cathodes, lays a foundation for researchers to devise strategies to improve these materials. This study has also demonstrated the power of high resolution RIXS as a characterisation tool for tracking redox processes in energy storage materials. The capability of RIXS to detect homonuclear diatomic molecules trapped within the bulk of an inorganic material, is a unique strength and one which may find useful application beyond the battery field.

References:

1. Koga H. *et al.* Reversible Oxygen Participation to the Redox Processes Revealed for $Li_{1.20}Mn_{0.54}Co_{0.13}Ni_{0.13}O_2$. *J. Electrochem. Soc.* **160** (2013). DOI: 10.1149/2.038306jes
2. Lu Z. *et al.* Understanding the Anomalous Capacity of Li/Li[$Ni_xLi_{(1/3-2x/3)}Mn_{(2/3-x/3)}$]$O_2$ Cells Using In Situ X-Ray Diffraction and Electrochemical Studies. *J. Electrochem. Soc.* **149** (2002). DOI: 10.1149/1.1480014
3. Sathiya M. *et al.* Reversible anionic redox chemistry in high-capacity layered-oxide electrodes. *Nat. Mater.* **12**, 827–835 (2013). DOI: 10.1038/nmat3699
4. Saubanère M. *et al.* The intriguing question of anionic redox in high-energy density cathodes for Li-ion batteries. *Energy Environ. Sci.* **9**, 984–991 (2016). DOI: 10.1039/c5ee03048j
5. Gent W. E. *et al.* Coupling between oxygen redox and cation migration explains unusual electrochemistry in lithium-rich layered oxides. *Nat. Commun.* **8**, 2091 (2017). DOI: 10.1038/s41467-017-02041-x

Funding acknowledgement:
P.G.B. is indebted to the EPSRC, including the SUPERGEN programme (EP/L019469/1), the Henry Royce Institute for Advanced Materials (EP/R00661X/1, EP/S019367/1 and EP/R010145/1) and the Faraday Institution (FIRG007 and FIRG008) for financial support. We acknowledge Diamond Light Source for time on I21 under proposal MM23889-1. Support from the EPSRC (EP/K040375/1 'South of England Analytical Electron Microscope') is also acknowledged. We acknowledge the resources provided by the Cambridge Tier-2 system operated by the University of Cambridge Research Computing Service (http://www.hpc.cam.ac.uk) funded by EPSRC Tier-2 capital grant EP/P020259/1, via the BATTDesign and AMAiB projects. The UK 850 MHz solid-state NMR Facility used in this research was funded by EPSRC and BBSRC (contract reference PR140003), as well as the University of Warwick, which included via part funding through Birmingham Science City Advanced Materials Projects 1 and 2 supported by Advantage West Midlands (AWM) and the European Regional Development Fund (ERDF).

Corresponding author:
Dr Robert A. House, Department of Materials, University of Oxford, robert.house@materials.ox.ac.uk

Imaging and Microscopy Group

Paul Quinn, Science Group Leader

The Imaging and Microscopy Group at Diamond Light Source brings together eight experimental facilities (I08, J08, DIAD, I12, I13-1, I13-2, I14 and ePSIC, the Electron Physical Science Imaging Centre) which use electrons and X-rays to image samples under different experimental conditions across a diverse range of length scales and time scales.

As for everyone, 2020 was an unusual and challenging year. Planned maintenance had to be rescheduled due to lockdowns. However, across the group the facilities adapted as much as possible to meet the challenges by offering mail-in samples, remote access or when possible, for a time, socially distanced operation with small user teams. Working in these restricted conditions the group still achieved two major milestones with the delivery of first user on J08, the soft X-ray ptychography branchline, and on DIAD, the Dual Imaging and Diffraction beamline; both significant achievements and exciting new additions to the imaging facilities at Diamond. The Imaging Group has also used the last year to plan new developments to better serve the user community. For Diamond-II (the proposed upgrade programme) the Imaging Group, in collaboration with the Cryo-Biological Imaging Group, developed proposals for upgrades to beamline I13 to deliver new capabilities in nanoscale and multiscale imaging and transformative facilities to deliver large volume, high resolution imaging of biological tissue. These proposals were developed off the back of a series of user working group meetings, which engaged a wide spread of the community. The exciting science possibilities were presented through webinars and captured through strong user support statements from the community. On the beamlines, plans have been developed to update tomography scanning to provide increased functionality and capabilities. In ptychography, there have been collaborative projects to deliver fast and robust performance and expansion to include machine learning studies. Remote working has become a standard mode of operation and developments such as robotic sample transfer arms have sought to make the most of the current situation as well as transform the types of science possible. Further automation is planned across the beamlines.

The DIAD beamline for Dual Imaging and Diffraction offers two X-ray techniques: full-field radiography/tomography and micro-diffraction, used on the same sample quasi-synchronously. This setup enables *in situ* characterisation of the 3D microstructure of the material at the same time as its crystallographic phase and/or strain state. X-rays from a 10-pole wiggler are split into two independent beams and then combined at the sample position. The imaging beam can be operated in either pink or monochromatic mode; diffraction is conducted with monochromatic mode. Both beam energies can be chosen independently of each other in an energy range of 8-38 keV. In the summer, DIAD expects the delivery of a dedicated mechanical test rig with integrated tomography capabilities. It will be an integral part of the end station and enable a variety of scientific experiments in engineering, materials science, biomaterials and hard tissues, geology and mineralogy. DIAD is part-funded by the University of Birmingham. This collaboration has shown to be very successful, with a first user experiment taking place in February 2021 by a University of Birmingham fellow. The beamline is now in friendly user commissioning mode.

The Scanning X-ray Microscopy (SXM) beamline (I08) is for morphological, elemental and chemical speciation on a broad range of organic-inorganic interactions in a 250 - 4400 eV photon energy range, and sample investigations under ambient or cryogenic conditions. I08 has a range of applications including biological and biomedical sciences, earth and environmental science, geochemistry, and materials science. I08 improved and partially automated and simplified user operation. The new soft X-ray spectro- and tomo-ptychography branchline (J08) took first users in October 2020. Key developments, such as a new detector installation, are currently underway and are essential to allow the beamline to access the intended 250-2000 eV photon energy range. This will provide access to carbon for ptychographic studies and improve image quality and resolution. Developments to deliver cryogenic sample handling are also planned, subject to operational and commissioning commitments. A call for first experiments is expected in the second half of 2021, providing a step change in imaging and spectro-microscopic performance for soft X-ray imaging at Diamond.

The Joint Engineering, Environmental and Processing (JEEP) beamline (I12) uses a 4.2 T superconducting wiggler to provide polychromatic and monochromatic X-rays in the energy range 53 - 150 keV. These high photon energies provide good penetration through large or dense samples. The beamline offers beam sizes ranging from 50 x 50 μm^2 for diffraction, up to 90 x 25 mm^2 for imaging and tomography. Static objects larger than the available beam can be tomographically imaged using special scanning protocols. The beam characteristics enable the study of macroscale samples that are representative of bulk materials and processes. Another feature of I12 is the ability to use complex, enclosed sample environments without unacceptable attenuation of the beam. X-ray techniques available are radiography, tomography, energy-dispersive diffraction, monochromatic 2D diffraction and scattering. Radiography and tomography are performed predominantly with monochromatic X-rays. Polychromatic beam is reserved for energy-dispersive diffraction or non-routine special requests. I12 has a diverse user community (materials science and engineering, chemical processing, biomedical engineering, geoscience, environmental science, physics, palaeontology) who make full use of the beamline's capabilities. The two flexible experimental hutches at the beamline allow users to bring their own rigs and sample chambers. I12 continues to support a wide range of *in situ*, time-resolved experiments, notably in additive manufacturing, materials property testing and chemical processing. It is common for users to combine imaging and diffraction in the same experiment. Working with Diamond's Controls, Data Acquisition and Data Analysis teams, I12 has improved time-resolved tomography reliability, and increased utilisation of the Large Field of View camera for tomography of large objects, some over 100 mm in diameter.

The I13 Imaging and Coherence beamline is for multi-scale imaging in the energy range of 6 - 30 keV. The achievable resolution ranges from several microns to some tens of nanometers with two branchlines operating independently for this purpose. The Diamond Manchester Imaging branchline performs mainly in-line phase contrast tomography, with a strong emphasis on dedicated sample environments. A new full-field microscope using Zernike phase contrast imaging over a field of view of 50-100 µm and a resolution of 50 - 100 nm is now in operation, with a growing user community, allowing us to identify nano-sized structures under dynamic conditions. A new robot arm has been installed for high-throughput and remote studies with measurements of up to 300 samples per day demonstrated in early testing. This will allow for large sampling and parametric studies in a range of science areas and the possibility of sample mail-in services. The highest spatial resolution, of 30 nm, is achieved on the Coherence branch with ptychographic imaging. Continuous improvements have reduced ptycho-tomography scans from days to a few hours, and ongoing fly-scanning developments aim to reduce this even further. Ptychography has become a standard user-friendly experiment. Instrumental upgrades for Bragg-CDI (new detector robot software) expands the experimental capabilities for studying nano-crystalline structures and has been applied successfully in combination with ptychography.

> *"The Imaging Group has also used the last year to plan new developments to better serve the user community."*

The Hard X-ray Nanoprobe beamline (I14), offers a beam of 50 nm for high resolution imaging. I14 has expanded the core 2D techniques of X-ray fluorescence, diffraction, X-ray Absorption Near Edge Structure (XANES), differential phase contrast and ptychography for mapping inhomogeneities in a wide range of samples, to include tomography for volume imaging of elemental, structural and chemical states. The first joint PhD student on I14 completed in the summer and successfully developed and demonstrated X-ray Fluorescence (XRF) and XANES imaging of the fate of targeted drugs in cancer cells. To deliver faster scanning and greater stability, a new state of the art nano-positioning stage has been developed in-house, which is designed to also allow greater flexibility for *in situ* measurements. A new EIGER detector will also allow us to reduce measurement times for phase contrast and ptychography by an order of magnitude.

The Electron Physical Science Imaging Centre (ePSIC) at Diamond consists of two transmission electron microscopes, a JEOL ARM 200 and a JEOL GRAND ARM 300, which were brought to Diamond through a collaboration with Johnson Matthey and the University of Oxford respectively. The ARM 200 is a state-of-the-art probe-corrected analytical microscope capable of atomic resolution electron energy loss and X-ray spectroscopy. The ARM 300 is a dedicated imaging instrument aligned across a wide range of accelerating voltages (30 - 300 keV). It is both probe- and imaging-corrected and has numerous detectors, including a small pixel array (512 x 512) fast direct electron detector for low voltage work, and a newly installed large pixel array (4K x 4K) fast direct electron detector for high voltage imaging. These combined capabilities make this a unique resource for electron microscopy within the UK. With *in situ* sample holders, users at ePSIC can perform variable temperature measurements, from 100 to 1600 K, to directly image the atomic structure of materials during thermally driven transitions. An Oxford Instruments Energy Dispersive X-ray (EDX) detector has been added to the ARM 300 to allow combined X-ray spectroscopy and high-resolution imaging. The state of the art instrumentation available at ePSIC attracts both established electron microscopists looking to develop new techniques, and scientists with limited previous electron microscopy experience interested in the atomic structure of their samples. The collaboration of the expert staff at ePSIC with this range of users is helping to bring cutting-edge microscopy techniques to the wider material science community. Over the last twelve months, ePSIC users have made notable breakthroughs in fields such as catalysis and photovoltaic materials, as well as important contributions to the development of electron ptychography and scanning diffraction imaging.

Direct chemical imaging of neuromelanin in the most vulnerable brain cells in Parkinson's disease

Related publication: Brooks J., Everett J., Lermyte F., Tjhin V. T., Banerjee S., O'Connor P. B., Morris C. M., Sadler P. J., Telling N. D. & Collingwood J. F. Label-Free Nanoimaging of Neuromelanin in the Brain by Soft X-ray Spectromicroscopy. *Angew. Chemie - Int. Ed.* **59**, 11984–11991 (2020). DOI: 10.1002/anie.202000239

Publication keywords: Neuromelanin; Parkinson's Disease; Spectromicroscopy

Parkinson's disease causes the loss of a particular group of brain cells, the neurons that produce the neurotransmitter dopamine. As these cells contain a dark pigment, neuromelanin, the change is evident from the loss of pigment in this brain region. Characterisation of neuromelanin in tissue remains dependent on visible pigmentation. Faint pigmentation may be interpreted as cell loss, and so contrast-enhancing stains are commonly used. However, this staining constrains further chemical analysis of the tissue.

Researchers explored the use of synchrotron X-ray microscopy to visualise neuromelanin without relying on visible pigmentation or chemical staining. They performed combined imaging and spectroscopy (spectromicroscopy) on Diamond Light Source's Scanning X-ray Microscopy beamline (I08), allowing the creation of images from distinct X-ray absorption features. Nanoscale spatial resolution using soft (low energy) X-rays allowed the researchers to probe the organic structure of neuromelanin to seek distinguishing spectral features. This revealed a characteristic feature in the absorption spectrum for neuromelanin. The team used this feature to create maps of neuromelanin distributions, which matched those observed in stained tissue sections.

The team also used nanoscale X-ray Fluorescence (XRF) with hard (high energy) X-rays on the Hard X-ray Nanoprobe beamline (I14) to discover a signature for identifying neuromelanin. This showed that neuromelanin could be identified by its elevated sulfur content. However, this approach is not as specific to neuromelanin as the soft X-ray method. The discovery of the soft X-ray neuromelanin signature offers significant potential for non-destructive studies of the relationships between depigmentation, metal binding and neurodegeneration in Parkinson's disease.

Dopamine-producing neurons within the substantia nigra region of the brain normally show black/brown pigmentation with advancing age as granules of neuromelanin, a biological polymer formed by dopamine oxidation. In Parkinson's disease, loss of pigmentation is particularly evident in the substantia nigra pars compacta region and is directly associated with progressive neurodegeneration. Evaluating the loss of visible pigmentation in affected areas of brain tissue is fundamental to post-mortem staging of Parkinson's disease, yet is constrained by conventional methods of analysis. Emerging synchrotron techniques at Diamond Light Source may shed new light on neuromelanin and its long-debated role in Parkinson's disease.

Parkinson's disease is the second most common neurodegenerative disease globally (after Alzheimer's disease), and remains incurable, whilst the underlying causes are still unknown. Recognised clinical symptoms of Parkinson's, including tremor, rigidity and bradykinesia (slowness of movement), arise due to a characteristic depletion of neurotransmitter dopamine in the brain, caused by the death of dopamine-producing neurons. By the time a patient's symptoms become apparent, 80% of these neuromelanin-pigmented neurons may have already died. Whilst the role of neuromelanin in neurodegeneration is still unclear, the strong affinity of neuromelanin for metal ions is a factor receiving considerable attention[1].

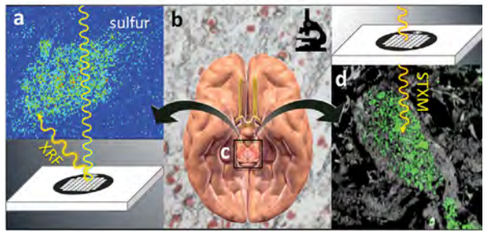

Figure 1: Enabling correlative analysis of neuromelanin in human substantia nigra using optical microscopy, Scanning Transmission X-ray Microscopy (STXM) and X-ray Fluorescence imaging (XRF). (a) XRF map of sulfur concentration distribution in a melanised neuron from Parkinson's substantia nigra, collected at beamline I14; (b) Optical image of melanised neurons in an unstained tissue section of approx. 30 µm thickness; (c) Axial view of the human brain, highlighting the region incorporating neuromelanin-pigmented substantia nigra; (d) STXM composite map showing neuromelanin (green) and surrounding tissue (grey) in control substantia nigra, for data collected at beamline I08. Part (c) was adapted, under license CCBY4.0, from Blausen.com staff, WikiJournal of Medicine 2014, 1, DOI: 10.15347/wjm/2014.010.

Despite the importance of recognising pigmentation loss in Parkinson's tissue, conventional analysis relies on visible light, restricting neuromelanin visualisation to only the biggest and darkest clusters and excluding those too faint to view using an optical microscope[2]. Enhancing neuromelanin contrast by staining is effective but prohibits chemical analysis of neuromelanin-associated metal ions. Although the need for a neuromelanin-specific marker was recognised over three decades ago[2], it has not yet been met. Meeting this analytical challenge requires a unique combination of measurement sensitivity, specificity and spatial resolution; synchrotron tools may hold the key.

The aim of this work was to use synchrotron X-ray microscopy in the hard and soft X-ray regimes to identify new means for mapping neuromelanin *in situ* without requirement for chemically-disruptive labelling.

At beamline I14, neuromelanin-rich regions of Parkinson's substantia nigra tissue were mapped for multiple elements simultaneously using nanoscale hard XRF imaging. Sulfur was shown to be unambiguously elevated in neuromelanin granules relative to surrounding tissue (Fig. 1a). Sulfur is also ubiquitously distributed throughout human brain tissue, for example in sulfates and in various amino acids. Hard XRF imaging is an exceptional tool for visualising the variety of elements associating with neuromelanin, but a more direct marker was still required to map neuromelanin with complete independence from surrounding tissue material (Fig. 1b). This was achieved using a soft X-ray approach (Fig. 1d) as described below.

Scanning Transmission X-ray Microscopy (STXM) was employed at beamline I08, with additional data obtained at beamline 11.0.2 at the Advanced Light Source, USA, to obtain images and spectral data from ultra-thin sections of human substantia nigra. Image sequences were acquired over a specified energy range known as a stack, enabling X-ray absorption spectra to be derived from target regions within the tissue. This approach was optimised in prior work to provide detailed compositional analysis of amyloid plaque cores[3]. Stacks were collected over the carbon K-edge at 100-200 nm spatial resolution to reveal organic compositional features associated with neuromelanin-rich regions within neurons, as well as tissue areas adjacent to the neurons known as the neuropil.

Neuromelanin-rich regions were identified using STXM in unstained tissue sections, guided by correlative silver nitrate staining of neuromelanin in adjacent tissue sections (Fig. 2a). X-ray absorption spectra acquired from neuromelanin granules displayed a different shape to spectra acquired from tissue regions, including a reproducible peak at 287.4 eV that was not present in the tissue spectra (Fig. 2e,f). Speciation maps, created by subtracting an off-peak image (not associated with any spectral features) from an image taken at 287.4 eV, revealed a detailed depiction of neuromelanin distribution (Fig. 2c).

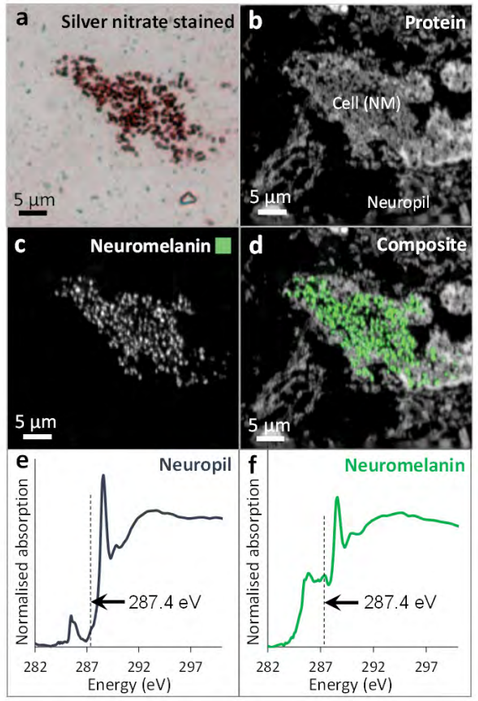

Figure 2: Melanised neuron identified in neurologically-healthy control substantia nigra using optical microscopy, then mapped using STXM at the carbon K-edge in an adjacent unstained tissue section. Data collected at beamline I08. (a) Silver nitrate stained cell showing neuromelanin (NM) distribution; (b) Protein map showing tissue structure; (c) Neuromelanin map generated using absorption peak at 287.4 eV; (d) Composite map showing tissue-derived protein (grey), neuromelanin (green); (e) Carbon K-edge spectrum from neuropil region;. (f) Carbon K-edge spectrum from neuromelanin-rich region. A dashed line marks the position of the absorption feature distinguishing neuromelanin at 287.4 eV.

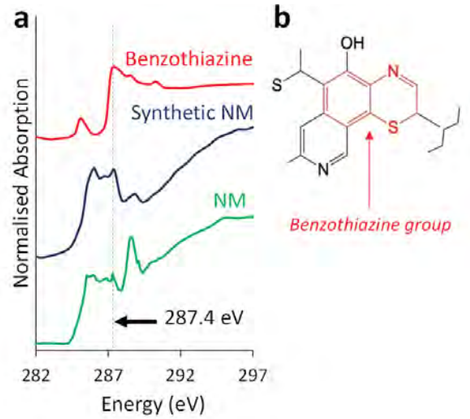

Figure 3: (a) carbon K-edge X-ray absorption spectra from intracellular neuromelanin (NM), synthetic NM analogue, and neuromelanin constituent group benzothiazine. Data collected at beamline I08. Intracellular and synthetic neuromelanin display the same spectral features. The peak at 287.4 eV (marked by a dashed line) is also shared with benzothiazine; (b) Benzothiazine group shown in red in the region of the neuromelanin polymer where it is incorporated.

Imaging at nanoscale resolution enabled individual neuromelanin granules to be clearly resolved, and the correlation between the neuromelanin distributions in stained and STXM-mapped tissue sections was verified. Iron mapping using STXM, and subsequently confirmed using XRF mapping, also demonstrated some neurons to be heavily loaded with iron. This is consistent with neuromelanin's strong affinity for iron.

The same spectral features observed for biological neuromelanin were reproduced in spectra acquired from synthetic neuromelanin analogues (with and without iron loading), confirming that the peak originated from the neuromelanin polymer (Fig. 3). The overall neuromelanin spectrum was distinct from those of its precursor materials, dopamine and L-cysteine. However, a sharp absorption feature was observed at 287.4 eV in the spectrum for benzothiazine, a constituent functional group of the melanin polymer (Fig. 3). The characteristic absorption peak at 287.4 eV was ultimately attributed to 1s → σ* (C-S) electron transitions in the benzothiazine spectrum, reported to occur around this energy in a range of similar organic, sulfur-containing molecules[4].

Using this novel approach to neuromelanin visualisation, neuromelanin contrast was verified for substantia nigra tissue from multiple Parkinson's cases, as well as for cases of Alzheimer's disease, Neurodegeneration with Brain Iron Accumulation, and neurologically healthy controls.

Use of soft x-ray STXM enabled neuromelanin to be distinguished from surrounding tissue, as well as from other intracellular proteins including ferritin and alpha-synuclein, without chemical labelling or prerequisite identification of cells. Application of multi-modal synchrotron techniques across different beamlines, including the nanoscale XRF imaging illustrated here in tandem with STXM, presents further opportunities to investigate neuromelanin's interactions with metal ions. This may help to understand better the enigmatic role of neuromelanin in Parkinson's disease and related disorders.

References:

1. Zucca F. A. *et al.* Interactions of iron, dopamine and neuromelanin pathways in brain aging and Parkinson's disease. *Prog. Neurobiol.* **155**, 96–119 (2017). DOI: 10.1016/j.pneurobio.2015.09.012
2. Hirsch E. *et al.* Melanized dopaminergic neurons are differentially susceptible to degeneration in Parkinson's disease. *Nature* **334**, 345–348 (1988). DOI: 10.1038/334345a0
3. Everett J. *et al.* Nanoscale synchrotron X-ray speciation of iron and calcium compounds in amyloid plaque cores from Alzheimer's disease subjects. *Nanoscale* **10**, 11782–11796 (2018). DOI: 10.1039/c7nr06794a
4. Myneni S. C. B. Soft X-ray spectroscopy and spectromicroscopy studies of organic molecules in the environment. *Rev. Mineral. Geochemistry* **49**, 485–579 (2002). DOI: 10.2138/gsrmg.49.1.485

Funding acknowledgement:
This work was supported by EPSRC grants EP/N033191/1, EP/N033140/1, EP/K035193/1, an EPSRC Doctoral Training Award to Jake Brooks (EP/N509796/1), and a Royal Society Newton-Bhahba International Fellowship for Samya Banerjee. We also thank Diamond Light Source, where the majority of the synchrotron data presented in this study were collected, for access to beamlines I08 (proposals SP15230, SP15854, SP20809, MG24526) and I14 (proposal MG24531).

Corresponding authors:
Dr Jake Brooks, School of Engineering, University of Warwick, j.brooks.1@warwick.ac.uk; Prof. Joanna Collingwood, School of Engineering, University of Warwick, J.F.Collingwood@warwick.ac.uk

Watching magma on the move

Related publication: Dobson K. J., Allabar A., Bretagne E., Coumans J., Cassidy M., Cimarelli C., Coats R., Connolley T., Courtois L., Dingwell D. B., Di Genova D., Fernando B., Fife J. L., Fyfe F., Gehne S., Jones T., Kendrick J. E., Kinvig H., Kolzenburg S., Lavallée Y., Liu E., Llewellin E. W., Madden-Nadeau A., Madi K., Marone F., Morgan C., Oppenheimer J., Ploszajski A., Reid G., Schauroth J., Schlepütz C. M., Sellick C., Vasseur J., von Aulock F. W., Wadsworth F. B., Wiesmaier S. & Wanelik K. Quantifying Microstructural Evolution in Moving Magma. *Front. Earth Sci.* **8**, 287 (2020). DOI: 10.3389/feart.2020.00287

Publication keywords: Volcanology; Rheology; Synchrotron; *in situ*; Magma; X-ray tomography

The magma stored beneath volcanoes is an evolving mixture of molten rock (liquid), crystals (solid) and bubbles (gas). The amount and distribution of these three phases control how, and if, the magma flows. When magma erupts and cools, it has a very different crystal and bubble content. As we cannot take a microscope down into the magma beneath a volcano, we need to develop laboratory techniques to understand how and when magma moves.

Previous experiments showed that interactions between the solid particles and gas bubbles control magma's ability to flow. In this study, researchers recreated flowing magma, using high-speed X-ray imaging on Diamond Light Source's Joint Engineering Environmental and Processing (JEEP) beamline (I12) to watch these interactions. This research developed the technical tools to look at magma at high magnification during deformation and flow. The 4D data (3 dimensions plus time) showed, for the first time, how much the distribution of bubbles, liquid and crystals changes during flow, how many bubbles coalesce into larger bubbles, and how different regions of the sample behave very differently.

This research is part of a larger project investigating how magma structure at the microscopic scale controls flow. A better understanding of how magma behaves will improve our ability to predict how a volcano will erupt. More widely, magmas are just one example of a complex multi-phase fluid. The methods developed here can be used to investigate other similar systems, such as concrete, ceramics and certain foodstuffs.

Magma is a constantly evolving mixture of crystals and bubbles suspended in silicate melt. Magmatic behaviour as it starts to move, as it flows, fragments and during any subsequent eruption is controlled by the rheological properties at that specific point in time and space. A complex rheological evolution is driven by the changing melt viscosity, volume, componentry, and size distribution of the suspended phase(s). In most magmas (where the crystal +/- bubbles are >25-30 volume %), the spatial distribution of, and interactions between crystals and bubbles is also critical.

A key challenge in volcanology is to describe magmatic processes as rheologically controlled behavioural 'tipping points', and ultimately to identify how these are recorded in volcano monitoring signals. Recent work on understanding the rheology of magmatic suspensions have demonstrated that changes in magma viscosity and the transition from Newtonian to non-Newtonian are controlled by the crystal and bubble content, shape, surface texture, size distributions and strain rate[1,2]. However, characterisation of the sample textures (critical for deriving rheological laws) is, without exception, restricted to snapshots before and after an experiment.

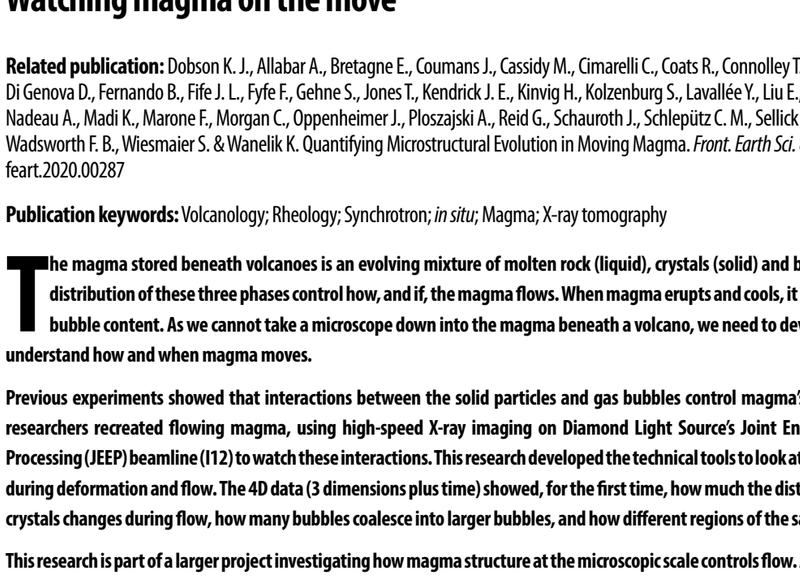

Figure 1: The XRheo system installed at I12 (a) Photo; (b) schematic. This system can be easily adapted to other synchrotron or laboratory imaging systems and used ex situ for laboratory bench testing. (c) single use cup and spindle configuration for high temperature set up (d) typical acquisition protocol used in this study, with the timing of the repeated multi-scan acquisitions adjusted to fit key sections of a deformation cycle.

To date, experimental work typically captures only a small piece of that evolution and then only the effects on bulk rheological behaviour. Understanding and predicting the rheological properties requires knowledge of particle-particle particle-bubble and bubble-bubble interaction microphysics that we currently lack because we cannot observe magmatic flow *in situ*. The rocks we can recover post-eruption contain textural and chemical overprints acquired during the entire evolution from initial melt formation to cooling, and do not represent the magma as it was in motion.

In this study we deploy a bespoke high temperature furnace and the XRheo rheological apparatus on I12, exploiting the high-speed X-ray tomography capability of the beamline to capture the evolution of magmatic microstructure during flow for the first time. The experimental set up that we developed and the analytical protocols illustrated in Fig. 1 now permits detailed, *in situ*, characterisation of sample textures, allowing accurate parameterisation of the rheological data: and opening up an entirely new field of study in magma rheology.

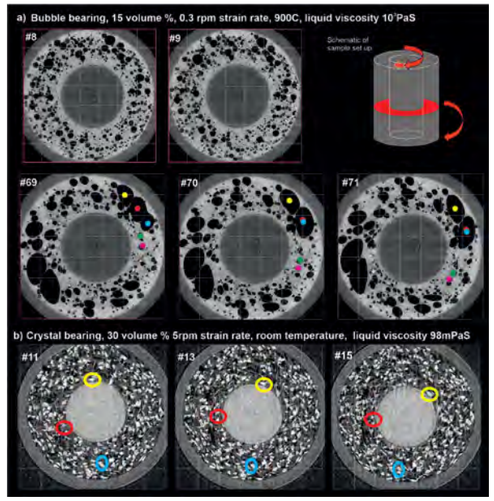

Figure 2: 2D greyscale images from mid-height slice perpendicular to the rotation axis (see insert) showing the microstructural evolution of two suspensions. A 1 mm grid has been overlain all images. (a) steady state deformation phase of a high temperature bubble bearing synthetic magmatic sample (900° C, 0.3 rpm differential spindle speed). Several bubbles are marked in frames #69-71 so you can track motion. (b) steady state deformation of a low temperature analogue system (N2700000 oil + 30% by volume olivine crystals, room temperature, 5 rpm differential spindle speed).

The focus of this study was primarily the successful deployment of the XRheo. The published study shows how standard wide gap Couette rheological testing protocols can be modified to work in a rotating frame of reference. The rotating reference is provided by the beamline and defined by the image acquisition requirements of the sample material. Initial imaging of the sample with the spindle applying zero torque gives a 3D understanding of the initial microstructure, before deformation is initiated (during imaging) by increasing the rotation speed of the spindle to the appropriate differential strain rate. By imaging before deformation and continuously through acceleration and into steady state deformation we were able to capture the evolving microstructure alongside the standard rheological measurements.

By using a 'gapped' acquisition protocol (1 tomography collected every n/2 rotations we were able to get spatially registered data, while balancing the competing needs of high acquisition rates (to prevent motion blur), obtaining measureable but not excessive displacements between 3D frames, and keeping total data volumes manageable. To explore a large experimental space we integrated complementary data from high viscosity-low strain rate experiments (>2 hours per experiment, ~1 s per 3D dataset) collected at the TOMCAT beamline (Swiss Light Source), with data from the full range of viscosity - strain rate conditions collected using high-speed monochromatic tomography at I12 (0.5 to 0.0125 s per 3D dataset). This covered off liquid viscosities of 10^{-3}-10^{4} Pa.s, crystal and bubble concentrations of 0-50 volume %, and more than 2 two orders of magnitude in strain rate without reaching the practical limit of data quality.

Focusing first on simple bubble-bearing crystal-free systems and then working towards increasing microstructural complexity we were also able to identify the complex range of microstructural changes that happen during the onset of deformation. The spatial and temporal heterogeneity in the displacements continue through the acceleration phase and still occur well into 'steady state' deformation. The textural evolution can be clearly seen in the reconstructed data, even when considering only a few time points within the longer time series (illustrated in Fig. 2). The benefit of the tomographic time series is that it enables more quantitative analysis of the heterogeneity in the microstructure using Digital Volume Correlation (DVC) (Fig. 3, the data shown are for the same part of the bubble-bearing time series as in Fig. 2). Although only just beginning the process of quantitative analysis in this study, by applying a multiscale nested global DVC[3] approach we can already identify regions of higher (and lower) than average displacement. The non-Newtonian behaviour and influence of the microstructural changes is clear in the heterogeneity and magnitudes of the displacements. For example, localised coalescence events accelerate regions of the melt beyond than maximum applied strain rate.

While the detailed work of developing the micro-mechanical understanding of phase interactions recorded here is the focus of ongoing work; this study showcases the potential of real-time tomography and *in situ* experiments to quantify the complex volcanic and magmatic processes of flow and deformation, and could provide new insight on a much wider variety of complex fluids.

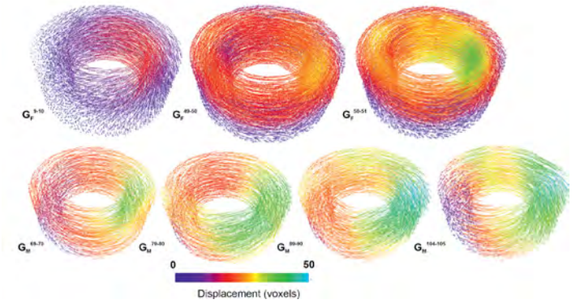

Figure 3: DVC outputs from several sequential time steps during acceleration (top) and steady state (bottom) deformation (including those shown in Fig. 2a).

References:

1. Mader H. M. *et al.* The rheology of two-phase magmas: A review and analysis. *J. Volcanol. Geotherm. Res.* **257**, 135–158 (2013). DOI: 10.1016/j.jvolgeores.2013.02.014
2. Truby J. M. *et al.* The rheology of three-phase suspensions at low bubble capillary number. *Proc. R. Soc. A Math. Phys. Eng. Sci.* **471**, 20140557 (2015). DOI: 10.1098/rspa.2014.0557
3. Madi K. *et al.* Computation of full-field displacements in a scaffold implant using digital volume correlation and finite element analysis. *Med. Eng. Phys.* **35**, 1298–1312 (2013). DOI: 10.1016/j.medengphy.2013.02.001

Funding acknowledgement:
This work was supported by NERC M018687/1 & M018687/2, ERC Starting Grant 406388 (SLiM), ERC ADV Grants 247076 (EVOKES) and 834225 (EAVESDROP) and the H2020 Marie Skłodowska-Curie fellowship DYNAVOLC – No.795044, and benefited from access to TOMCAT beamline X02DA of the SLS under proposal 20150413, as well as to Diamond Light Source for time on I12-JEEP under proposal EE15898.

Corresponding author:
Dr Katherine Dobson, University of Strathclyde,
katherine.dobson@strath.ac.uk

Understanding the complex 3D structures of metal carbides for optimising the manufacture of Ni superalloys

Related publication: Zhang Z., Khong J. C., Koe B., Luo S., Huang S., Qin L., Cipiccia S., Batey D., Bodey A. J., Rau C., Chiu Y. L., Zhang Z., Gebelin J.-C., Green N. & Mi J. Multiscale characterization of the 3D network structure of metal carbides in a Ni superalloy by synchrotron X-ray microtomography and ptychography. *Scr. Mater.* **193**, 71–76 (2021). DOI: 10.1016/j.scriptamat.2020.10.032

Publication keywords: Synchrotron X-ray microtomography; Ptychography; Metal carbides; Solidification; IN713LC Ni superalloy

Metal carbides are important microstructure constituents in polycrystalline Ni-based superalloys. They play a dominant role in determining the formation of cast defects and the strength of the alloys. However, the nucleation and growth dynamics of metal carbides, especially the true 3D network structure and morphology formed in different solidification conditions, have not been fully understood.

Researchers focused on studying the 3D network structures and distribution of the metal carbides in a widely used IN713LC Ni superalloy. Their objective was to reveal the true 3D spatial information of the metal carbides and to understand the nucleation and growth dynamics of the metal carbides in different solidification conditions.

The microtomography capability at the Diamond-Manchester imaging branchline (I13-2) offers a spatial resolution down to ~1 µm, while the ptychography capability at the Coherence branchline (I13-1) provides a spatial resolution down to ~30 nm. The research demonstrated clearly the advantage and technical potential of using the two complementary tomography techniques.

The team found individual MC carbides distributed on the grain boundary between the gamma and gamma prime phases. The dominant growth directions of carbide branches were mainly determined by the local composition of the remaining liquid phase and geometric constraints. The metal carbides exhibited spherical, strip or network structure depending on the solidification cooling rates. The 3D characteristics of those structures were quantified for the first time. The findings can assist in optimising the manufacture of Ni superalloys to reduce casting defects. Scientists can use the rich 3D datasets to understand the initiation and propagation of crack at metal carbides during plastic deformation and service more quantitatively.

Nickel based superalloys have been widely used for producing high-temperature structural components in aircraft and land turbine engines, rocket engines, nuclear power and chemical processing plants[1]. These superalloys present a unique microstructure where the ordered intermetallic γ′(Ni3Al) precipitates distribute coherently within a continuous γ(Ni) matrix. In addition, metal carbide is another important microstructure constituent in the polycrystalline Ni-based superalloys due to its excellent high-temperature stability. The carbide is designed to improve the high-temperature strength of the superalloy through strengthening the grain boundary and preventing grain boundary sliding[2]. However, metal carbides can cause casting defects during the solidification process as well as crack initiation and propagation during plastic deformation. Until now, the nucleation and growth dynamics of metal carbides, especially the true 3D network structure and morphology of metal carbides formed in different solidification conditions have not been fully understood.

In this research, synchrotron X-ray microtomography and ptychography were used complementarily to characterise, across the micro- and nanolength scale, the true 3D network structure, morphology and distribution of metal carbides in a widely used IN713LC Ni superalloy.

The microtomography experiments were carried out on branchline I13-2. Figure 1 shows the 3D network structure of the carbides in a relatively large volume for the two samples with solidification cooling rates of 0.27 K/s and 1.12 K/s respectively. It is clear that the carbide network distributed along the edge of the secondary dendrite arms in 3D space and within the interdendritic region. At a higher cooling rate of 1.12 K/s (Fig. 1b), the interval of the secondary dendrite arms became smaller, leading to smaller local volume for the carbide network. Moreover, the spherical (blocky type in 2D view) and irregular rod (strip type in 2D view) carbides were predominant in the sample of 1.12 K/s in spite of the formation of some small carbide networks (Fig. 1d). At a low cooling

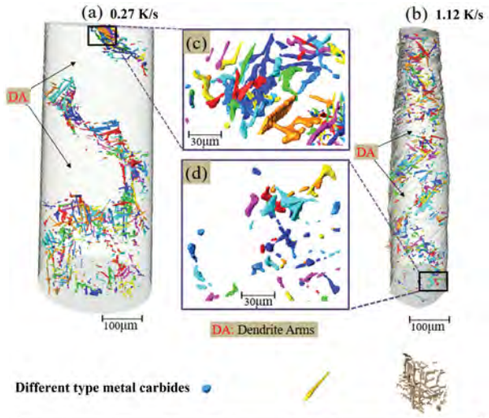

Cooling rate	Carbides		Spherical Carbides			Rod Carbides			Network Carbides		
K/s	Volume (µm³)	Volume Fraction (%)	Volume (µm³)	Number	Average Size (µm³)	Volume (µm³)	Number	Average Size (µm³)	Volume (µm³)	Number	Average Size (µm³)
0.27	64658	1.04	8345	663	13	39592	426	93	16720	51	328
1.12	35690	1.18	6355	463	14	24726	281	88	4609	16	288

Figure 1: The 3D morphologies, distribution and network of the carbides. (a) and (b) are the 3D morphology and network of the carbides in the samples with cooling rate of 0.27 K/s and 1.12 K/s, respectively; (c) and (d) are the enlarged local carbide morphology for (a) and (b); (e) and (f) are the particle size distribution and the shape factor distribution for the spherical and rod carbides.

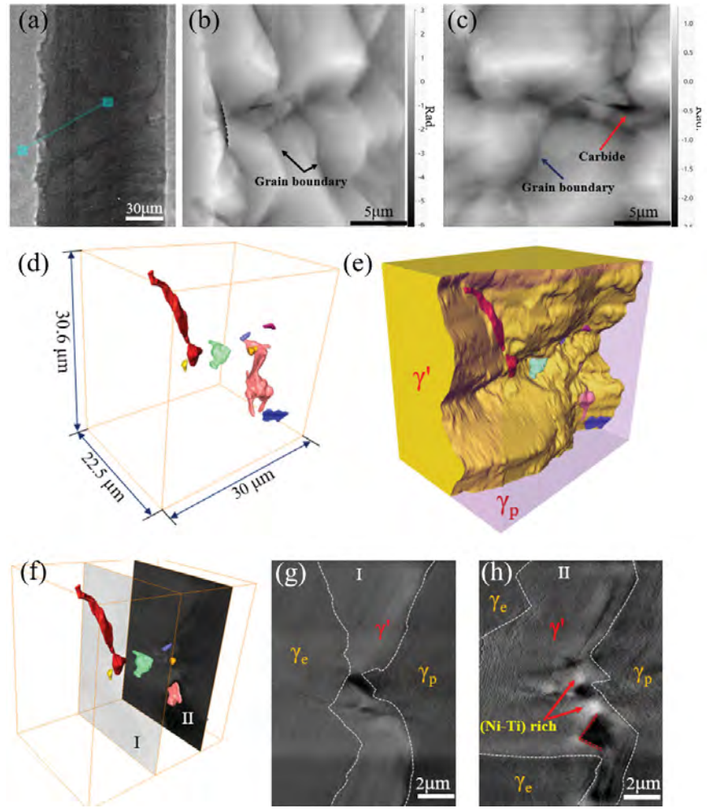

Figure 2: X-ray ptychography image and tomography for the carbides in the sample with a cooling rate of 1.12 K/s. (a) a transmission projection; (b) and (c) are the retrieved 2D projections at –83.5 ° and 45 °, respectively; (d) 3D morphologies for the carbides with a higher resolution of 30 nm; (e) the correlations of carbides, γ and γ′ phases in 3D space; (f) indicates the extract slice positions for (g) and (h); (g) shows the spherical carbide and its correlation with other phases; (h) is the strip carbide and its correlation with other phases.

rate of 0.27 K/s, the spherical and rod carbides interconnected each other and formed compact and complex carbide networks (Fig. 1c). Such a feature is often observed as script-typed carbides in a 2D projection (or sectional) view. The complex carbide network was due to further growth of the spherical and rod carbides and coalescence between each other. The average particle sizes for the rod carbides in the 0.27 K/s sample were 97 µm³, confirming the further growth and coalescence of the carbides due to having sufficient diffusion time in the low cooling rate sample. In particular, the average size of the network carbides changed from 288 to 328 µm³. The comparison of the shape factor (Fig. 1f) distribution for the samples with different cooling rate reveals that the individual carbides grew from the spherical morphology to rod morphology when reducing the cooling rate. The skeletonisation analysis of the network structure[3] further revealed the growth paths of the carbide branches during solidification.

The ptychographic X-ray computed tomography was carried out on the Imaging & Microscopy beamline (I13-1), revealing the detailed morphology and phase relationships of the metal carbides with the *γ* and *γ›* phases. Figure 2 shows that these carbides were localised on the grain boundaries between the matrix *γ and γ›* phase. The typical 2D slices containing carbides extracted from the 3D tomographic dataset (Fig. 2d-h) reveal that the dominant growth directions of carbide branches were mainly determined by the local composition of the remaining liquid phase and geometric constraints.

References:

1. Unocic R. R. *et al.* Mechanisms of creep deformation in polycrystalline Ni-base disk superalloys. *Mater. Sci. Eng. A* **483**–**484**, 25–32 (2008). DOI: 10.1016/j.msea.2006.08.148
2. Long H. *et al.* Microstructural and compositional design of Ni-based single crystalline superalloys - A review. *J. Alloys Compd.* **743**, 203–220 (2018). DOI: 10.1016/j.jallcom.2018.01.224
3. Zhao Y. *et al.* 3D characterisation of the Fe-rich intermetallic phases in recycled Al alloys by synchrotron X-ray microtomography and skeletonisation. *Scr. Mater.* **146**, 321–326 (2018). DOI: 10.1016/j.scriptamat.2017.12.010

Funding acknowledgement:
Project Funding & Financial Support: UK Engineering and Physical Sciences Research Council (Grant No. EP/L019965/1), the Royal Society Industry Fellowship (for J. Mi in 2012-2016) and the Chinese Scholarship Council (Funding No. 201806785038 for Z. Zhang's visiting fellowship in the academic year 2019-2020); the relevant synchrotron X-ray beamtime awarded by Diamond Light Source (MT9974, MT13488 and MG22525); access to the University of Hull supercomputer, Viper, and the assistance by the support team (Mr Chris Collins, in particular) for data analysis and visualisation.

Corresponding authors:
Prof. Jiawei Mi, Department of Engineering, University of Hull, J.Mi@hull.ac.uk; Dr Zhiguo Zhang, Institute of Advanced Wear & Corrosion Resistant and Functional Materials, Jinan University, China, zhigzhang@jnu.edu.cn

Tracking the shape of nutshells during biochar production

Related publication: Barr M. R., Jervis R., Zhang Y., Bodey A. J., Rau C., Shearing P. R., Brett D. J. L., Titirici M-M. & Volpe R. Towards a mechanistic understanding of particle shrinkage during biomass pyrolysis via synchrotron X-ray microtomography and in-situ radiography. *Sci. Rep.* **11**, 2656 (2021). DOI: 10.1038/s41598-020-80228-x

Publication keywords: Biomass pyrolysis; Biochar; X-ray imaging; Morphology; Adsorption

A charcoal-like product known as 'biochar' can be produced from agricultural waste biomass such as nutshells. One conversion method is pyrolysis, a process that involves heating the waste in the absence of oxygen. During pyrolysis, changes in the size and shape (morphology) of particles increase the surface area of the biomass. This surface area controls how biochar binds to (adsorbs) pollutants, speeds up chemical reactions, and stores energy. A lack of understanding of how biomass morphology changes during biochar production makes it difficult to tailor biochar properties for specific applications.

Facilities at the Diamond Manchester Imaging Branchline (I13-2) enabled a team of researchers to conduct rapid high-resolution X-ray imaging of biomass. This allowed real-time tracking of particle morphology and porosity during pyrolysis. The results showed that the morphology and porosity of different nutshells evolved differently during pyrolysis. However, these differences were less pronounced in biomass pre-soaked with an alkaline solution. Almond shells shrank more but gained less porosity than walnut shells, which have thicker-walled cells on average. The results suggest that the difference is related to how heat penetrates particles of biomass during pyrolysis. Porosity was found to accumulate towards the centre of particles during pyrolysis for the same reason.

The ability to customise biochar morphology would benefit its many environmental applications. These include removing pollutants from air, water, and soil; speeding up chemical reactions; and even storing energy. Tracking the morphology of biomass during biochar production is the first step towards achieving this.

Lignocellulosic biomass, the primary sources of which are agricultural and forestry waste, is naturally porous and thus has a high surface area to volume ratio. This allows it to adsorb (bind at the surface) a large quantity of molecules, materials, or organisms (adsorbates) relative to less porous materials. Upon heating without addition of an oxidising atmosphere, biomass undergoes a complex transformation that vastly further increases its adsorptive surface area[1]. The process leading to this transformation is known as pyrolysis and the result as biochar. For this reason, biochar is recognised as a universal adsorbent and is used for such applications as air, water, and soil treatment; catalysis; and energy storage.

Efficacy of biochar for these adsorption applications relies heavily on char morphology. Beyond simply maximising adsorbent surface area, adsorbates must be able to access the internal surface area of particles, which is dependent on pore and particle morphology. During pyrolysis, both pore and particle morphology evolve—these processes are commonly referred to as particle shrinkage, but in reality this term encompasses two parallel processes: bulk particle shrinkage and porosity gain.

Properly accounting for bulk particle shrinkage and porosity gain based on direct observation of morphological evolution during pyrolysis is the first step towards controlling biochar morphology by choice of production conditions. To achieve this, it was necessary to observe biomass particles during pyrolysis (*in-situ*). Imaging only after pyrolysis (*ex-situ*) would neglect the effects of cooling and recovering chars for analysis. This work represents the first *in situ* X-ray imaging study of biomass pyrolysis. A combination of *in situ* synchrotron radiography and *ex situ* synchrotron X-ray microtomography were used to track the evolution of external and internal particle morphology during pyrolysis.

Facilities at the Diamond Manchester Imaging Branchline (I13-2) allowed for rapid acquisition of microscopic phase-contrast-enhanced X-ray images, such that both particle morphology and internal biomass microstructure could be tracked in real time during reaction. A polychromatic 'pink' beam was used for both 2D imaging (radiography) and 3D imaging (tomography) to achieve the short acquisition times required. In-line phase-contrast enhancement ensured that solid-gas interfaces (surface area) within particles were highlighted in acquired images.

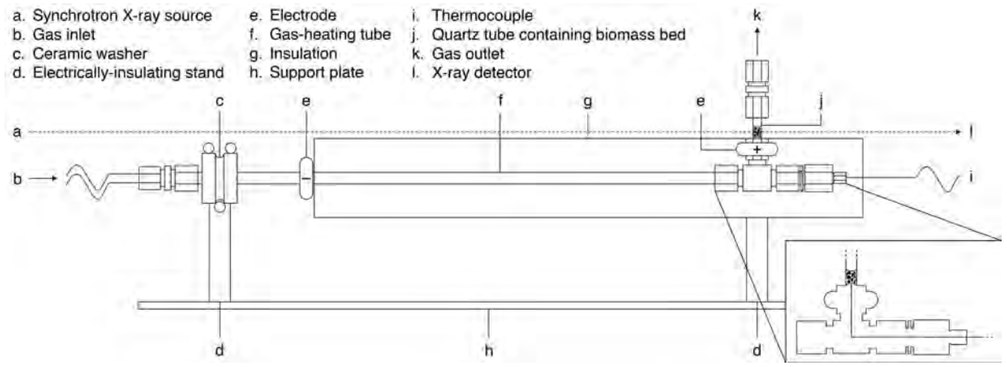

Figure 1: Schematic of the novel purpose-built reactor used to acquire in situ radiographs.

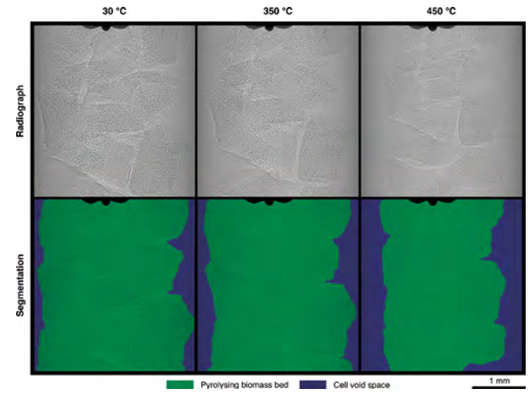

Figure 2: Radiographs and segmentations of a bed of almond shells undergoing pyrolysis.

A novel reactor (Fig. 1) was developed to enable *in situ* synchrotron radiography of fixed beds of pyrolysing biomass. Biomass was convectively heated by a stream of preheated argon to peak temperatures between 250 and 450 °C, during which radiographs were acquired in a single plane (Fig. 2). After pyrolysis, tomographic data were acquired for chars and representative raw samples. These were used to reconstruct tomograms (Fig. 3) with the open-source modular pipeline Savu[2]. Images were first normalised, followed by corrections for optical distortions and ring artefacts. Prior to reconstruction, a Paganin filter was applied to enhance phase contrast in images. Segmentation (determining which pixels represent which materials) to enable quantitative analysis of images relied on custom code, which has been made publicly available[3].

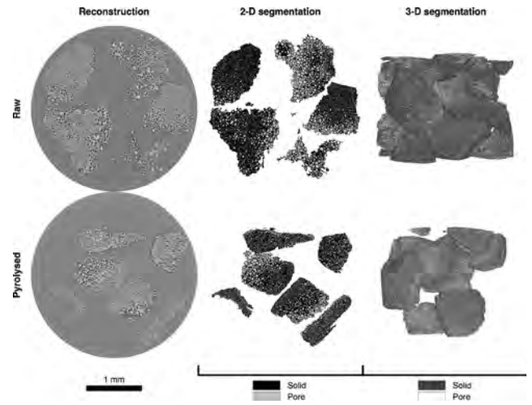

Figure 3: Reconstructed and segmented tomograms and corresponding 3D renderings of raw and pyrolysed almond shells. In 3D renderings, the scale bar corresponds to the frontmost plane.

In order to study the effects of feedstock morphology on particle shrinkage, two types of nut shells, almond and walnut, were used as pyrolysis feedstocks. These nut shells are quite similar, both botanically and chemically. However, almond shells, which contain highly porous vascular channels, were found to shrink more and to gain less porosity than were walnut shells, which have thicker-walled and more irregularly shaped cells[4]. In addition to pyrolysis of raw biomass, that of biomass treated with sodium hydroxide (known to increase porosity and reduce lignin content)[5], was observed and this alkaline pretreatment was found to reduce the difference between feedstocks with respect to morphological evolution during pyrolysis. These phenomena were thought to be related to differences in the heat-transfer properties of feedstocks.

The rate at which particles equilibrate to the temperature of their environment affects the way in which volume is lost as gas is formed and released from solid particles. Inside particles, during this transient phase, there exists a cooler region in which heat can move within the particle faster than reaction can occur. This region therefore reacts throughout its volume and thus porosity is gained here. Outside this region, towards the surface of particles, reaction occurs more quickly than heat is able to penetrate into the particle, meaning volume is lost only at the surface in this region and thus bulk shrinkage occurs. The faster a particle can equilibrate, the more bulk shrinkage and the less porosity gain it will experience. Structural differences, like those between almond and walnut shells[4] and those caused by alkaline pretreatment[5], affect this rate of equilibration.

Image analysis[3] of tomograms (Fig. 3) revealed that pyrolysis led to a redistribution of pore volume away from particle surfaces, meaning newly formed surface area may be less accessible to adsorbates. The observed concentration of pores, and therefore adsorptive surface area, towards the centre of particles during pyrolysis poses a challenge to optimising their adsorption capacity. Feedstocks with lower initial porosity have more potential for increased surface area upon pyrolysis. However, although surface area increases as pyrolysis proceeds, so too does it become increasingly inaccessible. One solution may be alkaline pretreatment of biomass, which increases feedstock porosity prior to pyrolysis[5], thus reducing the heat transfer limitations likely to be driving the concentration of pores towards particle centres. Another solution could be milling particles after pyrolysis to expose newly formed surface area when using biochar for adsorption applications. Equally, concentration of porosity towards the centre of particles may in fact prove beneficial for retention of adsorbates, which is critical when using biochar to remove harmful pollutants from the environment.

References:

1. Jones K. *et al.* New Applications of X-ray Tomography in Pyrolysis of Biomass: Biochar Imaging. *Energy & Fuels* **29**, 1628–1634 (2015). DOI: 10.1021/ef5027604
2. Atwood R. C. *et al.* A high-throughput system for high-quality tomographic reconstruction of large datasets at diamond light source. *Philos. Trans. R. Soc. A Math. Phys. Eng. Sci.* **373**, 20140398 (2015). DOI: 10.1098/rsta.2014.0398
3. Meredith Rose Barr. (2020, April 6). X-Ray Image Analysis Code (Version v1.0.1). Zenodo. http://doi.org/10.5281/zenodo.3742013
4. Queirós C. S. G. P. *et al.* Characterization of walnut, almond, and pine nut shells regarding chemical composition and extract composition. *Biomass Convers. Biorefinery* **10**, 175–188 (2020). DOI: 10.1007/s13399-019-00424-2
5. Brodeur G. *et al.* Chemical and Physicochemical Pretreatment of Lignocellulosic Biomass: A Review. *Enzyme Res.* **2011**, 787532 (2011). DOI: 10.4061/2011/787532

Funding acknowledgement:
This research was supported by Queen Mary University of London. We acknowledge Diamond for time on beamline I13-2 under Proposal MG21587. This research utilised Queen Mary's Apocrita HPC facility, supported by QMUL Research-IT. http://doi.org/10.5281/zenodo.438045.

Corresponding authors:
Meredith Rose Barr, Queen Mary University of London, m.r.barr@qmul.ac.uk; Dr Roberto Volpe, Queen Mary University of London, r.volpe@qmul.ac.uk

Characterising defects in lithium-ion battery particles

Related publication: Heenan T. M. M., Wade A., Tan C., Parker J. E., Matras D., Leach A. S., Robinson J. B., Llewellyn A., Dimitrijevic A., Jervis R., Quinn P. D., Brett D. J. L. & Shearing P. R. Identifying the Origins of Microstructural Defects Such as Cracking within Ni-Rich NMC811 Cathode Particles for Lithium-Ion Batteries. *Adv. Energy Mater.* **10**, 2002655 (2020). DOI: 10.1002/aenm.202002655

Publication keywords: Batteries; Cathodes; Degradation; Electric vehicles; Microstructure; NMC811; Particle cracking

Battery electrodes are composed of many millions of particles. Lithium-ions entering and leaving these particles charge and discharge the battery. Defects in the particles reduce the battery's capacity. This would impact electric vehicle range in automotive applications, for example, requiring drivers to stop more frequently to recharge. Therefore, it is crucial to investigate which particles contain defects, whether different types of defects exist, and how we might prevent them forming.

Electrode particles are spheres with diameters on the order of tens of microns (smaller than a human hair). Due to their small size, investigating their properties requires high-resolution specialist facilities, such as those at the Hard X-Ray Nanoprobe beamline (I14) at Diamond Light Source. The defects have complex origins, requiring the use of multiple investigation techniques at once, for which I14 was specifically designed.

Batteries that are nickel-based (around 80%), with manganese and cobalt making up the other 20%, are of particular interest to the automotive industry. By analysing various particles at I14 and comparing the results with data collected in the labs at University College London (UCL), researchers found a correlation between the manganese content and the ordering of the particle's crystals. However, they attributed the amount of cracking within the particle to the crystal orientations. Preventing the manganese from leaving the particles may maintain the crystal ordering. Aligning the crystals, or making larger single crystals, may avoid - or at least delay - particle cracking. Overcoming these issues would allow electric vehicles to travel for longer before needing to recharge.

The automotive sector is being rapidly electrified in an effort to improve air quality and combat global warming. However to achieve this, affordable battery electric vehicles (BEVs) are required that can drive a sufficient distance on a single charge and then recharge quickly, all while maintaining a suitable lifetime. The choice of electrode chemistry and microstructure strongly influence a BEV's ability to meet these demands and consequently, materials developments have accelerated in recent years.

Layered oxide cathodes such as $LiNi_xMn_yCo_zO_2$ (NMC) are promising candidates for the next-generation of BEVs. Particularly, Ni-rich variations (e.g. $LiNi_{0.8}Mn_{0.1}Co_{0.1}O_2$ or NMC811) are of interest because of the toxicity, expense and supply-chain issues associated with Co. Moreover, increasing the Ni content also promotes high electronic conductivities and fast Li^+ diffusivities, as well as increased volumetric and gravimetric energy densities. However, there is a significant disparity between the practical and theoretical performances of these materials due to complex degradation mechanisms. Furthermore, large voltage windows are employed with high upper cut-offs (e.g. > 4.5 V vs. graphite) in order to maximise the accessible capacity, which accelerates degradation. For instance, Ni-rich NMC is known to suffer from: lower thermal runaway temperatures; metal dissolution; surface species; accelerated lattice collapse; oxygen evolution; and surface rock-salt formation. There are many outstanding scientific questions relating to the performance loss of Ni-rich NMC in long term cycling. Therefore this work aimed to correlate several characterisation methods in order to determine cause and effect relationships for such degradation[1].

Commercial polycrystalline NMC811 materials generally consist of broad size distributions (e.g. 3 – 30 µm) of highly spherical particles (e.g. sphericity > 0.7) that are labelled 'secondary' and are composed of many 'primary' particles that are around an order of magnitude smaller in size (e.g. 0.1 – 1 µm). The primary particles are mostly single crystals and are often assembled randomly into the secondary particle agglomerate, resulting in the polycrystalline definition. The secondary particles are then made into a slurry with a carbon and binder domain (CBD), to be printed and calendared onto an aluminium current collector. See Fig. 1 for a visual representation of this material of interest.

For this work, commercial NMC811 electrode material was initially examined in the pristine state using lab-based nano X-ray computed tomography (CT) at UCL. This revealed that even before operation around one-third of the secondary particles exhibited some form of defect, especially towards the electrode-separator interface where calendaring affects during manufacturing are thought to produce localised pressure maxima which are dissipated by the cracking of particles. Cracking, that is particularly evident in the larger secondary particles, reduces the

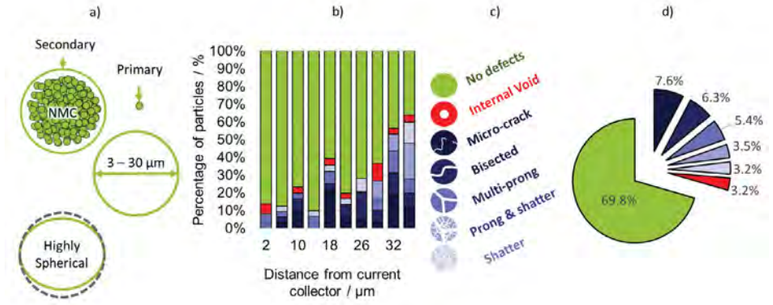

Figure 1: Microstructure of NMC811. (a) Diagrams of the NMC structure; (b) The number of defected secondary NMC particles with respect to electrode depth; (c) Visual aid for the various types of secondary particle defects; and (d) The average defect composition for a commercial NMC material.

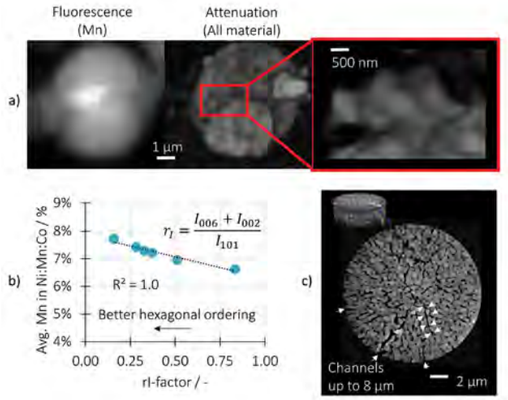

Figure 2: Multi-modal imaging for the correlation of X-ray absorption, fluorescence and diffraction data. (a) Aligned Mn fluorescence and (all material) attenuation maps of a single NMC particle, with a magnified section of Mn-rich surface cluster; (b) Correlated diffraction and fluorescence data for six individual NMC particles, displaying the r factor and minimum Mn content; and c) An absorption nano-CT cross-sectional ortho-slice of an NMC particle. All particles reported within this figure were cycled to 4.5 V for 5 cycles, before imaging.

effective particle size distribution, increasing the surface area and the population of possible sites for undesirable side-reactions. To observe such substantial particle cracking before operation is significant if it triggers severe degradation and capacity loss. It is therefore advised that novel and improved manufacturing methods are explored in order to mitigate this issue.

To examine how these defects progress with operation, the NMC811 material was assembled into coin cells against graphite anodes and then cycled to various upper cut-off voltages (4.2 – 4.5 V). Using lab-based micro X-ray CT microstructural cracking defects were observed to deteriorate throughout the entire electrode volume after high voltage operation, thought to be triggered by the rapid contraction of the c lattice parameter above ca. 60 % State of Charge (SoC) - the level of charge of an electric battery relative to its capacity. Through multi-length-scale correlation a novel defect algorithm was developed that is capable of detecting defects within low resolution tomograms (three dimensional datasets), consequently improving materials statistics substantially, and allowing an order of magnitude more secondary particles to be examined at once. Developments such as this lend themselves well to advanced data processing such as machine learning and other artificial intelligence and as such, endeavours should be made to release such data openly for development and analysis by the wider computing and modelling community[2].

To expand the investigation into crystallographic and chemical analysis required synchrotron radiation and the world-class facilities of beamline I14 at Diamond. Focusing on the high voltage (4.5 V) material, individual secondary particles ranging from 2 – 8 µm in diameter were extracted from the bulk material and imaged in UCL's lab-based nano-CT before being transferred to the beamline. At I14 the Ni:Mn:Co content ratio could be studied via X-ray fluorescence (XRF) analysis (Fig. 2). It became evident that the amount of Mn within the secondary particles varied considerably, with some regions as low as 4%. Moreover, Mn-rich regions (detected using XRF) had formed not as coatings on the particles but as distinct surface clusters and, when correlated to the lab-based nano X-ray CT, were found to be of significantly lower density than the NMC. The importance of Mn-mobility during early-stage cycling has two key implications. Firstly, the correlative data confirms that the surface cluster is not the NMC that is desired during manufacturing and therefore will not contribute to the cell capacity as intended, occupying precious volume that could otherwise be filled by useful NMC. Secondly, if the Mn cluster is not inert/inactive in its current state, it may travel to the anode and deposit on the surface, impeding Li+ transport pathways. For future work it is therefore of interest to monitor the Mn mobility during early cycling in more detail and particularly possibility of its presence on the anode[3].

Due to the specialist set-up at I14, X-ray diffraction (XRD) data could be collected simultaneously to the XRF data, providing information of the particle crystal structure. Correlating the XRF and XRD data revealed a greater disordering in the particles that had lost more Mn. It is thought that the presence of Mn within the NMC structure alleviates Jahn-Teller distortion by the donation of a Mn electron at low voltages; if Mn is leaving the structure during early cycling, distortions may be reintroduced. The secondary particles were then examined using the lab-based nano-CT data to explore if there was a correlation between the crystal disordering (and Mn loss) with the degree of secondary particle cracking. Interestingly, there was no clear correlation at this stage suggesting that the c lattice contraction and the random orientation of the crystals likely dominates the secondary particle cracking at low cycle numbers but undesirable crystal strain accumulates in the primary particles due to Mn loss that is possibly not yet visible at the secondary particle scale. High resolution lab-based nano CT of single secondary particles at UCL strengthened this conclusion by the observation of cracking produces similar structures within NMC811 as within lower Ni content NMC (e.g. NMC111)[4]. Consequently, it was concluded that single crystal alternatives may provide some alleviation for cracking induced by lattice contraction but accumulative crystallographic strain, particularly in the presence of Mn loss, could remain problematic[5].

In this work we explore the various mechanisms that may lead to particle defects that are responsible for capacity loss and ultimately, the deterioration of BEV performance. Many of these findings were only possible through correlative characterisation methods requiring the specialist facilities such as those at I14. Multi-modal imaging such as this is highly powerful and will likely continue to advance many aspects of materials developments for years to come, not only in the field of Li-ion batteries but throughout various fields of science and engineering.

References:

1. Li W. *et al.* High-nickel layered oxide cathodes for lithium-based automotive batteries. *Nat. Energy* **5**, 26–34 (2020). DOI: 10.1038/s41560-019-0513-0

2. Heenan T. M. M. *et al.* Data for an Advanced Microstructural and Electrochemical Datasheet on 18650 Li-ion Batteries with Nickel-Rich NMC811 Cathodes and Graphite-Silicon Anodes. *Data Br.* **32**, 106033 (2020). DOI: 10.1016/j.dib.2020.106033

3. Dose W. M. *et al.* Effect of Anode Slippage on Cathode Cutoff Potential and Degradation Mechanisms in Ni-Rich Li-Ion Batteries. *Cell Reports Phys. Sci.* **1**, 100253 (2020). DOI: 10.1016/j.xcrp.2020.100253

4. Tsai P. C. *et al.* Single-particle measurements of electrochemical kinetics in NMC and NCA cathodes for Li-ion batteries. *Energy Environ. Sci.* **11**, 860–871 (2018). DOI: 10.1039/c8ee00001h

5. Liu Y. *et al.* Microstructural Observations of "Single Crystal" Positive Electrode Materials Before and After Long Term Cycling by Cross-section Scanning Electron Microscopy. *J. Electrochem. Soc.* **167**, 020512 (2020). DOI: 10.1149/1945-7111/ab6288

Funding acknowledgement:
This work was carried out with funding from the Faraday Institution (faraday.ac.uk; EP/S003053/1), grant number FIRG001 and FIRG003; and the EPSRC grant EP/M014045/1. The authors acknowledge Diamond Light Source for time on beamline I14 under proposals sp20841 and mg23858. The authors would like to acknowledge the Royal Academy of Engineering (CiET1718\59) for financial support.

Corresponding authors:
Dr Thomas Heenan, University College London/Faraday Institution, t.heenan@ucl.ac.uk; Prof. Paul Shearing, University College London/Faraday Institution, p.shearing@ucl.ac.uk

Studying biological structures using electron ptychography

Related publication: Zhou L., Song J., Kim J. S., Pei X., Huang C., Boyce M., Mendonça L., Clare D., Siebert A., Allen C. S., Liberti E., Stuart D., Pan X., Nellist P. D., Zhang P., Kirkland A. I. & Wang P. Low-dose phase retrieval of biological specimens using cryo-electron ptychography. *Nat. Commun.* **11**, 2773 (2020). DOI: 10.1038/s41467-020-16391-6

Publication keywords: Cryo-electron microscopy; Electron ptychography; Rotavirus; HIV-1 virus like particles

Cryo-electron microscopy (Cryo-EM) is an essential tool for obtaining high-resolution structural studies of biological systems. However, unstained biological samples are extremely sensitive to radiation and the images obtained have low contrast and low signal-to-noise ratios. There are techniques to overcome these limitations. However, it is more challenging to obtain high-resolution images for heterogeneous samples, specimens at low concentration, low symmetry structures and small or flexible molecules.

An international team of researchers working at Diamond's Electron Physical Sciences Imaging Centre (ePSIC) set out to develop a new method for imaging biological structures using electrons. Ptychography is an alternative method based on scanning diffraction microscopy. It uses a probe to illuminate the sample and records a series of far-field diffraction patterns. The team demonstrated that this novel method is suitable for studies of many biologically important structures, including small molecules below a size that can be imaged using conventional Cryo-EM.

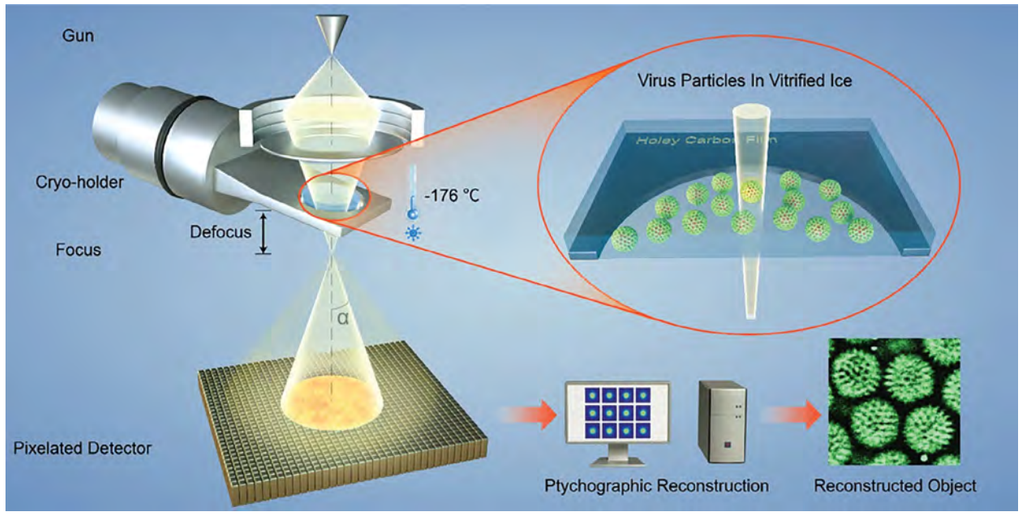

Figure 1: Schematic diagram of the optical configuration for cryo-electron ptychography.

Determining the three-dimensional (3D) structures of biological macromolecules and assemblies at high resolution in their native states has driven significant and sustained efforts to develop electron microscopy (EM) techniques, most notably phase contrast cryo-EM[1]. However, unstained biological samples embedded in thin vitreous ice are essentially pure phase objects that are extremely radiation sensitive[2]. As a result cryo-EM images must be recorded at very low electron dose and have a low signal-to-noise ratio and low contrast. In conventional cryo-EM high defocus values are used to boost low spatial frequencies, improving contrast, but at the expense of corrupting information at intermediate and high spatial frequencies due to rapid oscillations in the phase contrast transfer function. Despite these fundamental limitations, class averaging large numbers of homogeneous objects and using direct electron detectors to improve the signal-to-noise ratio has enabled a large number of 3D biological structures at close to atomic resolution to be solved[3]. There is therefore a need to develop new methods that improve information transfer over a wide range of spatial frequencies, which work efficiently at low electron dose and which can be used over wide fields of view.

Ptychography is one such method based on scanning diffraction microscopy, as originally proposed by Hoppe[4]. This approach uses a probe to illuminate the sample and records a series of far-field diffraction patterns as a function of probe position, as illustrated in Fig. 1, to recover the sample exit plane wavefunction using one of several iterative or direct methods. Ptychography has been most widely with X-rays as the wavefunction recovered can exceed the spatial resolution that can be obtained using conventional optics. Due to its efficient phase recovery, robustness under low electron dose conditions[5] and the quantitative recovery of the 3D wavefunction, electron ptychography has significant potential for application in the structure determination of biological samples. An important advantage of this method is the ability to tune information transfer to maximise low or high spatial frequencies by altering the probe convergence angle.

In the work reported in Nature Communications, a team from ePSIC, the Electron Bio-Imaging Centre (eBIC) and Oxford and Nanjing Universities, demonstrate the first application of cryo-electron ptychography (cryo-EPty) using a defocused electron probe to image biological structures. Electron ptychographic datasets were recorded 300kV using a double aberration corrected JEOL ARM300CF at ePSIC on a 256 × 256 pixel Merlin Medipix3 direct electron detector. The phase and amplitude of the complex specimen exit wavefunction were recovered using the ptychographic iterative algorithm

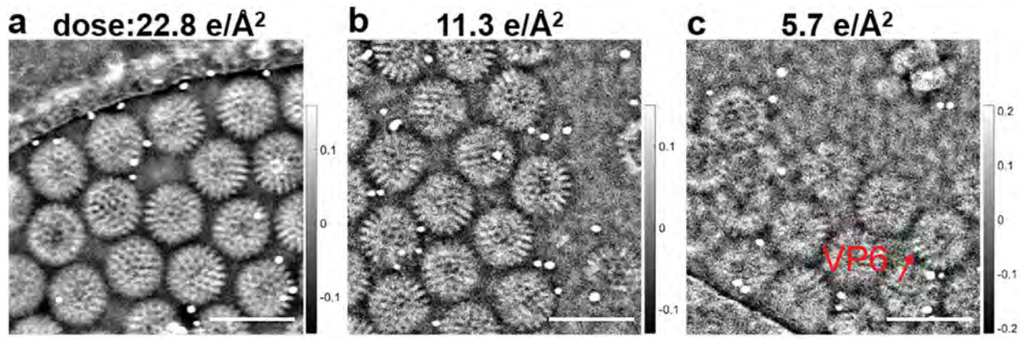

Figure 2: Reconstructed phase of rotavirus DLPs at doses of (a) 22.8 e/Å²; (b) 11.3 e/Å²; (c) 5.7 e/Å². The red arrow in (c) indicates the VP6 trimers. Scale bars: 100 nm.

(ePIE). To be generally applicable to structural studies of biological materials in a cryo state, ptychographic reconstruction must be effective under low dose conditions, similar to those used for conventional EM imaging. Defocused probe ptychography uses a relatively large probe (25-30 nm in diameter for the experiments reported here) and hence it is optimised to scan a large sample area with a small number of probe positions, reducing the total dose if the overlap between neighbouring probe positions is optimised. Fig. 2 shows ptychographic phase reconstructions of rotavirus double-layered particles (DLPs) embedded in vitrified ice for doses between 22.8 e/Å² and 5.7 e/Å². The ptychographic phase of rotavirus DLPs shows strong contrast from the virus particles, where both the capsid trimers of viral protein 6 (VP6) and the channels between these can be clearly seen. The observation of these features and the resolution of the viral capsid's symmetric elements are consistent with those observed using conventional defocused transmission electron microscope (TEM) images and with the known 3D structure (PDB ID 3KZ4).

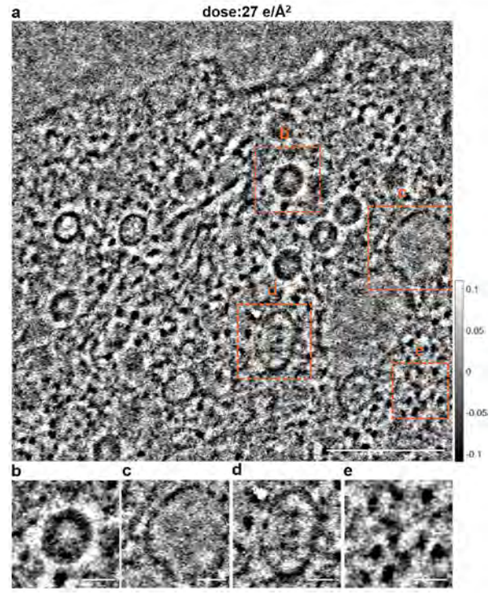

Figure 3: (a) Micrometre scale reconstructed phase of an Adenovirus-infected cell recorded at a dose of 27 e/Å²; (b) Magnified views of a viral particle; (c) A vacant vesicle; (d) A transport vesicle; and (e) Free ribosomes taken from regions indicated with orange squares in (a). Scale bars are (a) 300 nm and (b to e) 50nm.

The final requirement for the application of ptychographic reconstruction in structural and cellular biology is the ability to recover information from large fields of view corresponding to cellular ultrastructure. To demonstrate this, a micrometre (1.14 × 1.14 μm) area of a resin-embedded Adenovirus-infected cell was reconstructed at a dose of 27 e/Å² (Fig. 3). The ptychographic phase shows good visibility of ultrastructural features of varied size, including cytoskeletal elements, viral particles, vacant vesicles, transport vesicles and free ribosomes. Moreover, as already noted, reconstruction of the ptychographic phase preserves low spatial frequency information, facilitating the location of these key molecular features in a cellular context.

In conclusion, the studies reported demonstrate that cryo-electron iterative ptychography provides high contrast quantitative phase recovery at an electron dose of 5.7 e/Å² over wide fields of view making this approach suitable for biological macromolecular imaging. This approach provides tunable, continuous wide-band information transfer including low spatial frequencies that are inaccessible using conventional phase contrast imaging. In addition, the efficiency of the phase recovery using ptychography provides higher signal-to-noise data than phase contrast imaging in cryo-EM, which potentially reduces the particle numbers required for 3D reconstruction, facilitating 3D classification of heterogeneous specimens at low concentration or from structures with low symmetry.

References:

1. Adrian M. *et al.* Cryo-electron microscopy of viruses. *Nature* **308**, 32–36 (1984). DOI: 10.1038/308032a0
2. Henderson R. The potential and limitations of neutrons, electrons and X-rays for atomic resolution microscopy of unstained biological molecules. *Q. Rev. Biophys.* **28**, 171–193 (1995). DOI: DOI: 10.1017/S003358350000305X
3. Bartesaghi A. *et al.* 2.2 å resolution cryo-EM structure of β-galactosidase in complex with a cell-permeant inhibitor. *Science.* **348**, 1147–1151 (2015). DOI: 10.1126/science.aab1576
4. Hoppe, W. Diffraction in inhomogeneous primary wave fields 1. Principle of phase determination from electron diffraction interference. Acta Crystallogr. A 25, 495-501 (1969).
5. Song J. *et al.* Atomic Resolution Defocused Electron Ptychography at Low Dose with a Fast, Direct Electron Detector. *Sci. Rep.* **9**, 3919 (2019). DOI: 10.1038/s41598-019-40413-z

Funding acknowledgement:
National Natural Science Foundation of China (11874199); UK Medical Research Council (MR/N00065X/1). We thank Diamond Light Source for access and support in the use of the electron Physical Science Imaging Centre (Instrument E02, EM17918) that contributed to the results presented.

Corresponding author:
Prof. Angus Kirkland, University of Oxford, angus.kirkland@materials.ox.ac.uk

Well defined single-site catalysts enabled by surface coordination chemistry

Related publication: Kang L., Wang B., Thetford A., Wu K., Danaie M., He Q., Gibson E. K., Sun L. D., Asakura H., Catlow C. R. A. & Wang F. R. Design, Identification, and Evolution of a Surface Ruthenium(II/III) Single Site for CO Activation. *Angew. Chemie - Int. Ed.* **60**, 1212–1219 (2021). DOI: 10.1002/anie.202008370

Publication keywords: Single-site; Coordination chemistry; Catalysis

First discovered in the 19th century, Ru^{II} compounds are widely used in catalysis, photocatalysis, and medical applications. They are usually obtained in a reductive environment, as molecular oxygen can oxidise Ru^{II} to Ru^{III} and Ru^{IV}. Researchers designed an air-stable Ru^{II} site that is coordinated on the polyphenylene-bipyridine (PPhen-bipy) based system. The team used the Electron Physical Science Imaging Centre (ePSIC) at Diamond Light Source to confirm the presence of Ru single-site. They performed their study at atomic resolution with High Angle Annular Dark-Field Scanning Transmission Electron Microscopy (HAADF-STEM). X-ray Absorption Spectroscopy (XAS) at Ru K-edge carried out at beamline B18 followed the evolution of the geometric structures of the Ru single-site during CO oxidation.

In addition, the HAADF-STEM study confirmed the successful synthesis of eight other metal single-sites coordinated with the PPhen-bipy framework. Those single-sites have well-defined geometric and electronic structures for catalytic applications. Such single-site catalysts exhibit great potential in life sciences and the pharmaceutical industry. The PPhen-bipy framework also enables the study of coordination chemistry at solid/gas interface, helping to understand structure-performance relationship of the surface single-sites.

Single-sites are the smallest catalytic active centres. They have discrete molecular orbitals that can be controlled *via* the geometric coordination environment, enabling the selective bond breaking and formation at the surface. Here a series of surface single-sites are designed at the surface of the polyphenylene-bipyridine (PPhen-bipy) framework (Fig. 1a). The bidentate bipy group coordinate single metal cations, forming well-defined and dispersed single-sites on the surface. High Angle Annular Dark-Field Scanning Transmission Electron Microscopy (HAADF-STEM) enables the direct observation of those single-sites with atomic resolution (Fig. 1b and Fig. 2). The images confirm the uniform dispersion of the single-site with very high density (from 2-5wt%). The X-ray Absorption Fine Structure (XAFS) study of those single-sites reveals their local coordination environment. Due to the fact that bidentate nitrogen coordinative environment in bipy is well preserved, the formation of surface -[bipy-MX_n] site is predictable according to coordination chemistry. Across the thirteen metal cations that is studied, nine single-sites are successfully prepared and validated. They are -[bipy-$Ru(III)Cl_4$]$^-$ (Fig. 1b), -[bipy-$FeCl_4$]$^-$, -[bipy-$CoCl_2$], -[bipy-$Ni(H_2O)_4$]$^{2+}$, -[bipy-$CuCl_2$], -[bipy-$ZnCl_2$] (Fig. 2a), -[bipy-$RhCl_4$]$^-$ (Fig. 2b), -[bipy-$PdCl_2$] (Fig. 2c) and -[bipy-$PtCl_4$] (Fig. 2d). Ag, Sn, Ir and Au form clusters instead of single-sites, due to their low coordination strength with bipy ligands. In addition to metal cations, the selection of ligands is also controllable. -[bipy-$RuCl_4$]-, -[bipy-$RuBr_4$]-, -[bipy-$CuCl_2$] and -[bipy-$Cu(H_2O)_4$]$^{2+}$ are achieved accordingly. The diverse selection of metal cations and ligands provides a single-site library with controllable geometric and electronic structures for a target catalytic reaction.

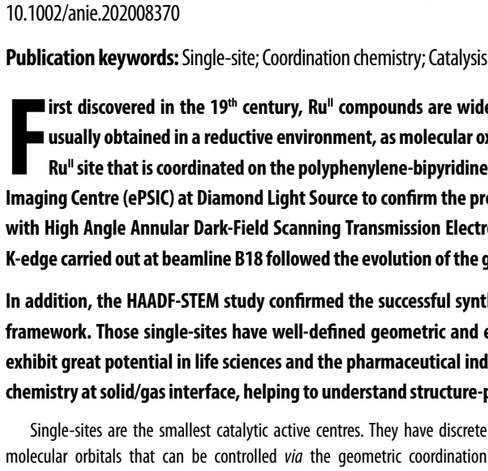

Figure 1: (a) Schematic of the general approach in creating the single-site coordination environment; (b) HAADF-STEM images of PPhen-[bipy-Ru(III)Cl_3]H; (c) Experimental and fitted EXAFS data of PPhen-[bipy-Ru(III)Cl_4]H. The inlet is the DFT simulation of the -[bipy-Ru(III)Cl_4]$^-$ structure.

The -[bipy-Ru(III)Cl_4]$^-$ site is further studied as a model system for catalytic CO oxidation. Upon heating in the presence of CO and O_2, a release of HCl is observed starting from 433 K. A surface adsorbed C≡O vibration is found in the Diffuse Reflectance Infrared Fourier Transform Spectroscopy (DRIFTS) at 2057 cm^{-1} (Fig. 3a). This vibration corresponds well to the FTIR spectrum of molecular mer(Cl)-[Ru(bipy)(CO)Cl_3][1]. The fitted extended XAFS spectrum shows the decrease of Ru-Cl coordination number from 4.0 ± 0.4 to 3.2 ± 0.2 while maintaining the bond distance at 2.35 ± 0.01 Å (Fig. 3b). A new Ru-CO scattering is observed at 1.88 ± 0.02 Å with a coordination number of 1.1 ± 0.2. The bond lengths are the same as the values reported for molecular *mer*(Cl)-[Ru(bipy)(CO)Cl_3] (Ru-N 2.08 Å, Ru-Cl 2.33 Å and Ru-C 1.89 Å)[1].

Both -[bipy-Ru(III)Cl_4]$^-$ and *mer*(Cl)-[bipy-Ru(III)(CO)Cl_3] are not active for CO oxidation. H_2 is then used to convert *mer*(Cl)-[bipy-Ru(III)(CO)Cl_3] into its active Ru(II) form. HCl is detected in the online mass spectrometry, suggesting the reaction between H_2 and the Cl$^-$ ligand. DRIFTS and FTIR spectra show a second C≡O stretching at 1996 cm^{-1} (Fig. 2c). This result matches the FTIR spectrum of molecular *cis*(CO)-*trans*(Cl)-[Ru(II)(bipy)$(CO)_2Cl_2$][2] but is different from *cis*(CO)-*cis*(Cl)-[Ru(II)(bipy)$(CO)_2Cl_2$] (2040 and 1980 cm^{-1}) [3]. In the EXAFS spectra, the Ru-Cl coordination number is reduced to 2.2 ± 0.3 with a slight increase of bond length to 2.39 ± 0.01 Å, confirming the ligand exchange of Cl$^-$ *via* CO with the help of H_2 (Fig. 2d). The coordination number of Ru-CO at 1.88 ± 0.01 Å increases to 1.9 ± 0.3. The Ru oxidation states is further confirmed in Ru L-edge and Cl K-edge XAFS spectra. The newly formed *cis*(CO)-*trans*(Cl)-[bipy-Ru$(CO)_2Cl_2$] site does not have the Ru 2p to 4d t_{2g} and Cl 1s to Ru 4d t_{2g} transition. This indicates that the Ru has the t_{2g}^6 configuration with oxidation state of +2.

Once transformed into the *cis*(CO)-*trans*(Cl)-[bipy-Ru(II)$(CO)_2Cl_2$] form, the single-site is then active for CO oxidation. An initial light off is shown at 388 K and 35% conversion at 453 K, P_{CO} = 0.01 bar and WHSV 60,000 ml×h^{-1} g^{-1}. An activation energy (Ea) of 90 kJ×mol^{-1} is determined at the WHSV of 600,000 ml×h^{-1} g^{-1}. The corresponding Turnover Frequency (TOF) is then calculated as 3.89 x 10^{-2} s^{-1} at 498 K, which is similar to the state-of-the-art Cu and Pt single-site over metal oxide support for CO oxidation. HAADF-STEM images show the high density of Ru^{2+} cations well dispersed on the polymer framework after catalysis. There is no cluster or particle formation. The distinct differences in CO oxidation activity between Ru(III) and Ru(II) single-site are resulted from their geometric and electronic properties. The former has three or four Cl- ligands, which are strong binding ligands in metal complexes. In comparison, the latter offers two exchangeable CO ligands in *cis* configuration, enabling the local activation of CO within the Ru coordination environment.

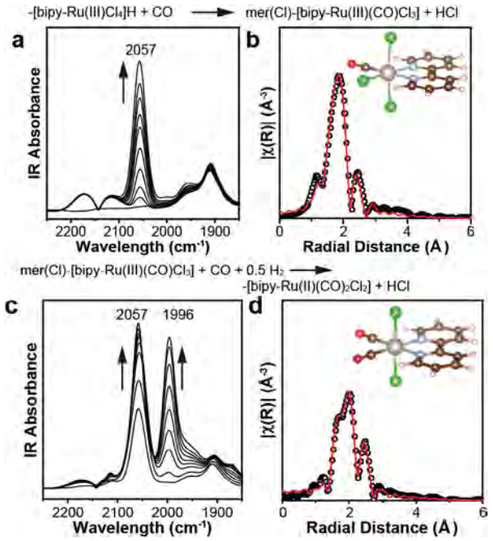

Figure 2: HAADF-STEM and EXAFS identifications of single-site PPhen-[bipy-MXn] structure. Cs-corrected HAADF-STEM images showing the single metal ions supported on PPhen-bipy for (a) Zn^{2+}, (b) Rh^{3+}, (c) Pd^{2+} and (d) Pt^{4+}. Corresponded experimental and fitted EXAFS result of (a) -[bipy-$ZnCl_2$], (b) -[bipy-$RhCl_3$], (c) -[bipy-$PdCl_2$] and (d) -[bipy-$PtCl_4$], respectively.

Single-site identification and characterisation is of great importance. The ePSIC and the Spectroscopy Group at Diamond provide state-of-the-art characterisation techniques and enable the accurate measurement of the single-site electronically and geometrically. More importantly, the rapid access and block allocation mode at these facilities enable the proof of concept design of single-site experiments, accelerating the materials, innovations for catalysis and energy applications.

References:

1. Pruchnik F. P. *et al.* Carbonyl ruthenium(III) complexes with 1,10-phenanthroline and 2,2'-bipyridine. *Polyhedron* **18**, 2091–2097 (1999). DOI: 10.1016/S0277-5387(99)00079-0
2. Kelly J. M. *et al.* Synthesis and spectroscopic characterisation of [Ru(bpy)2(CO)2](PF)6)2. *Inorganica Chim. Acta* **64**, L75–L76 (1982). DOI: 10.1016/S0020-1693(00)90282-2
3. Chardon-Noblat S. *et al.* Selective Synthesis and Electrochemical Behavior of trans(Cl)- and cis(Cl)-[Ru(bpy)(CO)2Cl2] Complexes (bpy = 2,2'-Bipyridine). Comparative Studies of Their Electrocatalytic Activity toward the Reduction of Carbon Dioxide. *Inorg. Chem.* **36**, 5384–5389 (1997). DOI: 10.1021/ic9701975

Funding acknowledgement:
EPSRC (EP/P02467X/1 and EP/S018204/1), Royal Society (RG160661, IES\R3\170097, IES\R1\191035, IES\R3\193038) and the Newton International Fellowship (NF170761).

Corresponding author:
Dr Feng Ryan Wang, Department of Chemical Engineering, University College London, ryan.wang@ucl.ac.uk

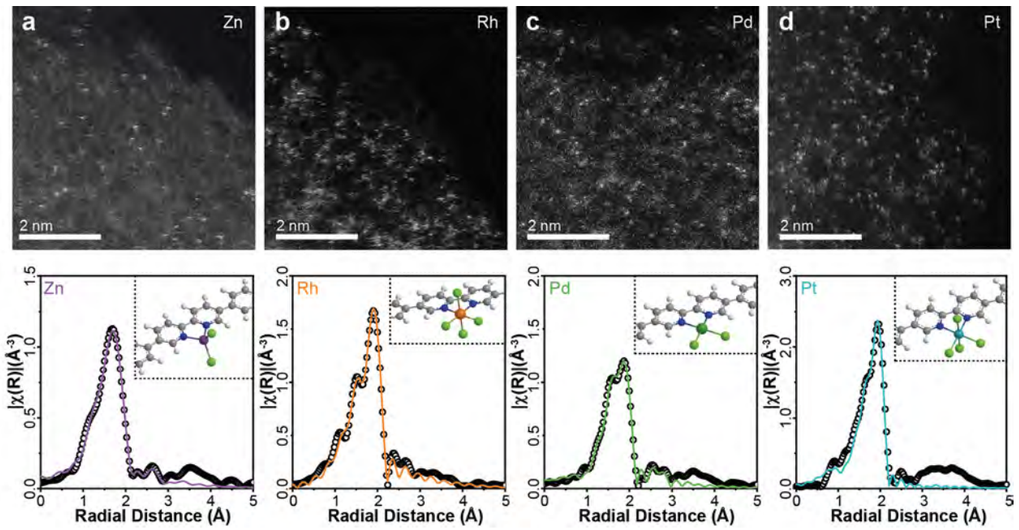

Figure 3: (a,c) In situ DRIFTS spectra, showing the formation of the CO stretching from -[bipy-Ru(III)Cl_4]- to -[bipy-Ru(III)(CO)Cl_3] and from mer(Cl)-[bipy-Ru(III)(CO)Cl_3] to cis(CO)-trans(Cl)-[bipy-Ru(II)$(CO)_2Cl_2$], respectively; (b,d) Corresponded experimental and fitted EXAFS data, respectively.

Crystallography Group

Joe Hriljac, Science Group Leader

The Crystallography Group at Diamond Light Source comprises the High-Resolution Powder Diffraction beamline (I11), the Extreme Conditions beamline (I15) the X-ray Pair Distribution Function (XPDF) beamline (I15-1) and the Small-Molecule Single-Crystal Diffraction beamline (I19). Bringing these beamlines together into one science group means we can fully exploit the technical and scientific expertise within its teams to provide the basis for future development and pioneering experiments.

The past year was a challenge for everyone with the COVID-19 pandemic, but especially so for beamlines in the Crystallography Group that were undergoing upgrades such as I11. At the time of writing, all the beamlines are fully operational again and we look forward to resuming a full user programme once safe working protocols allow. During the periods when there was user beam, I15-1 and I19 kept their programmes running via extensive use of mail-in and remote operations and both of these, as well as I15, hosted a few user experiments in the summer of 2020 when it was deemed safe. The hard work and dedication of the beamline and technical staff was commendable. In 2021 there will be fewer major projects being done in the group, but most significantly the I15/I15-1 wiggler source will be upgraded by a complete replacement of the cryocooling system in order to provide greater reliability of operation. The other significant investments agreed in 2020 were purchases of new DECTRIS detectors for I15 (a PILATUS3 X CdTe 2M) and I19 Experimental Hutch 2 (EH2) (an EIGER2 X CdTe 4M). Both detectors are on-site and commissioning of the I15 system has already started with that for I19 expected before the summer.

The other major effort in the Crystallography Group in 2020 was the development and presentation to the Diamond Scientific Advisory Committee (SAC) and the Diamond Industrial Science Committee (DISCo) of two Diamond-II (proposed upgrade programme) flagship proposals. The Nanofocus Extreme Conditions Undulator Beamline (NExCUBe) is designed to deliver a high energy (ca. 30 keV) sub-micron beam for diffraction and crystallographic studies and micro-focussed I15 (μ15) is designed as an extensive upgrade to optimise the beamline for higher energy (ca. 80 keV) *operando* and *in situ* diffraction and crystallographic studies. The two projects are interlinked as the full plan for μ15 can only be realised if the extreme conditions science currently done at I15 can be moved and NExCUBE is more than just a move. It would provide much greater brightness at 30 keV over the I15 wiggler source and, in conjunction with the supplementary facilities (e.g. gas loading, DAC provision) and I15 staff expertise, it would make Diamond internationally leading in the field. It is significant that the two proposals gathered excellent community support from 189 scientists that came from an international spread of universities (28 UK) and 15 companies/agencies.

I11 update

The high brightness beamline uses monochromatic X-rays in the range of 6 - 25 keV for high-resolution and time-resolved powder diffraction experiments in the first Experimental Hutch (EH1) or for Long Duration Experiments (LDEs) in EH2. The varied science programme supports a wide range of studies by chemists, physicists, materials scientists and environmental scientists in particular for non-ambient applications and experiments requiring unusual hardware setups such as toxic/corrosive gas absorption studies at cryogenic temperatures, resonant diffraction at high temperature and time-resolved *in operando* lithium-ion (Li-ion) battery work.

After running for over ten years, many components such as the monochromator, diffractometer and Multi-analyser Crystal (MAC) detector began to show signs of wear. An upgrade plan, endorsed by the SAC and DISCo at the end of 2017, to replace these components started in 2019 and the new Newport diffractometer was partly installed when site was shut down in March 2020. During the course of the remainder of 2020, the installation and commissioning resumed when possible under the COVID-19 working protocols. Finally in January 2021 the last stage, commissioning of the robot sample changer, was completed and the beamline is operational again. A superconducting undulator to replace the original in-vacuum system and provide better flux at high energy has undergone extensive specification and early prototype testing, and this should be complete and ready for installation late summer of 2021. Finally, an upgrade to the linear Position Sensitive Detector (PSD) in EH1 is planned, and it is anticipated that a next-generation detector should be available in late 2021 or early 2022.

I15 update

The Extreme Conditions beamline, I15, employs high energy X-rays to explore the structure of materials at high pressures, high and low temperatures, as well as other *in situ* and *in operando* conditions. The beamline receives an X-ray continuum from the superconducting wiggler; this allows for experiments that require monochromatic X-rays between 20 and 80 keV, as well as polychromatic beam. I15 was originally designed to serve the mineral physics community, which it has, whilst also assisting material scientists, chemists and solid-state physicists with their structural investigations, at pressure or otherwise.

I15 continues to offer extensive capabilities and support to users to assist their high-pressure studies. I15 users have pre-experiment access to bespoke assistance and training from our highly skilled staff in diamond anvil cell (DAC) preparation and loading, as well as the usage of beamline DACs for novice users for I15 experiments. The high-pressure gas loader available at I15 offers users the choice of many possible gases to use as their pressure transmitting media (PTM), allowing them to optimise for hydrostaticity with helium or neon, or choosing a PTM based on desired interactions with the sample at pressure. Work is underway to add hydrogen to our gas loading capabilities, originally scheduled for 2020 this has had to be pushed back into 2021 due to the pandemic. The recent addition of the laser heating system adds a further unique capability – the I15 system is capable of quickly ramping the laser power to perturb a sample without delivering too much heat to the bulk. Several small upgrades started in 2019, these include improved network infrastructure and a better design of the laser system. The network upgrade is complete and the upgraded laser system is currently being commissioned. In 2020 the low-temperature cryostat for DAC work was completed and commissioned off-line and in early 2021 commissioning work started with beam. The DECTRIS PILATUS3 X CdTe 2M arrived in late 2020 and it will provide much greater sensitivity to high-energy X-rays and the capability for much faster data collections. The first data was collected in early 2021 and now software and hardware improvements to take advantage of the speed and sensitivity offered by the new detector are being explored. Diffraction mapping with automated processing has been successfully tested with the existing Perkin Elmer detector - this functionality will be improved with the CdTe PILATUS3. Further upgrades to I15 to take full advantage of fast hardware-based scanning and mapping are planned.

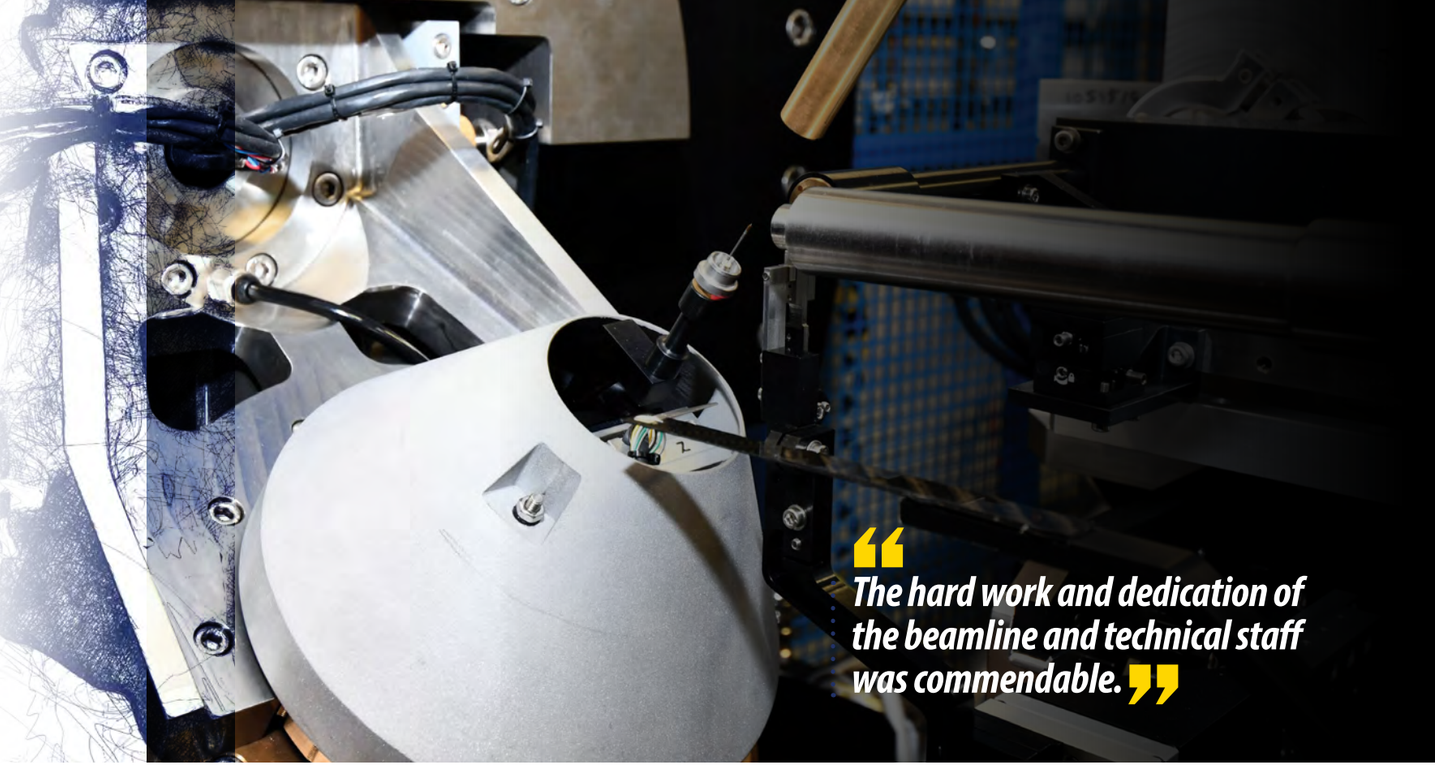

> *"The hard work and dedication of the beamline and technical staff was commendable."*

I15-1 update

The XPDF beamline, I15-1, is dedicated to producing high-quality X-ray scattering data for Pair Distribution Function (PDF) analysis. Operational since 2017, I15-1 has illuminated samples from diverse fields, from Earth sciences to pharmaceuticals, as well as material science and chemistry. XPDF receives X-rays from the inside edge of the wiggler fan, and this light is monochromated and directed to the end station in three energies: 40, 65 and 76 keV. PDF data are collected at high energies to produce the low sample absorption and high Q-range required for successful interpretation. Gaining structural information on amorphous samples is a primary goal of many XPDF experiments, but crystalline samples can also display local structure variations such as defects and disorder, which can be studied via PDF analysis. PDF data collections are rarely available at home institutions so in order to allow more people to exploit this powerful technique, I15-1 complements the standard proposal route with popular Rapid and Easy Access routes, where PDF data can be collected via a mail-in procedure.

Consisting of a sample position, with an optional sample-changing magazine, and two large area detectors, the end station is highly flexible and has been adapted to many *in situ* and *in operando* experiments, including variable temperature, gas flow, hydrothermal synthesis and electrochemical cycling. For more routine measurements, the 15-position sample changer has been a popular choice, allowing automatic data collection. Further upgrades, including a new end station and a sample-changing robot, progressed during 2020, and both should be commissioned during 2021. The final aspect of the current upgrade is a new detector based on CdTe sensors that will be much more sensitive at high energy and with faster electronics for data readout. These upgrades will be a synergistic addition to the existing autoprocessing infrastructure and will allow users to collect better data with less manual intervention.

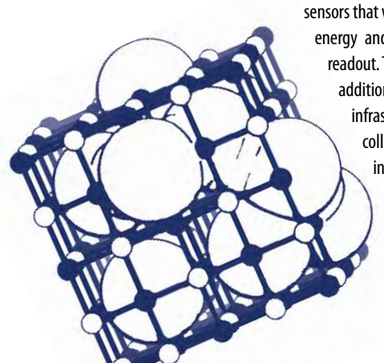

I19 update

The Small-Molecule Single-Crystal Diffraction beamline, I19, uses X-rays in the 5 – 25 keV energy range to determine the structures of small-molecule and extended three-dimensional systems, e.g. metal-organic frameworks (MOFs), with single-crystal diffraction techniques. These methods can be applied to the characterisation of novel materials or for investigating the variation in the structure of a crystalline material under an external physical influence such as a change in temperature, the exposure to a gas, photo-excitation or through the application of high-pressure.

The use of the robotic sample changer, and remote access, is now well established in EH1 of the beamline, where premounted samples are sent to Diamond under cryogenic storage, and users then run their beamtime from their home institutions. This mode of operation makes it possible to carry out chemical crystallography studies in a more responsive manner as beamtime can be scheduled in more regular, and shorter, periods. We now schedule individual shifts, rather than whole one-day (three shifts) blocks of beamtime, for those wishing to run their beamtime via the remote access route. For EH2, we have recently developed a cell which allows a high static electric field to be applied to the sample crystal. The application of electric fields to materials can result in a variety of responses that may have important technological applications, spanning electronic and ionic conductivity to piezo- and ferro-electricity.

In 2019, the original monochromator was replaced with an upgraded one of a new design, and this now affords greater beam stability and ease of wavelength change. The recent arrival of the DECTRIS EIGER2 X CdTe 4M to be placed in EH2 will see even further improvements in beamline capabilities for *in situ* studies.

The data collection software has also seen substantial work with greater integration of SynchWeb, ISPyB and dials/xia2, but also with local development more relevant to chemical crystallography in terms of optimising sample screening and choice of attenuation to minimise exposure times and subsequent beam damage. Overall, these have led to data collections at two-four times faster rates with equally good quality.

Fighting fatigue in lithium-ion batteries

Related publication: Xu C., Märker K., Lee J., Mahadevegowda A., Reeves P. J., Day S. J., Groh M. F., Emge S. P., Ducati C., Layla Mehdi B., Tang C. C. & Grey C. P. Bulk fatigue induced by surface reconstruction in layered Ni-rich cathodes for Li-ion batteries. *Nat. Mater.* **20**, 84–92 (2021). DOI: 10.1038/s41563-020-0767-8

Publication keywords: Lithium-ion batteries; Degradation; X-ray diffraction

Lithium-ion (Li-ion) battery technology is the most popular choice for electrification of transport, an essential step in reducing fossil fuel consumption and developing a more sustainable society. Layered nickel-rich lithium transition metal oxides offer excellent energy densities when used as state-of-the-art cathodes for electric vehicle batteries. However, this group of materials suffers from rapid performance loss. It is essential to understand the degradation mechanisms at the material level, particularly during long-term ageing.

Researchers used the Long Duration Experiments (LDE) facility at Diamond Light Source's High-Resolution Powder Diffraction beamline (I11) to track the evolution of the crystal structure of battery materials *operando* during their ageing. The LDE facility's unique capability, performing experiments over several months, is crucial to understanding battery degradation, which continues as the battery ages.

The results showed that a portion of the cathode material cannot reach the fully charged state after ageing, i.e. becomes fatigued and this portion increases as the ageing progresses. Combining the results from multiple techniques, the team proposed a 'pinning' mechanism, where the crystal lattice of the material is pinned by its surface, preventing the material from being fully charged. These layered nickel-rich lithium transition metal oxides are the most popular cathode materials in the foreseeable future and the degradation mechanism proposed is expected to be universal for all such materials. These findings are, therefore, highly relevant to the practical development of Li-ion batteries. They also highlight the vital importance of surface protection to mitigate degradation.

Layered nickel-rich lithium transition metal oxides ($LiTMO_2$, TM = Ni, Co, Mn, Al, etc.) are the state-of-the-art cathode materials for Li-ion batteries for electrical vehicle applications due to many of their merits, for instance, excellent energy densities and less usage of costly raw materials[1]. However, these Ni-rich materials typically suffer from more rapid performance fading compared to the canonical $LiCoO_2$ and their lower Ni-content analogues and the reason, at least in part, is nested in their structural instability during electrochemical cycling[2]. Layered Ni-rich materials possess an α-$NaFeO_2$ type structure with TM and Li occupying alternating layers as illustrated in Fig. 1a. During delithiation, the structure exhibits anisotropic changes such that the lattice gradually contracts in the *a* direction while expanding initially but then contracts rapidly in the *c* direction. In addition, as the material approaches highly delithiated state, the structure is also thermodynamically less stable. Moreover, the large anisotropic lattice change, particularly the rapid lattice collapse at high state-of-charge (SoC), can lead to mechanical degradations, for instance, particle fracturing.

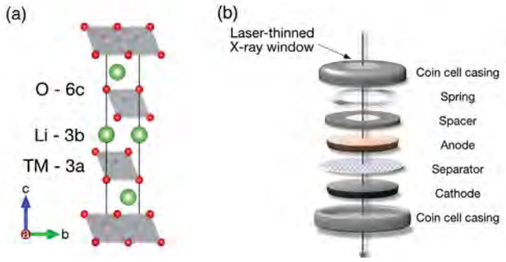

Figure 1: (a) Illustration of the crystal structure of the pristine NMC-811; (b) Schematic drawing of the laser-thinned coin cell. Reproduced with permission[3]. Copyright 2020, Nature Publishing Group.

In this study, a long-duration *operando* X-ray diffraction study was conducted to monitor the structure evolution of NMC-811 ($LiNi_{0.8}Mn_{0.1}Co_{0.1}O_2$) during its ageing[3]. Such long duration experiments possess significant technical challenges as many of the electrochemistry cells designed for *in situ*/*operando* X-ray diffraction studies often do not provide good air-tightness over the required timescale. Herein, a novel coin cell setup is reported for the first time with top and bottom casings thinned to ~50 μm in thickness using laser technology, as illustrated in Fig. 1b. The NMC-811/graphite cell studied here achieved more >1,000 cycles (~ 6-month time), providing an excellent opportunity to study the structural evolution of the NMC-811 cathode over a long period of ageing.

Our previous study showed that NMC-811 exhibits a solid-solution mechanism, that is, no phase transition, during initial lithiation and delithiation[4]. However, after ageing, evident peak broadening is observed at SoCs as shown by the (003) reflection in Fig. 2, which is indicative of the presence of multiple phases. In conjunction with *ex situ* diffraction results, a co-existence of a minimum of three NMC phases which have discernible lattice parameters, i.e. at different SoCs, has been confirmed. The phase with the (003) peak at the lowest position (hence largest *c*-parameter) is attributed to the one that is least charged, i.e. fatigued. Moreover, the population increases as evidenced by the change in the line-shape as well as phase quantification obtained from Rietveld refinements.

The lattice parameters of the fatigued phase in various aged samples, i.e. at different number of cycles, are found to be highly similar, which is a strong indication that this fatigue phenomenon is a structure-driven process. The fact that no long-range structure transformation is observed in the LDE results excludes the possibility that fatigue degradation is induced by bulk structure transformations. As for local environments, no obvious increase in the anti-site mixing (i.e. Ni present in the Li site, which is a known phenomenon in Ni-rich materials) nor drastic change in the lithium mobility (by solid-state Nuclear Magnetic Resonance (NMR) spectroscopy) has been observed. The possibilities that such heterogeneity in the SoC was introduced by intergranular cracking and kinetic limitation have also been excluded based on the fact that the fatigue phase is still detected in an electrochemically aged single-crystal NMC charged at an extremely slow rate.

One common phenomenon observed on the surface of Ni-rich cathodes is structure transformation from layered to more densified, rock salt-like structure. Unlike the bulk which expands and contracts considerably during delithiation (illustrated in Fig. 3a), the crystal structure of the surface rock salt remains unchanged due to its electrochemically inactive nature. This will, however,

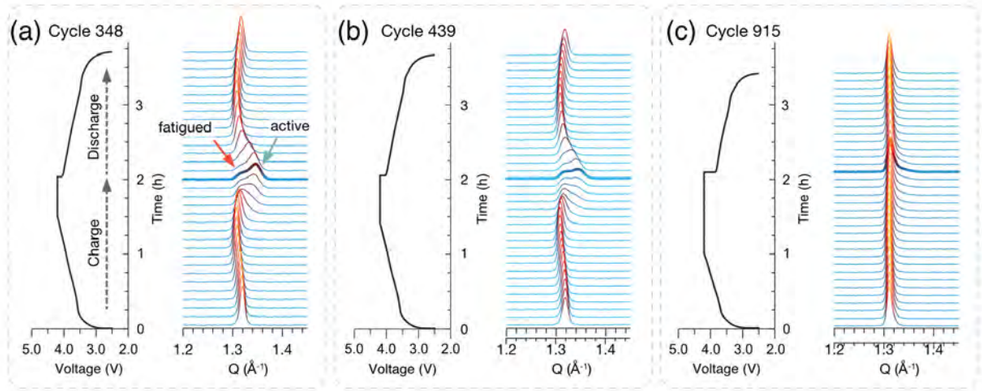

Figure 2: Evolution of the NMC (003) reflection at (a) cycle 348; (b) cycle 439; (c) cycle 915. The thickened line is the diffraction pattern collected at the end of the charging step. Reproduced with permission[3]. Copyright 2020, Nature Publishing Group.

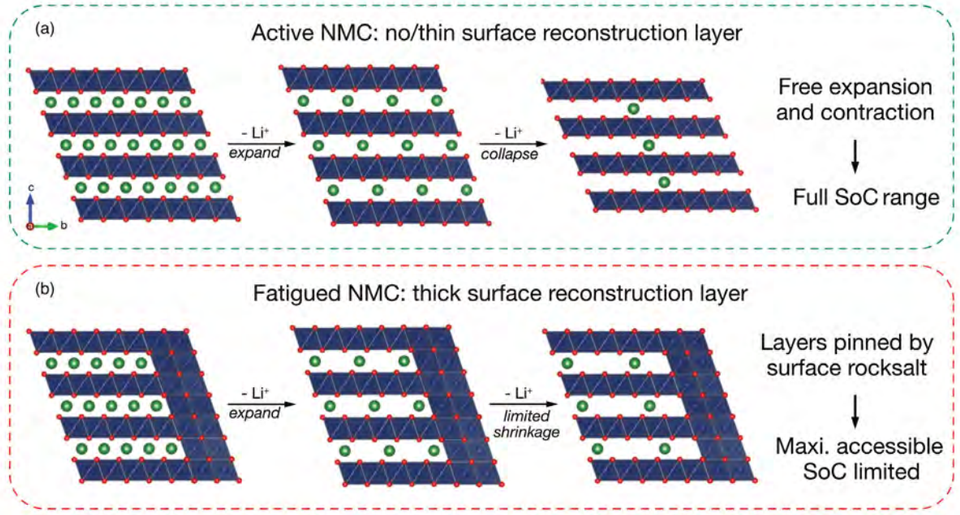

Figure 3: Illustrations of the structural evolution of (a) the active phase; (b) the fatigued phase during the delithiation process. The red, blue and green circles represent oxygen, transition metal and lithium, respectively. Reproduced with permission[3]. Copyright 2020, Nature Publishing Group.

generate substantial dynamic lattice mismatch at the interface between the surface rock salt layer and the bulk. We therefore proposed a 'pinning' mechanism that the fatigue degradation lies in the high lattice strain at the interface between surface and bulk when the NMC cathode is at SoCs above the threshold of ~ 75%. Without a surface layer, as illustrated in Fig. 3a, the initial delithiation leads to a small expansion in the *c* direction and further delithiation is accompanied by a rapid collapse (Fig. 3a) and the material is able to access the full SoC range. However, when a surface rock salt layer is present, the drastic lattice collapsed at high SoCs are obstructed due to the large lattice strain and therefore further delithiation is no longer achieved.

In summary, we demonstrated a novel coin cell setup which is suitable for long-duration *operando* X-ray diffraction studies. The results obtained on an NMC-811/graphite cell shows that a proportion of the NMC-811 becomes fatigued after cycling and the fraction of this fatigued population increases as the ageing continues. The origin of such fatigue degradation is proposed to stem from the high interfacial lattice strain between the reconstructed surface and the bulk layered structure. Our study provides novel insights into designing strategies to help mitigate this degradation process.

References:

1. Li W. *et al.* High-nickel layered oxide cathodes for lithium-based automotive batteries. *Nat. Energy* **5**, 26–34 (2020). DOI: 10.1038/s41560-019-0513-0
2. Xu C. *et al.* Phase Behavior during Electrochemical Cycling of Ni-Rich Cathode Materials for Li-Ion Batteries. *Adv. Energy Mater.* **11**, 2003404 (2021). DOI: 10.1002/aenm.202003404
3. Xu C. *et al.* Bulk fatigue induced by surface reconstruction in layered Ni-rich cathodes for Li-ion batteries. *Nat. Mater.* **20**, 84–92 (2021). DOI: 10.1038/s41563-020-0767-8
4. Märker K. *et al.* Evolution of Structure and Lithium Dynamics in $LiNi_{0.8}Mn_{0.1}Co_{0.1}O_2$ (NMC811) Cathodes during Electrochemical Cycling. *Chem. Mater.* **31**, 2545–2554 (2019). DOI: 10.1021/acs.chemmater.9b00140

Funding acknowledgement:
This work is supported by the Faraday Institution under grant no. FIRG001.

Corresponding author:
Dr Chao Xu, Department of Chemistry, University of Cambridge/The Faraday Institution, cx237@cam.ac.uk

A nanoscale perspective of explosive volcanic eruptions

Related publication: Di Genova D., Brooker R. A., Mader H. M., Drewitt J. W. E., Longo A., Deubener J., Neuville D. R., Fanara S., Shebanova O., Anzellini S., Arzilli F., Bamber E. C., Hennet L., La Spina G. & Miyajima N. In situ observation of nanolite growth in volcanic melt: A driving force for explosive eruptions. *Sci. Adv.* **6**, eabb0413 (2020). DOI: 10.1126/sciadv.abb0413

Publication keywords: Magma; Volcanoes; Volcanic eruptions; Iron oxide nanoparticle; X-ray diffraction

The viscosity of magma is a critical factor in the explosiveness of volcanic eruptions. However, our current knowledge of the mechanisms that regulate the style of volcanic eruptions fails to explain an anomaly; some volcanoes with low viscosity magmas have unexpectedly explosive eruptions. We know that micro-sized crystals (microlites) can significantly increase the viscosity of magmas and promote bubble formation. However, a relatively large volume of these crystals (more than 30%) is needed to impact the viscosity. Recent observations of volcanic products have shown that magmas may contain nanometric crystals (i.e. nanolites), 10,000 times smaller than the width of a human hair, whose formation and influence on both viscosity and bubble formation is unknown.

An international team of researchers used Diamond Light Source's Extreme Conditions beamline (I15) and Small Angle Scattering & Diffraction beamline (I22) to subject a basaltic magma erupted explosively by Mount Etna in 122 BCE to X-ray diffraction measurements at high temperature (from about 900 up to 1,500 Celsius) by varying the cooling rate. This allowed the *in situ* observation of nanolite formation and growth. Their results showed that nanolites can form in the magma within milliseconds during rapid cooling, grow to ~50 nm in two minutes and even aggregate. These new aggregates effectively disrupt the remaining free liquid flow, increasing the magma's viscosity and resulting in an explosive eruption. This information will inform new numerical models of volcanic eruptions, used to establish risk scenarios in volcanic areas.

Volcanoes are messengers from the depth and connect the interior of the earth with its surface and atmosphere. Volcanic activity contributed to set the stage for life and its evolution through the injection of gas into the primordial atmosphere and the generation of new and fertile land. Nonetheless, increasing population growth and urbanization mean that volcanoes can also pose a threat to our society and economy. This is the case of explosive eruptions, such as those of Vesuvius in 79 BCE and Tambora in 1815, where the violent sustained volcanic explosions can eject ash and gas over several kilometres on timescales of minutes to hours or days. Yet, the current understanding of volcanic processes has identified an apparent anomaly; the occurrence of explosive eruptions fed by low viscous magmas, such as basalt that is the object of this study.

Viscosity describes a fluid's internal resistance to flow and it is known[1] to play a key role in controlling the eruptive style of volcanoes. If the magma is relatively low viscosity (very fluid), then most of the exsolving buoyant gas bubbles, which are generated due to the decompression of the magma during its ascent towards the Earth's surface, have a good chance of escaping before that magma nears the surface, averting an explosive outcome. By contrast, when the magma viscosity is relatively high (>10^6 Pa s, 100,000 times higher the viscosity of honey) the gas bubbles remain trapped into the magma and the gas pressure builds up inexorably during the ascent and consequent decompression of the magma. Furthermore, the continuous exsolution of gas upon decompression promotes both the formation of crystals and the increase of magma buoyancy by reducing its density. The occurrence of these conditions, associated with the enormous shear stresses to which the magma is subjected in the volcanic conduit, is dominantly responsible for explosive eruptions.

The viscosity of bulk magma varies by orders of magnitude depending on the chemical composition of the melting phase, temperature, water and crystal content of the magma. At low crystal content (less than 20-30 vol.%), the SiO_2 content and temperature heavily control the magma viscosity. SiO_2-poor magmas such as basalts, which are erupted at a temperature of about 1,100° C, do not exceed viscosity of 10^2 Pa s and thus these magmas commonly feed effusive eruption. Yet, several pieces of evidence both in the geological record and from recent observations that basaltic volcanoes can interrupt their normal and calm effusive activity with sudden explosive eruptions such as the Plinian eruption of 122 BCE[2] at Mt. Etna volcano in Italy.

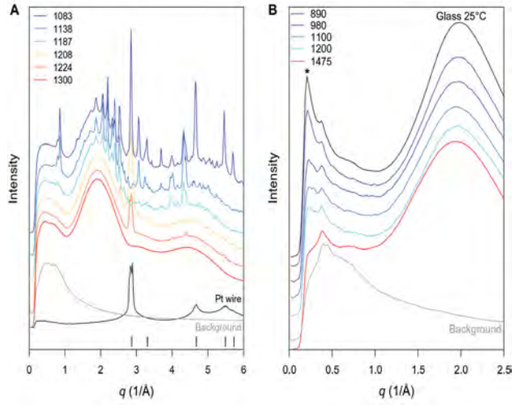

Figure 1: In situ synchrotron XRD patterns of molten Mt. Etna basalt during slow and fast cooling. (a) the basalt was slow cooled from 1,300° C down to 1,083° C. Results show the microlite crystallisation (e.g., plagioclase) for 60-s acquisitions at the temperatures indicated. The sharp peak observed at 2.9 $Å^{-1}$ at 1224° C is the Bragg diffraction peak of crystalline Pt heating wire; (b) spectra collected from a much faster cooling of the basalt from 1,475° C to room temperature (in black) and then to each target temperature in the legend. The asterisk (*) indicates the small-angle 'nanolite peak,' which increases systematically with deeper cooling.

One common explanation for this explosivity is late stage, rapid growth of small crystals (microlites, typically from 1 to >100 µm) above 20-30 vol. % in the fast-rising magma that causes a sudden increase in magma viscosity. However, the role of microlites is sometimes controversial since their volume percent appears to be too low. Interestingly and at a different size scale, nanocrystals (nanolites, typically <100 nm) are increasingly being discovered in volcanic products[3]. This study reveals the conditions leading to their formation and their effect on magma viscosity.

Nanolite formation is suspected to occur within seconds during the fast magma ascent within the volcanic conduit and impact magma rheology[3,4]. However, standard laboratory facilities alone cannot allow answering many questions behind nanolite formation and its effect on volcanic eruptions. Therefore, high-temperature and milliseconds-resolution X-ray diffraction (XRD), small-angle and wide-angle X-ray scattering (SAXS-WAXS) measurements were made at beamlines I15 and I22 to observe the dynamics of nanolite nucleation and growth in Mt. Etna basalt.

Figure 1a illustrates the XRD patterns collected at different temperatures during slow, 1° C min^{-1} (0.017° C s^{-1}) cooling of the magma from 1,300° C. The appearance of clear diffraction peaks in the XRD pattern (e.g. 4.4, 5.1 and 5.4 $Å^{-1}$) shows the onset of microlites crystallization between ~1,224° and ~1,208° C. Fig. 1b shows XRD patterns taken at the end of a series of relatively fast (~10° to 20° C s^{-1}) single cooling steps from 1,475° C down to four different target temperatures. Here, while sharp diffraction peaks were not observed, a marked increase in the intensity at 0.3° (0.2 $Å^{-1}$) was. That is consistent with the coexistence of a melt matrix and a separated phase on the order of nanometers in size. Therefore, results suggest that nanoscale phase separation was formed with a rapid perturbation of the temperature of the magma, which is expected to occur before an explosive eruption[5].

The SAXS modelling allowed the determination of the size and time scale of nanolite formation and growth (Fig. 2) in a sample rapidly cooled in a single step from above the liquidus temperature and then held at 950° C. During the first 50 s of experiment (Fig. 2) the melt evolved into a suspension carrying a first population of spherical iron-bearing nanolites up to 50 nm. Afterwards, a second population of spherical polydisperse iron-bearing nanolites emerges in the melt that measures ~8 nm by the end of the cycle. Moreover, the analysis of SAXS patterns suggested the formation of particle aggregates in the melt. This is consistent with the agglomeration seen in natural samples, including Mt. Etna products erupted in 122 BCE.

Viscosity measurements of magma analog allowed the observation and quantification (Fig. 3) of the effect of nanolite on the viscosity of Mt. Etna basalt. The results suggest that during the aggregation process of nanolites some liquid that makes up the magma can be trapped between the nanolites and stick to their surface. This immobile liquid behaves like a solid and can eventually lead the magma to approach the explosive condition of ~10^6 Pa s at 8, 11 and 32 volume % of nanolites at shear rates of 1.0, 3.5 and 100 s^{-1}, respectively. Notably, approximately 65 volume % of microlites (in orange) is required to reach such a condition.

This study demonstrates that nanolite formation, growth and agglomeration occurs within seconds and triggers a rapid and substantial increase in magma

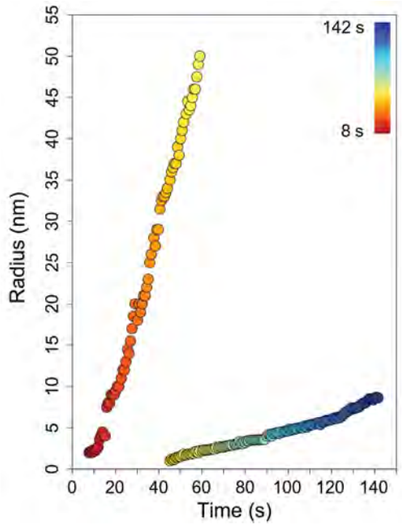

Figure 2: Nanolite growth with time. The evolution of the nanolite radius with time for the two populations of nanolites is derived by modelling the SAXS patterns collected during nanolite crystallisation. The colour changes from hot (red) to cold (blue) with time.

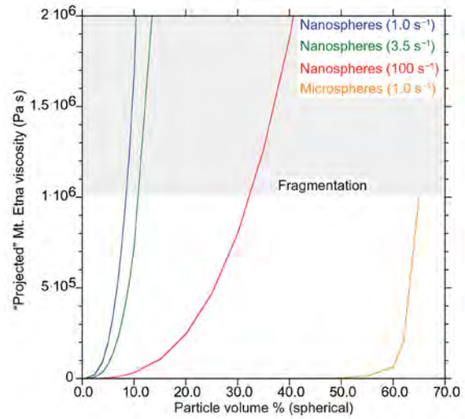

Figure 3: The effect of ~15nm diameter nanolite on viscosity at different shear rates. The calculated expected viscosity of nanolite-bearing melt with an initial viscosity of 200 Pa s, equivalent to Mt. Etna basalt at pre-eruptive conditions (temperature and water content). We also show the equivalent curve for microlites at a shear rate of 1 s^{-1}. It is clear that <10 volume % of nanoparticles is equivalent to >60 volume % of microparticles and can raise the viscosity to ~10^6 Pa s required for magma fragmentation.

viscosity of several orders of magnitude. The increase in viscosity is sufficient to exceed the maximum stresses that can be supported by the magma during the eruption and hence triggering explosive eruptions. Future studies will focus on the understanding of the subtle factors that define the nanolite-controlled window between high (explosive) and low (effusive) viscosities that may be fundamental in predicting the "unpredictable" switches in eruptive style of volcanoes.

References:

1. Gonnermann H. M. *et al.* The fluid mechanics inside a volcano. *Annu. Rev. Fluid Mech.* **39**, 321–356 (2007). DOI: 10.1146/annurev.fluid.39.050905.110207
2. Coltelli M. *et al.* Discovery of a Plinian basaltic eruption of Roman age at Etna volcano, Italy. *Geology* **26**, 1095–1098 (1998). DOI: 10.1130/0091-7613(1998)026<1095:DOAPBE>2.3.CO;2
3. Mujin M. *et al.* A nanolite record of eruption style transition. *Geology* **42**, 611–614 (2014). DOI: 10.1130/G35553.1
4. Di Genova D. *et al.* A compositional tipping point governing the mobilization and eruption style of rhyolitic magma. *Nature* **552**, 235–238 (2017). DOI: 10.1038/nature24488
5. Arzilli F. *et al.* Magma fragmentation in highly explosive basaltic eruptions induced by rapid crystallization. *Nat. Geosci.* **12**, 1023–1028 (2019). DOI: 10.1038/s41561-019-0468-6

Funding acknowledgement:
This project was supported by the NSFGEO-NERC grant 'Quantifying disequilibrium processes in basaltic volcanism' (NE/N018567/1) to H.M.M., R.A.B., F.A., G.L.S. and D.D.G. J.W.E.D. was funded by a NERC standard grant NE/P002951/1. Access to DLS was via experiment sessions EE17615-1 (XRD, February 2018) and SM20447-1 (SAXS-WAXS, February 2019). We acknowledge facility funding from NE/N018567/1, which supports the ARS STEM at Oxford Material Sciences department. The German Research Foundation is acknowledged (DFG grant INST 91/251-1 FUGG) for the STEM-EDS analysis at the Bayerisches Geoinstitut.

Corresponding author:
Dr Danilo Di Genova, Universität Bayreuth, Germany,
danilo.di-genova@uni-bayreuth.de

A cathode additive improves lithium-ion batteries

Related publication: Diaz-Lopez M., Chater P. A., Bordet P., Freire M., Jordy C., Lebedev O. I. & Pralong V. Li2O:Li–Mn–O Disordered Rock-Salt Nanocomposites as Cathode Prelithiation Additives for High-Energy Density Li-Ion Batteries. *Adv. Energy Mater.* **10**, 1902788 (2020). DOI: 10.1002/aenm.201902788

Publication keywords: Li-ion batteries; *In situ* pair distribution function; Cation disordered rock-salts; Sacrificial additives

During the first charging cycles in lithium-ion (Li-ion) batteries, lithium from the cathode material is irreversibly bound at the surface of the anode. This loss of lithium from the cathode reduces the overall cell capacity and limits the battery's performance. Additives can provide extra lithium ions to the cathode by reacting during the first charge, compensating for lost lithium ions. However, many of these sacrificial cathode materials produce gases, which can be dangerous.

Researchers developed a sacrificial cathode additive, made from a nanoscale mixture of Li_2O and Li-Mn-O, with outstanding first charge capacities. They monitored the sacrificial cathode reaction during the first charging cycles, using *in situ* Pair Distribution Function (PDF) on the I15-1 beamline at Diamond Light Source. They made use of the Diamond Radial *In situ* X-ray (DRIX) electrochemical cell, which is optimised for fast *operando* PDF analysis. The low and constant background scattering from the DRIX cell provides excellent total scattering data quality, even on nanostructured or weakly-scattering samples. This design allows for a comprehensive understanding of reactions within battery materials including knowledge of the short-range ordering, nanostructures and amorphous intermediates.

The study demonstrated that the first charge capacities of Li_2O:Li-Mn-O sacrificials are achieved by the electrochemical activation of Li_2O. Adding the sacrificial to the battery cathode improved the first charge capacity of $LiFePO_4$ and $LiCoO_2$ by 13%. Due to their low cost, ease of preparation and compatibility with industrial battery fabrication, Li_2O:Li-Mn-O sacrificials are highly promising, outperforming currently used additives.

The irreversible loss of lithium from the cathode material during the formation of a Solid Electrolyte Interface in the first battery charge notably reduces the capacity of Li-ion batteries, with capacity losses ranging from 7-20 % for graphitic anodes to up to 30 % for silicon (Si). Several prelithiation strategies have been explored which incorporate sacrificial additives acting as Li^+-donors into the cell, such as the addition of Li metal to the anode side. Usually, anode prelithiation routes lead to the formation of unstable reaction products and low battery potentials. Thus, the incorporation of small amounts of sacrificial additives (5-10 wt%) to the cathode side constitutes a more attractive route to counteract capacity losses in Li-ion batteries[1]. Several compounds with high initial charge capacity (e.g. $Li_2Mn_2O_4$, Li_2NiO_2 and Li_6CoO_4) have shown promising results for cathode prelithiation, although their performance is limited by low specific capacities of <300 mAh g^{-1}. Here, we report a significant improvement of the capacity of sacrificial cathodes reaching 1157 mAh g^{-1} in the Li_2O:$Li_{2/3}Mn_{1/3}O_{5/6}$ nanocomposites, where $Li_{2/3}Mn_{1/3}O_{5/6}$ was previously reported as a cathode material with a strongly disordered and non-stoichiometric manganese oxide (MnO)-type rock-salt (RS) structure[2].

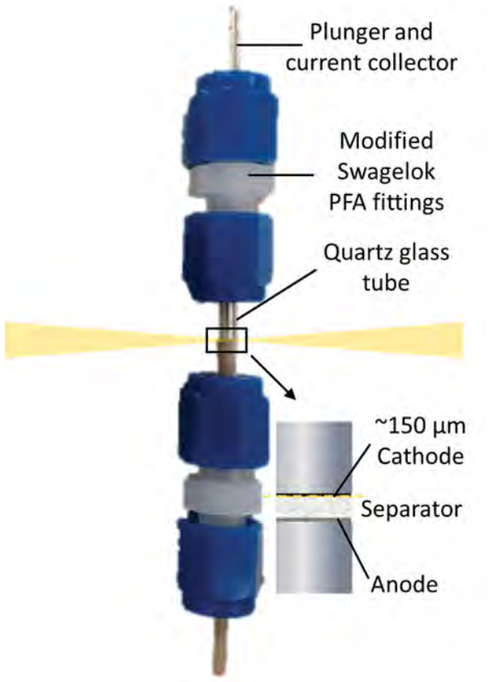

Figure 1: Photograph of a DRIX cell with a schematic representation of the battery stack. The incoming and transmitted X-ray beams are represented in yellow.

In our work, the initial capacity of single phase $Li_{2/3}Mn_{1/3}O_{5/6}$ RS of 250 mA h g^{-1} was improved by the increase of the Li_2O content in 35 and 55 mol% Li_2O-rich composites with exceptional 898 and 1157 mAh g^{-1} first charge capacities. The increased capacities correspond to the extraction of 1.55 and 3.04 Li^+ per $Li_{2/3}Mn_{1/3}O_{5/6}$ formula unit in 35 and 55 mol% Li_2O composites respectively, amounting to larger quantities than originally present in the RS; this observation indicates a reaction between Li_2O and $Li_{2/3}Mn_{1/3}O_{5/6}$. The reaction mechanism was studied by *in situ* total scattering using the DRIX electrochemical cell[3]semi-crystalline and amorphous phases present during (dis (Fig. 1) at Diamond's I15-1 (XPDF) beamline. The improved DRIX cell design with a radial geometry allowed for a comprehensive understanding of the electrochemical activation of the nanostructured sacrificial.

Figure 2 shows a solid solution response of the 0.35Li_2O:0.65RS nanocomposite with a continuous evolution of the lattice parameters, which mimic the shape of the electrochemical curve. The unit cell of the active RS phase contracts with the extraction of lithium after the first charge at 4.5 V and expands during cell discharge. After the first charge, an irreversible contraction of the RS cell volume is observed, ascribed to a lattice densification motivated by the migration of Mn into cation vacancies created after the extraction of lithium. Such a material's densification is commonly observed in Li-rich cathode materials. The main Bragg reflections from Li_2O in the diffraction pattern of 0.35Li_2O:0.65RS, highlighted with an asterisk in Fig. 2, disappear gradually until they are no longer observed

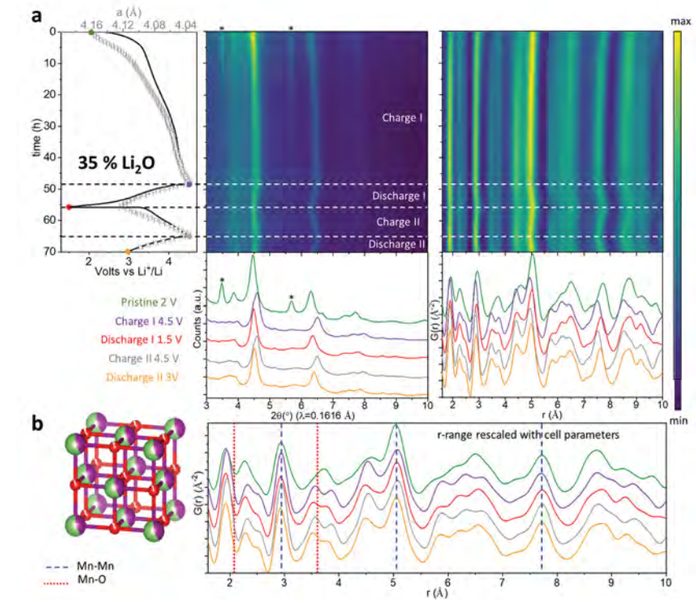

Figure 2: (a) 0.35Li_2O:0.65$Li_{2/3-x}Mn_{1/3}O_{5/6}$ evolution with cycling characterised by in situ X-ray Total Scattering. From left to right: Electrochemical performance (solid line) overlaid with lattice parameters from a sequential Rietveld refinement (empty circles with error bars), reciprocal and real space (PDF) total scattering data. Bottom figures show the data at selected potential values marked by solid spheres in the electrochemical curve. (b) PDFs at selected potential values rescaled on the r-range by the lattice parameter ratio. Vertical lines indicate the expected distances in the average RS structure for the most strongly scattering atom pairs: Mn-Mn and Mn-O.

at the end of the first charge, and no traces of other crystalline or amorphous secondary phases could be detected. After the first charge, the RS cycles reversibly between charged and discharged states with an exchange of ~0.4 Li per formula unit without the further participation of Li_2O.

The local structural evolution of the RS phase remaining after the initial charge is investigated in more detail in Fig. 1b, where the effect of the lattice parameter changes was removed by multiplying the *r*-scale by the ratio of the lattice parameters determined by Rietveld refinement. The narrow Mn-Mn distributions centred around the expected values for the average RS structure indicate the Mn-framework is well ordered, while the broader, asymmetric and shifted Mn-O distributions indicate a high degree of disorder within the oxygen site. Thus, the RS component can accommodate varying concentrations of lithium thanks to the breathing of the cubic Mn-framework that isotropically contracts and expands to extract and incorporate lithium, accompanied by displacements of oxygen atoms.

These observations evidence the electrochemical activation of Li_2O catalysed by nanostructured RS could act as a Li^+-donor and explain the continuous evolution of the first charge capacity vs Li_2O content in Li_2O:RS. Note the increased capacity is only limited to the first charge; only the capacity of the active RS component is retained over the following cycles.

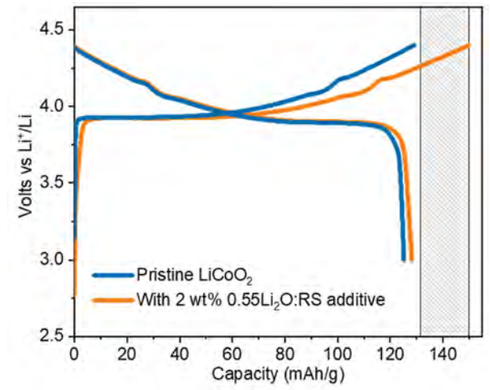

Figure 3: Improved first charge performance of $LiCoO_2$ (blue) with 2 wt% 0.55Li_2O:0.45$Li_{2/3-x}Mn_{1/3}O_{5/6}$ sacrificial additive (orange).

The 0.55Li_2O:0.45RS nanocomposite with the largest capacity has been evaluated as an additive of $LiCoO_2$ cycled against Li metal in Fig. 3. The addition of 2 wt% of 0.55Li_2O:0.45RS resulted in a 13 % increase of the first charge capacity, and matching discharge capacities to that of $LiCoO_2$ with no interference of the sacrificial additive with the electrochemical performance of the cathode. The large initial charge capacity of 0.55Li_2O:0.45RS allows for the use of a small amount of additive (2 wt% vs. 5-10 wt% which is commonly used to compensate similar capacity losses with other materials). Moreover, ~55 mol% of the sacrificial is consumed after the first charge and only <1 wt% remains in the cathode, and the smaller volumes of released gas vs sacrificial salts mitigates potentially detrimental effects related to gas evolution during battery cycling.

The low cost, ease of preparation, compatibility with industrial battery fabrication and outstanding first charge capacities of Li_2O:RS nanocomposites make them highly promising additives for the prelithiation of cathode materials.

References:

1. Sun Y. *et al.* High-capacity battery cathode prelithiation to offset initial lithium loss. *Nat. Energy* **1**, 15008 (2016). DOI: 10.1038/nenergy.2015.8
2. Freire M. *et al.* Investigation of the exceptional charge performance of the 0.93Li4-: XMn2O5-0.07Li2O composite cathode for Li-ion batteries. *J. Mater. Chem. A* **6**, 5156–5165 (2018). DOI: 10.1039/c8ta00234g
3. Diaz-Lopez M. *et al.* Fast operando X-ray pair distribution function using the DRIX electrochemical cell. *J. Synchrotron Radiat.* **27**, 1190–1199 (2020). DOI: 10.1107/S160057752000747X

Funding acknowledgement:
This work was supported by the ANR Grant No. ANR15-CE05-0006-01DAME.

Corresponding authors:
Dr Maria Diaz-Lopez, Diamond Light Source, maria.diaz-lopez@diamond.ac.uk;
Dr Philip Chater, Diamond Light Source, philip.chater@diamond.ac.uk

Finding order in disordered porous materials

Related publication: Simonov A., De Baerdemaeker T., Boström H. L. B., Ríos Gómez M. L., Gray H. J., Chernyshov D., Bosak A., Bürgi H. B. & Goodwin A. L. Hidden diversity of vacancy networks in Prussian blue analogues. *Nature* **578**, 256–260 (2020). DOI: 10.1038/s41586-020-1980-y

Publication keywords: Prussian blue analogues; Porous materials; Correlated disorder

Prussian blue analogues (PBAs) are a family of solids used in batteries and hydrogen gas storage, and as catalysts to make high-value chemicals. These practical applications use a network of connected tunnels (pores) within the solids that allow ions or molecules to move in and out. This pore network is so disordered that no-one has ever been able to work out its structure.

An international team of researchers investigated the disordered pore structures of a range of PBAs to determine their characteristics (*e.g.* how well connected they are) and the extent to which they vary from material to material. They used Diamond Light Source's Small-Molecule Single-Crystal Diffraction beamline (I19), which allowed them to measure the single-crystal X-ray diffuse scattering patterns of various PBA crystals. The diffuse scattering is extremely weak continuous scattering between the Bragg peaks typically used for structure determination, and contains information about the disordered structure.

Their results show that the pore networks of all PBAs — although disordered — are far from random. The patterns that persist within these non-random network structures affect the physical properties of the materials, such as their ability to store gases or the rate at which ions can be moved in and out. Tuning the type of disorder present by varying the composition and synthesis route of the PBAs could produce improved materials, for example battery cathodes.

Prussian blue analogues (PBAs) are a broad family of materials used as cathode materials, heterogeneous catalysts, and in gas-storage applications.[1] Chemically they are obtained as the insoluble hexacyanometallate salts of transition metals, and they crystallise with structures related to the simple cubic net (Fig. 1). A general formula is $M[M'(CN)_6]_{2/3}\square_{1/3}$, where M and M´ denote, respectively, a divalent and trivalent transition metal, and □ represents a hexacyanometallate vacancy. The vacancies create large (~5 Å-sized) voids in the network structure that connect to form an internal three-dimensional pore network. This network is what allows PBAs to reversibly store gases, for example; it also facilitates the transport of ions in PBA battery materials. A longstanding problem in the field has been to determine the structure of these PBA pore networks: it has long been known they are disordered, but the extent to which this disorder is correlated or random was unknown.

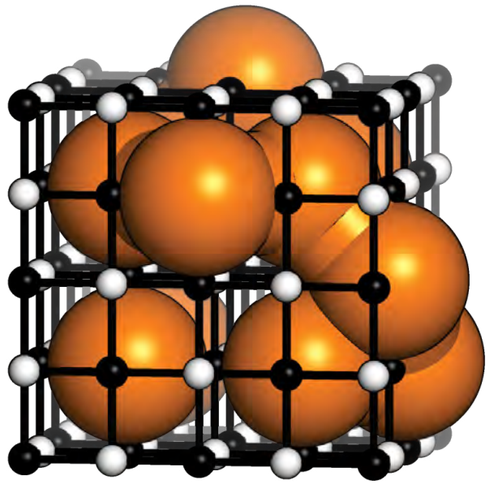

Figure 1: Representation of the structure of PBAs, $M[M'(CN)_6]_{2/3}\square_{1/3}$. M^{2+} and $[M'(CN)_6]^{3-}$ ions (black and white spheres, respectively) occupy alternating nodes of a simple cubic net; the edges correspond to M–N–C–M´ linkages. Vacancies occupy one third of the hexacyanometallate sites, giving rise to internal voids (orange spheres). These voids connect to form the disordered PBA pore structure.

Single-crystal X-ray diffuse scattering measurements, such as those performed on the I19 beamline, are sensitive to the existence and nature of correlations within disordered states.[2] Because PBAs are so insoluble, they are usually obtained as extremely fine powders, and while the diffraction patterns of these powder samples in principle also contain diffuse scattering signatures, in practice this information is buried in the background and has been essentially impossible to interpret. Using slow-diffusion techniques, a series of PBA single crystals have now been grown and their three-dimensional diffuse scattering patterns measured (Fig. 2a). In all cases this scattering is highly structured — a sign that the disorder from which it arises is strongly-correlated rather than random — and variable as a function of PBA composition.

There are many possible methods of interpreting diffuse scattering patterns, but one particularly interesting recent approach is to focus on their Fourier transform, known as the three-dimensional difference pair distribution function (3D-ΔPDF).[3] This function quantifies the difference between local correlations in occupation or position and the configurational averages. One two-dimensional slice of the 3D-ΔPDF for a representative PBA is shown in Fig. 2b. To first order, it is characterised by a set of cross-like features with alternating positive and negative values. These crosses correspond to the correlations *within* an individual $[M'(CN)_6]^{3-}$ cluster, and so the function can be interpreted in terms of the local correlations in the occupation of entire clusters relative to those expected for a statistical distribution. The negative peak at (½,½,0), for example, indicates that cluster vacancies are less likely to occupy neighbouring sites of the face-centred cubic hexacyanometallate sublattice than expected if they were distributed randomly. By determining and interpreting the 3D-DPDFs for each PBA it is possible then to characterise the correlations in pore network structure for each system.

The particular vacancy correlations measured in this way are consistent with a simple model based on just two considerations: (i) local electroneutrality – *i.e.* that vacancies tend to be distributed uniformly; and (ii) the preference for the non-vacant M^{2+} site to adopt centrosymmetric or acentric coordination geometries. It can be shown, using Monte Carlo (MC) simulations for example, that these two factors give rise to a particularly complex phase space for the 1/3-vacancy fraction common to many PBAs; this complexity reflects an incompatibility between the quadripartite nature of the face-centred cubic lattice and a 2:1 ratio of $[M'(CN)_6]^{3-}$ clusters and their vacancies. As the energetic balance between electroneutrality and centrosymmetry is varied in MC simulations, so too do the correlations

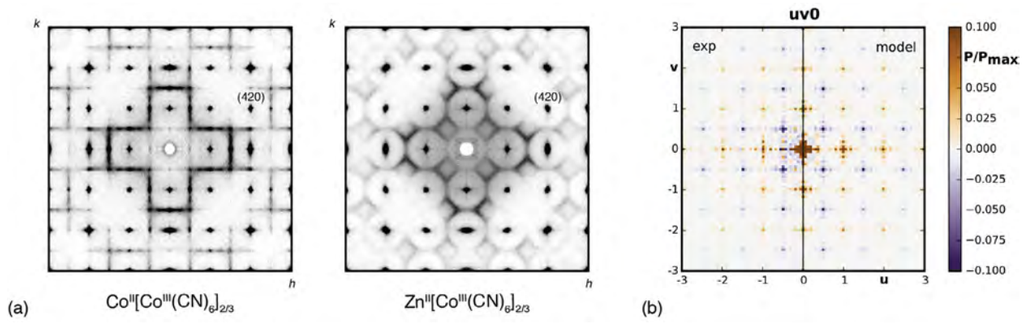

Figure 2: (a) Single-crystal X-ray diffraction patterns (hk0 plane) for two representative PBAs showing the presence of highly-structured diffuse scattering and its variation with composition; (b) The 3D-ΔPDF (uv0 slice) of $Co[Co(CN)_6]_{2/3}$ generated from the corresponding data in (a): red and blue features correspond to pair correlations respectively stronger and weaker than the statistical limit.

within the corresponding vacancy networks. It is possible to calculate from these MC configurations the expected single-crystal diffuse scattering patterns and, by comparing these with experiment, propose representative pore network geometries for each PBA sample. Two such networks are illustrated in Fig. 3. Both

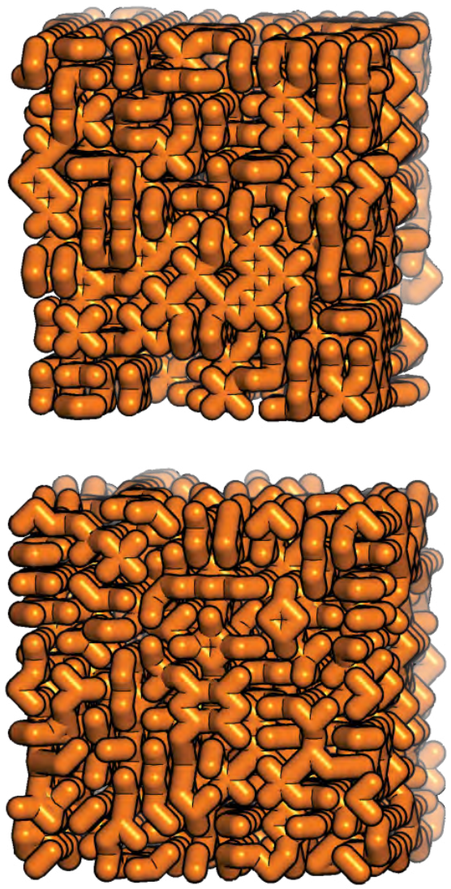

Figure 3: Representative pore network structures for two PBAs. While both are disordered, the distribution of pore node connectivity and pore geometries differs meaningfully between the two. Consequently, network characteristics that govern e.g. mass transport rates are determined by the nature of the correlations within these disordered states.

are heavily disordered; neither one is random. And both have different physical characteristics, such as tortuosity (a measure of the internal curvature of the network structure) or accessible pore volume. Moreover, the distribution of PBA systems throughout MC phase space is consistent with chemical intuition: those with open-shell M^{2+} electronic configurations tend to preserve centrosymmetry, and those based on closed-shell (d^{10}) Zn^{2+} or Cd^{2+} adopt acentric vacancy distributions, consistent with the tetrahedral coordination geometries of their parent pseudobinary cyanides.[4]

So, the important family of PBAs is in fact a system in which there is scope for genuine synthetic control over the nature of correlated disorder in order to optimise their physical properties. For example, the performance of PBA-based cathode materials might be improved by choosing compositions that give rise to pore networks with high internal connectivity and low tortuosity. The family also highlights the broader challenge of establishing disorder–property relationships in functional materials more generally, for which single-crystal X-ray diffuse scattering measurements clearly have a central role to play.[5]

References:

1. Kaye S. S. *et al.* Hydrogen storage in the dehydrated prussian blue analogues M 3[Co(CN)6]2 (M = Mn, Fe, Co, Ni, Cu, Zn). *J. Am. Chem. Soc.* **127**, 6506–6507 (2005). DOI: 10.1021/ja051168t
2. Welberry T. R. *et al.* One hundred years of diffuse scattering. *Crystallogr. Rev.* **22**, 2–78 (2016). DOI: 10.1080/0889311X.2015.1046853
3. Weber T. *et al.* The three-dimensional pair distribution function analysis of disordered single crystals: basic concepts. **227**, 238–247 (2012). DOI: doi:10.1524/zkri.2012.1504
4. Dunbar K. R. *et al.* Chemistry of transition metal cyanide compounds: Modern perspectives. in *Progress in Inorganic Chemistry, Volume 45* 283–391 (John Wiley & Sons, Ltd, 2007). DOI: 10.1002/9780470166468.ch4
5. Simonov A. *et al.* Designing disorder into crystalline materials. *Nat. Rev. Chem.* **4**, 657–673 (2020). DOI: 10.1038/s41570-020-00228-3

Funding acknowledgement:
This research was supported by the Leverhulme Trust UK (Research Grant RPG-2015-292), the F.W.O.-Vlaanderen (Postdoctoral Fellowship), the Swiss National Science Foundation (Fellowships PZ00P2_180035, P2EZP2_155608), the Consejo Nacional de Ciencia y Tecnología (Mexico), and the European Research Council (Starting Grant 279705 and Advanced Grant 788144).

Corresponding author:
Prof. Andrew Goodwin, University of Oxford, andrew.goodwin@chem.ox.ac.uk

Spectroscopy Group

Sofia Díaz-Moreno, Science Group Leader

The Diamond Spectroscopy Group consists of four beamlines; the Microfocus Spectroscopy beamline, I18, the Core EXAFS (Extended X-ray Absorption Fine Structure) beamline, B18, and the two independently operating branches of the Versatile X-ray Absorption Spectroscopy beamline, I20-Scanning and I20-EDE (Energy Dispersive EXAFS). These four spectrometers are complementary in the energy ranges they cover, the size of their focussed beam spots delivered to the sample, and the time resolutions they are able to reach. This complementarity means that they can support research across many different scientific disciplines, from chemistry and catalysis through materials science, condensed matter physics, environmental and life science, energy materials and cultural heritage.

During last year, the activities of the Spectroscopy Group have been heavily impacted by the restrictions imposed by the COVID-19 pandemic, affecting both operations and technical developments. Thanks to the effort invested by the beamline staff, we have continued to support the spectroscopy user community and as far as possible, maintain its research programmes. Several initiatives have been dedicated to enhancing the capabilities of the beamlines in the group to perform remote experiments, and to mitigate the challenges of operating under the COVID-19 restrictions, some of which are described below.

Besides maintaining the user programme on the beamlines, several technical developments and improvements have also been realised during the last year. At B18, the replacement of the 4-element silicon drift detector for a 7-element instrument with faster pre-amplifiers is underway and will significantly increase the throughput over the tender energy regime. The procurement of a multichannel potentiostat for I20-EDE will enable fast electrochemical measurements. An IR-DRIFTS instrument that will be integrated into B18 and I20-EDE, has been procured to complement the time-resolved X-ray Absorption Spectroscopy (XAS) measurements performed on these instruments.

I18 update

The Microfocus Spectroscopy beamline, I18, uses a finely focused X-ray beam to study heterogeneous material on the micrometre scale using a variety of techniques, such as X-Ray Fluorescence (XRF) mapping, XAS, X-ray Diffraction (XRD), and fluorescence and diffraction Computed Tomography (CT).

Several changes in the I18 experimental setup have been implemented over the last year to allow remote experiments, as well as to maximise the data collection efficiency. The need for human intervention for sample changing was reduced by the design of a new holder able to hold many samples. Using motion stages that were already available at the beamline, a sample carousel solution was implemented. The sample carousel allows uninterrupted data collection from 12 hours up to several days, depending on the experimental requirements, and can be controlled remotely. The beamline data acquisition software has also been updated and user-friendly scripting capabilities are now available, so data collection sequences can be programmed. A similar multiple sample carousel compatible with the cryojet is being designed, to allow low temperature measurements for beam-sensitive samples. All these developments have allowed I18 to run 27 remote experiments and one industrial session.

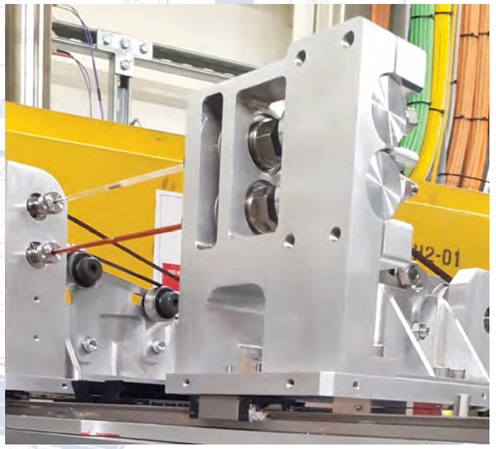

The sample spinning system on I20-EDE.

Significant effort has also been dedicated to improving the automated post-processing of the collected experimental data. Reconstructed computed tomography and reduced X-ray diffraction data can now be viewed within minutes of the end of a data collection, without the need of staff input. The current automated post-processing system also allows the use of custom user Python scripts.

Beside the described efforts dedicated to ease remote operations of the beamline, other developments have been carried out. A new monochromator that will improve the position stability of the microfocus beam has been procured. The monochromator has been designed in-house and the assembly is well advanced. This new instrument is expected to be installed on the beamline and ready for user operations after the summer.

B18 update

The Core EXAFS (Extended X-ray Absorption Fine Structure) beamline, B18, is characterised by a wide energy range, a focused beam and a continuous scanning monochromator. The availability of a flexible experimental space combined with a large range of sample environment equipment make this beamline ideal to perform experiments under real conditions of operation.

Last year significant efforts were dedicated to enhancing the capabilities of B18 to perform remote experiments with the minimum of human interaction. Although the B18 long-term strategy included the increased use of automation, this development has been accelerated by the need to address the challenges posed by the pandemic. For example, a multiple-sample motorised cryostat has been commissioned, enabling low temperature remote experiments. In addition, a 6-axis compact industrial robot has been procured, and it is in an advanced stage of software integration. This system will give additional flexibility in automated positioning and orienting challenging samples. In parallel, the interface to the data acquisition has been improved so that a large number of samples can be handled. Experimental programme tables with basic information regarding sample location and required absorption edges can be prepared in advance and can be directly imported into an automatic series of scans.

In the meanwhile, and to ensure that B18 continued to support the spectroscopy user community during the last year, a series of additional developments have been carried out. Soon after experiments with remote users were approved, a system able to measure up to 200 pellets was designed. The system comprises a 3D printed sample holder and a large manipulator system that was put together using available motorised stages. This setup has been used to run intense experimental sessions during the Catalysis Hub and Energy BAG (Beamtime Allocation Group) visits.

Attendees of the XAS workshop at Diamond in March 2020.

A further complementary development to enhance automation on the beamline has been the construction of a motorised gantry and cassette system that offers improved flexibility in sample positioning. The system holds up to 36 sample frames of nine pellets and has now been integrated into the beamline. The cassette system will also be used with the advanced robot system in the future.

These developments have enabled B18 to host 40 experimental sessions in remote access mode, including five industrial beamtimes.

I20-Scanning update

The Scanning branch of I20 exploits the high flux provided by the wiggler source through two different end stations. The XAS end station is optimised to examine the structure of very low concentration samples. The X-ray Emission Spectroscopy (XES) end station is dedicated to the performance of high-energy resolution studies of the electronic structure of samples.

Last year has seen a rapid adaptation of the beamline to undertake remote experiments on samples that did not require extensive on-site preparation. Sample plates have been made for both the XAS and XES end stations, that allow up to nine room temperature samples to be mounted for measurement without manual intervention. The first remote experiment with users from Germany was performed at the end of June 2020. Since then, 23 remote experiment sessions have run, including the first industry session using XES, and one supporting a user group based in Australia.

Besides maintaining operations, a project to replace the current three analyser crystal spectrometer with a 14-crystal spectrometer has been approved, and the new spectrometer is in the design phase. This new instrument will enable faster data collection times and substantially reduce the concentration of samples that can be studied, which is particularly relevant for weak emission lines. The spectrometer has been designed so a two 'colour' running mode will also be available, where half of the analyser crystals will measure at one emission line while the other half is aligned to collect a different energy. This should enable two different emission spectra to be taken simultaneously as well as facilitate rapid switching for high energy resolution data collection from different edges.

As part of the process to build a new four-bounce monochromator for the beamline, a liquid nitrogen direct cooled first monochromator crystal has been tested. This technology will be key for the new instrument to ensure that the beamline can operate at high energies. The design of the new monochromator will start in the summer of 2021.

I20-EDE update

The Energy Dispersive EXAFS (EDE) branch of I20 uses a polychromator to perform XAS experiments in a dispersive geometry. It is designed for *in situ* and *operando* studies with time resolutions ranging from seconds down to milliseconds or even microseconds. The very nature of these studies imposes the need for users to be on-site to prepare the samples and control the operating conditions of their systems. Furthermore, an additional constraint is that toxic/explosive gases are frequently required, which means experiments cannot be safely run by a lone worker. Remote experiments under pandemic operating conditions were thus deemed infeasible at the beamline. When the operating restrictions were partially lifted in October 2020 the beamline managed to run one user experiment.

Several developments started last year to improve the quality of the data collected by the beamline, but unfortunately progress has been seriously hindered by the pandemic. A 12-week programme to replace the beamline harmonic rejection mirrors was initiated in March 2020, but when the restrictions for working on-site were put in place as a response to the pandemic, the work had to be stopped as the mirror replacement needed the support of a large group of people. At that time, it was decided to reverse the work that had already been started. This reversion could not be completed before lockdown restrictions kicked in, and it took until early August 2020 to get the system returned to the original state. Unfortunately, it will not be possible to replace the mirrors until social distancing requirements are substantially relaxed. More positively, progress has been achieved on the development of a sample spinning system so that samples in a tube furnace can be spun in the beam path to present a more homogeneous sample to the beam. The system was commissioned and optimised during last year.

Community support and development

As part of our ongoing role to support the development of the spectroscopy user community, the Spectroscopy Group organised the annual three-day X-ray Absorption Spectroscopy (XAS) workshop in March 2020. The workshop covered a brief introduction to the spectroscopy beamlines at Diamond, as well as methods to process and analyse spectroscopy data. As was the case in previous years, the workshop was in high demand, with more than 150 applications, although venue limitations and required staff to student ratios limited the successful applications to 30 participants. This year, the workshop will be held in June, and will be run remotely for the first time.

Diamond, through the Spectroscopy Group, together with the University of Newcastle, are the principal partners of the COllaborative NEtwork for X-ray Spectroscopy (CONEXS), an Engineering and Physical Sciences Research Council (EPSRC) funded network that aims to bring together experimentalists and theoreticians who are working in the area of X-ray spectroscopy. The network aims to improve members' abilities to fully exploit and interpret experimental data. As part of the activities of the network, a Summer School and an International conference were organised. The Summer School was originally scheduled to take place in September 2020, but it had to be postponed to March 2021, when it was run just before the International Conference. Both events were run remotely, and they were very well attended. More than 90 applicants registered for the workshop and over 190 for the conference. The network also runs monthly webinars where international speakers give an overview of the fundamentals of X-ray spectroscopy from the experimental and theoretical points of view. The webinars have proven to be very popular over the pandemic year.

As part of the Diamond-II (proposed upgrade programme) activities, the Spectroscopy Group organised a series of webinars from September to November 2020 to discuss with the user community the two flagship beamline projects that were presented in late 2020 to the Diamond Scientific Advisory Committee (SAC) and the Diamond Industrial Science Committee (DISCo) for prioritisation. The webinars for each project attracted a large number of participants and served to gather information from the community that helped shape the proposals.

Analysing deep Antarctic ice to understand a Martian mineral

Related publication: Baccolo G., Delmonte B., Niles P. B., Cibin G., Di Stefano E., Hampai D., Keller L., Maggi V., Marcelli A., Michalski J., Snead C. & Frezzotti M. Jarosite formation in deep Antarctic ice provides a window into acidic, water-limited weathering on Mars. *Nat. Commun.* **12**, 436 (2021). DOI: 10.1038/s41467-020-20705-z

Publication keywords: Antarctica; Mars, Jarosite; Geochemistry; Ice cores; Mineral dust

Jarosite is a common mineral on the surface of Mars, but relatively rare on Earth. Since the Opportunity rover reported widespread jarosite at Meridiani Planum in 2004, the mineral has been repeatedly identified on Mars. On Earth, jarosite forms through the weathering of iron-bearing minerals in water-limited settings. However, scientists have struggled to understand how the mineral may have formed on Mars. An international group of researchers have therefore studied whether glaciers played a role in the precipitation of jarosite on Mars in its geologic past.

The 'ice-weathering model' suggests that the precipitation of jarosite on Mars could be related to the presence of massive ice deposits developed during ancient glacial ages. To test this hypothesis, the researchers investigated the properties of deep Antarctic ice, as an Earth analogue for paleo-ice deposits on Mars.

Diamond Light Source's B18 beamline is dedicated to X-ray Absorption Spectroscopy (XAS). This technique can characterise geochemical and mineralogical properties, even on tiny mineral dust samples extracted from Antarctic ice. The team measured more than 50 samples retrieved from the Antarctic Talos Dome ice core. They observed jarosite present in deep ice and depicted a coherent scenario to describe the formation of this mineral. Their scenario is consistent with the ice-weathering model, supporting the hypothesis that glaciers had a fundamental role in shaping the geologic and geochemical past of Mars.

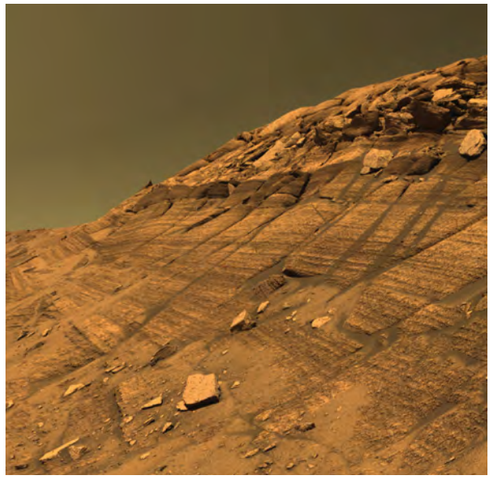

Figure 1: The 'Burns' formation on the flank of Endurance crater at Merdiani Planum; the photograph was captured by the Opportuniy rover. Jarosite and other iron-minerals are common constituents of the layered formations portrayed in the picture. Credits: NASA/JPL/ Cornell.

In 1987 it was predicted that jarosite, a ferric-potassium hydrated sulphate, would have been stable on Mars[1]. The confirmation came about 20 years later from the Opportunity rover, which identified jarosite in the layered sediments outcropping at Meridiani Planum[2] (Fig. 1). The identification of this mineral was a major scientific result, since its formation requires liquid water. Finding jarosite on Mars was thus regarded as evidence for the presence of liquid water on the planet, at least in its geologic past[3]. Since then jarosite has been observed at multiple sites on Mars, but scientists are still struggling to understand how it formed. Jarosite not only requires liquid water to form, it also needs iron-rich minerals and an acidic-oxidative environment.

Several hypotheses have been made to describe the environment where such conditions could have been found on Mars. Most of them deal with the presence of evaporative basins resulting from the upwelling of acidic groundwater, or with volcanic and/or hydrothermal processes. An additional hypothesis, known as the 'ice-weathering model', proposed that Martian jarosite formed within massive paleo-ice deposits, rich in mineral dust and acidic volcanic aerosols[4]. According to it, in the deepest part of such deposits, high pressure and ice-metamorphism would have promoted the formation of micro-pockets where impurities and liquid water interacted, favouring the precipitation of jarosite.

No evidence was available until now to test this model, neither on Mars, nor in other planetary contexts, Earth included. This study tried to fill the gap, looking for an appropriate Earth analogue suitable to assess if the englacial formation of jarosite is geochemically reliable. From many points of view, Antarctica is the region of Earth more similar to Mars. This is even more true when considering glaciers. The conditions found in the depths of Antarctic ice sheets and the ones characterising ancient Martian glaciers are expected to be comparable from several perspectives. Antarctic ice contains mineral dust, acidic atmospheric species and salts, exactly what the ice-weathering model predicted for Martian paleo-ice.

To assess if jarosite is present in deep Antarctic ice, about 50 samples of mineral dust extracted from an Antarctic ice core were prepared at the University of Milano-Bicocca (Italy) and measured at beamline B18. Samples were obtained from the Talos Dome ice core, a 1620 m long ice core extracted from a peripheral region of the East Antarctic ice sheet, near the Ross Sea and the Transantarctic mountains. This site was selected because it is influenced by the local mountains outcropping from ice, which provide to Talos Dome mineral dust consisting in micrometric fragments of basaltic rocks[5]. Such conditions make the site suitable for a comparison with Mars, since Martian atmospheric dust is mostly produced from the alteration of basaltic outcrops. The core encompasses more than 150,000 years of Earth climatic history.

Samples were analysed at B18 through X-ray Absorption Spectroscopy; this is a powerful technique allowing the gathering of accurate pieces of information about selected chemical elements, even on extremely diluted samples, such as the impurities present in Antarctic ice. The study focused on iron, a major constituent of jarosite. Over some years, a clean protocol suited to measure such extreme samples - each one consisting of a few micrograms

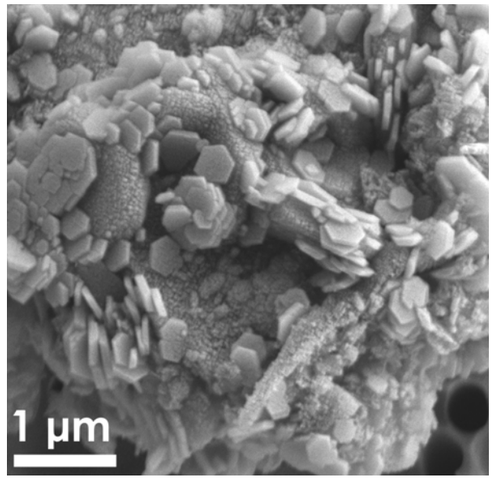

Figure 2: A Scanning Electron Microscope image of a mineral grain extracted from the deep part of the Talos Dome ice core. The hexagonal platelets, as revealed by X-ray Absorption Spectroscopy and other techniques, are sub-micrometric jarosite crystals precipitated on mineral dust grains.

of dust deposited on a filter - was developed at B18[5]. Samples were irradiated with an X-ray beam to induce X-ray fluorescence. A detector recorded the signal, and in particular the small variations in the emission resulting from the changing energy of the incident beam. Analysing the variations, it was possible to infer about the following properties of iron: coordination, oxidation and mineralogy. To obtain this information it was necessary to measure not only Antarctic dust samples, but also mineralogical specimens and standard materials.

The signature of jarosite was identified in X-ray absorption spectra, confirming that this mineral is present in Antarctic ice. The identification was also confirmed by an independent analysis carried out at the NASA Johnson Space Center (USA). However, jarosite is not uniformly distributed along the core. Results showed that the properties of dust are not stable with ice depth. Some oscillations are associated with the alternation of glacial and interglacial periods, but other trends are not linked to climate and seem more dependent on ice depth, as in the case of jarosite abundance. The mineral is present only deeper than 1000 m into ice, in the form of sub-micrometric crystals as it is possible to appreciate in Fig. 2. Below this depth jarosite firstly appears and its concentration rapidly increases, until becoming the most abundant iron-mineral present in the bottom sections of the ice core (Fig. 3a). Concurrently

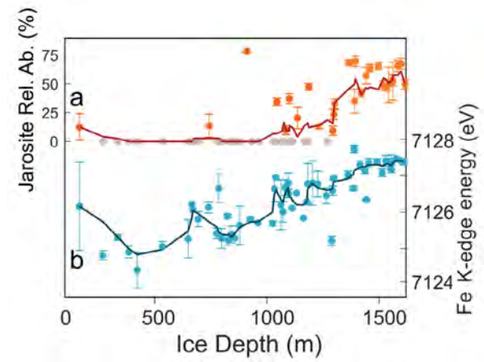

Figure 3: The analysis of X-ray absorption data gathered at beamline B18 allowed identification of the presence of jarosite in the dust samples extracted from the Talos Dome ice core; (a) abundance of jarosite within the dust samples; (b) Fe K-edge energy along the core, this is a parameter related to iron oxidation state and to jarosite precipitation. Details can be found in a Nature publication[3].

we observed a progressive oxidation of the iron fraction of dust (Fig. 3b). This is compatible with jarosite accumulation since this mineral is completely oxidised. Our evidence suggests that jarosite is not originally deposited with snow at Talos Dome, but that it forms into deep ice, supporting the Mars ice-weathering model.

Considering other records and analyses, a coherent scenario describing the formation of jarosite in deep Antarctic ice was depicted. Deep ice is subjected to metamorphism, i.e. the re-crystallisation of ice grains. During this process, the impurities present in ice are expulsed from ice grains and accumulated at their junctions, favouring the interaction between mineral dust, acids and salts. The concurrent presence of these species lowers the local pressure melting point of ice, allowing for the occurrence of liquid water. Dust, iron minerals, acids and liquid water: the ingredients for jarosite! This scenario perfectly resembles the one described by the ice-weathering model to understand the formation of jarosite on Mars.

This study is the first direct evidence supporting the hypothesis that Martian jarosite formed as the result of geochemical reactions occurred in past massive glaciers that were present on the planet. Once these glaciers disappeared through sublimation because of climate change, jarosite and other sublimation residues were accumulated and re-worked by winds, reaching wide sectors of the planet and allowing for the formation of layered rocks, such as the ones analysed by the Opportunity rover. This finding is extremely important with respect to our comprehension of Mars and of the geologic and geochemical processes that defined its present state. Martian glaciers have been more important than previously thought.

References:

1. Burns R. G. Ferric sulfates on Mars. *J. Geophys. Res.* **92**, 570–574 (1987). DOI: 10.1029/jb092ib04p0e570
2. Klingelhöfer G. *et al.* Jarosite and hematite at Meridiani Planum from opportunity's Mössbauer spectrometer. *Science (80-.).* **306**, 1740–1745 (2004). DOI: 10.1126/science.1104653
3. Madden M. E. E. *et al.* Jarosite as an indicator of water-limited chemical weathering on Mars. *Nature* **431**, 821–823 (2004). DOI: 10.1038/nature02971
4. Niles P. B. *et al.* Meridiani Planum sediments on mars formed through weathering in massive ice deposits. *Nat. Geosci.* **2**, 215–220 (2009). DOI: 10.1038/ngeo438
5. Baccolo G. *et al.* Regionalization of the Atmospheric Dust Cycle on the Periphery of the East Antarctic Ice Sheet Since the Last Glacial Maximum. *Geochemistry, Geophys. Geosystems* **19**, 3540–3554 (2018). DOI: 10.1029/2018GC007658

Funding acknowledgement:
This work is part of the TALDEEP project funded by MIUR (PNRA18_00098). The Talos Dome Ice core Project (TALDICE), a joint European programme, is funded by national contributions from Italy, France, Germany, Switzerland and the United Kingdom. Primary logistical support was provided by PNRA at Talos Dome. This study was generated in the frame of Beyond EPICA. The project has received funding from the European Union's Horizon 2020 research and innovation programme under grant agreement No. 815384 (Oldest Ice Core). It is supported by national partners and funding agencies in Belgium, Denmark, France, Germany, Italy, Norway, Sweden, Switzerland, The Netherlands and the United Kingdom. Logistic support is mainly provided by PNRA and IPEV through the Concordia Station system.

Corresponding author:
Giovanni Baccolo, University of Milano-Bicocca, Italy,
giovanni.baccolo@unimib.it

Searching for new sources of rare earth elements

Related publication: Borst A. M., Smith M. P., Finch A. A., Estrade G., Villanova-de-Benavent C., Nason P., Marquis E., Horsburgh N. J., Goodenough K. M., Xu C., Kynický J. & Geraki K. Adsorption of rare earth elements in regolith-hosted clay deposits. *Nat. Commun.* **11**, 4386 (2020). DOI: 10.1038/s41467-020-17801-5

Publication keywords: Rare earth elements; Critical metals; Clay minerals; Resources

The Rare Earth Elements (REE) are essential for high-tech industries. Most of the world's heavy REE come from clay deposits formed by weathering of granites in China, and the extraction of rare earths is often performed with little care for the environment. A lack of understanding of how these clay deposits form and how REE are held in them hampers the search to identify alternative resources outside China. Many metals are loosely stuck ('adsorbed') to the outer surfaces of clay crystals. An international team of researchers led by the Universities of St Andrews and Brighton used synchrotron techniques to determine where the REE were in the deposit and what surrounded them. They investigated deposits from China and a prospective site in Madagascar.

Using Diamond Light Source's Microfocus beamline (I18) allowed them to study the samples micron by micron. Combining X-ray Absorption Spectroscopy (XAS) with Scanning X-ray Fluorescence (SXRF) element mapping showed what surrounded the metals and their distribution in the sample. Although the rock samples from the two areas are different, the REE in both stick to the clay surfaces identically. At the atomic level, the Madagascan clay deposits are the same as those currently exploited in China. Understanding how the metals stick to the clay crystals will allow us to develop easier, more environmentally friendly ways to extract them. These results hint that deposits like those currently found in China may be more widespread than we thought. The hunt is now on to find other rare earth deposits to provide alternative supplies for the technologies that underpin a carbon-free future.

Rare earth elements (REE, the lanthanides and Y) are critical metals for modern technologies[1]. Their importance comes from uses in high strength magnets and other high-tech applications such as phosphors, catalysts and rechargeable batteries. At present, ~80% of rare earths produced globally are mined in China. China's dominance over the REE market has led to global concerns because restricted access to these metals would be a bottleneck to high-tech industries elsewhere. The most valuable rare earths (i.e. Nd and the heavy REE, or HREE, Gd-Lu) are dominantly mined from Chinese clay deposits which form by intense subtropical weathering of granitic bedrock. Despite relatively low concentrations of REE (0.05 - 0.2 wt.% REE oxides) compared to some hard-rock REE ores, the metals can easily be extracted via *in situ* or heap leaching[2]. The key requirement for this to work is that the majority of REE (>50%) are loosely stuck, or 'adsorbed' to the surfaces of clay minerals. Similar weathering profiles occur outside China and might provide alternative sources for REE, allowing a wider supply network. However, the exact nature of these deposits remained unclear and the detailed mechanisms by which they form was still poorly understood.

This study combines X-ray Absorption Spectroscopy with detailed geochemical and mineralogical work to identify the distribution and coordination of REE in economically mineralised weathering profiles from Southern China, and compares these to clay deposits from Madagascar. Synchrotron X-ray Fluorescence (SXRF) maps, X-ray Absorption Near Edge Structure (XANES) and

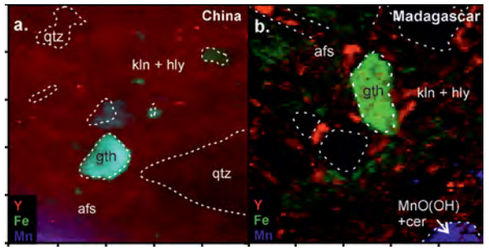

Figure 1: SXRF elemental maps (500x500 µm) showing Y (red), Fe (blue), Mn (green) counts in (a) Chinese pedolith sample with high concentrations of leachable REE and (b) a REE-rich lower pedolith sample from the studied profiles in Madagascar. Note heterogeneous enrichment of Y along kaolinite grains. Adapted from main article.

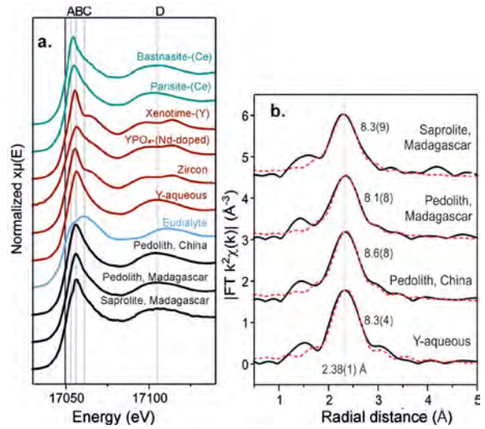

Figure 2: (a) Normalized Y K-edge XANES for REE-mineral standards with REE in different coordination states (Coordination Numbers: CN=9 in green, CN=8 in red, CN=6 in blue). Black lines represent Y XANES for clay-hosted Y in the Malagasy and Chinese pedolith and saprolite samples. (b) Radial distribution functions and EXAFS fits for clay-hosted Y in the samples and Y in aqueous solution, showing best fit coordination numbers for Y and average bond distances of its nearest neighbours. Measured spectra shown in black and fits shown in red.

Extended X-ray Absorption Fine Structure (EXAFS) data were collected on the I18 beamline to determine in which phases the REE are hosted at different levels along the weathering profile, and to determine the local bonding environment of the easily leachable REE fraction as well as the non-recoverable REE fraction that is built into mineral structures. Yttrium K-edge (17038 eV) and Nd L_3-edge (6208 eV) X-ray absorption spectra were measured as proxies for light and heavy REE, respectively. The overall aim is to identify whether clay deposits in northern Madagascar represent direct structural analogues to the easily leachable Chinese deposits.

The weathering profiles from China were developed on a biotite granite from Zhaibei, Yiangxi province[3], which are economically mined for REE. The sample selected for detailed study was a strongly weathered sample (pedolith) with the highest concentration of ammonium sulphate leachable REE (1000 mg/kg REE, of which 37% are HREE and Y), from the upper 2 m of a 12 m thick weathering profile. Rare earths in the granitic bedrock are hosted in minerals such as zircon, apatite, monazite, REE-fluorcarbonates, xenotime and fluorapatite[3]. Intense weathering along the soil profile replaced the original minerals with Fe-Mn oxides and clay minerals. Scanning Electron Microscopy (SEM) and X-ray Diffraction (XRD) examination show the clays dominantly consist of kaolinite, K-feldspar, quartz and iron oxides (goethite) and minor illite (Fig 1a).

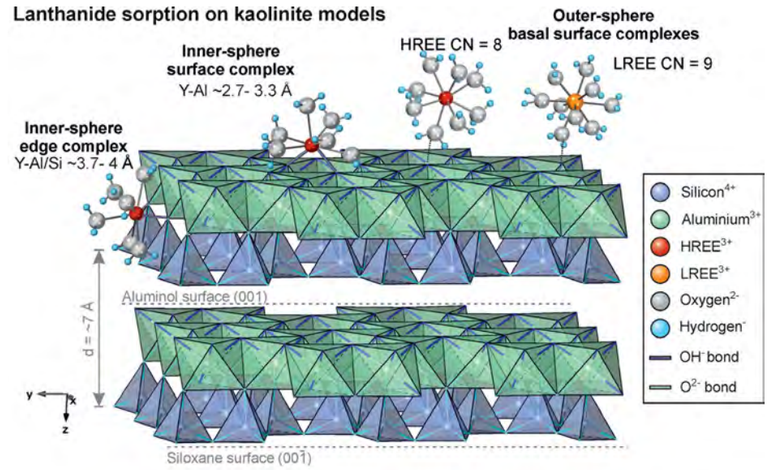

Figure 3: Schematic adsorption model of rare earth elements onto kaolinite. Crystal structure shows the 1:1 stacking of Al-octahedral (O) and Si-tetrahedral (T) sheets in kaolinite. XAS data demonstrate that Y are dominantly present as 8-fold hydrated outer-sphere basal surface complexes on the aluminol surface (O sheet). The EXAFS data show no evidence for Al or Si scattering within 4 Å, thereby excluding the inner-sphere adsorption models. Adapted from main article.

Samples from Madagascar were taken from weathering profiles over peralkaline granite and syenite from the Ambohimirahavavy complex caldera complex[4,5]. The rocks underlying these profiles generally have higher REE concentrations and are more enriched in heavy REE than the granitic rocks that underlie the Chinese deposits. The hypothesis was that weathering profiles developed over better precursors may be more favourable for the development of high grade and HREE rich clay-hosted REE deposits, and provide more attractive and economically viable alternatives to the Chinese deposits. Samples selected for this study were previously characterised by Estrade *et al*[5], and chosen to reflect a range in exchangeable REE grades. This included a strongly weathered sample (pedolith) with high grades in leachable REE (1962 mg/kg REE, of which 29% HREE) developed over bedrock with REE-rich pegmatite veins[5]. The mineralogy was similar to the Chinese pedolith sample, dominantly composed of kaolinite, minor halloysite, K-feldspar, Fe and Mn oxyhydroxides with accessory zircon and cerianite (Fig 1b). We also analysed partially weathered rock (saprolite) from deeper parts of the profile with more primary minerals still preserved, including K-feldspar, zircon and a range of primary Nb-Ti-Zr minerals.

Synchrotron SXRF element maps of selected areas demonstrate local enrichment of Y (in red, Fig 1) along boundaries of clay minerals (kaolinite and halloysite) in both the Chinese and Madagascar pedolith and saprolite samples. The results summarised here focus on the easily leachable (economic) REE fraction. XANES data for the clay-hosted REE all show identical Y K-edge XANES and are compared to mineral standards in which the REE occupy differently coordinated sites (Fig 2a). The XANES spectra for Y associated with clay minerals in the pedolith and saprolite samples are near-identical to Y in aqueous solution, and similar to the rare earth minerals parisite-(Ce) and bastnasite-(Ce), in which the REE occupy sites surrounded by 8 to 9 other elements (mostly oxygen).

The structural state of Y associated with kaolinite in the pedolith and saprolite samples was further constrained from quantitative EXAFS refinements. Best fits were obtained for a configuration where Y occurs in simple hydration spheres surrounded by 8.1 - 8.6 ± 0.9 oxygens (of water molecules), at average distances of 2.35 – 2.38 ± 0.01 Å. The fit obtained for this configuration of Y in the clays was within error of the best fit obtained for Y in aqueous solution (Fig 2b). This suggests that Y are indeed fully hydrated, and not directly bound to the clay structure. Furthermore, the radial distribution functions (Fig 2b) show no evidence for a scattering peak at 4 Å, suggesting there are no atoms of Al or Si within a radial distance of 4 Å as would be expected for inner-sphere adsorption mechanisms (Fig 3). These results indicate that REE in both the Chinese and Madagascar samples are present as 8- to 9-coordinated, fully hydrated, outer sphere complexes which are loosely adsorbed onto the flat basal surfaces of kaolinite (Fig 3), and not tightly bound as inner sphere 5-6 coordinated edge or surface complexes (Fig 3). It can therefore be concluded that REE-adsorbed kaolinites from Madagascar and China are direct structural analogues. Our data explain the easily leachable nature of these economically important ore types and suggest a common adsorption mechanism at both locations. The identification of a common adsorption mechanism confirms that this process operates globally, and further supports the search for critical rare earth deposits in the weathering environment.

References:

1. Goodenough K. M. *et al.* The Rare Earth Elements: Demand, Global Resources, and Challenges for Resourcing Future Generations. *Nat. Resour. Res.* **27**, 201–216 (2018). DOI: 10.1007/s11053-017-9336-5
2. Wall F. *et al.* Responsible sourcing of critical metals. *Elements* **13**, 313–318 (2017). DOI: 10.2138/gselements.13.5.313
3. Wang L. *et al.* Petrological and geochemical characteristics of Zhaibei granites in Nanling region, Southeast China: Implications for REE mineralization. *Ore Geol. Rev.* **64**, 569–582 (2015). DOI: 10.1016/j.oregeorev.2014.04.004
4. Estrade G. *et al.* Unusual evolution of silica-under- and -oversaturated alkaline rocks in the Cenozoic Ambohimirahavavy Complex (Madagascar): Mineralogical and geochemical evidence. *Lithos* **206**–**207**, 361–383 (2014). DOI: 10.1016/j.lithos.2014.08.008
5. Estrade G. *et al.* REE concentration processes in ion adsorption deposits: Evidence from the Ambohimirahavavy alkaline complex in Madagascar. *Ore Geol. Rev.* **112**, 103027 (2019). DOI: 10.1016/j.oregeorev.2019.103027

Funding acknowledgement:
This work was supported by the NERC SoSRARE consortium (grant numbers NE/M010856/1, NE/M011267/1 and NE/M01116X/1) awarded to the University of St Andrews, University of Brighton and the British Geological Survey and analyses were carried out at the I18 beamline (grants SP14793 and SP15903).

Corresponding author:
Dr Anouk Borst, KU Leuven and Royal Museum for Central Africa, Belgium, anouk.borst@africamuseum.be

When iron atoms behave like rare-earth elements - and why

Related publication: Huzan M. S., Fix M., Aramini M., Bencok P., Mosselmans J. F. W., Hayama S., Breitner F. A., Gee L. B., Titus C. J., Arrio M.-A., Jesche A. & Baker M. L. Single-ion magnetism in the extended solid-state: insights from X-ray absorption and emission spectroscopy. *Chem. Sci.* **11**, 11801–11810 (2020). DOI: 10.1039/D0SC03787G

Publication keywords: Single-ion magnetism; Solid state; Magnetic anisotropy; Electronic structure; Transition metal dopant; X-ray spectroscopy

The clean energy revolution demands large quantities of rare-earth elements in applications ranging from wind turbines to electric car motors. However, rare-earth metals are toxic, and extraction is an energy-intensive and environmentally damaging process. Iron-doped lithium nitride has extraordinary magnetic properties, with single-ion magnetism that exceeds any other transition metal system and a magnetic coercivity field that surpasses even the largest values observed in rare-earth-based permanent magnets. However, unanswered questions concerning the fundamental geometric and electronic structure of the iron sites limit its impact.

Researchers used a combination of element-sensitive X-ray techniques on Diamond Light Source's Scanning Branch of beamline I20 to investigate the iron sites. They used K-edge X-ray Absorption Near Edge Structure (XANES) to quantify iron coordination geometry, Extended X-ray Absorption Fine Structure (EXAFS) to deduce the bond lengths around iron sites and Kβ X-ray Emission Spectroscopy (XES) to measure iron oxidation state as a function of dopant concentration. To directly access the electrons that contribute to the magnetism at iron sites, they used I10: Beamline for Advanced Dichroism Experiments (BLADE). The insights gained into the electronic structure will inform the preparation of improved bulk magnets that do not require rare-earth elements. The results of this study provide insights into how transition metals within host lattices could one day offer a viable alternative to rare-earth bulk magnets. It may also become possible to use the direction of magnetisation at the iron atoms to store binary information at the atomic scale, for future high-density information storage applications and advances in quantum computing.

The magnetic properties of Fe doped in lithium nitride are extraordinary, with a magnetic coercivity field greater than values observed in rare-earth-based permanent magnets[1]. Unusually, the displayed coercivity field persists down to extremely low Fe doping concentration inferring that the magnetism is of atomic, single-ion, nature. Single-ion magnetism occurs due to an effective anisotropic barrier to the reversal of atomic magnetic moments. The observed single-ion magnetism in Fe doped lithium nitride exceeds any other transition metal compound and is comparable to high-performance rare-earth-based single-ion magnets. While this effect does not occur at room temperature, it arises below 50 K and is clearly observed below 10 K, a temperature that can be reached in the lab using liquid helium. An understanding into the origin of the displayed magnetic properties have been inhibited by limited knowledge of the geometric and electronic structure at the Fe dopant sites. Theoretical studies have considered either a situation where Fe sites occupy Li+ positions, resulting in a two-coordinate Fe with a +1 oxidation and general formula $Li_2[Li_{1-x}Fe_x]N$, or due to coupling with additional Li+ vacancies within the lattice, a +2 oxidation state[2]. Defining the geometric and electronic structure of Fe dopants in lithium nitride is motivated by a desire to further understand how transition metals could be used to replace rare-earths in high-performance magnetic materials. Improved understanding of electronic structure also informs research into how magnetic operating temperatures could be raised. This observation of single-ion magnetism within Fe doped lithium nitride is of relevance to atomic-scale information storage applications, since the direction of magnetisation at Fe sites could be harnessed in the storage of binary information at the atomic level.

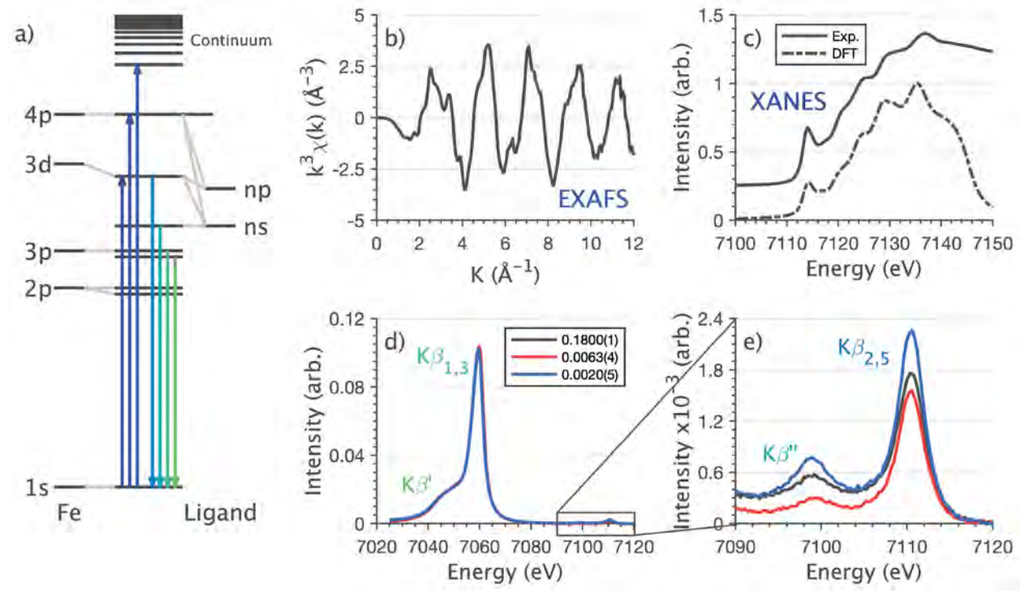

Figure 1: (a) The Fe X-ray spectroscopic transitions accessed during the study of $Li_2[Li_{1-x}Fe_x]N$ at the I20-Scanning beamline; (b) Background subtracted k^3-weighted EXAFS; (c) Single crystal Fe K-edge XANES with calculated DFT spectrum; (d) Kβ XES for Fe dopant concentrations ranging from 0.2 to 18 %; (e) The valence-to-core region of the Kβ XES.

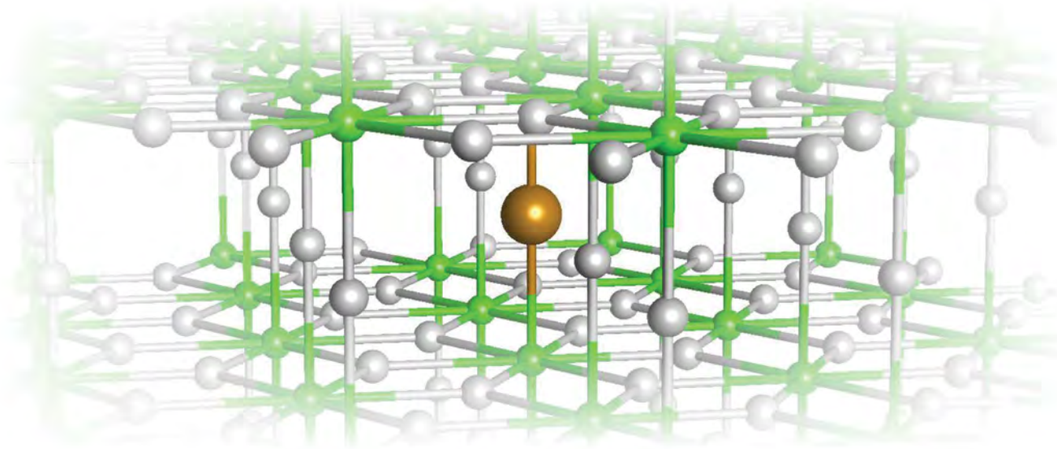

Figure 2: The structure of lithium nitride including an Fe impurity, $Li_2[Li_{1-x}Fe_x]N$. Fe, brown; N, green; Li, grey.

The random distribution of Fe sites within the lithium nitride crystal prohibits access to the structure of dopant sites by diffraction methods. Accessing the dopant sites, therefore, requires element selective techniques, hence a combination of Fe X-ray absorption and emission spectroscopies at Diamond were applied. Each of the selected techniques carries a unique sensitivity due to the specific transitions and core-holes involved that together enable a holistic characterisation of both geometric and electronic structure (Fig. 1a). Fe K-edge extended X-ray absorption fine structure (EXAFS) measurements at the I20-Scanning beamline were applied to analyse local bond lengths around the Fe sites, from which two extremely short Fe-N 1.873 Å bonds were determined (Fig. 1b and Fig. 2). Fe K-edge X-ray absorption near edge structure (XANES) measurements were performed to probe the Fe coordination geometry via an analysis of Fe 4p ligand-field splitting. An intense low-energy peak centred at 7113 eV is assigned as corresponding with electric dipole transitions into a degenerate pair of $4p_{x,y}$ orbitals; a signature for a linear coordination geometry (Fig. 1c). This assignment was then confirmed by DFT calculations based on a linear structure using the Fe-N bond lengths determined by EXAFS (Fig. 1c). A lack of suitable reference spectra meant that Fe K-edge measurements could not be analysed to conclude the Fe oxidation state. Furthermore, predictions in the literature of a minority divalent species and a monovalent majority species with a ratio that changes as a function of dopant concentration added additional complexity to the characterisation[2]. To solve this particular question Fe Kβ X-ray emission spectroscopy (XES) measurements were performed with Fe doping concentrations (x) ranging from 18 % down to 0.2 % in $Li_2[Li_{1-x}Fe]N$. The spectra show no variation in the intensity ratio or splitting between the Kβ′ and $K\beta_{1,3}$ emission lines, confirming that the Fe oxidation state does not vary with dopant concentration (Fig. 1d). Furthermore, measurements in the valence-to-core region of the spectra confirm no variation in bonding at Fe sites with respect to dopant concentration (Fig. 1e). Finally, to confirm the oxidation state of Fe sites, Fe $L_{2,3}$-edge X-ray absorption spectroscopy (XAS) measurements were performed at the I10-BLADE beamline to directly probe the 3d valence shell. These measurements were analysed using ligand-field multiplet simulations. The Fe sites are confirmed to have a +1 oxidation state with a $^4D_{7/2}$ ground state of ^4E symmetry. The energetic order of the 3d orbitals are found to be affected by strong Fe 4s–$3d_{z^2}$ mixing that lowers the energy of the $3d_{z^2}$ orbital resulting in a $a_{1g}{}^2e_{2g}{}^3e_{1g}{}^2$ ground state configuration. The Fe $L_{2,3}$-edge XAS analysis enabled experimental quantification of $3d_{z^2}$ energy reduction. The linear ligand field with large $3d_{z^2}$ energy reduction results in the first-order spin-orbit coupled ground-state that gives rise to the rare-earth like magnetic anisotropy barrier in Fe doped lithium nitride.

Together the X-ray spectroscopy results identify the Fe dopant sites in lithium nitride to be clean of stoichiometric vacancies and geometrically equivalent. It is proposed that the combination of a short Fe-N bond, related strong 3dπ bonding and high point symmetry imposed by the hexagonal lithium nitride lattice contribute to suppress vibronic effects, resulting in increased magnetic coercivities with respect to other linear single-ion magnets. These findings are key to furthering understanding of how transition metal ion dopants could be used to replace toxic and expensive rare-earth ions in magnets and next-generation nanoscale information storage devices.

References:

1. Jesche A. *et al.* Giant magnetic anisotropy and tunnelling of the magnetization in Li2(Li1−xFex)N. *Nat. Commun.* **5**, 3333 (2014). DOI: 10.1038/ncomms4333

2. Xu L. *et al.* Spin-reversal energy barriers of 305 K for Fe2+ d6 ions with linear ligand coordination. *Nanoscale* **9**, 10596–10600 (2017). DOI: 10.1039/C7NR03041J

Funding acknowledgement:
We acknowledge the support of the Royal Society of Chemistry (RM1802-4019) and Deutsche Forschungsgemeinschaft (DFG, German Research Foundation) - Grant No. JE748/1.

Corresponding authors:
Dr Michael L. Baker, Department of Chemistry, the University of Manchester, and The University of Manchester at Harwell, michael.baker@manchester.ac.uk; Mr Myron S. Huzan, Department of Chemistry, the University of Manchester, and the University of Manchester at Harwell

Using synchrotron radiation to understand mechanochemically-prepared catalysts

Related publication: Blackmore R. H., Rivas M. E., Tierney G. F., Mohammed K. M. H., Decarolis D., Hayama S., Venturini F., Held G., Arrigo R., Amboage M., Hellier P., Lynch E., Amri M., Casavola M., Eralp Erden T., Collier P. & Wells P. P. The electronic structure, surface properties, and: In situ N_2O decomposition of mechanochemically synthesised $LaMnO_3$. *Phys. Chem. Chem. Phys.* **22**, 18774–18787 (2020). DOI: 10.1039/d0cp00793e

Publication keywords: Mechanochemistry; N_2O decomposition; Perovskite; Catalysis; XAS; *in situ* NAP-XPS

The commercial catalysts currently used to remove polluting gases from vehicle exhausts rely on expensive precious metals, with demand continually growing. Preparing these catalysts often requires solvents, waste treatment and elevated temperatures, all with an environmental cost. One solution is to investigate the use of an alternative, more abundant material. $LaMnO_3$ has shown promising catalytic behaviour and is made by physically mixing two solid reactants.

The catalytic activity of materials is highly dependent on how they are produced. In this work, researchers synthesised $LaMnO_3$ by a novel method, ball milling, to improve its catalytic properties. To replicate or optimise the final material structure, it is vital to investigate the chemical steps occurring within the ball mill. However, the ball mill setup makes it difficult to perform real-time analysis. Therefore, the research team replicated the conditions experienced within the ball mill by applying extreme pressures to the starting materials.

Using Diamond Light Source's Energy Dispersive EXAFS beamline (I20-EDE) meant they could monitor how the structure changes with increasing pressure, using X-ray Absorption Fine Structure (XAFS) measurements in real-time. This beamline setup also allowed them to use a specialised high-pressure cell. They used complementary measurements on Diamond's Versatile Soft X-ray (VerSoX) beamline (B07) to study the surface properties of the materials during catalysis. Beamline I20-Scanning was used to look at electronic structure.

For industrial companies researching ball milling as an alternative production route, i.e. for autocatalysis or battery materials, this research highlights that though the preparation route produces beneficial properties at a lower environmental cost, understanding its underlying chemistry is hugely challenging.

As the UK moves towards a net zero carbon future, as enshrined in law, current technologies will need to adapt to the changing legislative and environmental requirements. Catalysis will be a major component of the solution to reducing our carbon emissions; it will be an essential tool in sustainable energy production, allow us to upgrade waste carbon streams, and by its very nature make processes more atom efficient and reduce the associated energy burden. However, the need to reduce carbon emissions will touch all areas of industrialised processes, including the production of catalysts themselves. This means that catalysts will need to be comprised of 'Earth abundant' elements that reduce the need for energy intensive and wasteful extraction processes of scarce resources, alongside routes to preparing materials that produce less waste, have reduced number of process steps, and are less energy intensive.

An example of this can be seen in the remediation of environmental pollutants (for example, N_2O). N_2O is a by-product of major industrialised processes (e.g. production of nitric acid for manufacture of fertilisers) and has a global warming potential (GWP) that is roughly 310 times higher than that of CO_2 and an atmospheric half-life of over 115 years. The decomposition of N_2O is traditionally achieved using catalysts based on precious metals. One promising alternative is to use perovskite structures of mixed-metal oxides, for example in this work we have focussed on $LaMnO_3$. $LaMnO_3$ is traditionally prepared in a multi-step process, where chemical precursors of La and Mn are mixed with other chemical reagents to make a 'sol-gel'. This step allows for intimate mixing of La and Mn components before high thermal treatments allow for the crystallographic perovskite $LaMnO_3$ structures to be produced. Clearly, it is desirable to move towards catalysts that rely on more plentiful (and secure) resources. However, is there more that can be done to prepare these materials in a more sustainable process? In recent years, mechanochemistry has emerged as a viable alternative to traditional synthetic methods for the production of advanced functional materials; this is to say that chemical reactions can be achieved through the physical action of mechanically mixing materials, without the need for additional solvents and thermal annealing steps. For $LaMnO_3$, it is now well documented that this can be prepared through the use of planetary ball-milling applied to single oxide precursors (e.g La_2O_3 and Mn_2O_3) [1].

The activity of a heterogenous catalyst is heavily dependent on the precise structures of materials, which are in turn reliant on the chosen preparation route. The use of mechanochemistry to produce $LaMnO_3$ gives rise to materials that contain significant amounts of both crystalline and amorphous materials. This is not necessarily a disadvantage. We recently demonstrated that mechanochemically prepared $LaMnO_3$ has a superior activity towards N_2O decomposition, when working under low temperature conditions[1]. As the preparation method is crucial in controlling catalyst activity it is important to understand the chemical steps that take place during mechanochemical synthesis. This is an extremely challenging endeavour; the act of ball-milling produces collision events that generate high pressure and temperature conditions that facilitates the chemical transformation. Ideally, the evolution of chemical changes would be followed in real-time during the process of ball-milling. However, the fast rotation of the milling jars and the presence of milling media means that an alternative approach is required.

In our study on the I20-EDE beamline at Diamond we were able to simulate the high-pressure conditions during ball-milling and isolate the effect this has on the chemical transformations (Fig. 1). Previously, we have mechanochemically synthesised perovskite $LaMnO_3$ from Mn_2O_3 and La_2O_3 at room temperature in atmospheric conditions using a high energy planetary ball mill. X-ray absorption spectroscopy (XAS) has proven extremely vital in analysing ball-milled samples due to the amorphous, disordered content when

Figure 1: DAC installed on the I20-EDE experimental hutch.

analysing *ex situ* XAS at 'time slices' through the synthesis[1]. Our approach was to isolate and simulate high-pressure conditions using a diamond anvil cell (DAC) and the collect XAS data during this process at the Mn K-edge. Using I20-EDE was crucial as the configuration is better suited to coupling with the DAC that generates the high pressure. In our experiment, we were able to use perforated diamond windows (0.5 mm thick) in order to reduce the diamond absorption at the Mn K-edge (6.54 KeV). Pressure readings were performed using ruby fluorescence as a standard, on an iHR320 Raman spectrometer from Horiba using the 532 nm laser. XAFS measurements were performed with a spot size of 0.05 mm diameter with pressure readings every 2 GPa up to 30 GPa at room temperature. Achieving these pressure conditions and being able to measure data at the relatively low-energy Mn K-edge is a significant technical achievement. In this experiment, we were not able to induce any structural transformation as a result of the application of pressure. However, this provides important information on the likely conditions required to produce perovskite structures from the application of ball-milling on Mn_2O_3 and La_2O_3[2].

To further improve our knowledge of these mechanochemically prepared materials, we used B07 at Diamond. These measurements allowed us to follow how the surface structure of the catalyst evolved under operating conditions using Near-Ambient Pressure X-ray Photoelectron Spectroscopy (NAP-XPS) and the effect of the atmospheric conditions during milling. The NAP-XPS experiments allowed us to look at specific oxygen environments on the surface of the catalyst during the decomposition of N_2O. This oxygen signature, when the catalyst was milled with argon, showed a higher proportion of adsorbed species on exposure to N_2O at room temperature. This indicated that the argon milled samples were more adept at activating N_2O, which subsequently resulted in improved performance of N_2O decomposition at lower temperatures. The overall study – including other work looking at the electronic structure on I20-Scanning – shows the importance of synchrotron radiation methods in studying the structurally diverse materials produced during mechanochemistry. This is an important necessity as we seek to develop sustainable methods for producing enhanced catalyst materials.

References:

1. Blackmore R. H. *et al.* Understanding the mechanochemical synthesis of the perovskite $LaMnO_3$ and its catalytic behaviour. *Dalt. Trans.* **49**, 232–240 (2019). DOI: 10.1039/c9dt03590g

2. Blackmore R. H. *et al.* The electronic structure, surface properties, and: In situ N_2O decomposition of mechanochemically synthesised $LaMnO_3$. *Phys. Chem. Chem. Phys.* **22**, 18774–18787 (2020). DOI: 10.1039/d0cp00793e

Funding acknowledgement:
The UK Catalysis Hub is kindly thanked for resources and support provided via our membership of the UK Catalysis Hub Consortium (portfolio grants EP//K014706/1, EP/K014668/1, EP/K014854/1, EP/K014714/1 and EP/I019693/1). The University of Southampton and EPSRC are thanked for the iCASE studentship of RHB. Peter Wells and KM wish to acknowledge the STFC for funding the position of KM (ST/R002754/1). Peter Wells and MC wish to acknowledge the EPSRC for funding the position of MC (EP/R011710/1).

Corresponding author:
Dr Peter Wells, University of Southampton/Diamond Light Source, ppwells@soton.ac.uk/peter.wells@diamond.ac.uk

Soft Condensed Matter Group

Robert Rambo, Science Group Leader

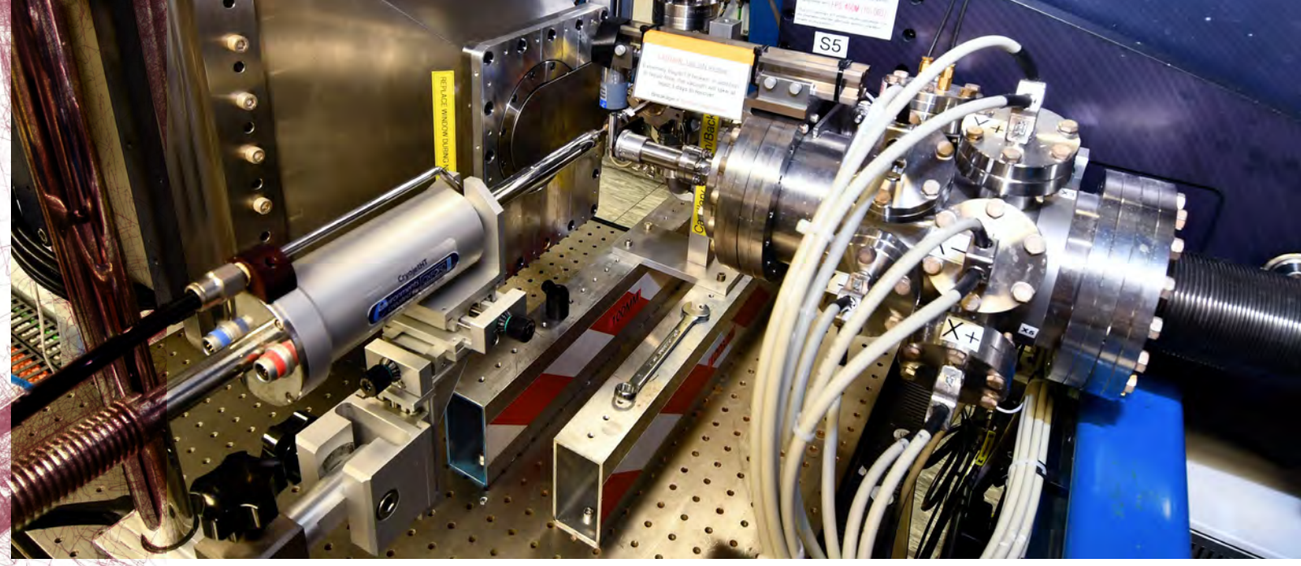

The Soft Condensed Matter (SCM) Group at Diamond Light Source is comprised of the High Throughput Small Angle X-ray Scattering (SAXS) (B21), the Multimode Infrared Imaging and Microspectroscopy (MIRIAM) (B22), SAXS and Diffraction (I22) and the Circular Dichroism (CD) Microspectroscopy (B23) beamlines at Diamond Light Source. This unique portfolio of instruments enables studies of non-crystalline materials at micro to meso-scale resolutions that include two-dimensional thin-films (photovoltaics), living mammalian cells, three-dimensional matrices (e.g. metal-organic frameworks, gels and waxes) and nano-particles in non-crystalline states. The SCM group now offers mail-in services for SAXS and CD measurements through UAS (User Administration System) announcements. In addition, I22, B22 and B23 offer off-line access to IR microscopy and imaging, CD spectroscopy and SAXS measurements.

In the last year, the SCM Group contributed to 172 scientific publications, a 30.3% increase over 2020 with B21 increasing their publications to a new record of 83. SCM publications covered many aspects of healthcare including use of metal-organic frameworks in drug release, anti-microbial films and peptoids, diagnostic imaging and vaccine stabilisation at room temperature. Further publications looked at contributing factors associated with prominent diseases such as the role of intrinsically disordered proteins associated with *Helicobacter pylori* (stomach disease) and hepatitis C virus (liver disease), as well as specific proteins in *Vibrio cholera* (cholera), dengue virus, cancer, tuberculosis, infertility, *Pseudomonas aeroginosa* (disease associated with cystic fibrosis), heart disease, Alzheimer's disease and malaria. Outside of healthcare, SCM instruments were critical to investigations examining self-assembled systems that included innovations in liquid crystals, nano-tubes, hydrogels, light-sensitive and functionalised graphene thin-films, nano-structured cages for carbon capture and industrial processes and improving perovskite stability in solar photovoltaics.

The 2020 COVID-19 working restrictions created many challenges for our scientific community. In response, B21 and B23 optimised for mail-in experiments in support of COVID research, whereas B22 and I22 quickly invested in infrastructure to support both mail-in and remote experiments. At the start of the 2020 academic year, a new cohort of students joined our existing SCM doctoral students, which now include the Universities of Pisa (Italy), Surrey and Chalmers, Southampton, College London, Imperial, Sheffield, Reading, Leeds and Durham. SCM provided several training workshops via online platforms including the popular S4SAS meeting led by I22, which had the prominent SAXS Professor Otto Glatter as keynote speaker. B22 organised a series of training workshops using machine learning software (Quasar) in infrared image analysis and B21 hosted a series of online, small group data analysis sessions for users, which is now a routine part of our user programme.

2020 has been a transformative year for all beamlines in SCM. B21's mail-in services motivated a new web-interface for users to schedule and manage mail-in experiments through ISPyB. This will be extended to B23 and I22 in 2021. B23 increased its capacity to perform high-throughput CD experiments including automated thermal studies. I22 developed new sample environments for mail-in and remote experiments allowing users to set-up experiments for 1,000s of liquid and solid samples.

B21 update

B21 studies noncrystalline, randomly oriented particles using high-throughput approaches. SAXS measurements can be made on any type of sample and in any physical state. The life sciences community comprises our largest user group since such measurements provide the opportunity to study biological machines in conditions that are comparable to their liquid, hydrated environment. During 2020, B21 provided over 70 mail-in experiments that included research in COVID-19, RNA helicases, antibody complexes, gelation, photocatalysis, gelation, statins, stress proteins, oncogenes and biotech industry.

In planning for Diamond-II (proposed upgrade programme), B21 commissioned the design and manufacturing of a new sample delivery environment that exploits laminar liquid flow. Radiation damage is a major contributor to measurement error in SAXS. Under the flow conditions used in size-exclusion chromatography coupled SAXS, the liquid flows much slower at the walls of the capillary used in the actual X-ray scattering measurement. The slow flowing liquid with protein leads to deposition of protein on the walls of the capillary (fouling) during X-ray exposure, contributing significantly to measurement background thus reducing the instrument's sensitivity. The new co-flow device creates a flow of inert liquid around the sample that pushes the sample away from the walls of the capillary, thereby eliminating fouling. It can be expected that the performance of B21 in Diamond-II will lead to significant capillary radiation induced fouling.

B22 update

The Multimode Infrared Imaging and Microspectroscopy (MIRIAM) beamline B22 is used to assess the molecular composition and microscopic spatial distribution of a sample at the highest, optically-achievable resolution in the infrared (IR). B22 operates two end stations for scanning IR spectro-microscopy and IR imaging, with a suite of single and 2D detectors that seamlessly cover the whole IR range, from near-IR to mid-IR and further into terahertz (THz). B22 has been used in the analysis of inorganic-organic combinations in biomineralogy or composite materials, chemical degradation in conservation and archaeology, as well as studying live mammalian cells under the IR microprobe for *in situ* drug response, an important tool in anti-cancer research. This past year, B22 provided nano- and micro-spectroscopy imaging experiments on rubber composites, pluripotent stem cells in cardiomyocytes, macrophage phenotyping, spinal cords, retinas and photovoltaics.

In 2020, scientists from the University of Manchester led by Dr Martin Schröder developed a new separation method based on metal-organic frameworks (MOFs) to separate xylene isomers at low temperatures. Currently, industrial-scale xylene isomer separation requires fractional crystallisation at moderately high temperatures (>220 K). Xylenes are critical compounds in many industrial sectors where lower temperature separation methods will lead to major reductions in energy consumption and waste. Dr Schröder's group showed that by modulating the chemical environment and internal pore size of MOFs, the MOFs can be used to effectively discriminate xylene isomers. B22 used its THz spectroscopy capabilities to look inside the MOFs and show definitive and specific uptake of xylenes in the non-crystalline material.

The beamline made major changes in support of remote experiments with new IT hardware and changes in working protocols. B22 continues with collaborative calls for IR nanospectroscopy in photothermal mode (AFM-IR) by synchrotron radiation (SR). This cutting-edge method is suitable for molecular analysis of submicron to micron scale organic matter and biomaterials - from mammalian cells to microplastic - with exceptional sub-micron resolution (i.e. up to 100 times below the IR wavelength scale). However, B22 will be commissioning a new AFM end station (summer 2021) that will allow tapping AFM-IR and scattering Scanning Optical Microscopy (s-SNOM) measurements by SR. The modernisation will improve data acquisition rates and spatial resolution, allowing IR nanospectroscopy to be performed at tens of nanometers resolution.

B23 update

The B23 synchrotron radiation Circular Dichroism (CD) beamline uses circularly polarised light to characterise the structure-architecture of complex chiral materials in solution and in solid-state thin films. Chiral materials have a handedness (like our right and left hands that are not superimposable) and absorb differently the circularly polarised light, generating CD fingerprint ID spectra. For optoelectronic materials, the measurement of CD at 50 µm of spatial resolution can inform about the homogeneity of the supramolecular structure, which is strictly related to their efficacy. For biological samples, CD is also used to monitor in microfluidic chips structural changes, drug binding, protein instabilities as a function of temperature, pressure, ionic strength, surfactant, pH, ligand interactions and ageing.

Pioneered by the B23 team, CD Imaging (CDi) technology exploits a highly collimated, synchrotron microbeam for scanning thin-films of solid materials. Unlike absorption, CDi can inform on the homogeneity of the chiral supramolecular structure. Led by Dr Jessica Wade (Imperial College London), new research in polymers showed that large-scale chiral properties can emerge from self-assembling of achiral polymers doped with small chiral molecules. This represents a breakthrough in material engineering for spintronic devices and high-performance electronic displays. CDi at B23 is the only synchrotron-based instrument with the required sensitivity to guide the researchers on how to improve the properties of chiral materials. Combined with Diamond's high-resolution microscopy, B23 is a unique worldwide facility for material science and life sciences.

I22 update

The Small Angle Scattering and Diffraction beamline (I22) offers combined Small and Wide Angle X-ray Scattering (SAXS and WAXS) studies on a range of low order biological, natural and synthetic samples. I22 excels at providing structural information on partially ordered materials, ranging from colloidal nanoparticles and thin-films to large hierarchical structures such as bone. During COVID-19 restrictions, I22 supported 18 individual user visits distributed as 10 remote and eight on-site visits. However, in support of mail-in operations, I22 supported 45 additional user visits utilising bespoke sample environments for high-throughput experiments on solid and liquid samples.

I22 completed its major Beam Condition Optics (BCO) upgrade project allowing for precise and stable control of a microfocus X-ray beam for SAXS. The new optical layout has significantly reduced divergence for microfocus experiments and has provided access to much lower q (scattering vectors) than previously available. The upgrade has been a step change in mapping experiments particularly examining deformation in bones and eye lenses. I22 upgraded its bimorph mirror controller in 2020 to complement the BCO upgrade and also sought approval of a new double crystal monochromator (DCM) to upgrade its original 2007 DCM. The new DCM is due for installation in June 2021 along with an upgraded, in-vacuum WAXS detector.

The I22 Principal Beamline Scientist Dr Nick Terrill, in collaboration with Prof Michael Rappolt from the School of Food Science and Nutrition at the University of Leeds, manage an Engineering and Physical Sciences Research Council (EPSRC) grant to support an offline SAXS facility at Diamond. The Multi-User Facility for SAXS/WAXS (DL-SAXS) now has an installed Xenocs Xeuss 3.0 instrument operating with an Eiger-2R 1M detector. The facility is under commissioning and will accept a limited number of users in 2021. This instrument will be critical to the SCM Sample Environment Development Laboratory for independent development/testing of sample environments prior to beamtime. Studying materials under intended use, such as lubricants under frictional strain or simply the stretching of a novel bioengineered material requires bespoke sample environments. Testing these sample environments prior to beamtime drives innovation and optimises the available beamtime.

Priming human elastic proteins for assembly into elastic tissues

Related publication: Lockhart-Cairns M. P., Newandee H., Thomson J., Weiss A. S., Baldock C. & Tarakanova A. Transglutaminase-Mediated Cross-Linking of Tropoelastin to Fibrillin Stabilises the Elastin Precursor Prior to Elastic Fibre Assembly. *J. Mol. Biol.* **432**, 5736–5751 (2020). DOI: 10.1016/j.jmb.2020.08.023

Publication keywords: Tropoelastin; Elastin; Fibrillin; Tissue transglutaminase; Elastic fibres; Coacervation

Elastic fibres are the main elastic component of mammalian elastic tissues such as major arteries, the lungs and skin. They provide resilience and recoil, enabling these tissues to expand and contract up to two billion times over a person's lifetime. The two most abundant components of elastic fibres are tropoelastin and fibrillin. The process by which elastic fibres assemble is not well understood. This information is needed in regenerative medicine, which aims to replace or regenerate cells, tissues or organs to restore or establish normal function.

We know that the enzyme transglutaminase-2 covalently links tropoelastin and fibrillin and that this interaction between tropoelastin and fibrillin enhances tropoelastin assembly. However, we do not understand the importance of the linkage between tropoelastin and fibrillin and why this supports elastic fibre assembly. As part of a long-term collaboration, researchers from the University of Manchester, the University of Sydney and the University of Connecticut used the BioSAXS beamline B21 to collect Small-Angle X-ray Scattering (SAXS) data. They used the data to generate models of tropoelastin and fibrillin, and a tropoelastin-fibrillin complex. These models were used to understand what effect cross-linking had on the dynamics of these proteins. The models suggest that tropoelastin and fibrillin interact in an end-to-end manner and that cross-linking these two proteins together reduces their molecular motions, suggesting a stabilising effect due to this interaction. These findings suggest that the cross-link formation between tropoelastin and fibrillin stabilises the elastin precursor so that it is primed for elastic fibre assembly.

Elastic fibres are the main elastic component of mammalian elastic tissues such as major arteries, the lungs and skin, where they provide resilience and recoil. These tissues expand and contract up to two billion times over a person's lifetime. This extraordinary resilience is needed to carry out essential elasticity to ensure viability. The two most abundant components of elastic fibres are elastin and fibrillin microfibrils: tropoelastin (TE) is assembled to make elastin, and fibrillin microfibrils are assembled from the glycoprotein fibrillin-1. The assembly of elastic fibres occurs outside of the cell and is a highly organised and multistep process. TE can spontaneously and rapidly self-assemble, or coacervate, from a monomer to a multimer which is deposited onto a scaffold of fibrillin microfibrils[1]. Once deposited on fibrillin microfibrils, the TE multimers coalesce to form stable, insoluble elastic fibres. The enzyme transglutaminase-2 catalyses a transamidation reaction that covalently connects lysine residues to glutamine residues and forms a covalent intermolecular cross-link between TE and fibrillin[2]. The initial deposition of TE multimers onto fibrillin microfibrils is thought to be the primary step required for further assembly and TE recruitment to form larger elastic fibres, but the molecular details of this process are unknown. In order to understand the impact of cross-link formation on the structure and properties of TE and fibrillin, the structure and dynamics of TE and fibrillin were analysed individually and within the cross-linked TE-fibrillin complex.

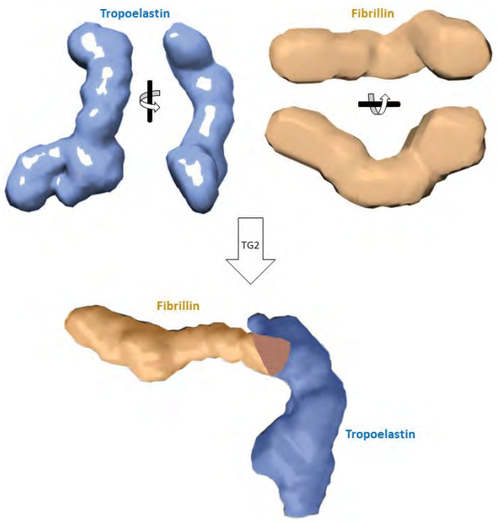

Figure 1: Models of the region of fibrillin (orange) that interacts with TE (blue) calculated from experimental SAXS data are shown in two orthogonal orientations. The TE-fibrillin complex has an elongated L-shape which supports an interaction (shown in orange/blue) between the N-terminal region of TE and fibrillin.

Due to their size and flexibility, TE and fibrillin are not suitable for structural determination techniques such as X-ray crystallography or NMR so we had previously worked as a team to obtain the structure of the TE monomer in solution, using small-angle X-ray scattering (SAXS) and small-angle neutron scattering (SANS). SAXS and SANS can provide shape information on proteins in solution without the need for crystallisation or labelling. We found that it has an extended, asymmetrical shape ~20 nm in length[3]. The region of fibrillin involved in the TE cross-link has also been analysed by SAXS[4] and this region of fibrillin was used for further analysis (referred to as fibrillin). After purifying a cross-linked TE-fibrillin complex, it was analysed by multi-angle light scattering and analytical ultracentrifugation to determine its size, shape and the way that it moves in solution. The structural parameters were then analysed by SAXS on beamline B21. SAXS data for the complex and both individual components were collected and parameters including its overall size, shape and dimensions were compared. From these SAXS data, bead modelling was performed. The resulting model of the complex was L-shaped, comprising a thin, elongated region connected perpendicularly to a shorter, wider region. Comparison of the models of the fibrillin, TE and the TE-fibrillin complex showed that the model of the complex had elements of both fibrillin and TE combined, and displayed dimensions consistent with the addition of these components (Fig. 1). Moreover, docking the N-terminal region of TE to the rounded end of fibrillin gave a shape entirely consistent with the model of the complex which supports an interaction between the N-terminal region of TE and the terminal domain of fibrillin.

To computationally simulate the dynamics of TE, fibrillin and the TE-fibrillin complex, bead-spring elastic network models were developed. Bead spacing

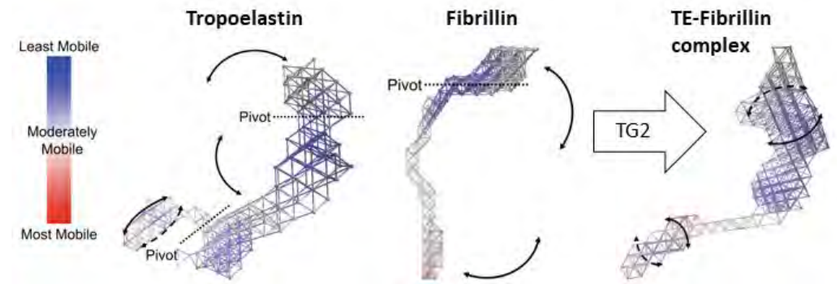

Figure 2: Normal mode analysis of beads of the elastic network model of combination of modes 1-6 of TE, showing a bending coil; the dashed line and pivot indicates the axis about which bending occurs; the TE-binding region of fibrillin, showing an overall bending motion; the dashed line and pivot indicates the axis about which bending occurs. Upon formation of a transglutaminase-2 (TG2) cross-link, the TE-fibrillin complex shows a twisting extension and twisting base; colours correspond to a mobility scale for low mobility (blue), moderate mobility (white) and high mobility (red).

was assigned based on a regular lattice derived from the SAXS bead models[5], for the complex and both individual components. Beads were interconnected through elastic springs. Normal mode analysis was performed to extract each of the structures' least energetically expensive, biologically accessible oscillating modes of motion e.g. the molecule's natural fluctuations. The oscillating motions that characterise each mode within TE, fibrillin and the TE-fibrillin complex were analysed for their dynamic patterns. These data showed that specific movement patterns found in the TE and fibrillin structures individually were not translated to the complex. TE exhibited its characteristic scissor-twist motion, as described previously[5]. For fibrillin, there was an overall bending motion perpendicular to the length of the molecule and a pivot between the upper and lower regions. However, the multiple twisting motions shown in TE were not seen in the TE-fibrillin complex, which had a stationary base with a mild twist in the lower region (Fig. 2). Therefore, cross-linking of TE and fibrillin points to a stabilising effect on the base of the complex, where the cross-linking site is expected to reside.

In this research, we describe the low-resolution structure, hydrodynamic properties and simulated dynamics of a transglutaminase cross-linked complex of TE and fibrillin. A previous study showed that a transglutaminase cross-link between fibrillin and TE could be formed which facilitated tropoelastin assembly, but the mechanism by which cross-linking supported coacervation was unknown. Hydrodynamic data on the TE-fibrillin complex suggests that fibrillin and TE interact in an end-to-end manner which is supported by the SAXS data on the complex showing an elongated L-shaped molecule which retained elements of the individual molecules' shapes. Our data show that the cross-link between fibrillin and tropoelastin restricts their molecular movement, therefore we propose that the microfibril-elastin interface similarly displays reduced motion (Fig. 3). Moreover, dynamic analysis of elastic network models of the complex supports our theory of a pronounced stabilising effect. In this model, the stiffened interface helps to dissipate substantial amounts of elastic energy by structural damping. Furthermore, this stabilisation of tropoelastin by binding to fibrillin microfibrils likely contributes to the mechanical response of mature elastic fibres.

References:

1. Godwin A. R. F. *et al.* The role of fibrillin and microfibril binding proteins in elastin and elastic fibre assembly. *Matrix Biol.* **84**, 17–30 (2019). DOI: 10.1016/j.matbio.2019.06.006
2. Clarke A. W. *et al.* Coacervation is promoted by molecular interactions between the PF2 segment of fibrillin-1 and the domain 4 region of tropoelastin. *Biochemistry* **44**, 10271–10281 (2005). DOI: 10.1021/bi050530d
3. Baldock C. *et al.* Shape of tropoelastin, the highly extensible protein that controls human tissue elasticity. *Proc. Natl. Acad. Sci. U. S. A.* **108**, 4322–4327 (2011). DOI: 10.1073/pnas.1014280108
4. Baldock C. *et al.* Nanostructure of fibrillin-1 reveals compact conformation of EGF arrays and mechanism for extensibility. *Proc. Natl. Acad. Sci. U. S. A.* **103**, 11922–11927 (2006). DOI: 10.1073/pnas.0601609103
5. Yeo G. C. *et al.* Biomolecules: Subtle balance of tropoelastin molecular shape and flexibility regulates dynamics and hierarchical assembly. *Sci. Adv.* **2**, e1501145 (2016). DOI: 10.1126/sciadv.1501145

Funding acknowledgement:
The Wellcome Centre for Cell-Matrix Research is supported by funding from Wellcome (203128/Z/16/Z). CB gratefully acknowledges BBSRC funding (Ref: BB/N015398/1, BB/R008221/1 and BB/S015779/1). This work utilised the Extreme Science and Engineering Discovery Environment (XSEDE), which is supported by National Science Foundation grant number ACI-1053575. XSEDE resources Stampede 2 and Ranch at the Texas Advanced Computing Center and Comet at the San Diego Supercomputing Center through allocation TG-MCB180008 were used.

Corresponding author:
Prof. Clair Baldock, University of Manchester,
clair.baldock@manchester.ac.uk

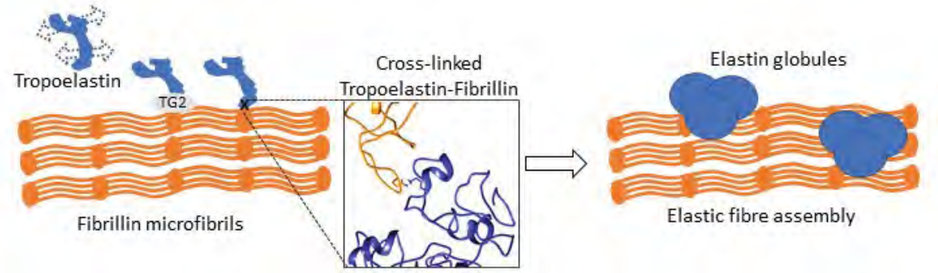

Figure 3: In the process of elastic fibre assembly, tropoelastin molecules, which are inherently flexible, are deposited onto fibrillin microfibrils. The enzyme transglutaminase-2 (TG2) forms a covalent bond between fibrillin and tropoelastin which reduces their molecular movement and stabilises the microfibril-elastin interface, to facilitate elastic fibre assembly.

Viewing drug action in a cell by infrared nanoprobe

Related publication: Chan K. L. A., Lekkas I., Frogley M. D., Cinque G., Altharawi A., Bello G. & Dailey L. A. Synchrotron Photothermal Infrared Nanospectroscopy of Drug-Induced Phospholipidosis in Macrophages. *Anal. Chem.* **92**, 8097–8107 (2020). DOI: 10.1021/acs.analchem.9b05759

Publication keywords: RE-AFM-IR; Synchrotron IR; Photothermal nanospectroscopy; NanoFTIR; PTIR

Detecting metabolic changes inside a biological cell as a result of drug treatment is fundamental in pharmaceutical development. Currently, most techniques require the addition of dye (staining) to reveal some chemical changes, which may alter the natural process and potentially produce misleading results. Infrared (IR) microspectroscopy can probe chemical changes in biological matter without the use of dye or chemical label, but the images produced optically so far are too coarse to see clearly inside a single cell.

Macrophages are a type of white blood cell that defend against infection. They produce many tiny fatty droplets when exposed to drugs, but the exact reason for this response was not clear. Knowing the chemical composition of these droplets will help scientists better understand the process and could help develop better medicines.

A team of researchers investigated a new Synchrotron IR spectroscopic imaging method, developed on Diamond Light Source's Multimode InfraRed Imaging And Microspectroscopy (MIRIAM) beamline (B22), to probe the molecular changes inside macrophages. The results showed that IR nanospectroscopy can measure a drug's effect inside a single mammalian cell by clearly identifying the chemical changes within the tiny fatty droplets before and after the application of the drug. Researchers will be able to use this powerful new molecular imaging tool to understand the responses of macrophages exposed to different drugs. This will help to identify new drug candidates that are more suitable for further development versus those that are for example ineffective or toxic, improving the chance of success in delivering better medicines in the near future.

In the development of inhaled medicines, poor understanding of alveolar macrophage cellular responses to new drug compounds have been identified as a key barrier[1]. Phospholipidosis or adaptive responses has been associated with the appearance of 'foamy macrophages' but the exact mechanism remains poorly understood. Xenobiotics (e.g. amiodarone, poorly soluble drugs, polymeric nanoparticles) could induce the 'foamy macrophage' phenotype whereby cells express with a granular or vacuolated cytoplasmic appearance (Fig. 1). As a result, within the context of pre-clinical safety studies, the appearance of foamy macrophage is usually sufficient to halt compound development contributing to an already high rate of attrition in drug development.

An electron micrograph of the foamy macrophage is shown in Fig. 1 highlighting the well-defined vacuoles of 0.5-2 µm in diameter. A chemically-resolved analytical technique with a nanoscale spatial resolution would shed new light in the understanding of macrophages' responses to drug treatment.

Resonance-Enhanced Infrared Atomic Force Microscopy (RE-AFM-IR) developed with Synchrotron Radiation at Diamond beamline B22 is a near-field IR probe capable of measuring infrared spectra (thereby the chemical information) from a 100 nm spot[3] offering an ideal tool to probe the composition inside the vacuoles, potentially solving a major obstacle in inhaled drug discovery. The specific advantage of using a synchrotron source over tunable IR lasers[4,5] is that the light source covers a broader IR range, the spectral profile is more uniform and the whole spectrum can be collected simultaneously. These advantages are important for exploratory analysis of biological matters, where the samples are complex and often molecular changes can only be detected by the analysis of multiple spectral bands. In this work, we have applied the novel method for the first time at B22 on biological matter to highlight its potential in the study of drug induced phospholipidosis (DIPL).

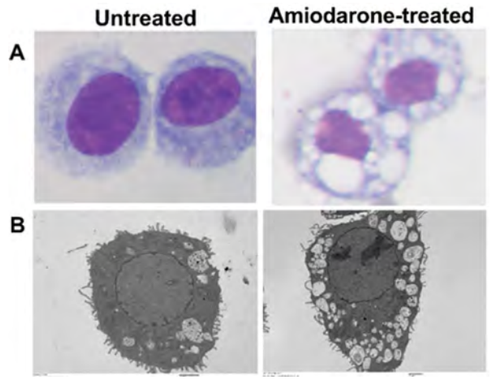

Figure 1: Microscopic characterisation of untreated and amiodarone-treated cells. The spatial distribution of phospholipid inclusion bodies is shown by: (A) light microscopy with hematoxylin and eosin staining, (B) TEM.

Randomly selected untreated (UT) and amiodarone-treated (AM) cells were characterised via SR RE-AFM-IR. The integrated RE-AFM-IR intensity map (i.e. molecular response to all IR wavelengths indiscriminately) has revealed a sub-micrometre structure within the cytoplasm of the cell (Fig. 2) that is not the same as the AFM (topographical height) map. The ratio of the RE-AFM-IR map against the AFM map, which removes the contribution due to topography, has shown the nano-scale heterogeneity within the cytoplasm region. The AM cells has shown a more heterogeneous chemical distribution as a result of the formation of increase in number and size of vacuoles than the UT cells, which is in good agreement with the micrograph shown in Fig. 1.

Spectra extracted from the RE-AFM-IR map, which shows specific spectral discriminations, are shown in Fig. 3A,B revealing the local chemical compositions from the 100 nm spot. The RE-AFM-IR spectra were compared to the optical IR microscopy, confirming that spectral bands that correspond to various functional groups are all clearly captured by the novel method. It is important to highlight that the far-field spectra were captured in 5 µm spot in contrast to 100 µm spot by the RE-AFM-IR measurement. The improved spatial resolution enables the comparison of chemical differences between different sub-cellular regions (e.g. the nuclear and perinuclear regions of UT and AM cells). Results show that the AM- perinuclear scans have consistently higher carbonyl absorbance from the phospholipid than those of the AM-nucleus region and UT cells. Furthermore, the phosphate peaks have shown on average

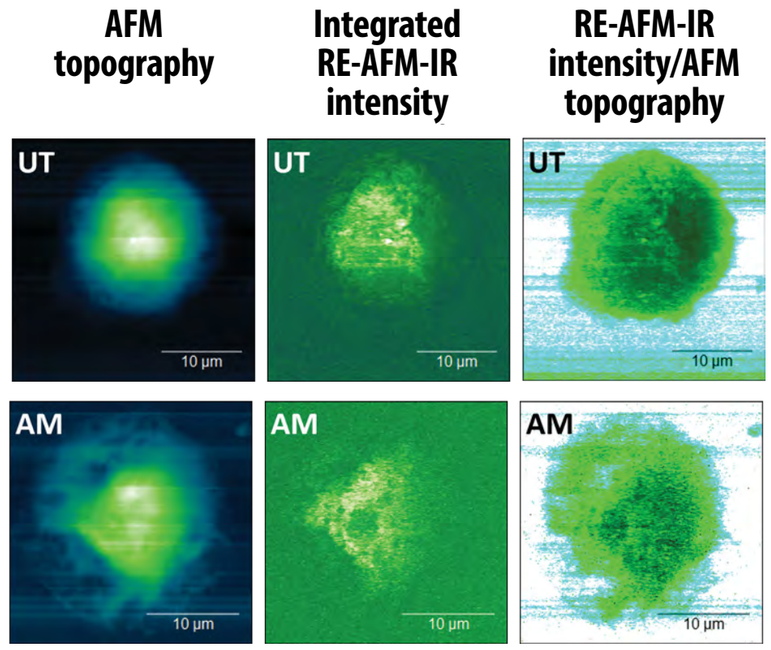

Figure 2: AFM micrographs depicting topology features are compared with overall and normalised integrated RE-AFM-IR amplitude maps for UT and AM cells.

an increase for the AM cells but with a higher variance across the scanned area because of the more heterogeneous cytosol of the AM cells, where many tiny lipid droplets were produced as shown in Fig. 2. Taken together, the RE-AFM-IR measurement has shown a general increase in absorption for all phospholipid bands suggests that the cytosol (perinuclear) region of the AM-treated cells have elevated phospholipid that are heterogeneously distributed, which is not observed in the UT cells. The data was further analysed using principal component analysis, showing a statistically significant difference between the UT/AM cells and the nucleus/perinucleus area in the phospholipid spectra regions, confirming the results observed made from the changes in band intensities.

In summary, synchrotron-based RE-AFM-IR was shown to be capable of directly measuring the entire mid-infrared absorption spectra of mammalian cells and their internal molecular composition at the 100 nm scale. To our knowledge, it is the first successful application worldwide of synchrotron RE-AFM-IR to interrogate biological soft matter at subcellular level, in this case on a cellular model of DIPL.

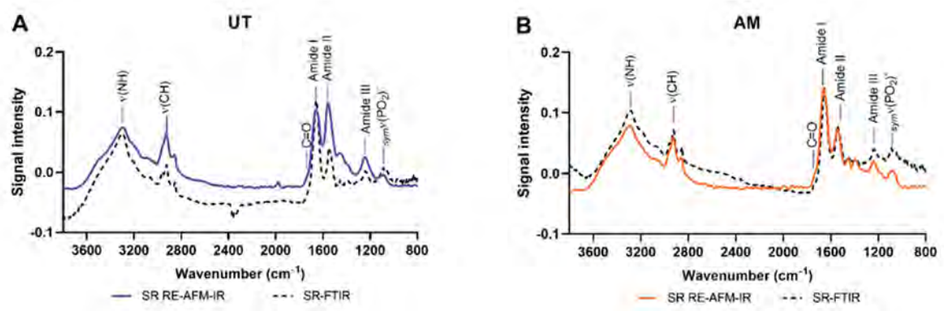

Figure 3: Averaged synchrotron RE-AFM-IR spectra (solid lines) from 15-20 scan points in three UT (A) or AM (B) cells compared to synchrotron-FTIR spectra from a single cell (dotted lines). The aliphatic lipid band (3020-2800 cm^{-1}), the lipid carbonyl ν(C=0) band (1774-1709 cm^{-1}), the phosphate bands at (1310-1147 cm^{-1}) and (1142-1020 cm^{-1}) have been used to show an increased phospholipid content (a biomarker of DIPL).

References:

1. Forbes B. *et al.* Challenges for inhaled drug discovery and development: Induced alveolar macrophage responses. *Adv. Drug Deliv. Rev.* **71**, 15–33 (2014). DOI: 10.1016/j.addr.2014.02.001
2. Chan K. L. A. *et al.* Synchrotron Photothermal Infrared Nanospectroscopy of Drug Induced Phospholipidosis in Macrophages. *Anal. Chem.* **92**, 8097–8107 (2020). DOI: 10.1021/acs.analchem.9b05759
3. Donaldson P. M. *et al.* Broadband near-field infrared spectromicroscopy using photothermal probes and synchrotron radiation. *Opt. Express* **24**, 1852 (2016). DOI: 10.1364/oe.24.001852
4. Dazzi A. *et al.* AFM-IR: Technology and applications in nanoscale infrared spectroscopy and chemical imaging. *Chem. Rev.* **117**, 5146–5173 (2017). DOI: 10.1021/ acs.chemrev.6b00448
5. Giliberti V. *et al.* Protein clustering in chemically stressed HeLa cells studied by infrared nanospectroscopy. *Nanoscale* **8**, 17560–17567 (2016). DOI: 10.1039/c6nr05783g

Funding acknowledgement:
KLAC acknowledges EPSRC for support (EP/L013045/1). Ali Atharawi thanks Prince Sattam Bin Abdulaziz University (Saudi Arabia) for his PhD sponsorship. Diamond Light Source is acknowledged for beamtime at MIRIAM beamline B22 – commissioning/collaborative call 2019 (SM21061). A special thanks to Dr Ioannis Lekkas and Dr Mark Frogley for crucial experimental support and data analysis help.

Corresponding authors:
Dr Ka Lung Andrew Chan, King's College London, ka_lung.chan@kcl.ac.uk;
Dr Gianfelice Cinque, Diamond Light Source, gianfelice.cinque@diamond.ac.uk

A potential new method for vaccines without refrigeration

Related publication: Doekhie A., Dattani R., Chen Y. C., Yang Y., Smith A., Silve A. P., Koumanov F., Wells S. A., Edler K. J., Marchbank K. J., Elsen J. M. H. va. den & Sartbaeva A. Ensilicated tetanus antigen retains immunogenicity: in vivo study and time-resolved SAXS characterization. *Sci. Rep.* **10**, 9243 (2020). DOI: 10.1038/s41598-020-65876-3

Publication keywords: Vaccine; Thermal stability; SAXS; *in vivo; in situ*; Tetanus toxoid; Silica; Ensilication; Protein; Protein unfolding; Aggregation; Denaturation

Almost all vaccines require refrigeration or freezing conditions for storage and transport. A vaccine cold chain has been developed to distribute vaccines worldwide in our fight against infectious diseases. However, if vaccines were not dependent on refrigeration or freezing, they would be available to more people, leading to higher vaccination rates and eradicating more diseases.

An international team of researchers, led by Dr Asel Sartbaeva, has developed a novel method of making existing vaccines thermally stable so that they will not depend on cold chain distribution. The process uses silica (SiO_2) to create layers of inorganic materials around individual vaccine components. This ensilication results in nanoparticles of silica with protein in the middle. The team performed *in situ* Small Angle X-ray Scattering (SAXS) measurements during ensilication, on Diamond Light Source's Time-Resolved SAXS & Diffraction beamline (I22). They chose to study tetanus toxin C fragment (TTCF), an inactive component of the tetanus toxin present in the diphtheria, tetanus and pertussis (DTP) vaccine. Their results demonstrated that ensilication maintained the vaccine effect.

All biopharmaceuticals have unique functions that require different environments for their operation. For some, lyophilisation (freeze-drying) may be the optimum choice for stabilising and transporting the bioactive compounds. However, this new methodology provides another solution for biopharmaceutical stabilisation and could help to increase vaccine transport and administration all around the world.

Vaccination is one of the greatest interventions of modern medicine. It is thought to have prevented at least 10 million deaths between 2010 and 2015[1] and has helped to successfully eradicate diseases such as smallpox and rinderpest. In the 1970s, the vaccine cold chain was devised for storage and transport of vaccines in refrigerated conditions, between 2 and 8 °C, the temperature regime that suits most vaccines for long term storage and transport (Fig. 1). While in most developed countries this was an easier undertaking due to the availability of refrigerators, electricity, infrastructure and staff training, developing countries are still lagging behind on even the most basic vaccines, leading to a large difference in infant vaccination and mortality from infectious, vaccine-preventable diseases.

The cold chain dependency prevents effective distribution of many vaccines in poorer countries, necessitating the development of thermally stable, cold chain independent vaccines. One such method of vaccine thermal stabilisation is being developed at the University of Bath and is called ensilication.

Ensilication is a method of applying a silica, SiO_2, network in layers on top of vaccine components to prevent them from denaturation. Most vaccine components include proteins, protein complexes, viruses, viral particles, protein constructs, enzymes and toxoids, thus their primary structure consists mainly of amino acid chains. Protein unfolding and aggregation are the two most damaging processes for amino acid chains that lead to denaturation due to temperature increase. The silica network, when applied, prevents this amino chain unfolding and aggregation, thus creating protection against temperature degradation.

In this study on beamline I22, our aim was to gain understanding of the ensilication mechanism by performing *in situ* ensilication and collecting high resolution data on the onset of ensilication process. Previously, our hypothesis was that silica could be grown to fully surround the target biological and follow the targets' surface structure, mimicking the surface shape and size.

At I22, we devised an experimental set up for *in situ* ensilication (Fig. 2) consisting of a line through which we continuously pumped the solution with a target biological and a syringe pump that would inject prehydrolysed silica at a specific time. Data were collected just before the injection and for up to 60 minutes after the injection. This allowed us to observe the progress of ensilication at the onset of the reaction and through ensilication and further growth of the silica nanoparticles until they precipitated out of the solution. About 40 such ensilication runs during our two-day experiment were performed, on three different targets, an enzyme, a toxoid and a protein complex. Each set up required at least an hour of preparation, as silica prehydrolysis takes about 50-60 minutes and the line had to be thoroughly cleaned before each run to avoid contamination.

The analysed data show that the ensilication is a diffusion driven process

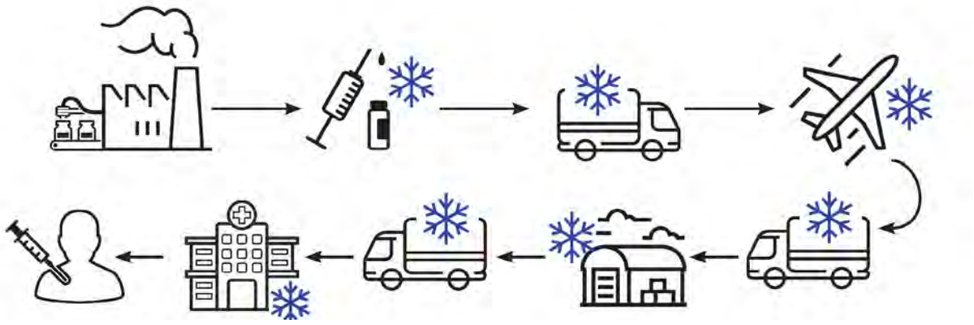

Figure 1: Vaccine cold chain. Figure modified from Sartbaeva A., "Vaccines: the end of the cold war? How the award-winning ensilication technology could remove the need to refrigerate life-saving vaccines", The Chemical Engineer, 921, 24 -29, 2018.

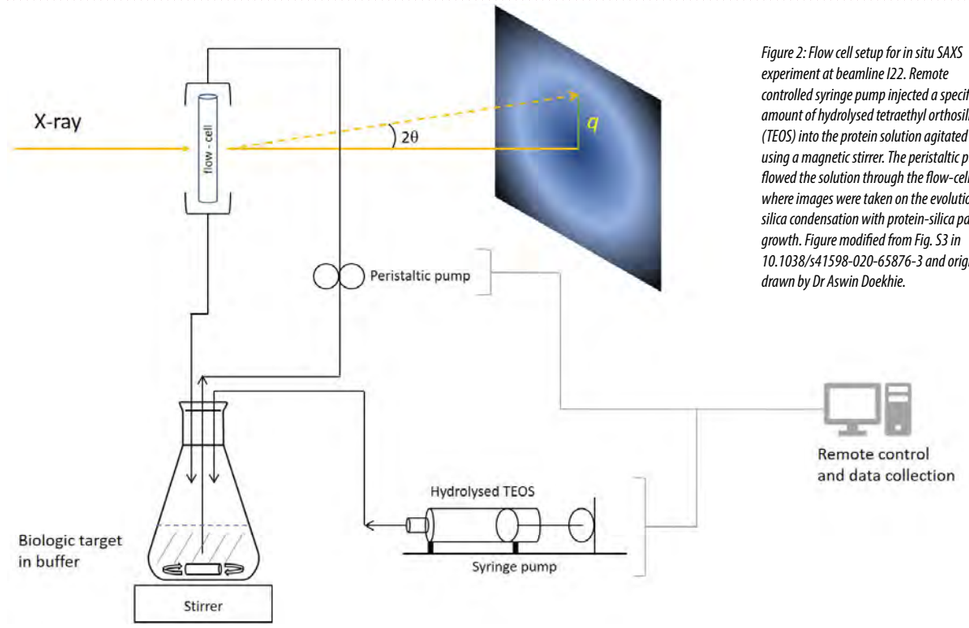

Figure 2: Flow cell setup for in situ SAXS experiment at beamline I22. Remote controlled syringe pump injected a specific amount of hydrolysed tetraethyl orthosilicate (TEOS) into the protein solution agitated using a magnetic stirrer. The peristaltic pump flowed the solution through the flow-cell where images were taken on the evolution of silica condensation with protein-silica particle growth. Figure modified from Fig. S3 in 10.1038/s41598-020-65876-3 and originally drawn by Dr Aswin Doekhie.

when silica network is being formed. This was clearly seen from the early onset data where the shape of the initial silica nanoparticles resembled the shape of the target molecule. As the particles grew, they eventually became more spherical, as we have previously seen from Transmission Electron Microscopy (TEM) and Scanning Electron Microscopy (SEM) studies. We knew before that the more positively charged the surface of the target, the faster the ensilication, indicating that these positively charged areas attract silica first. Silica then rapidly grows in a network as it diffuses around the target and rapidly (within seconds) creates the network surrounding the target. What was interesting to see from these data was that the shape of the target dictated the shape of the silica nanoparticle at least in the first stages of ensilication, confirming our hypothesis that the silica 'shell' mimics the shape of the target.

A comprehensive understanding for the ensilication mechanism was built, where we have defined three stages for the ensilication (Fig. 3). Stage I – nucleation, where silica monomers get attracted to the positively charged areas on the surface of the target and the first silica layer start growing from those nucleation areas. Stage II – a rapid growth of further silica layers. Here the growing silica nanoparticle still mimics the shape of the original target. For example, tetanus toxoid C fragment, TTCF, has an oval shape, which is clearly seen during the Stages I and II. Stage III is associated with growth through silica aggregation. Particles that have resembled the target shape during Stages I and II rapidly change their shape during Stage III. We know that silica particles aggregate when they reach a specific size, exactly as we are seeing here. During such aggregation, which is also called a mass fractal growth, we see a formation of largely spherical silica particles that we frequently observe with the aid of an SEM.

In conclusion, this study helped us in explaining the mechanism of ensilication of biologicals. Understanding the mechanism helps in controlling ensilication, controlling the size of particle formation and in eventually explaining why some biologicals are easier to ensilicate compared to others. Ensilication may help us in thermal stabilisation of vaccines, which could be a game-changing discovery that may help in expanding vaccination and potentially saving millions of lives.

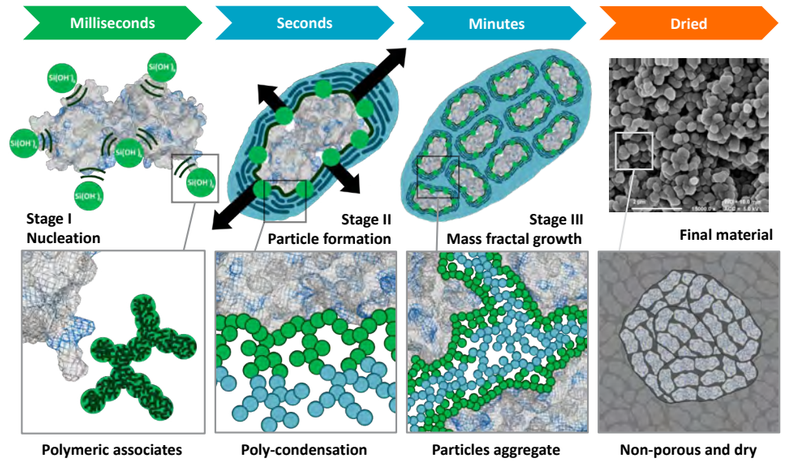

Figure 3: Schematic representation of ensilication stages. Nucleation, induced via electrostatics, initiates ensilication at positive external residues present on the protein. Poly-condensation of TEOS results in ensilication of individual proteins which triggers aggregation. Vacuum filtration of the then turbid solution results in dried powder material containing protein loaded silica nanoparticles. Modified from Fig. 4 in 10.1038/s41598-020-65876-3

Reference:

1. https://www.who.int/publications/10-year-review/vaccines/en/

Funding acknowledgement:
Diamond Light Source beamtime at I22 was granted on project SM-14148. Dr Asel Sartbaeva thanks Annett Trust and the University of Bath Alumni Fund, The Royal Society and the British Council Newton Fund for funding.

Corresponding author:
Dr Asel Sartbaeva, University of Bath, a.sartbaeva@bath.ac.uk

Asthma medication offers a potential new treatment for dementia

Related publication: Townsend D. J., Mala B., Hughes E., Hussain R., Siligardi G., Fullwood N. J. & Middleton D. A. Circular Dichroism Spectroscopy Identifies the β-Adrenoceptor Agonist Salbutamol As a Direct Inhibitor of Tau Filament Formation *in vitro*. *ACS Chem. Neurosci.* **11**, 2104–2116 (2020). DOI: 10.1021/acschemneuro.0c00154

Publication keywords: Alzheimer's disease; Tau; Amyloid; β-Adrenoceptor; Salbutamol; Dobutamine; Circular Dichroism Spectroscopy

Alzheimer's disease is a neurological condition that affects the large ageing population. There is currently no cure for the disease, which is associated with the formation of large protein plaques in the brain that kill neurons. A group of scientists led by Professor Middleton of Lancaster University, with the help of Diamond Light Source's Circular Dichroism beamline (B23) team, observed that the asthma drug salbutamol disrupted the formation of tau protein deposits that would otherwise accumulate in the brain. Salbutamol could, therefore, be a potential treatment for Alzheimer's disease.

The team conducted the laboratory study using various techniques. These revealed that salbutamol, by interacting with the tau protein, substantially prevented the formation of abnormal tangled clumps that at the early stages are thought to damage brain neurons and progressively induce dementia. In this work, high-throughput screening of libraries of generic chemicals enabled the identification of adrenalin as a successful candidate that precluded the formation of tau deposits. Subsequent screening of several drugs with similar chemical features identified salbutamol.

Developing new drugs is slow and very expensive. It is far quicker and cheaper to repurpose clinically approved drugs for other diseases. This more economical approach can be applied to other neurological disorders (such as Parkinson's and Huntington's diseases) and any other disorder associated with protein deposits, such as type II diabetes, TTR amyloidosis and cancer.

Alzheimer's disease (AD) is classed by the World Health Organisation as a global health priority affecting 47 million people worldwide. With an increasingly aging population, this figure is expected to triple to over 130 million cases by the year 2050, with an economic burden of $0.8 trillion[1]. The increase in the incidence of AD is compounded by the lack of a significant breakthrough in drug therapies in the past 40 years and no successful disease modifying treatment since its discovery in 1907[2]. Currently, only four drugs have been approved for use though none provide disease modifying therapeutic treatments.

AD is characterised pathologically by the deposition of amyloid-β (Aβ) and tau proteins in the brain as insoluble amyloid fibrils and neurofibrillar tangles (NFT), respectively. The formation of NFT, which leads to neuron destabilisation and ultimately cell death, is thought to occur after the aggregation of Aβ and the related inflammatory response in AD.

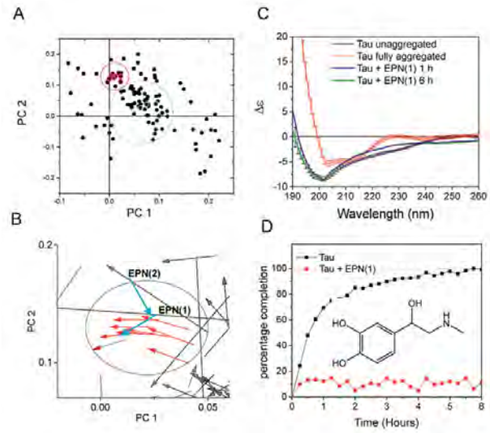

Figure 1: HT-SRCD of drug-like compounds for inhibition of tau aggregation. (a) PC score plot of variance after 6 h incubation. Red circled for the compounds having greatest inhibitory effect, and the cyan circled for partially or full aggregated tau; (b) PC trajectory plot of spectral change, 1-6 h. Red arrows represent tau spectra non-aggregated, cyan arrows largest inhibitory effect of epinephrine (EPN(1)) and (EPN(2)). (C) HT-SRCD spectra of tau with EPN(1) (blue/green), tau under nonaggregating conditions t = 0 (black; n=10) and with heparin after 6 h (red; n=6). (D) CD spectra of heparin-induced tau aggregation (black) and with EPN(1) (red).

It has been known for a long time that the distribution of tau pathology in AD correlates much better with the clinical severity of AD than the distribution of Aβ plaques[3]. Finally, the central role of tau in neurodegeneration is evident in diseases such as primary age-related tauopathy where Aβ plaques are absent.

One therapeutic approach for AD is to block or impair Aβ amyloid formation or tau NFT deposition. A common first step toward identifying potential inhibitors is *in vitro* screening of compounds that reduce tau or Aβ self-assembly kinetics and yield. The amyloid-sensitive fluorescent dye thioflavin T (ThT) is a convenient tool that is amenable to high-throughput screening but can report false positives when compounds compete for the same binding sites as the dye. Circular dichroism (CD) spectroscopy is an alternative approach, which reports directly on the structural changes of the protein as it undergoes aggregation and is therefore not prone to the ThT-type errors, but a high-throughput analysis is more challenging.

High-throughput synchrotron radiation circular dichroism (HT-SRCD) has been used as a novel primary screening platform to compare the inhibitory effects of a small library of drug-like compounds against tau filamentous assembly.

B23 HT-SRCD has been developed as a powerful new method for the rapid analysis of protein structures under a range of different conditions[4]. A library of 88 drug and drug-like compounds, covering a broad range of chemical structures and indications, was selected. With large numbers of spectra to process and analyse, a multivariate approach of a principal component analysis was used to ascertain which compounds were most effective at stabilising tau in its native unaggregated structure. HT-SRCD indicates epinephrine to inhibit tau aggregation *in vitro* and is a good starting point from which to identify chemically similar compounds that may have more favourable properties *in vivo*.

Figure 1a shows the principal component (PC) scores plot for the HT-SRCD spectra obtained 3 h after initiating tau aggregation. A PC trajectory plot, representing the change in the spectra between 4 and 6 h (Fig. 1b) reveals two samples that overlap or lie close to the control data for tau under nonaggregating conditions. These correspond to (±)-epinephrine hydrochloride (Fig. 1c) and (−)-epinephrine bitartrate. All other spectra (represented by arrows outside of the circled region in (Fig. 1b) indicated a partial or full aggregation of tau between 1 and 6 h, were not representative of tau in its unaggregated and aggregated structures. Follow-up benchtop CD spectra of tau in the presence of epinephrine confirmed that the compound inhibited tau aggregation (Fig. 1d).

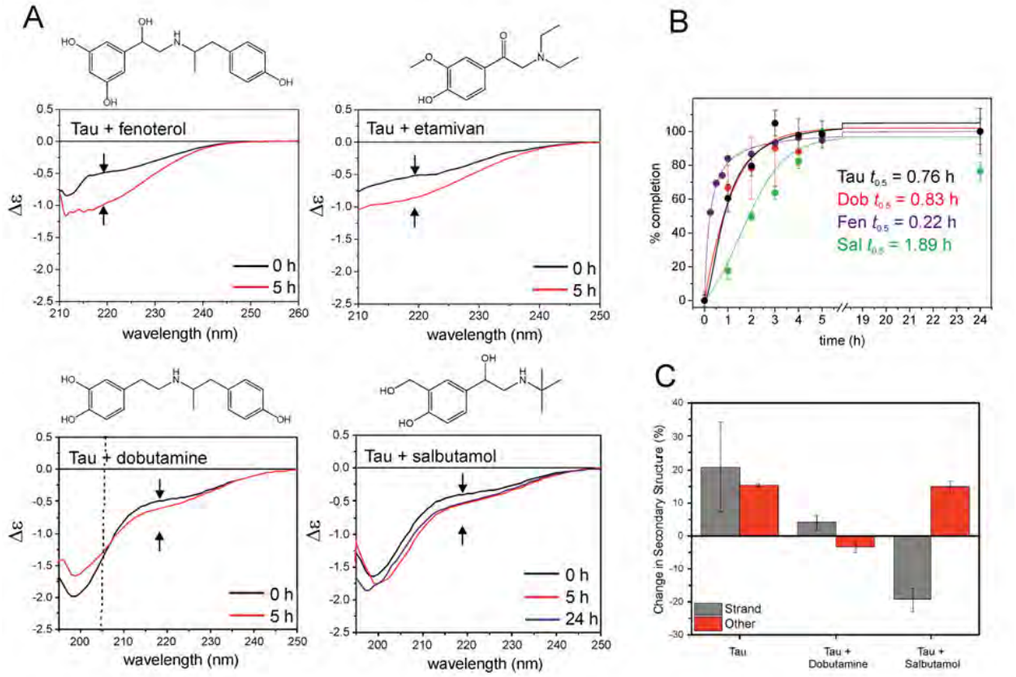

Figure 2: (a) Far-UV CD spectra of tau (20 μM) after incubation for 0 (black) and 5 h (red) with equimolar concentrations of four catecholamine-derived β2-adrenergic receptor agonist drugs. The double arrows represent the increase signal at 218 nm consistent with β-sheet formation from the spectra of tau alone at 0 and 5 h. For salbutamol, an additional spectrum is shown after 24 h of incubation (blue); (b) Kinetics of tau aggregation with the four drugs, monitored at 218 nm; (c) Percent change in the secondary structure of tau with dobutamine and salbutamol incubated for 5 h.

B23 HT-SRCD indicates that epinephrine is superior to all other drugs screened, which cover a wide chemical space, in its ability to inhibit tau aggregation *in vitro* and is therefore a good starting point from which to identify chemically similar compounds that may have more favourable properties *in vivo*. Of the four investigated drugs chemically similar of epinephrine (Fig. 2), the CD data suggest that salbutamol impairs tau aggregation and stabilises tau in a structure close to its initial native state. By contrast, dobutamine appears to not have a significant effect on the rate of tau structural modification.

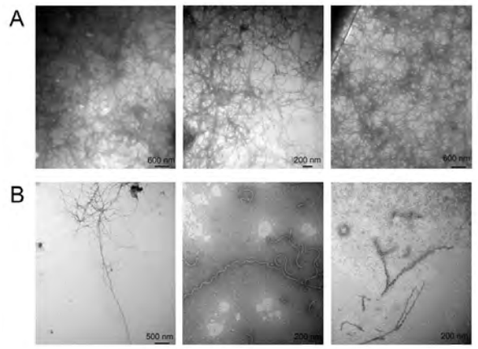

Figure 3: Negatively stained TEM images of tau (20 μM) aggregates formed in the presence of heparin (5 μM) after 24 h of incubation at 37 °C. (a) and with the addition of 20 μM salbutamol; (b) Three different regions of the TEM grids are shown for each sample group.

In the presence of heparin, tau aggregates into insoluble aggregates after 24 h and the visualisation by negative staining transmission electron microscopy (TEM) reveals a loose mesh of interwoven filaments with a typical amyloid morphology, consisting of networks of long unbranched fibres from 500 nm to 1 μm (Fig. 3). The treatment of tau with salbutamol results in the deposition of fibrillar structures with different morphologies to the untreated tau. The TEM images concur with ThT and CD and indicate that salbutamol interferes with the fibril formation of tau.

In summary, the *in vitro* ability of salbutamol to inhibit tau amyloidosis has been demonstrated providing the basis for further *in vitro* and eventually a full *in vivo* evaluation as a potential therapeutic for AD.

References:

1. Improving Healthcare for People Living with Dementia — Coverage, Quality and Costs Now and in the Future - https://www.alz.co.uk/research/World Alzheimer Report 2016.pdf
2. Lane C. A. *et al.* Alzheimer's disease. *Eur. J. Neurol.* **25**, 59–70 (2018). DOI: 10.1111/ene.13439
3. Arriagada P. V. *et al.* Neurofibrillary tangles but not senile plaques parallel duration and severity of Alzheimer's disease. *Neurology* **42**, 631–639 (1992). DOI: 10.1212/wnl.42.3.631
4. Hussain R. *et al.* High-throughput SRCD using multi-well plates and its applications. *Sci. Rep.* **6**, 38028 (2016). DOI: 10.1038/srep38028

Corresponding author:
Prof. Giuliano Siligardi, Diamond Light Source,
giuliano.siligardi@diamond.ac.uk

Integrated Facilities and Collaborations

As a world-leading centre for synchrotron science and a cornerstone of a world-class site for scientific discovery and innovation at Harwell, Diamond Light Source has powerful synergies with its neighbouring research institutes and beyond the campus, through collaborations and shared visions. The integrated facilities at Diamond present academic and industrial users with a one-stop-shop for research opportunities, enabling them to combine cutting-edge techniques and capabilities to advance their studies. These facilities and partnerships bring together expertise from UK universities, research institutes and industry to help us tackle 21st century challenges through internationally leading cooperation.

Integrated Facilities

The Membrane Protein Laboratory (MPL)

The Membrane Protein Laboratory (MPL) is a well-established, state-of-the-art facility that enables membrane protein research. Since its inception, the MPL has supported visiting researchers from around the world to work towards the visualisation of their membrane protein of interest at resolutions that allow structure-function relationships to be understood. Membrane proteins are found at the junctions between the outside world and the inner workings of the cell. Multicellular organisms, such as humans, use membrane proteins for communication, to acquire nutrients and detect threats. Membrane proteins are important targets for biomedicine with over half of all medicines altering membrane protein function. Understanding the structure and function of these proteins will help us to develop future therapeutics to tackle disease.

The MPL is one of Diamond's integrated facilities and located within the Research Complex at Harwell (RCaH), it provides support to scientists interested in membrane protein structural biology. Having a dedicated laboratory with cutting-edge equipment, and close to the experimental end stations and electron microscopes, greatly enhances scientists' ability to successfully characterise these important targets. Recently, a post-doctoral researcher has been recruited to enhance the MPL's single-particle cryo-electron microscopy (cryo-EM) capabilities, working with Diamond's Electron Bio-Imaging Centre (eBIC) and the MPL.

The MPL is open to user applications from anywhere in the world, and proteins crystallised here have been used in experiments in other facilities. Recently published work in *Nature Communications*[1] details research supported by MPL facilities that has led to a series of Archarhosdopsin-3 (AR3) structures. AR3 is a photoreceptor that harvests energy from sunlight to pump protons out of the cell driving ATP synthesis. Properties of AR3 make it ideally suited for optogenetic experiments, in which it is used to silence individual neurons and to detect changes in cell membrane voltage. These new structures open the way for the development of new tools and methodologies in the fields of neuroscience, cell biology and beyond.

In other work, a combination of *in vitro* and *in cellulo* approaches were used to characterise disulphide bonding found in the major outer membrane protein (MOMP), an important Chlamydia vaccine target[2]. A low-resolution (~4 Å) X-ray crystal structure was used to identify a series of cysteine rich pockets and pint mutants made to investigate disulphide bonding. Working with the Central laser Facility (CLF), super-resolution fluorescence microscopy methods were used to follow localisation of MOMP in E. coli cells and measure the clustering behaviour of the different cysteine mutants. Disulphide bonding was found not to be disrupted by single point mutations and found to be compensated by neighbouring cysteines within the cysteine-dense pockets.

References:

1. Bada Juarez J. F. *et al.* Structures of the archaerhodopsin-3 transporter reveal that disordering of internal water networks underpins receptor sensitization. *Nat. Commun.* **12**, 629 (2021). DOI: 10.1038/s41467-020-20596-0

2. Danson A. E. *et al.* Super-resolution fluorescence microscopy reveals clustering behaviour of chlamydia pneumoniae's major outer membrane protein. *Biology* **9**, 1–16 (2020). DOI: 10.3390/biology9100344

XChem

It has been a busy year for Diamond's XChem facility for fragment screening, staying open throughout lockdown for experiments aimed at accelerating development of new treatments for COVID-19. Early in the pandemic, XChem joined a collaboration to identify fragment compounds bound to the Main protease (Mpro), a key enzyme in the life cycle of the SARS-CoV-2 virus. Since such compounds provide templates for designing bespoke molecules to block the enzyme and thus the virus, the data were placed online immediately. This triggered an avalanche of interest, and XChem became a founding partner of the COVID Moonshot, a global non-profit initiative aiming to develop a novel antiviral drug with no IP constraints, by crowdsourcing designs of new inhibitors from chemists world-wide who could mine the rich fragment data measured at Diamond. The project continues to release its data in real-time, which has driven very rapid progress.

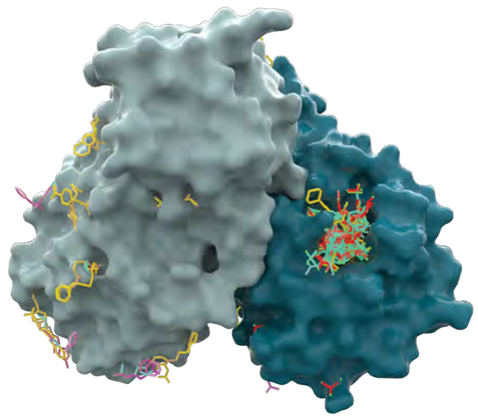

Representation of the chemicals binding to the main protease of the SARS-CoV-2 virus.

Along with collaborators, the XChem team performed screens against a further seven COVID-19 proteins, data that can trigger equally productive drug discovery efforts. By April 2021, the combined international efforts had discovered 234 fragment compounds that directly bind to sites of interest on the surface of this cohort of seven proteins, mapping out chemical motifs and protein-compound interactions. Many of these data are already public, providing large numbers of starting points for designing compounds aimed at directly-acting antivirals with novel modes of action, targeting either pandemic or else helping for pandemic preparedness.

Highlighted publications:

- Douangamath A. *et al.* Crystallographic and electrophilic fragment screening of the SARS-CoV-2 main protease. *Nat. Commun.* **11**, 5047 (2020). DOI: 10.1038/s41467-020-18709-w
- Chodera J. *et al.* Crowdsourcing drug discovery for pandemics. *Nat. Chem.* **12**, 581 (2020). DOI: 10.1038/s41557-020-0496-2
- Schuller M. *et al.* Fragment binding to the Nsp3 macrodomain of SARS-CoV-2 identified through crystallographic screening and computational docking. *Sci. Adv.* **7**, eabf8711 (2021). DOI: 10.1126/sciadv.abf8711
- Newman J. A. *et al.* Structure, Mechanism and Crystallographic fragment screening of the SARS-CoV-2 NSP13 helicase. *bioRxiv* 2021.03.15.435326 (2021). DOI: 10.1101/2021.03.15.435326

XFEL Hub

The XFEL (X-ray Free-Electron Laser) Hub at Diamond continues to provide expertise and support to the UK community engaged in serial crystallography and XFEL-related life science research; from experimental conception to beamtime proposals, through sample preparations and testing, to XFEL data collection, analysis and publication. Our Diamond-based activities continue to include organising and running the Block Allocation Group 'Dynamic Structural Biology at Diamond and XFELs' for serial crystallography and time-resolved studies.

Nearly all XFEL beamtime awards over the past year have been impacted by the COVID-19 pandemic. Since February 2020, our XFEL activities included more than a dozen beamtime awards fielded at XFELs SACLA (Japan), PAL-XFEL (South Korea), LCLS (USA), and the European XFEL (Germany). Nearly all have focused on time-resolved Serial Femtosecond Crystallography (SFX) data collection that was often correlated with X-ray Emission Spectroscopy (XES). Starting in August 2020 the Hub participated in all XFEL beamtime through remote connections, including the Hub-led COVID-19 experiments at LCLS and the European XFEL that probed the structure, function and dynamics of the two viral cysteine proteases: the main protease(M^{pro})and the papain-like protease (PL^{pro}).

The XFEL Hub and scientists from the University of Oxford are collaborators in a newly awarded Scientific Campaign at the LCLS titled, 'Structural Dynamics of Metalloenzymes' and will receive multiple beamtimes over several years. The goals include "to conduct combined time-resolved X-ray crystallography and X-ray spectroscopy [on methane monooxygenase, several hydrogenases, and nitrogenases], under turn-over conditions, to elucidate details of the structural and redox changes happening at the active site of each of these systems."

The XFEL Hub initiated major projects at Diamond to establish strategies for time-resolved Macromolecular Crystallography (MX) studies with on-demand sample delivery and reaction initiation methods that can be correlated with X-ray Emission Spectroscopy (XES) too. This includes establishing deeper collaborations with several XFEL facilities, including SwissFEL which may also host the capabilities developed at Diamond.

Dr Allen Orville led the life science team for the UK XFEL project that was tasked by the Science and Technology Facilities Council (STFC) to create an updated science case for a UK-based X-ray Free Electron Laser (UK-XFEL). The Revised Science Case was completed and submitted to STFC/UKRI and can be downloaded from the web link below. The project continues to seek input to the process from across the scientific community. More information can be found here: *www.clf.stfc.ac.uk/Pages/UK-XFEL-science-case*

Highlighted publications:

- Orville A. M. Recent results in time resolved serial femtosecond crystallography at XFELs. *Curr. Opin. Struct. Biol.* **65**, 193–208 (2020). DOI: 10.1016/j.sbi.2020.08.011
- Srinivas V. *et al.* High-Resolution XFEL structure of the soluble methane monooxygenase hydroxylase complex with its regulatory component at ambient temperature in two oxidation states. *J. Am. Chem. Soc.* **142**, 14249–14266 (2020). DOI: 10.1021/jacs.0c05613
- Ibrahim M. *et al.* Untangling the sequence of events during the S2 → S3 transition in photosystem II and implications for the water oxidation mechanism. *Proc. Natl. Acad. Sci. U. S. A.* **117**, 12624–12635 (2020). DOI: 10.1073/pnas.2000529117
- Sethe Burgie E. *et al.* Photoreversible interconversion of a phytochrome photosensory module in the crystalline state. *Proc. Natl. Acad. Sci. U. S. A.* **117**, 300–307 (2020). DOI: 10.1073/pnas.1912041116

Collaborations

The Rosalind Franklin Institute

Along with ten universities and UKRI-STFC, Diamond is a founding member of the Rosalind Franklin Institute (The Franklin) which is dedicated to bringing about transformative changes in life science through interdisciplinary research and technology development. Last year the Wellcome Trust awarded The Franklin, along with partners Medical Research Council Laboratory of Molecular Biology (MRC LMB) and Diamond, a £25m grant to support the development of three new electron imaging technologies that will have the capacity to revolutionise how we see life, pushing the boundaries of imaging in life science. Diamond's share of the grant is to fund the development of HeXI, a Hybrid electron - X-ray Instrument set to play a major role in drug discovery efforts.

Collectively known as 'Electrifying Life Science', the electron imaging technologies will create globally unique capabilities for the UK. The overall project is led by Professor James Naismith, Director of The Franklin, Professor Sir David Stuart, Director of Life Sciences at Diamond and Joint Head of Structural Biology at the University of Oxford, Dr Gwyndaf Evans, Deputy Director Life Sciences at Diamond and Head of Technology at The Franklin and Dr Richard Henderson, group leader at MRC LMB. Together, the team will change by a factor of ten the accessibility and capability of cryo-EM, in both tomography and single particle sub-fields.

HeXI will be a dedicated electron diffraction instrument embedded within Diamond's VMXm micro/nano focus X-ray beamline facility and accessible through the Diamond user programme. It will combine and build upon state-of-the-art technologies from electron and X-ray fields to create brand new scientific opportunities for structural biology and drug discovery. HeXI will make electron diffraction easily accessible to all of Diamond's existing life science users, as well as attract new users, to routinely study pharmaceutical compounds and their binding.

The Franklin is leading on the Amplus project with Thermofisher Scientific and Diamond as collaborating partners. The project will develop instruments that will be built at The Franklin Hub and which will deliver a revolution in cryo-electron tomography – using electron microscopy to build up three-dimensional models inside the cell. This will bring into view the possibility of imaging whole cells at the atomic scale quickly and accurately. Although technically challenging, the applications are vast and include genetic disease, intracellular pathogens, understanding the mechanisms of microbial drug resistance, and observing viral infection. To make the process robust and accessible, automation will be built into every step, from sample handling to data processing.

Halina Mikolajek, Senior Support Scientist and Manager of Diamond's Crystallisation Laboratory at RCaH, pictured.

In collaboration with The Franklin and SPT Labtech, a designer and manufacturer of automated instrumentation and consumables for life science applications, Diamond is developing methods for sample preparation using SPT Labtech's chameleon, an automated system for next generation cryo-EM sample preparation. Diamond is employing its experience and user base to help develop the system, thus improving sample preparation, one of the crucial steps in structure determination by cryo-EM.

Research Complex at Harwell (RCaH)

The Research Complex at Harwell (RCaH) is a joint venture between Diamond and the UK research councils, now UKRI, and provides a research hub on the Harwell campus for the physical and life sciences. It currently has in excess of 180 researchers from universities across the UK working in a mix of wet and dry laboratory space supported by research grants. In addition, there is a mix of research facilities or consortia based at RCaH e.g. Diamond's Membrane Protein laboratory (MPL), the Central Laser Facility (CLF), CCP4 and CCP-EM. This rich environment of research facility hubs welcome around 500 scientific visitors and users yearly.

RCaH provides the majority of the wet laboratory space for Diamond group leaders, hosts the MPL, the UK XFEL Hub, XChem and the Harwell crystallisation facility. The latter is run as a partnership between Diamond, RCaH and the Rosalind Franklin Institute and provides state-of-the-art facilities for Harwell-based groups as well as external users. The platform is being integrated with the *in situ* and serial crystallography beamline VMXi at Diamond, which is in the final stages of commissioning and will provide a new way of access for users of this beamline.

The last year has been extremely busy for RCaH, which kept its doors open throughout the first lockdown in the UK and enabled groups working on COVID-19 research to continue unabated. This was critical for the work started on the SARS-CoV-2 proteases by the Walsh group at Diamond which, in collaboration with the von Delft group at XChem, generated the first deluge of fragment screening data from Diamond[1]. The groups of Naismith and Owens from The Franklin and the University of Oxford, in collaboration with Diamond groups, have successfully targeted the spike protein to generate potent nanobodies through a structure guided approach[2]. Finally, work led by Peijun Zhang at eBIC, in collaboration with Maria Harkiolaki's group at beamline B24 and Marissa Fernandez at the CLF, has shown the power of the correlative workflows now available on the Harwell campus to visualise the SARS-CoV-2 viral assembly and egress pathway combining cryo-super resolution fluorescence, X-ray and electron microscopies[3].

References:

1. Douangamath A. *et al.* Crystallographic and electrophilic fragment screening of the SARS-CoV-2 main protease. *Nat. Commun.* **11**, 5047 (2020). DOI: 10.1038/s41467-020-18709-w

2. Huo J. *et al.* Neutralizing nanobodies bind SARS-CoV-2 spike RBD and block interaction with ACE2. *Nat. Struct. Mol. Biol.* **27**, 846–854 (2020). DOI: 10.1038/s41594-020-0469-6

3. Mendonça L. *et al.* SARS-CoV-2 Assembly and Egress Pathway Revealed by Correlative Multi-modal Multi-scale Cryo-imaging. *bioRxiv* 2020.11.05.370239 (2020). DOI: 10.1101/2020.11.05.370239

Active Materials Building

Construction of a new, dedicated Active Materials Building (AMB) at Diamond commenced in 2020. The new facility, which is anticipated to open to users later this year, will provide space for radioactive materials research, enabling experiments that were previously impossible in the UK. Increased knowledge of active materials is essential for the community as it wishes to understand better how materials behave under radiation, such as engineering materials used in nuclear power stations, as well as investigating safe storage of active materials and understanding interactions with the environment as old sites are decommissioned as part of the UK's nuclear legacy. This new laboratory is part of phase 2 of the National Nuclear User Facility (NNUF) project, which is a Government investment in the UK's nuclear future, providing state-of-the-art experimental facilities for research and development in nuclear science and technology. NNUF was established to support the Government Nuclear Industrial Strategy launched in March 2013.

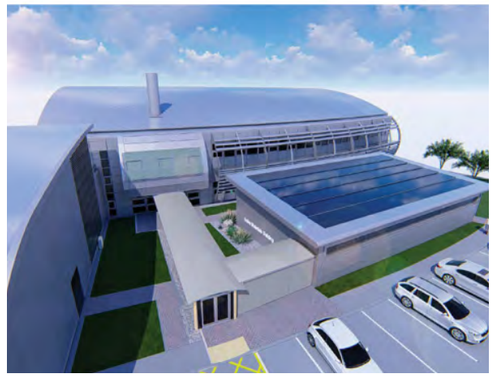

Architect's impression of the new Active Materials Building at Diamond.

The University of Manchester

Diamond has joined a new partnership to help researchers carry out experiments using X-ray computed tomography, a non-destructive technique to construct 3D scientific images. Funded by the Engineering and Physical Sciences Research Council (EPSRC), National X-ray Computed Tomography (NXCT) is the National Research Facility for lab-based X-ray computed tomography providing 3D imaging facilities and data analysis, research knowledge and technical experience. It brings together world-leading capability in lab-based X-ray Computed Tomography (XCT) from the universities of Manchester, Southampton, Warwick, University College London and Diamond. The NXCT facility in Manchester is hosted by the Henry Royce Institute for advanced materials.

NXCT's mission is to provide access and expert support for both academia and industry, embracing both first-time users and more experienced researchers to run cutting-edge 3D and 3D time-lapse imaging experiments. Diamond's role in the partnership is to provide expertise to bridge across the activities of the NXCT to help deliver unparalleled 3D imaging capability for the UK. Diamond will work with NXCT to help guide potential users toward the right facilities for their studies, whether that be part of the extensive catalogue of lab-based instruments that the NXCT has put together, or one of Diamond's beamlines. NXCT users will access Diamond via the standard routes and will benefit from the support of a joint appointee between Diamond and Manchester, a post funded 50% by the EPSRC grant to specifically support NXCT activities.

The University of Manchester at Harwell (UoMaH) is hosted by Diamond and provides the interface with the Harwell national facilities, enabling UoM researchers to access world-class research at Diamond and all the Science and Technology Facilities Council (STFC) facilities at Harwell, including the ISIS Neutron and Muon Source, Scientific Computing Department (SCD) and the Central Laser Facility (CLF). UoMaH is comprised of core administrative and technical teams and research fellows and their groups.

The core technical team specialises in developing sample environments and equipment in support of experiments, involving high risk materials and extreme sample environments, fielded at the national facilities. In early 2021, UoMaH expanded its core team capabilities with the recruitment of a Data Analysis Manager. UoMaH plans to grow its Data Analysis Group in the coming years. The group's purpose will be to work with National Facilities to facilitate users' data reconstruction and analysis, with the aim to reduce the time it takes for users to publish their findings.

UoMaH research fellows are affiliated with different departments within the University's Faculty of Science and Engineering and pursue research in critical themes to both the University and the facilities. Currently, UoMaH has a growing contingent of fellows based at Harwell; two fellows working on resilience and catalysis are sponsored by Diamond, one fellow working on fusion is sponsored by ISIS and one 'extreme science' fellow, is currently in the recruitment stage and will be sponsored by US office of Scientific research. Alongside them, six further fellows and their groups are based in Manchester. The fellows strengthen the University's link with Harwell by bringing their research, networks and new users from Industry and Faculty academics to Diamond.

In December 2020, UoMaH in collaboration with Diamond, ISIS, SCD and CLF, started an Imaging webinar series, with events being run on a monthly basis until December 2021. The aim of the series is to introduce the National Facilities and the work being done by the UoMaH research fellows at Harwell to UoM, other universities, and other organisations on the Harwell site.

The Faraday Institution

Diamond is directly and indirectly involved in several Faraday Institution projects. As part of the characterisation project 'Imaging Dynamic Electrochemical Interfaces', Diamond has a joint Post-Doctoral Research Associate (PDRA) developing emerging techniques such as Bragg-coherent diffractive imaging to look at displacement and strain within battery electrodes as they are charged and discharged. This project also includes mathematics developments in super-resolution techniques and machine learning to enhance correlative imaging. The Faraday CATMAT project is tasked with a mechanistic understanding of cathode materials and investigation of new materials. One particular area is the use of oxygen-redox materials to increase cathode energy density, but which are impacted by structural changes that occur in operation. The role of oxygen is key to understanding these materials and collaborations between the I21 beamline and Faraday Institution researchers have allowed users to successfully resolve, for the first time, that the oxidised oxygen species in the bulk of the material is molecular oxygen rather than peroxide or other species. The CATMAT project also supports a PDRA based on beamline I14 to develop 3D spectroscopic and structural imaging to aid characterisation of materials resulting from the project. More widely, recent developments in automation on beamline I13 are being used to screen electrode materials and electrode processing techniques developed in Faraday projects to provide links between performance, degradation and structure and morphology.

As part of the Degradation project, high-resolution X-ray powder diffraction on beamline I11 has been used to obtain valuable information on the structural evolution of novel, high energy-density electrode materials, *in situ*. In particular, the Long Duration Experiment (LDE) facility has been used to perform long-term, *operando* cycling experiments, providing a better understanding of the degradation mechanisms leading to capacity loss and poor cycle life. I15-1, the X-ray Pair Distribution Function (XPDF) beamline, is a collaborator in the Recycling, Degradation and SOLBAT projects. Recent developments in cell design at I15-1 will facilitate fast *operando* XPDF studies for Faraday researchers investigating next generation cathodes, solid-state batteries and recycled battery materials.

Machine Operation and Development

Richard Walker, Technical Director

In 2020/21, our 14th year of operation has of course been unlike any other year due to the global pandemic, which has inevitably curtailed both machine operation and development to some extent.

A total of 212 days (5,088 hours) had been scheduled for User Mode operation, including five beamline start-up days. When the first UK lockdown was announced on 23rd March 2020, we were in the first scheduled shutdown of the year. We resumed User Mode operation on 31st March on schedule, however with a reduced number of operating hours – instead of the usual six day running (09:00 Wednesday to 09:00 Tuesday interspersed with Machine Development days), it was reduced to four days, settling eventually on a pattern with User Mode running from 09:00 Tuesday to 09:00 Saturday, with start-up/Machine Development on Mondays and we have been operating in that mode since then. This has resulted in the number of User Mode hours delivered this year being reduced to 3,445 hours. All operation was in standard multi-bunch mode (900 bunch train) with total current of 300 mA, there was no 'hybrid' or 'low-alpha' operation.

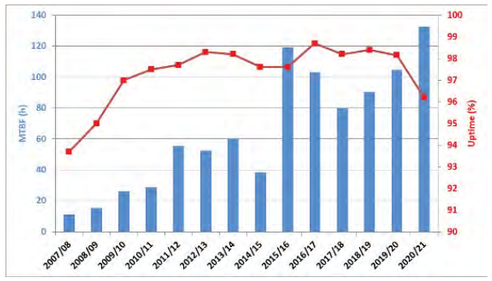

Figure 1: Mean Time Between Failures (MTBF) and Uptime by operating year.

The annual operating statistics are shown in Fig. 1. Despite the significantly increased number of switching off and on, the machine ran remarkably well, there were only 26 trips during User Mode throughout the year leading to our highest ever MTBF of 132 hrs. However, the uptime was poorer at 96.2%. This was primarily caused by three events, a failure in the cryo-plant, a loss of domestic water to the site which meant that staff had to leave and the machine be switched off and an electrical outage which resulted in a long recovery time, which together accounted for over half of the downtime.

Radio frequency (RF) upgrades

This year saw the first practical application of the Diamond synchrotron's new high-power solid-state amplifiers. With all of the original inductive output tube (IOT) RF amplifiers powering two superconducting cavities and two normal-conducting cavities in the storage ring, the first solid state amplifier is being used in the RF Test Facility, currently for high-power test and conditioning of the third normal-conducting cavity (Fig. 2). This solid-state amplifier can generate 80 kW without the high voltage required for IOT operation and uses the redundancy of multiple power transistor modules to provide a reliable high-power output. Once tests of the cavity are complete, the new cavity will be installed in the storage ring to provide further back-up of the superconducting cavities and cryogenic system. Two further solid-state amplifiers will be delivered in 2021, a 60 kW unit that will power the already installed second booster RF cavity, and a 120 kW amplifier that will power the 3rd normal conducting cavity in the storage ring.

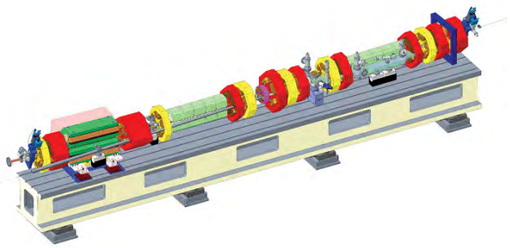

Figure 3: CAD model of one of the four girder types that are required for Diamond-II.

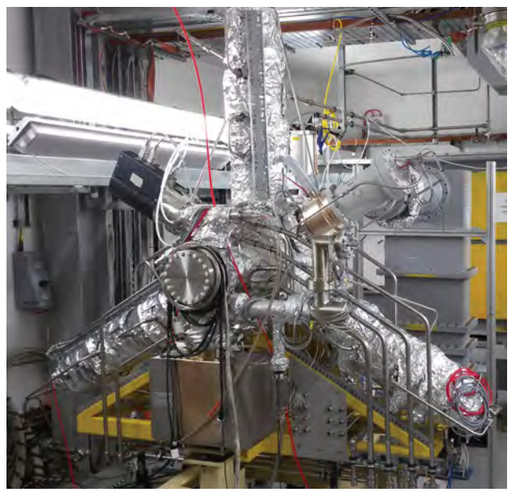

Figure 2: Diamond's first 500 MHz solid-state amplifier (left) powering the third normal conducting cavity in the RF Test Facility (right).

Figure 4: Testing new girder materials for their vibration performance for Diamond-II.

Diamond-II update

Significant progress has been made with the design of the Diamond-II machine upgrade in the last year during the Technical Design Report (TDR) phase, due to complete at the end of 2021. A revised lattice incorporating 'anti-bends' (actually quadrupole magnets which are offset horizontally to produce a bending field which is in the opposite direction of the principal bending magnets) has been adopted. A new solution for the vacuum system with a mixture of vessels with antechamber and conventional pumping and simple circular vessels with Non-Evaporable Getter (NEG) coating to provide the necessary pumping has also been adopted, both of which have been endorsed by the Diamond-II Machine Advisory Committee. Figure 3 shows the latest CAD model of one of the girder types that support the magnets and vacuum vessels, complete with vacuum pumps, ports for vacuum gauges etc. and photon extraction pipe.

Design of all the major components is proceeding apace while various prototypes have been made and tested. Different materials for the girders have been tested to assess whether they offer improved performance compared to the standard use of machined steel (Fig. 4).

The vacuum system for Diamond-II has to meet stringent requirements. It has to achieve the target pressure of 10^{-9} mbar or lower in operation, it has to be able to handle high power densities due to synchrotron radiation from the bending magnets and the insertion devices and it has to present a smooth surface (low impedance) for the electron beam transport around the storage ring and to prevent heating by trapped radiofrequency (RF) energy. The dense magnetic lattice and small cross-section vacuum vessel (typically 20 mm diameter) mean that discrete pumps, as used on Diamond's existing storage ring, are not adequate and a special low-outgassing and pumping NEG coating has to be applied to about half of the interior of the vacuum vessels to reach the specified pressure.

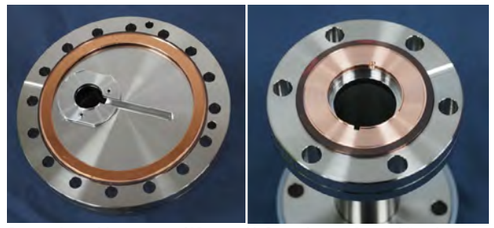

Figure 5: Some of the test pieces of RF compatible flanges for use in Diamond-II, with a keyhole (for transmitting undulator radiation (left) and a standard circular aperture (right).

For practical reasons, the storage ring vacuum system has to be manufactured as a series of smaller vessels, which are joined together with bolted flanges. There are more than a thousand of these joints around the storage ring; their design is critical as they have to provide a strong mechanical joint, a reliable ultra-high-vacuum (UHV) seal and near-perfect radiofrequency continuity with accurate alignment and a smooth internal surface throughout. In addition, the vacuum vessel has different cross-sections around the storage ring: in some places circular or elliptical and in other places a more complex shape such a 'keyhole'. Furthermore, an all-metal construction is necessary to ensure high tolerance to radiation.

The standard UHV Conflat® (CF) seal cannot be used as there is a 2 mm gap in the interior which would cause RF heating and potentially also beam instabilities. We have evaluated six different candidate designs of RF flange for Diamond-II, based on successful designs already in use at Diamond and at other accelerators. Figure 5 shows two examples, one (left) based on a standard UHV CF flange where the vacuum seal is made using a high purity copper gasket compressed between two circular knife edge flanges. The RF continuity is made by a separate aluminium gasket which closely conforms to the shape of the electron beam channel. The second (right) is again based on a standard CF flange but in this case, both the vacuum seal and the RF continuity are made simultaneously by a single copper gasket.

The laboratory tests we have carried out on the flanges include vacuum leak tests and metrology after repeated making and breaking of the seal, bakeout to 200 °C and mechanical stressing as well as destructive testing where the test pieces are sectioned and examined under a microscope. Further tests are in progress and a full set of prototype vessels for an 8 m section of storage ring will be manufactured, assembled and tested before the final choices are confirmed.

X-ray Technologies at Diamond

It is self-evident that in order for our instruments to produce world-leading science, we need to have world-class optics, detectors and computing technologies at our fingertips; technological advances never stop but are continually evolving. This section describes the support and advances in the Optics and Metrology Group, Detector Group and Scientific Software Controls and Computation department at Diamond Light Source. Advances which are supporting and enhancing our capabilities today are described, but also developments that will keep us competitive over the next few years. These groups are very active in calculations and specifications for beamlines and instruments being put forward and planned for Diamond-II, an integrated upgrade of the synchrotron, beamlines and computational facilities. The pandemic may have slowed some developments and made it harder to work physically alongside our colleagues, but it has also opened opportunities for remote operation for staff, users and collaborators. These advances continue to keep us competitive worldwide, and Diamond is proud to be at the forefront of many of these technologies.

Optics and Metrology Group

Kawal Sawhney, Optics and Metrology Group Leader

Over the past year, the Optics and Metrology Group has remained active despite the year's access restrictions and has continued to provide a full range of services to Diamond's beamlines, whilst expanding its own capabilities. This includes work on optics designs for current and new flagship beamlines to take the fullest advantage of Diamond-II, metrology testing in the Optics and Precision Metrology labs, and optics R&D projects[1-5] on the B16 Test beamline. A new Optics Fabrication Building that will house a state-of-the-art multilayer deposition laboratory is being designed.

Optics design for Diamond-II

Design and feasibility studies for beamline optics on Diamond-II have been ongoing since 2015. A lattice based on a Modified-Hybrid 6 Bend Achromat structure will reduce horizontal electron beam emittance to about 1/20 of its current value. Smaller and more collimated photon sources will produce nearly round beams. The increase in electron beam energy from 3 GeV to 3.5 GeV will enhance brightness and flux, as will new insertion devices on several beamlines.

Outlines and advanced optical designs have been prepared for flagship beamline proposals. These show that the planned instruments for spectroscopy, coherent imaging, nano-Angle-Resolved Photoemission Spectroscopy (ARPES), Macromolecular Crystallography (MX) and coherent soft X-ray scattering will be highly competitive, and they formed a core part of the flagship proposals presented by Diamond Science Group Leaders to the Diamond scientific advisory panels.

Some of the current bending magnet beamlines will be equipped with new source types such as three-pole wigglers. The possibility that radiation from the different magnets will interfere was investigated and it was shown that the new emittance of Diamond-II will not degrade the performance of any of the wiggler beamlines.

The higher ring energy and new undulators will increase the power load on the X-ray optics. The impact on the temperature distribution and deformation of several double crystal monochromators has been assessed by a simple, intuitive model that adds physical insights to more accurate finite element analysis (FEA) simulations. This model predicts critical power levels below which the crystal deformation remains acceptable. Monochromators will be kept below this threshold by using slits, filters, or cooling.

Upgrades to Optics Metrology instruments

Diamond's Optics Metrology Lab (OML) is well equipped with a suite of high-quality metrology instruments. Over the years, hundreds of X-ray mirror systems have been measured for all Diamond beamlines. Recently, the Diamond-Nanometre Optical Metrology (NOM) slope-measuring profiler has been upgraded with a 10x faster autocollimator, a more sophisticated motion controller, an automated pitch stage for remote working and reduced downtime, and better motion synchronisation and data capture through the Experimental Physics and Industrial Control System (EPICS). The reduction of systematic errors has created a faster, more accurate Diamond-NOM.

Similarly, the Zygo HDX Fizeau interferometer has been upgraded with a stitching system developed in-house (Fig. 1). A Fizeau interferometer images only a small portion of the surface of an X-ray mirror in a single shot. However, with motion stages that translate and rotate the mirror, a series of overlapping images is captured. Stitching these images together produces a panoramic view of the entire optical surface. This process has been automated by Python scripts written by the OML team.

The upgraded Diamond-NOM and HDX agree almost perfectly on a state-of-the-art mirror from JTEC (a manufacturer of X-ray mirrors for synchrotron facilities) that deviates from the ideal elliptical surface by a slope error of < 50 nrad rms (Fig. 2) and a height error of < 1 nm peak-to-valley. This gives confidence for measuring the next-generation X-ray optics required for Diamond-II.

Overcoming partial coherence with multi-modal ptychography for wavefront sensing

The quality of the X-ray beam delivered to samples depends strongly on the fabrication and alignment of the optics which transport it. Accurate characterisation of errors is essential for correction and is best performed *in situ* at the optics' designed wavelength. Ptychography is a scanning coherent diffraction imaging technique capable of accurately recovering the two-dimensional complex sample and probe functions with high spatial resolution. It is normally used by high-coherence undulator beamlines such as I13, but has been developed by the Optics Group as an imaging and wavefront sensing technique using partial coherence on B16.

Figure 1: Murilo De Bazan, Metrology Scientist, with the Fizeau interferometer stitching system built at Diamond.

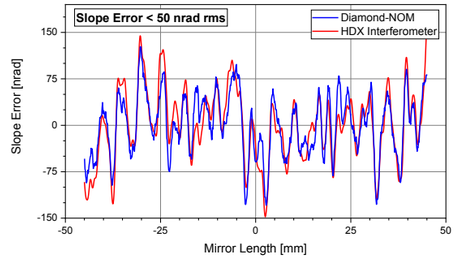

Figure 2: Near-perfect agreement between the upgraded Diamond-NOM and the HDX Fizeau stitching system for an elliptically curved mirror with a slope error < 50 nrad rms.

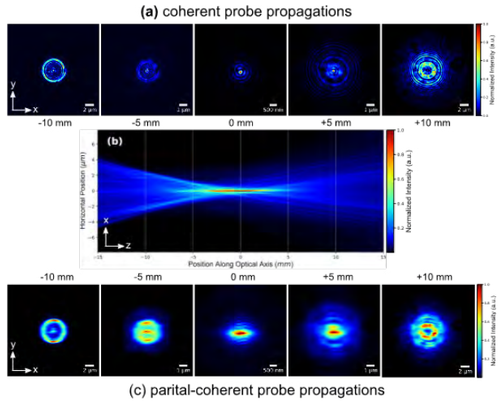

Figure 3: Coherent and partially coherent propagations of the reconstructed probe using multi-modal ptychography with a beryllium compound refractive lens.

Ptychography applies iterative phase retrieval to diffraction patterns from overlapping sample positions. Blurring of the diffraction patterns caused by partial coherence is treated by modelling the sample or probe as a sum of coherent multi-modal states. The reconstruction algorithm does not determine which one is causing loss of coherence, but a coherent probe reconstruction is possible if the loss of coherence is ascribed to the sample, even though in reality it is the beam that is partially coherent (Fig. 3).

The technique has been demonstrated for a wide range of X-ray focusing optics and has been validated with other wavefront sensing techniques. Additionally, the method has extended the imaging capabilities of B16 to a resolution of 100 nm over extended samples. This work paves the way for synchrotron beamlines to offer nanoscale imaging and optics characterisation without special coherent sources or expensive optics upgrades.

References:

1. Dhamgaye V. *et al.* Correction of the X-ray wavefront from compound refractive lenses using 3D printed refractive structures. *J. Synchrotron Radiat.* 27, 1518–1527 (2020). DOI: 10.1107/S1600577520011765
2. Moxham T. E. J. *et al.* Hard X-ray ptychography for optics characterization using a partially coherent synchrotron source. *J. Synchrotron Radiat.* 27, 1688–1695 (2020). DOI: 10.1107/S1600577520012151
3. Hu L. *et al.* Fast convolution-based performance estimation method for diffraction-limited source with imperfect X-ray optics. *J. Synchrotron Radiat.* 27, 1539–1552 (2020). DOI: 10.1107/S1600577520012825
4. Sutter J. P. *et al.* Bragg-case x-ray dynamical diffraction propagator in SRW: application to thin crystal phase retarders. in *Proc.SPIE* 11493, 114930V (2020). DOI: 10.1117/12.2567341
5. Hu L. *et al.* Perturbation perspective of partial coherence discussion on imperfect x-ray optical elements. in *Proc.SPIE* 11493, 114930D (2020). DOI: 10.1117/12.2567207

Low dose X-ray single-pixel imaging at high frame rates

Related publication: Sefi O., Klein Y., Strizhevsky E., Dolbnya I. P. & Shwartz S. X-ray imaging of fast dynamics with single-pixel detector. *Opt. Express* **28**, 24568 (2020). DOI: 10.1364/oe.396497

Publication keywords: X-ray; Single-pixel imaging; Ghost imaging; Lens less

X-ray imaging methods have numerous applications in various areas, ranging from basic science to medicine and security. The main advantage of using X-rays for imaging is their unique capability to penetrate through surfaces. Most X-ray pixelated detectors are used for static applications. However, there is a growing need for detectors that combine high spatial resolution with high frame rates. These detectors will allow the application of X-rays for measurements of dynamic systems, including acoustic waves in matter, phase transitions and medical imaging.

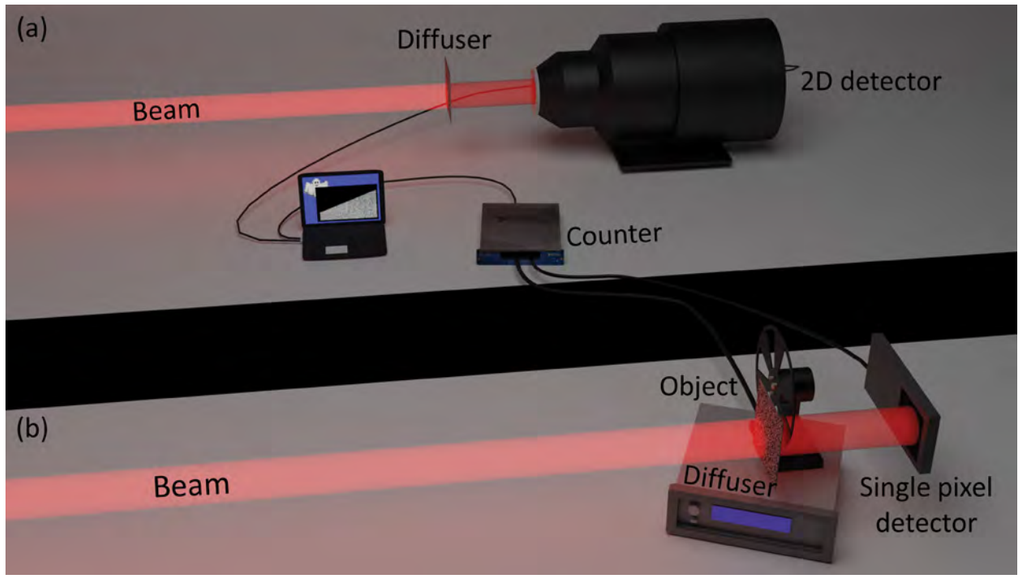

Figure 1: A schematic description of the experimental system for the (a) reference and (b) test measurements.

In traditional imaging methods that use pixelated detectors, the readout time increases with the number of pixels. This means there is a fundamental trade-off between the frame rate and the number of pixels. Single-pixel detectors can be much faster than pixelated detectors but cannot provide spatial information directly.

Researchers from Bar-Ilan University in Israel investigated a novel imaging technique that offers high frame rate imaging at high resolution based on thermal (or pseudothermal) ghost imaging (GI). As the concept had never been demonstrated with X-rays, they used B16 - a beamline at Diamond Light Source dedicated to testing new techniques and concepts. They successfully demonstrated the imaging of a rotating object at a frame rate of 100 kHz and a resolution of about 40 µm. This technique can be applied for medical imaging where measurements of fast dynamics are required, e.g. non-invasive cardiac imaging, and for non-destructive imaging of moving mechanical components.

X-ray imaging methods are used for numerous applications in a variety of areas. Recently, there is a growing need for detection schemes with combined high spatial resolution and high frame rates, which are essential for the understanding of numerous phenomena and processes and can lead to novel applications. However, there is a fundamental trade-off between the resolution and the frame rate, which rectrices the capabilities of two-dimensional (2D) X-ray detectors.

A novel imaging technique, which is based on the method of thermal ghost imaging (GI) offers high frame rate imaging at high resolution. GI is a single-pixel imaging technique, which uses intensity fluctuations, which are introduced into the beam by a diffuser. In the current demonstration of this method, which resembles the computational GI approach[1], the measurements are performed in two steps: first, the distributions of the intensity fluctuations for the various realisations are recorded by a 2D detector in the absence of the object. In the second step, the object is inserted, and the measurements of the test beam are recorded by a single-pixel detector. After the two sets of measurements are completed, the image is reconstructed by correlating the measurements from each realisation.

In the present work we extended the applicability of GI for periodically moving objects[2] by simply measuring a sequence of tests at high sampling frequency for each position of the diffuser. Each test sequence is taken along the entire period of the motion of the object. Thus, each position of the diffuser produces a set of test signals, corresponding to different positions along the trajectory of the object. Finally, each frame, which corresponds to a specific position of the object, is reconstructed separately.

This work is the first experimental demonstration of X-ray GI for fast dynamics, where the motion of a chopper spinning at 200 Hz was captured with a frame rate of 100 kHz, a spatial resolution of about 40 µm, and a field of view of 0.6 mm × 0.6 mm.

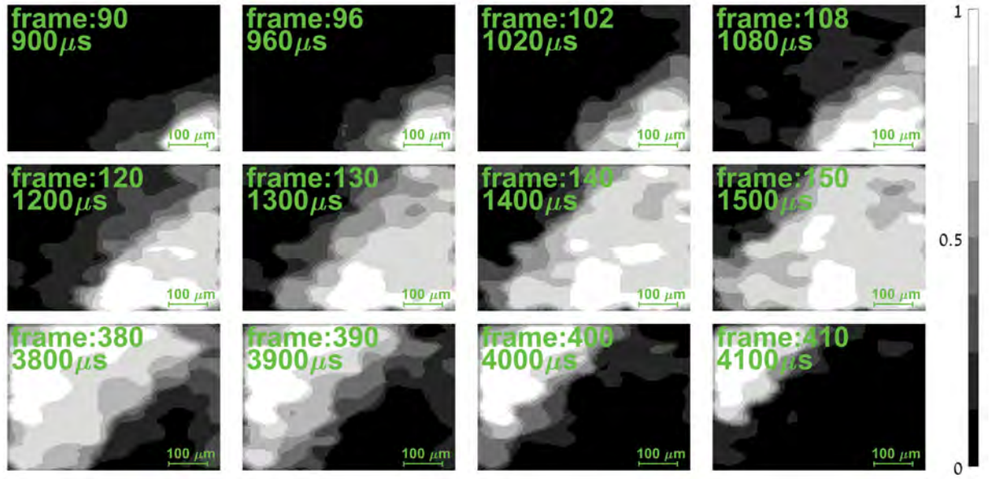

Figure 2: Reconstructed movie frames of an optical chopper rotating at 200 Hz. The movie is recorded at a frame rate of 10^5 frames per second at resolution of about 40 µm.

The experiment was conducted on B16 with a monochromatic beam at 9 keV. The experimental setup consists of a sandpaper diffuser, a rotating optical chopper, a slow 2D detector for the reference measurements and a single-pixel detector for the test measurements. For the reconstruction a compressive sensing algorithm[3,4] was used. A schematic description of the experimental setup is shown in Fig. 1.

Several snapshots from the reconstructed movie of the rotating chopper are shown in Fig. 2. The number of pixels in each frame is 8550 and the frame rate is 10^5 frames per second. The reconstruction was done using 4900 realisations per each frame with an average of $8.5 \cdot 10^3$ counts per realisation. In the upper left frame, the blade of the chopper blocks almost the entire beam except from a small area near the bottom right corner. The next panel shows the 6th later frame where the chopper blocks a smaller portion of the beam. The rest of the frames show the motion of the chopper at measurement times that are indicated in Fig. 2 until the bottom right panel.

One important aspect of GI is the possibility to reconstruct the object under low doses of radiation. In Fig. 3 the dependence of the signal-to-noise ratio (SNR) on the number of the photons detected by the test detector is shown. Here, the blue dots indicate the SNR calculated from the measured data and the error bars indicate the counting statistics. The insets (a)-(c) are the corresponding reconstructed images for different radiation doses. It is clear that satisfactory reconstructions were achieved under low dose conditions.

To summarise, a demonstration of the ability to use the method of GI for high-resolution large field of view X-ray imaging of fast dynamics was made, as well as the possibility for low dose imaging, and therefore can be implemented with conventional X-ray tubes.

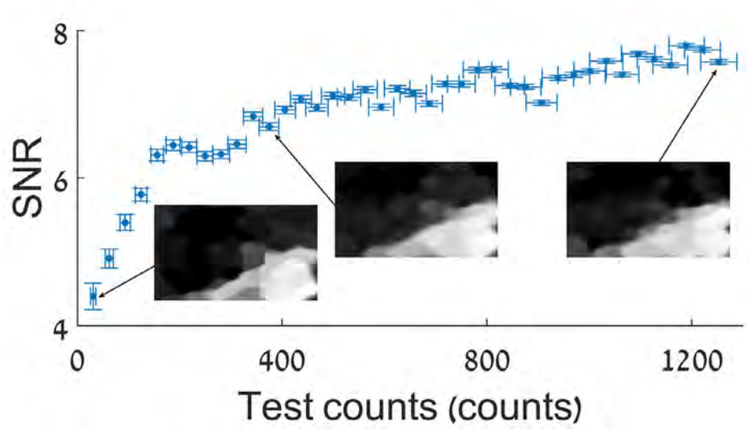

Figure 3: Dependence of the signal-to-noise ratio on the flux of the test beam for one frame from the movie. The horizontal error bars indicate the counting statistics. In the insets (a-c) the reconstructed images corresponding to 30, 375 and 1160 counts at the detector, are shown respectively.

References:

1. Klein Y. *et al.* X-ray computational ghost imaging with single-pixel detector. *Opt. Express* **27**, 3284 (2019). DOI: 10.1364/oe.27.003284
2. Zhao W. *et al.* Ultrahigh-Speed Color Imaging with Single-Pixel Detectors at Low Light Level. *Phys. Rev. Appl.* **12**, 34049 (2019). DOI: 10.1103/PhysRevApplied.12.034049
3. Katz O. *et al.* Compressive ghost imaging. *Appl. Phys. Lett.* **95**, 131110 (2009). DOI: 10.1063/1.3238296
4. Li C. *et al.* An efficient augmented Lagrangian method with applications to total variation minimization. *Comput. Optim. Appl.* **56**, 507–530 (2013). DOI: 10.1007/s10589-013-9576-1

Funding acknowledgement:
EU Framework Program for Research and Innovation Horizon 2020 Framework Programme (CALIPSOplus 730872).

Corresponding authors:
Prof. Sharon Shwartz, Bar-Ilan University, sharon.shwartz@biu.ac.il; Dr Or Sefi, Bar Ilan University, orsefi@gmail.com

Detector Group

Nicola Tartoni, Detector Group Leader

Last year saw the Detector Group focusing on the scientific exploitation of the time-resolved Tristan10M, an innovative detector system developed entirely by the group. The Tristan project was recently completed with the delivery of a Tristan10M system to Diamond's Small-Molecule Single-Crystal Diffraction beamline (I19) and commissioned with a time-resolved experiment in March 2021. The group's other major development project is the Arc-detector, a cadmium telluride (CdTe) photon-counting detector for Diamond's X-ray Pair Distribution Function (XPDF) beamline (I15-1).

The Tristan10M detector

The Tristan10M detector is a photon counting hybrid pixel area detector based on the read-out ASIC (application specific integrated circuit) Timepix3[1], a photon counting ASIC with the format of a square matrix of 256 x 256 pixels with 55 µm pixel pitch. Sixteen Timepix3 ASICs are flip-chip bump bonded to monolithic silicon sensors 500 µm thick. Ten modules arranged in a matrix of five rows and two columns make up the detector (Fig. 1).

Unlike conventional photon counting ASICs, Timepix3 places a time stamp to each event detected and immediately sends the information about the time of arrival and location of the event to the data bus. The notional accuracy of the time stamp is 1.56 ns and the measured accuracy is down to 8 ns r.m.s.[2]. This mode of operation opens the possibility of achieving unprecedented time resolution without gating the detector, which results in a much better overall detection efficiency.

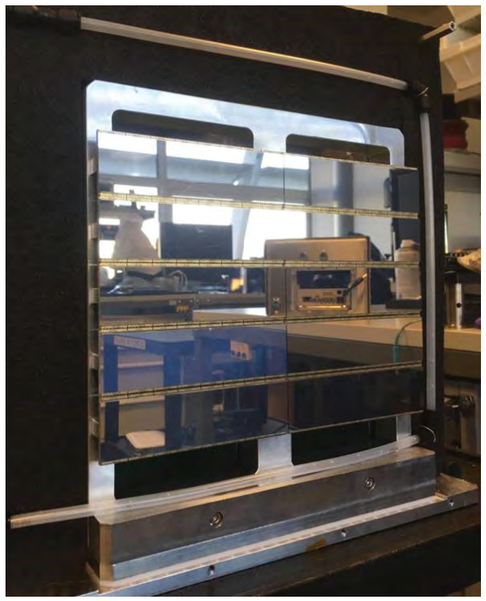

Figure 1: The assembly of Tristan10M has just been completed in the Detector lab and the detector is ready to be delivered to I19. The photograph shows the 10 modules of the detector Tristan10M mounted on the detector chassis.

Because of Timepix3, the data produced by Tristan10M consists of a stream of events instead of an array of images. The data are recorded as a list of events in an HDF5 file. To obtain images from the list of events, appropriate post-processing codes were developed. This gives the scientist great flexibility in the choice of the time slicing, meaning they can choose the most appropriate time intervals between images.

The commissioning at I19 EH2 on the Newport 4-circle diffractometer used a wavelength of 0.4859 Å (25.25 keV). The Tristam10M detector gives a resolution of >0.6 Å at a detector distance of 111 mm. The beam centre and detector distance was quickly calculated from analysis of LaB6 powder pattern standard (Fig. 2). The powder also showed good alignment of the modules.

A single crystal rotation dataset was obtained for [NiDppeCl2] at RT 300 K. The event data was then converted into a series of 0.1 deg images and processed using DIALS, a data analysis package for Macromolecular Crystallography (MX). The resulting structure has good merging and refinement statistics.

The Tristan M10 detector was then tested in a time-resolved experiment by monitoring the laser induced heating recovery of platinum (Pt) powder at various repetition rates of a pulsed laser (100 Hz to 50 kHz). During the final stages of the beam test, a Europium complex (organic electroluminescent device) was studied using a full time-resolved single crystal rotation procedure. The setup was pushed to its limits with the ultra-long four-hour data collection. The data analysis is ongoing and the results will be published at future conferences.

The way the data are stored and processed in Tristan inspired a novel use of the Xspress4 pulse processor[3] for quick Extended X-ray Absorption Fine Structure (EXAFS) experiments. The quick EXAFS technique usually uses germanium (Ge) multi-element fluorescence detectors and takes frames (multi-channel analyser (MCA) spectra sets) in quick succession, up to 1 kHz in the current generation of experiments and up to 20 kHz or more in the future upgrades. The current pulse processors associated with spectroscopy detectors calculate the MCA spectra in real time; however, it becomes more and more difficult to allocate the events to the right time slot as the frame rate increases. This is due to the unpredictable latency of the event processing when building the MCA spectra that results in time jitter of the events.

A mode of operation known as list mode was developed by using the time stamp capability of Xspress4. In this mode of operation, a record for each event, which consists of the time stamp, the detector channel, and the photon energy of the event, is sent to the data storage. The data structure is then a list of events rather similar to the Tristan data structure. This enables the reconstruction of MCAs as a function of time with the desired accuracy. External trigger events are also time stamped and recorded and provide the reference to the position of the monochromator or other events in the sample environment. A first test of this mode of operation proved effective and it could become the standard mode of operation for quick EXAFS experiments at Diamond.

The Arc-detector

The development of the Arc-detector has been progressing at a good pace, recently meeting a few important milestones: the CdTe sensors have been hybridised and tested and the front-end electronics are finished.

A total of 39 CdTe sensors were hybridised. Each of them was bump-bonded to three Medipix3RX ASICs, then attached and wire-bonded to the sensor carrier board. The hybridisation was performed in different batches so that process performance could be fed back to the manufacturers to allow process improvement if necessary. The CdTe hybrids were tested and characterised with X-rays to evaluate the image performance, leakage current and to debug the sensor carrier PC board, which had been developed the previous year. These tests were carried out using the Merlin readout system[4] and a readout PC board, which was purposefully developed for the ARC detector project.

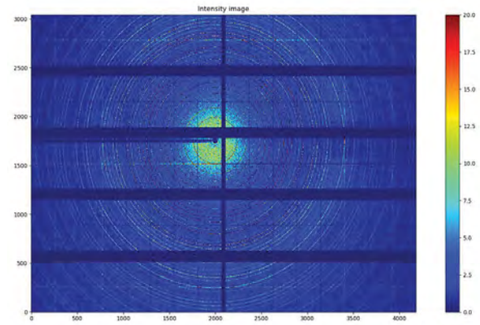

Figure 2: LaB6 powder diffraction pattern measured by Tristan10M at I19 for calibration purposes during the detector commissioning. The image has been reconstructed in the post processing from the list of events.

Simultaneously, the ARC detector readout boards were designed and tested. A Merlin-to-fibre optic interface board was also designed to initially test and debug the readout board and attached sensors, prior to full back-end firmware development. The Merlin-to-fibre interface board may also benefit other beamlines using the Merlin system, as it could allow the data acquisition system to migrate from a 68-way very-high-density copper cable interconnect to fibre optic, which extends physical separation possibilities and in due course, may allow increased frame rate.

The development of the mechanics took place in parallel; the super-modules have been designed and delivered. Figure 3 shows one of the super-modules populated with four CdTe sensors, two readout boards and all the connections in place (chiller pipes, high voltage bias, low voltage power and fibre optic cables), which are currently being tested in the Detector Group laboratories.

Next steps are focussed on: development of the back-end firmware targeted at two FEM II boards where work is in progress; the delivery of a new batch of 30 CdTe sensors and associated sensor carrier boards, in order to hybridise more modules; and the design of back-end mechanics and development of the associated boards (optical fanout and midplane printed circuit boards (PCBs)) that will be required to complete the data acquisition system.

References:

1. Poikela T. *et al.* Timepix3: A 65K channel hybrid pixel readout chip with simultaneous ToA/ToT and sparse readout. *J. Instrum.* **9**, C05013–C05013 (2014). DOI: 10.1088/1748-0221/9/05/C05013
2. Yousef H. *et al*. Proceedings, 14th Vienna Conference on Instrumentation (VCI 2016): Vienna, Austria, February 15-19, 2016. Nuclear Instruments and Methods in Physics Research Section A: Accelerators, Spectrometers, Detectors and Associated Equipment, **845**, pp. 639 – 643 (2017).
3. Dennis G. *et al.* First results using the new DLS Xspress4 digital pulse processor with monolithic segmented HPGe detectors on XAS beamlines. *AIP Conf. Proc.* **2054**, 60065 (2019). DOI: 10.1063/1.5084696
4. Plackett R. *et al.* Merlin: A fast versatile readout system for Medipix3. *J. Instrum.* **8**, C01038–C01038 (2013). DOI: 10.1088/1748-0221/8/01/C01038

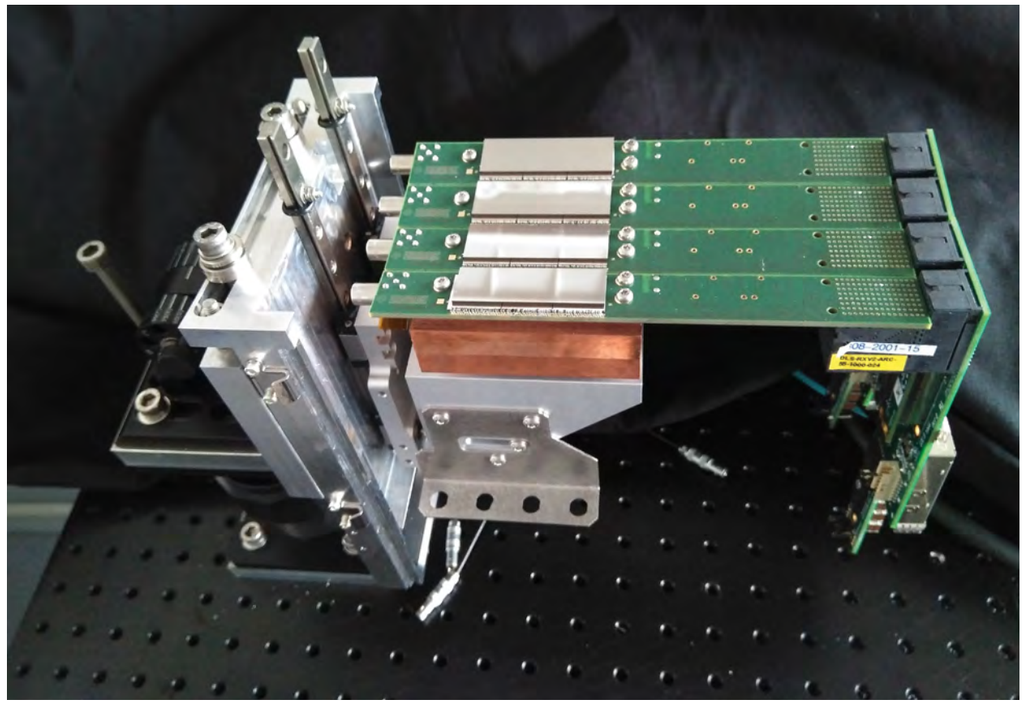

Figure 3: A super-module with the four sensor modules and the two readout boards (on the right-hand side) mounted on the mechanical support. Each CdTe sensor is flip chip bump-bonded to three Medipix3RX ASICs.

Scientific Software, Controls and Computation

Mark Heron, Head of Scientific Software Controls and Computation

The Scientific Software, Controls and Computation (SSCC) department manages all software, computing and control systems to facilitate and support the science programme of Diamond. It functions as eight groups: Scientific Computing, Data Analysis, Data Acquisition, Beamline Controls, Accelerator Controls, Electronic Systems, Business Applications and Cyber Security. The overall structure and function of these areas recognises the importance of, and is optimised to provide, the best possible delivery and support for software, computing and control systems.

In March 2020, Diamond responded to societal restrictions resulting from the national lockdown, a consequence of the COVID-19 pandemic. For SSCC staff this meant transitioning to developing software, managing systems and providing support to the facility, while working remotely. In a matter of days, the department transitioned to home working successfully, and established new communication channels and ways of working to support the science programme effectively. This was doubly important given that the science programme during the initial part of the lockdown was focused on understanding the structure and function of SARS-CoV-2; the very virus that was shutting down society.

Diamond has a long track record of pioneering remote operation of synchrotron beamlines. While well-developed in some science domains this was the opportunity, and a driver to expand, to opening up remote operation of nearly all beamline instruments. Additional IT hardware was delivered and commissioned to facilitate the performant network access required to support all instruments. Remote operation meant a distributed management team. Maintaining effective and timely communication was seen as imperative to be able to support operations effectively. A routine of thrice weekly video calls kept the SSCC Management team in touch with each other and the department's business function.

Whilst maintaining operations during the pandemic was challenging, SSCC was busy with new developments in many areas. A Strategy for the Scientific Software, Controls and Computation was published, and the first of two technical roadmaps, detailing implementation, developed. New software and control systems were delivered in line with requirements determined by the science programme, and new computing hardware was commissioned to address the challenges of processing increasingly big and complex data as a consequence of new detectors. Finally, the year saw detailed planning of implementation of new capabilities as part of the Diamond-II proposed upgrade programme.

The following presents selected highlights from exciting developments across a broad range of activities that have taken place within the SSCC department during the past year.

Strategy for the Scientific Software, Controls and Computation

The Strategy was the first published by SSCC. It is designed to present a vision for how the department will meet forthcoming challenges in software, controls and computing. Its development included extensive consultation within Diamond to explore and understand future science needs and drivers. From this a Vision and a set of Goals were derived, and these in turn informed development of a series of critical objectives to define future direction. Implementation of the objectives will be realised through a series of technical research and development roadmaps. Following an internal review of the Strategy at the end of 2019, an overview was presented to Diamond's Science Advisory Committee (SAC) in 2020, and a programme to develop the technical R&D roadmaps is underway. The result of this strategic exercise forms a foundation on which to build and deliver essential services to support Diamond's science programme.

Vision for SSCC

SSCC's vision is encapsulated as follows:

- The SSCC Department will **maximise knowledge generated** by Diamond **across every science discipline**, through a modern, integrated approach to delivery and management of software and computing.
- SSCC will **enhance science capabilities** through: more intuitive user applications, greater automation of analysis, increased remote capabilities, greater automation, faster detector readout and real-time visualisation.
- SSCC will enable **greater data usability** through Findable, Accessible, Interoperable and Reusable (FAIR) and Open Data, and through new capabilities in data science (Machine Learning and Artificial Intelligence), modelling and analysis.

Goals for SSCC

SSCC's goals are to:

- Deliver **high quality** software, computing and controls **provision and support** in order to enable Diamond's science programme: **from experiment approval to publication**.
- Establish **strong partnerships**, internally and externally the Science and Technology Facilities Council (STFC), other facilities, universities, etc); to deliver best in class software and computing in a **collaborative, effective and sustainable** way.
- Deliver **a step change in** experiment **capabilities** and **efficiencies**, across the science programme, through: intuitive useable applications; automated analysis of data; remote access capabilities; automation of instrument and sample management; high speed readout of detectors; and near real-time data process for visualisation feedback.
- **Widen experimental data exploitation** through delivering: FAIR and Open Data, and through new capabilities in data science (Machine Learning (ML) and Artificial Intelligence (AI)), modelling and analysis.
- Realise a **hybrid computing model**, which delivers on-site computing services to those applications for which low latency and high bandwidth are essential, with all other services delivered through cloud computing.

Scientific Computing for remote operations

Diamond has led internationally in providing remote access for its users to synchrotron beamlines and electron microscopes. Remote operation is delivered through a NoMachine NX software service, which provides users with a remote desktop experience, equivalent to being physically at the

Figure 1: Full remote operation and data acquisition on a Diamond beamline is possible using the infrastructure provided by the Scientific Computing team. Image courtesy Juan Sanchez-Weatherby.

instrument, and so enable sophisticated experiments to be performed completely remotely. In response to the COVID-19 induced changes to working practices, remote operation capability has been significantly expanded. The suite of instruments that can offer users remote operation now includes 12 Electron Microscopes and 29 photon beamlines and end stations; with remote operation enabled on 17 of those beamlines in the past year. Remote operation of instruments relies on more than just software to provide secure and easy access, it relies on software applications and control protocols that ensure the experiment can be conducted safely and reliably. Diamond continues to innovate to improve scientists' experience of remote operations and to ensure scientific exploration can continue efficiently and effectively. In the past year this has enabled Diamond to deliver science that otherwise would not have been possible.

Data Analysis to support COVID-19 science programme

Timely and effective development in data processing and analysis capabilities, in response to the pandemic, has been a significant feature of data analysis developments undertaken over the past year. The Macromolecular Crystallography (MX) analysis team has both contributed directly to the COVID-19 science programme at Diamond, and also worked to ensure Diamond can operate as normal a service as possible for external users of the facility. Some of Diamond's academic and industrial users have programmes of scientific research that directly address understanding of the function of the SARS-CoV-2 virus.

The MX instruments were already strongly placed following historical emphasis on remote operation of data collection, and recent initiatives to enable Unattended Data Collection (UDC). Social restrictions resulting from COVID-19 accelerated developments, as follows:

- UDC was subject to continuous improvements related to experimental decision making, including an extension to be able to screen samples to inform experimental parameters. This significantly increased capacity for the number of data collections per day on beamline I03 where it is fully implemented. The extension is being deployed and tested on three further beamlines.
- Processing prioritisation was addressed, to enable best utilisation of computing resources. By automating data collection, it is possible to support analysis of large data sets, enabling timely data analysis.
- Significant improvements in multi-crystal data analysis (Fig. 2) were realised through close collaboration between the MX data analysis team and beamline staff. The improvements were applied to room temperature *in situ* ligand-screening experiments on SARS-CoV-2 Main Protease (MPro).
- Automatic data uploads to Zenodo (https://zenodo.org/record/3730917) were implemented for the early phase of MPro drug binding studies, in order to make this data accessible to the scientific community as early as possible.

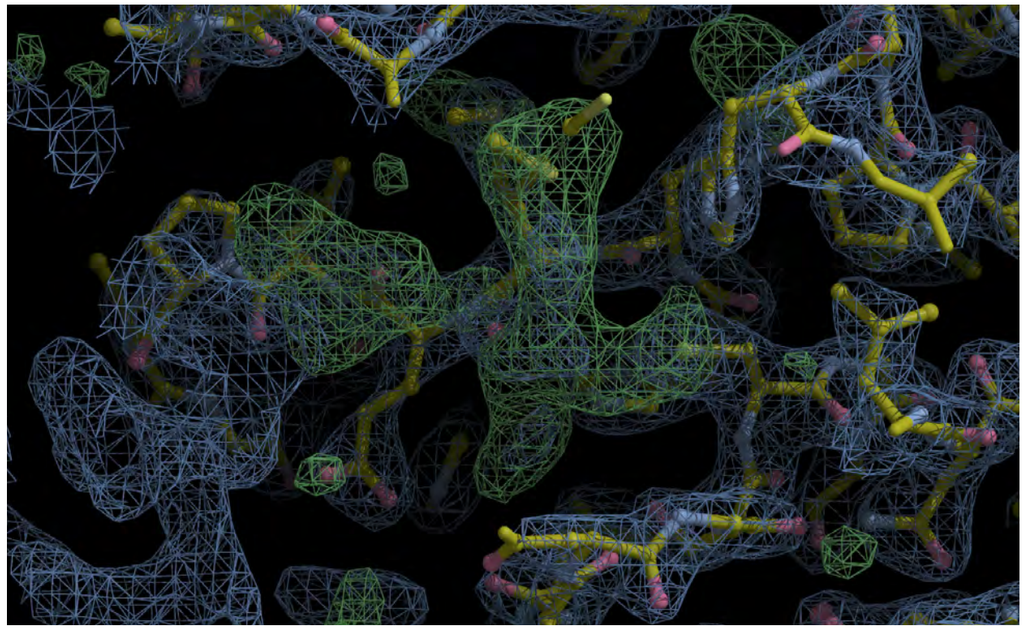

Figure 2: Automated multi-crystal analysis for SARS-COV-2 on beamlines I24 and VMXi.

- Before structures were released to the Protein Data Bank, fragment screening *(https://fragalysis.diamond.ac.uk/viewer/react/landing/)* was used to find lead compounds for the development of drugs, and results were published *(https://www.diamond.ac.uk/covid-19/for-scientists/NSP13-Helicase-Structure-and-XChem.html)*.

Taken together, improvements to UDC and priority processing have allowed hundreds of COVID-related samples (DOnCoV19 protease: 318 Mpro: 242 CovidRBD:154) to be collected on MX beamline I03 with no manual interaction. This success represents a good basis on which to develop future highly automated beamlines for Diamond-II. While it was necessary in the early phases of the COVID-19 research to do specific data analysis enabling work, recent improvements do not require special treatment.

Developing Open Data, and FAIR Data

Diamond manages an archive of users' data which contains some 3.2 billion files and 28 PB data being collected (Fig. 3), SSCC has led a number of initiatives to develop and support an improved data archiving service for Diamond's user community. Planned improvements include providing easy and convenient access, and better long-term management of data.

A Diamond Data Store (DDS) project is responsible for planning and managing continued development of the data archive at Diamond. The project is a collaboration between STFC and Diamond, and is considering all aspects of Diamond's archiving needs. Over the last year significant analysis work has taken place on whether the current archive infrastructure remains best placed to serve Diamond's needs, or whether alternative solutions would provide a better service. The conclusion from this evaluation is that the current approach remains suited to meet requirements, and the next step is to develop and improve the service.

Further work undertaken as part of the DDS project has been to improve the amount and quality of scientific and administrative metadata collected within the current data archive. Metadata facilitates searching and finding datasets and is particularly important for users unfamiliar with the data. The metadata work looks to increase the amount of data that is extracted from other systems such as the User Administration System (UAS), the Laboratory Information Management System (LIMS), and raw data files – in order to contextualise data that is being stored long term.

Other work planned for the next year is to support minting of Digital Object Identifiers (DOIs) to provide persistent, interoperable identifiers for each data set, together with implementation of an open interface as a mechanism to support data interoperability at Diamond.

SSCC has made a substantial contribution to the ExPaNDS *(https://expands.eu/)* project, which supports development of Findable, Accessible, Interoperable and Reusable (FAIR) data, through a European initiative to deliver integrated and interoperable data sources and data analysis services for photon and neutron national research infrastructures. Diamond is proud to be part of a work package developing European Open Science Cloud (EOSC) Data Catalogue Services and EOSC Data Analysis Services (the Communications Group at Diamond leads a work package on Outreach and Communications). Diamond also supports management of other work packages developing ontologies and analysis services to support interoperability. Working with colleagues from light sources across Europe, it embodies a collaborative approach to improving FAIR data services.

Data Acquisition for Diamond's newest beamline, DIAD

A significant Data Acquisition achievement in the past year was to provide the Generics Data Acquisition (GDA) Software with new functionality and features to support Diamond's newest beamline, DIAD (Dual Imaging And Diffraction). New functionality included development of highly cohesive and user-friendly perspectives for configuring and monitoring diffraction and tomography scans on the same sample. In addition, a new data service for communicating scan requests to the GDA server was commissioned.

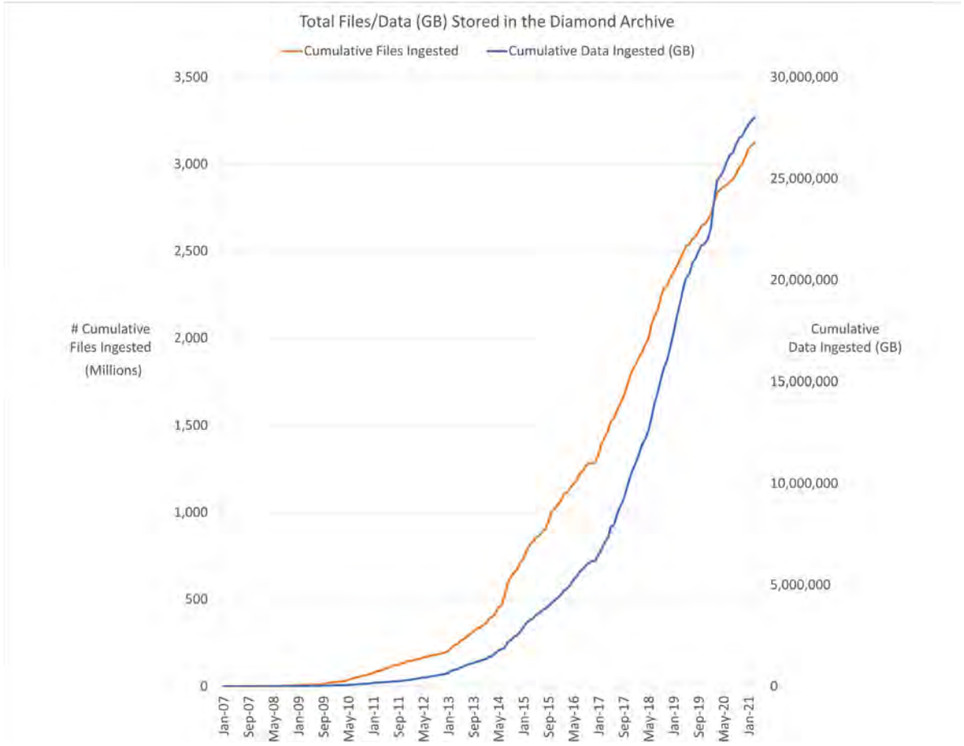

Figure 3: Total number of files and volume of data stored in Diamond Archive.

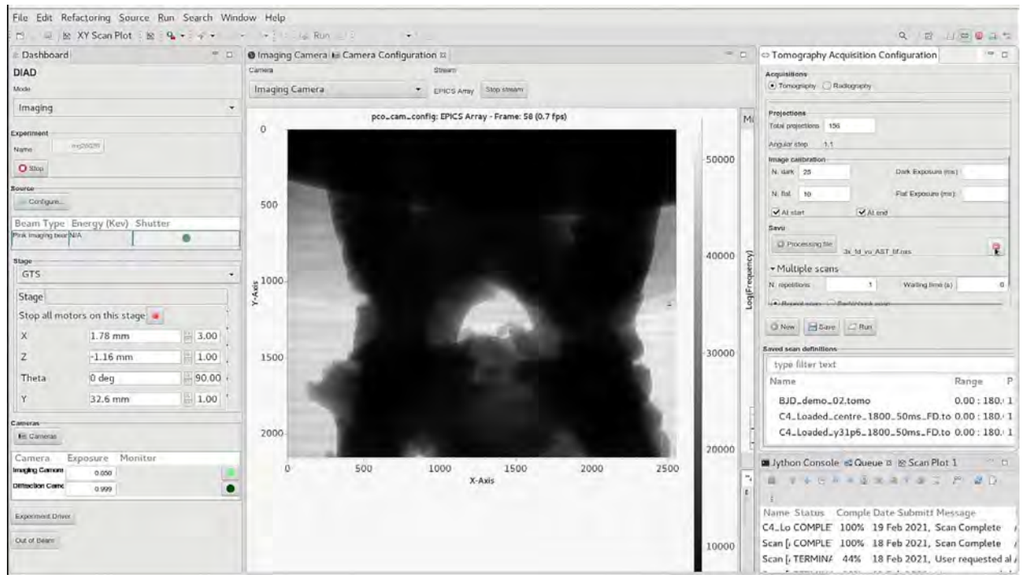

Figure 4: DIAD User Interface showing the Tomography Perspective.

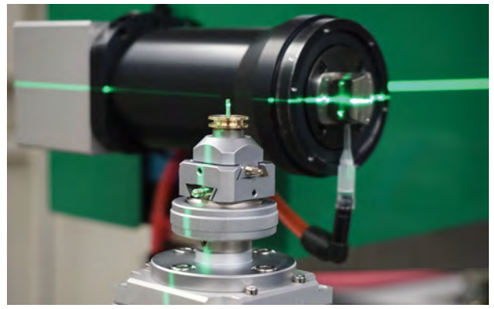

Figure 5: Sample being aligned in on DIAD beamline (green light is sample alignment laser).

A tomography (cross-sectional imaging) perspective (Fig. 4), developed for DIAD, was designed to be highly flexible and was developed following consultation with Diamond's Tomography Working Group. The solution will be re-used for the I12 Tomography project, along with a scan requests service.

A new scan requests service, developed for DIAD, provides a more flexible mechanism which describes an acquisition as a simple text document encoded in JavaScript Object Notation (JSON). The JSON acquisition request conforms to a hierarchical data model. This is part of a solution which will form the basis of a generic client-to-server service interface for any kind of acquisition. The Data Acquisition Group plans to adapt the scan requests service as part of ongoing server developments, thereby making it more widely available to other beamline in Diamond.

DIAD successfully hosted its first user experiment in February 2021. This looked at a shape memory alloy (Fig. 5) under deformation; with tomography used to visualise large-scale changes, and diffraction used to measure atomic strain. The new DIAD perspectives were used both to define the experiment and to collect the data (Fig. 6).

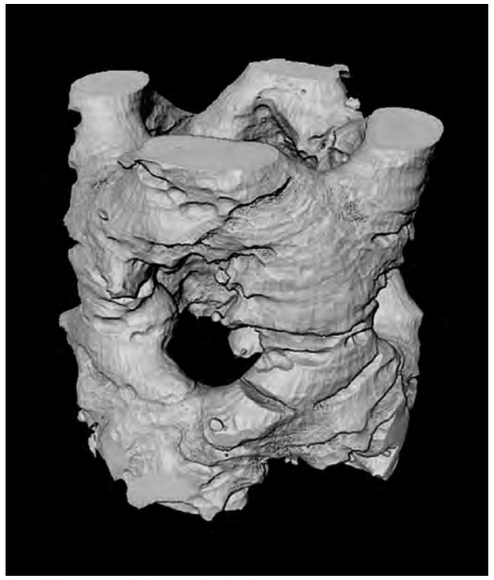

Figure 6: 3D Tomographic Reconstruction of the Sample.

SSCC perspective

Over the past year, SSCC has matured as a department, published its strategy, defined a vision and goals, and worked in close partnership with Diamond's scientific community. Highlights included in this Annual Review give a glimpse into SSCC's achievements; there are many more that could have been reported. SSCC has invested significantly in preparing for Diamond-II, resources identified, initial recruitment undertaken, and started project planning to ensure future Diamond-II deadlines will be met. SSCC has put foundations in place that will enable it to continue to provide the best possible delivery and support for software, computing and control systems.

Industrial Liaison

Industrial Liaison Office Team

An annual review is a time to reflect on the activities of the previous year; to highlight the achievements and celebrate the successes of the team and our industrial partners and colleagues. This has been a year like no other, and while we mourn for those lost and remember those struggling, it is also right that we should take time to recognise some of the most positive moments of the last year.

The huge changes at Diamond Light Source, throughout the UK and across the globe have presented unexpected situations, but we are pleased to report that our colleagues and team members have risen to the challenge and successfully moved the behind-the-scenes operations of the Industrial Liaison Office (ILO) team to home offices across Oxfordshire and Berkshire. Through many hours of Zoom and Teams calls we have got to know our clients better, often quite literally being welcomed into their lives and homes, meeting their families and their pets as they have come to know us better too. Our shared understanding of the pressures and goals and strong desire to collaborate to achieve results in extraordinary circumstances has highlighted this as a period in which the most human elements of scientific research have been brought to the fore.

When lockdown started in mid-March 2020, and Diamond's operations were restricted to COVID-19 research, the ILO XChem team - Alex Dias and Ailsa Powell - had already spent a significant amount of time working on a variety of Diamond's collaborative COVID-19 research projects. This continued at a pace until industrial life science services resumed in May. Their work has been featured widely in the media and has contributed to our understanding of the SARS-CoV-2 virus and helped support the design of potential therapeutics.

Ailsa Powell mounting and freezing XChem crystals.

Of course, remote working is not a new concept for Diamond's life science beamlines and the years of preparation and optimisation have ensured a very smooth and easy transition to this new way of working. Data management systems are in place to support sample shipments and tracking and secure external access, making preparations from the client side simple and straightforward. State of the art robotics and automation enable fast, accurate and reliable instrument control from labs, offices and kitchen tables all over the world. Data processing pipelines and access to our computer cluster permits data to be downloaded remotely in an easily digestible and useful form, ready to provide insight into the project at hand. Cryo-electron microscopy, macromolecular crystallography, fragment screening and small angle scattering services are in high demand and the industrial programme is thriving.

Our mail-in data collection services continue to be very popular, as travel restrictions limit movement of personnel, and samples can be prepared and shipped directly to us for experiments. The samples can then be prepared by our expert staff, if needed, or proceed directly to data collection. Our team has many years of experience in successfully designing and delivering mail-in experiments and therefore are easily able to accommodate any additional challenges presented by the current circumstances. Although Diamond has been running a limited operational timetable, the demand from academia has in some areas reduced while university lab access was restricted, creating opportunities for greater flexibility and access for industry in some cases.

In the late summer and autumn of 2020, physical sciences experiments resumed for industrial clients. These instruments tend to accommodate a wide range of different sample and technique options and, as such, require more staff time physically on site to optimise the experiments. As local and national restrictions were relaxed, the possibilities of more complex experiments were realised and the physical science team were able to put their long-held plans into action. Diffraction, imaging, small angle scattering and spectroscopy services are running regularly to support our clients across a wide range of sectors.

A significant body of work was also undertaken across our marketing and communications portfolio to ensure that the most relevant and accessible information is available to our clients whatever their area of interest or level of expertise with synchrotron techniques. If you would like to learn more about any of these aspects or for further updates, please visit our website at *www.diamond.ac.uk/industry* or follow us on LinkedIn (Diamond Industrial Liaison Group) or Twitter (@DiamondILO).

Throughout the pandemic, Diamond has supported our industrial clients across a wide range of techniques and we continue to do so, so rest assured that if you have a project in mind or an analytical need to discuss, please do get in touch on industry@diamond.ac.uk and we will do our utmost to make it a reality.

Designing complex experiments for efficiency and success is a skill at the best of times, but designing, planning and executing experiments mid-pandemic successfully takes a special blend of experience, expertise, forethought and excellent communication, ably demonstrated by the ILO team this year. We would also like to take this opportunity to recognise our Diamond colleagues across the organisation who have been instrumental in ensuring that industrial beamtime has the minimal possible disruption as we continue to offer excellent services, safely, to our highly valued clients.

Alex Dias loading pucks onto the beamline for MX data collection.

Jitka Waterman handling client samples for mail in data collection.

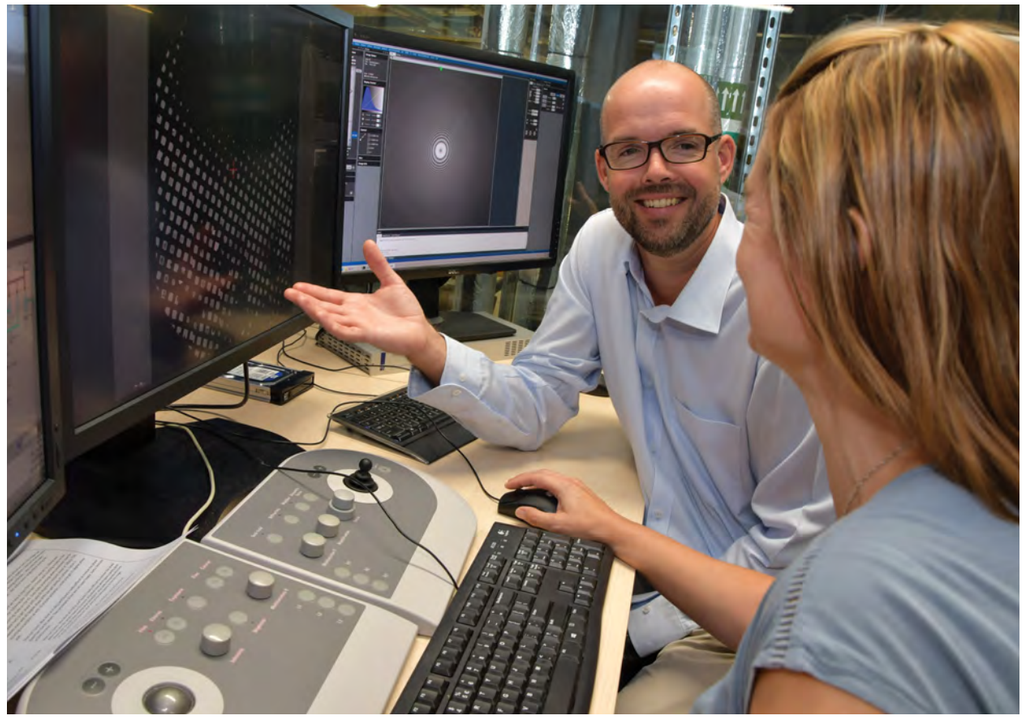

Jason van Rooyen demonstrating cryo-EM experiments to Rachel Freeman. All photos taken pre-pandemic.

Engaging with Diamond Light Source

Communications and Engagement Team

Engaging with and inspiring the public continues to be a key part of the Diamond vision. The COVID-19 pandemic over the past year has had a major impact on engagement; it has not ceased, but the focus has shifted from on-site to virtual and remote activities. Diamond has moved rapidly to develop new programmes and systems to reach new and existing audiences and keep engaging and supporting during this unusual time.

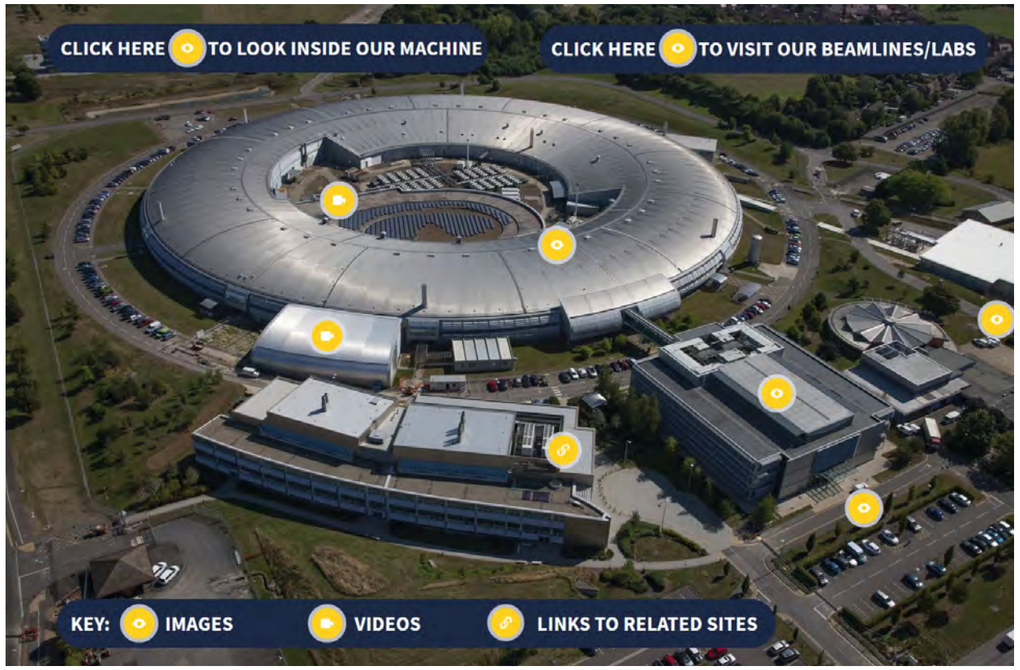

Screenshot of Diamond's interactive map – enabling the public to take virtual visits of the synchrotron.

During the past year Diamond has had approximately 9,606 significant interactions (30 + minutes) with 'virtual' visitors, including 3,077 for scientific and technical events, 286 undergraduate and postgraduate interactions, 6,161 school students and members of the public, and 82 VIPs and stakeholders.

The increased need to engage remotely has this year seen Diamond embrace technology to engage with audiences, supporting schools, students and other publics often restricted to being at home for long periods. A new series of family webinars has been developed, working with Diamond staff and users to cover a range of subjects, and new video technologies have been used to allow us to deliver 'live' virtual tours to students, academics, and the general public. Interactive video and other media resources have been developed, allowing visitors to our website to virtually explore the Diamond facility for themselves.

> *"It was great to be able to see inside the beamline and the experimental hutch. The link between the crystallography results and the 3D structure of the protein was also excellent.*
>
> *Thank you so much, it's difficult to do much extra-curricular at the moment so this is a real treat."*
>
> ***-A schoolteacher who brought their year 12 class to a virtual schools visit***

While schools have been unable to visit, we have continued to support students, running virtual schools events and moving our schools work experience programme online. This had the benefit of allowing us to expand the programme and offer a virtual experience to all of the original applicants. In July 2020, we welcomed over 100 students to three days of talks and workshops run by staff across all areas of Diamond, from vacuum systems to growing proteins, giving students a flavour of many different areas of work and a real insight into the variation of roles available as a career.

> *"I thought it was great that it was offered to everyone who applied.*
>
> *I have very much enjoyed the experience and would encourage other people to do this work experience. Lots of information, detailed, in-depth and fascinating!"*
>
> ***- 2020 work experience students***

Over the past year we have updated our public engagement strategy and reinforced our commitment to widening participation and diversity within STEM (Science, Technology, Engineering and Mathematics), and so were proud to partner with the Social Mobility Foundation, to distribute copies of the Diamond Board Game, and with BBSTEM (Black British Professionals in STEM) to coordinate a virtual visit for their members.

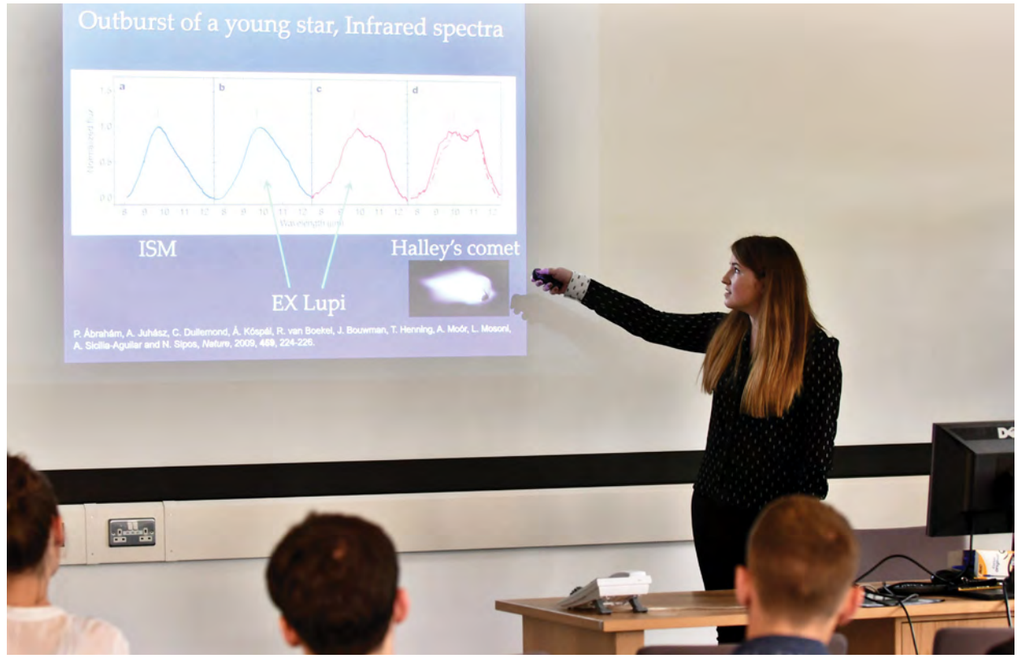

Pre-pandemic, Year in Industry student, Anna Herlihy, delivers a talk to the 2016-17 cohort.

The pandemic has not stopped either our core programme or our regular partnership events, in particular with our neighbours at the Science and Technology Facilities Council (STFC), with whom we have delivered virtual stargazing events; a 'Science in your future' event for girls; and particle physics masterclasses. The online nature of activities this year has helped in developing new partnerships as well, working with Daresbury Laboratory to support school events and SMASH_UK to help develop an interactive virtual reality (VR) science game for school students.

> *"I was inspired by the work we did crystallising haemoglobin in the labs at Diamond to read more about proteins...I wouldn't have thought to take the module if not for my week at Diamond.*
> *With all teaching at university being online this year the time I spent in the labs at Diamond has been really valuable."*
>
> ***- A previous work experience student now studying natural sciences at university***

Higher Education engagement

Training of students through our undergraduate placements and PhD programmes continues to be one of the core engagement activities, in support of the organisation's vision to continuously plan for Diamond's technical and scientific future. Diamond offers students a range of opportunities to engage with and learn from world-leading staff and resources, developing and inspiring the next generation of scientists and engineers.

Like many other areas within Diamond, Student Engagement activities were impacted by the COVID-19 pandemic. Our first priority was to make sure that our current PhD and Year in Industry students were well supported and kept informed of the changing circumstances as the pandemic evolved in late March 2020. We had regular meetings with the 2019 cohort of Year in Industry students and contacted all 13 university placement supervisors to make sure they knew the steps that Diamond had taken and how we were supporting students. We quickly established an extension request procedure for the PhD students who might have been impacted by closures at their university campus and laboratories. To date we have supported 15 PhD student extensions. Throughout the pandemic, Diamond has continued to allow access to PhD students for beamtime and access to laboratories as part of the priority access route.

Despite the restrictions, we welcomed 32 new PhD students as part of the 2020 cohort, co-funded with 17 different universities and world leading research facilities. This brings the total number of ongoing Diamond PhD studentships to 104. There were 46 submissions to the 2021 Diamond Doctoral Studentship call for proposals. These submissions were linked with 33 different universities and institutions. Following the internal review process, we will be welcoming 24 students in October 2021. The PhD student annual progress meetings with Diamond's Student Engagement team have been more valuable than ever this year, providing an opportunity to check-in with each student in year two and above individually. As we haven't been able to personally welcome the new 2020 cohort to Diamond site, we have also held virtual welcome meetings with each of the students to provide an opportunity for them to ask questions and to formally introduce them to the Diamond studentship programme.

Due to the uncertainty at the start of the pandemic in March 2020, we took the difficult decision to cancel the 2020 Summer Placement programme that was due to start in June the same year. Any students who had been recruited and would still be eligible for their placements in summer 2021

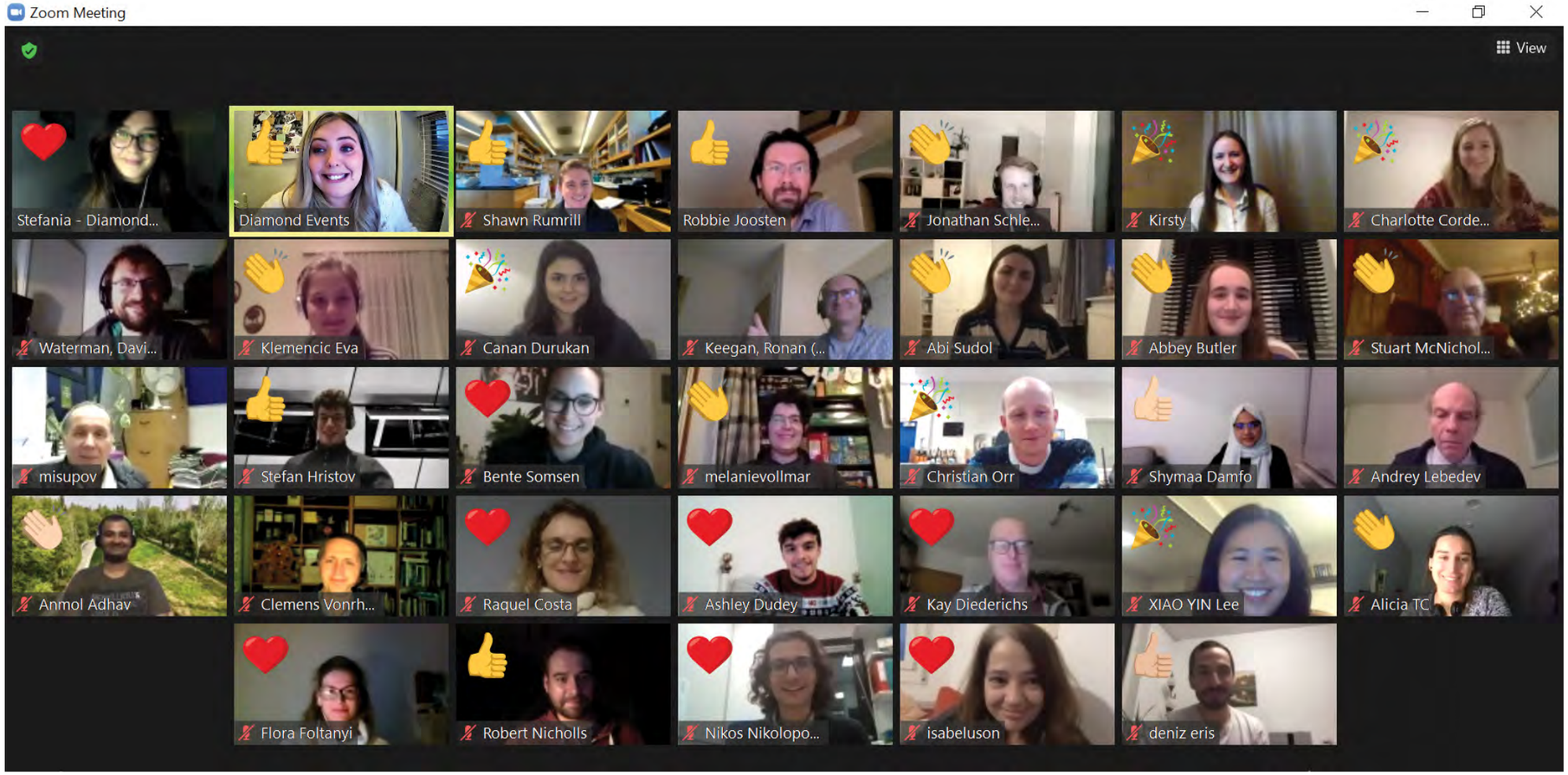

Zoom attendees of the Diamond-CCP4 Data Collection and Structure Solution Workshop, late 2020.

were offered the opportunity to join the 2021 cohort. We were able to transfer three students to start on the 2021 Summer Placement programme. For the thirteen 12-month Year in Industry students, the decision was made to delay the start of the placement from June to September of 2020. We were delighted to welcome the students to Diamond via a series of virtual events, and all students who needed to have been able to access Diamond when required for their project. The projects undertaken by the Year in Industry students ranged from scientific software and computing projects to life and physical science projects. These 12-month Year in Industry projects are ongoing. As well as the main student projects, Diamond also provides undergraduate students with training on presentation skills, media and public engagement.

Student visits were impacted quite heavily due to the pandemic, being affected both by access to site and a change in teaching arrangements at universities. However, Diamond managed to support 11 virtual visits from undergraduate and postgraduate groups, offering a range of talks and training.

Scientific workshops and conferences

In line with Diamond's Vision to drive and support science at UK universities and research institutes, the facility organises a broad portfolio of scientific and technical workshops, training courses and conferences tailored towards the needs of our staff and user community, with whom we continue to train, inform and learn from.

Due to the pandemic, several on-site events organised between March and May 2020 were cancelled or postponed. We worked swiftly to adapt them into virtual-friendly formats and began running online events from June 2020 onwards using Zoom's Webinar and Meeting licenses. Since then we have delivered seminars, conferences, training courses and even practical workshops requiring remote access to beamlines, and welcomed an increase in attendance up 57% on 2019/20.

"Access to very well maintained labs as well as being situated close to beamlines day to day enabled me to perform high quality work in a pleasant environment. The professional environment worked well for me and I feel is not only very conducive to individual achievement but also provides opportunity for advice and potential collaboration with experts in their respective fields."

- A Diamond PhD student sharing their thoughts on working within Diamond during their PhD studies

"This was an overall fantastic workshop. To date, I think this is the most valuable training I could have obtained as someone who is earning their PhD based in X-ray crystallographic research."

- PhD student attending the Diamond-CCP4 Data Collection and Structure Solution Workshop, Dec 2020

In addition, we delivered 13 community engagement webinars as part of the Diamond-II proposed upgrade programme. User Working Groups for each Diamond-II flagship beamline project presented their proposals and outline science cases to their respective user communities. Webinar attendees were able to glean further insight into these flagship projects through scientific case studies, as well as having the opportunity to feed into the proposals through interactive question and answer sessions.

Date	Event	Participants
22 June 2020	MX Bag Training	26
7, 10 July 2020	Infrared Analysis Training	26
13, 14, 20, 21 July 2020	Basic Small Angle Scattering Training School	18
30 July 2020	Mini MX Data Processing Workshop	42
9 September 2020	ePSIC User Meeting	110
14 - 19 September 2020	Introduction to Machine Learning Course	26
17 September 2020	Diamond-II Webinar: New Beamline for Fast Operando Spectroscopy (SWIFT)	97
21-22 September 2020	S4SAS Conference 2020	205
14 October 2020	Diamond-II Webinar: New Beamline for X-ray Raman Scattering and pink-beam XES (BERRIES)	131
22 October 2020	Diamond Seminar	45
26 October 2020	Diamond-II Webinar: New Nanofocus Extreme Conditions Undulator Beamline (NExCUBe)	79
26 - 30 October 2020	Early Career Scientist Symposium	200
28 October 2020	Diamond-II Webinar: New Beamline for Coherent Soft X-Ray Imaging and Diffraction (CSXID); I16 and I21 Upgrades	89
2 November 2020	Diamond-II Webinar: Upgrade to I15: reconfiguration to a high energy microfocus beamline (μ15)	99
3 November 2020	Diamond-II Webinar: I24 KMX – kinetics and microfocus upgrade	99
4 November 2020	Diamond-II Webinar: New Beamline for Fast Operando Spectroscopy (SWIFT)	86
5 November 2020	Diamond-II Webinar: Upgrade VerSoX: An undulator source for Ambient Pressure XPS	69
5 November 2020	Diamond Seminar	54
9 November 2020	Diamond-II Webinar: New Beamline for nano-ARPES	118
10 November 2020	Diamond-II Webinar: New Large Volume Nanoscale BioImaging Beamline	205
12 November 2020	Diamond Seminar	36
13 November 2020	Diamond-II Webinar: I13L Upgrade	145
16 November 2020	Diamond-II Webinar: K04 Rebuild for XChem	159
19 November 2020	Diamond Seminar	78
30 Nov - 11 Dec 2020	Diamond-CCP4 Data Collection & Structure Solution Workshop	20
3 December 2020	Diamond Seminar	54
10 December 2020	Diamond Seminar	18
12 February 2021	Diamond Data Store Seminar	96
18 February 20221	Diamond Seminar	41
4 March 2021	Diamond Seminar	57
15 - 17 March 2021	CONEXS (Collaborative Network for X-ray Spectroscopy) Workshop	32
17 - 19 March 2021	CONEXS (Collaborative Network for X-ray Spectroscopy) Conference	188
22, 23, 25 March 2021	Advanced Infrared Microspectroscopy Analysis Training	32

Governance and Management

Diamond Light Source Ltd was established in 2002 as a joint venture limited company funded by the UK Government via the Science and Technology Facilities Council (STFC), now under UK Research & Innovation (UKRI), and by the Wellcome Trust, owning 86% and 14% of the shares respectively. Diamond now employs 775 scientists, engineers, technicians and support staff from 44 countries worldwide. The Chief Executive and Directors are advised by committees representing key stakeholder groups, including the Science Advisory Committee (SAC), Diamond Industrial Science Committe (DISCo) and Diamond User Committee (DUC).

Diamond is free at the point of access for researchers accessing Diamond via peer review, and provided the results are published in the public domain for everyone's benefit. Allocation of beamtime is via a peer review process to select proposals on the basis of scientific merit and technical feasibility. Twelve peer review panels meet twice a year to assess the proposals submitted for each six-month allocation period. Diamond also welcomes industrial researchers through a range of access modes including proprietary research.

Board of Directors

Prof. Sir Adrian Smith (Chairman)
Prof. Andrew Harrison OBE
Anna Curson
Marshall Davies
Prof. Michael Fitzpatrick
Prof. Mark Thomson
Andrea Ward
Prof. Keith Wilson

Company Secretary
Dr Christopher Green

As at April 2021

Executive

Prof. Andrew Harrison OBE took the helm as CEO of Diamond Light Source in January 2014. He was previously Director General of the Institut Laue-Langevin neutron source in Grenoble, France, where he had worked since 2006. With a background as an inorganic chemist and Professor of Solid State Chemistry at the University of Edinburgh, Andrew brings a wealth of experience of scientific leadership to the organisation. Andrew was awarded an OBE in the Queen's Birthday Honours Lists 2020 for services to science during the COVID-19 response.

Prof. Laurent Chapon joined Diamond as Director of Physical Sciences in 2016 from the Institut Laue-Langevin in Grenoble, France. Whilst there, Laurent was Senior Fellow and Leader of the Diffraction Group for over five years. He is an expert in materials science as well as X-ray and neutron diffraction techniques. His principal interests include transmission metal oxides, frustrated oxides, and multiferroics.

Prof. Sir David Stuart is MRC Professor of Structural Biology at the University of Oxford, and Joint Head of the Division of Structural Biology at the Department of Clinical Medicine. He was appointed Director of Life Sciences at Diamond in 2008. His principal research interests include the structure of viruses and viral proteins as well as cellular proteins, especially those that interact with viruses. Dave was knighted in the New Year Honours list 2021 for services to medical research and the scientific community.

Prof. Richard Walker joined Diamond Light Source as Technical Director in January 2002. He was previously Director of the Light Sources Division at Sincrotrone Trieste in Italy, and prior to that he was a key member of the Daresbury Laboratory SRS team. Richard is a visiting Professor of Physics at the University of Oxford.

Andrea Ward joined Diamond as Director of Finance and Corporate Services in 2019, with 15 years' experience as a Senior Finance professional. During a 12-year tenure at Vertex Pharmaceuticals, she worked with the Board to lead finance and procurement functions in Europe, later moving to Canada with the business to assist with acquisition and commercialisation opportunities. Andrea has also worked at ResMed and the Ontario Lottery and Gaming Corporation.

Staffing and Financial Information

Outline Organisational Chart

Chief Executive's Office
Communications
Industrial Liaison
Safety, Health & Environment

Science Division

Science Groups:
Biological Cryo-Imaging
Crystallography
Imaging and Microscopy
Macromolecular Crystallography
Magnetic Materials
Soft Condensed Matter
Spectroscopy
Structures and Surfaces

Scientific Software, Controls & Computation Groups:
Accelerator Control Systems
Beamline Control Systems
Data Acquisition
Scientific Computing
Scientific Software

Detector Group
Experimental Hall Labs Services
Optics & Metrology
Planning & Projects Office
User Office

Technical Division
Accelerator Physics
Diagnostics
Engineering
Insertion Devices
Installation & Facility Management
Operations
Power Supplies
Radiofrequency Systems
Vacuum

Finance and Corporate Services
Corporate IT
Commercial Management, Governance & Legal
Finance
Human Resources
Procurement & Goods Handling
Soft Facilities

Summary of Financial Data

	2009/10	2010/11	2011/12	2012/13	2013/14	2014/15	2015/16	2016/17	2017/18	2018/19	2019/20	2020/21
Operating Costs £m	30.5	33.5	36.5	39.9	42.5	44.5	54.6	56.9	62.8	64.5	65.7	69.2
Total Staff (Year End)	401	419	438	481	507	534	582	609	639	680	742	775
Capital Expenditure – Operations £m	5.7	8.6	5.1	8.0	7.5	6.2	8.0	10.5	12.8	17.4	17.8	24.1
Phase II £m	22.0	16.2	9.9	2.8	0.8	0.2	0.0	0.0	0.0	0.0	0.0	0.0
Phase III £m	0.3	3.0	10.3	14.2	17.2	23.7	20.6	11.5	3.7	1.0	0.0	0.0
Other capital projects £m						4.8	5.6	7.3	4.3	5.3	1	2.1

Figures up to and including 2014/15 exclude VAT, thereafter figures include VAT. Figures for 2020/21 are subject to final published Statutory accounts.

Committee Membership

The Scientific Advisory Committee (SAC) advises the CEO and the Science Directors on the scientific and technical questions impacting the specification, design, commissioning and operation of the facility; experimental and user support facilities, and opportunities for scientific exploitation.

Dr Tom Hase (Chair)
University of Warwick (UK)

Dr Paul Adams
Lawrence Berkeley National Laboratory (USA)

Dr John Barker, Evotec
(DISCo Representative)

Dr Bridget Carragher
New York Center for Structural Biology (USA)

Prof. John SO Evans
University of Durham (UK)

Prof. Philip Hofmann
Aarhus University (Denmark)

Prof. Ken Lewtas
Lewtas Science & Technologies (DISCo Representative)

Dr Adrian Mancuso
European XFEL

Dr Lisa Miller
Brookhaven National Lab/NSLS-II (USA)

Dr Jörg Raabe
PSI (Switzerland)

Prof. Andrea Russell
University of Southampton (UK) - (Chair of the DUC)

Prof. Mary Ryan
Imperial College (UK)

Prof. Christian Schroer
DESY (Germany)

Prof. Sam Shaw
University of Manchester (UK)

Prof. Titia Sixma
Netherlands Cancer Institute (Netherlands)

Prof. Elizabeth Wright
University of Wisconsin-Madison (USA)

The Diamond Industrial Science Committee (DISCo) advises the CEO and Directors on opportunities for industry to be engaged in research at Diamond, industrial research priorities that will help shape operational strategy, including the best way to exploit the current suite of beamlines and to develop the case for investment in future beamlines, and to develop best practice for industrial engagement.

Dr Malcolm Skingle
GlaxoSmithKline (Chair)

Dr John Barker
Evotec

Dr Andrew Barrow
Rolls-Royce

Prof. Dave Brown
Institut de Recherches Servier

Dr Liz Carpenter
Vertex Pharmaceuticals (Europe) Ltd

Dr Paul Collier
Johnson Matthey

Dr Rob Cooke
Sosei Heptares

Dr Cheryl Doherty
GlaxoSmithKline

Prof. Peter Dowding
Infineum

Prof. Jonathan Hyde
NNL

Dr Andrew Johnson
IQE

Dr Olga Kazakova
NPL

Prof. Ken Lewtas
Lewtas Science & Technologies

Dr Ellen Norman
RSSL

Dr Richard Storey
AstraZeneca

Dr Pamela Williams
Astex Pharmaceuticals

The Diamond User Committee (DUC) has been set as a platform for discussion between Diamond and the user community of matters relating to the operation and strategy of Diamond.

Dr Imad Ahmed
University of Oxford

Dr Arnaud Basle
University of Newcastle

Dr Gavin Bell
University of Warwick

Dr Jamie Blaza
The University of York

Dr David Briggs
The Francis Crick Institute

Dr Ann Chippindale
University of Reading

Dr Sean Connell
CIC bioGUNE

Dr Kevin Edmonds
The University of Nottingham

Dr Enrique Jimenez-Melero
The University of Manchester

Dr Tim Knowles
University of Birmingham

Dr Marcus Newton
University of Southampton

Dr Robin Perry
University College London

Prof. Andrea Russell
University of Southampton (Chair)

Dr Neil Telling
Keele University

Dr Andrew Thomas
The University of Manchester

Dr Arwen Tyler
University of Leeds

Membership as at April 2021

Diamond Light Source Ltd
Harwell Science & Innovation Campus
Didcot, Oxfordshire OX11 0DE
Tel: +44 (0)1235 778 639
Fax: +44 (0)1235 778 499
www.diamond.ac.uk

Acknowledgement:
We would like to thank the authors and all colleagues who contributed to this publication.

MIX
Paper from responsible sources
FSC® C007881

Printed on Forest Stewardship Council (FSC) accredited paper stock.

Published June 2021